ISSN en trámite

instituto de astronomía

unam

revista mexicana de astronomía y astrofísica

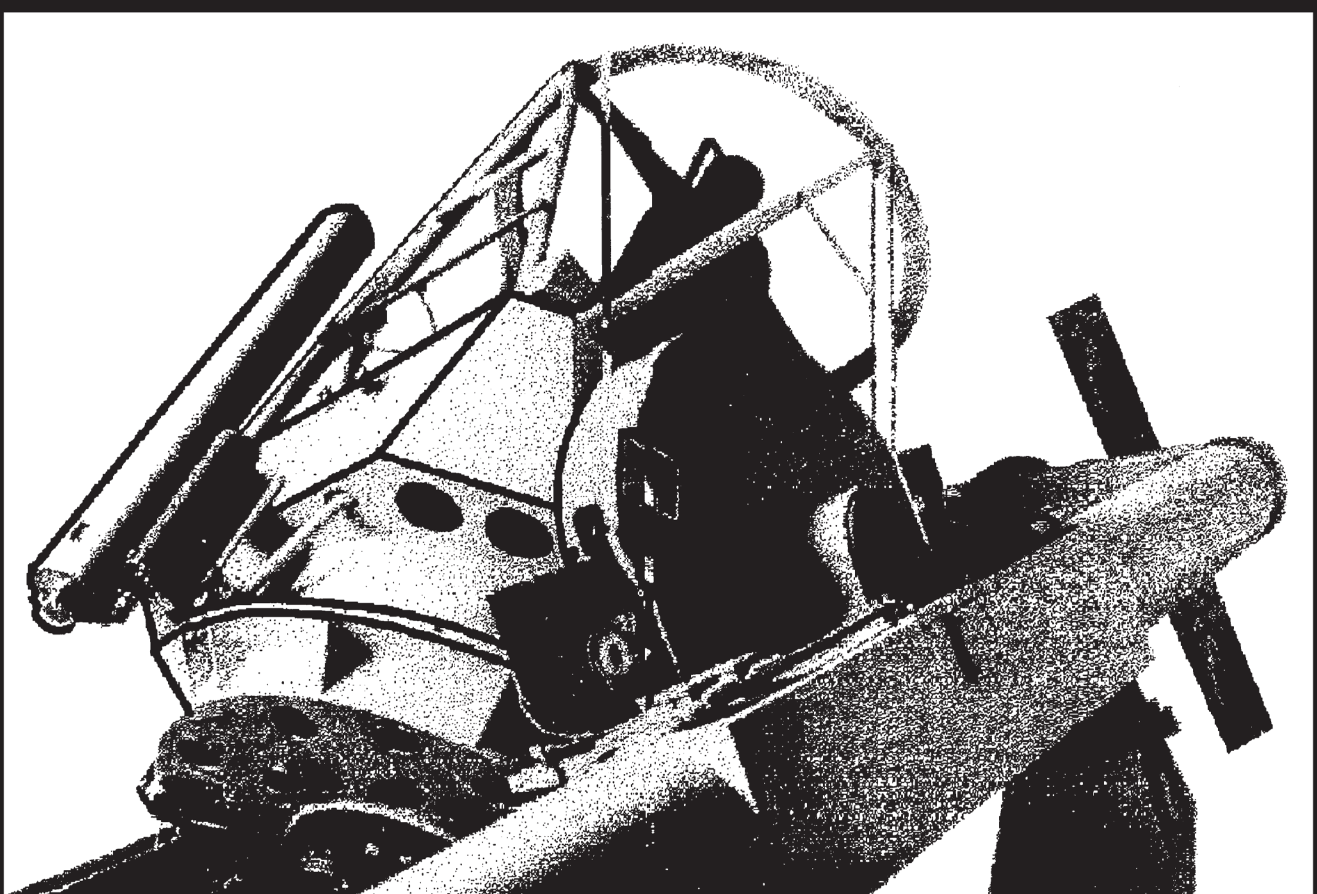

volumen 58
número 1
octubre 2022

volumen 58, número 1, abril 2022

revista mexicana de astronomía y astrofísica

Instituto de Astronomía
Universidad Nacional Autónoma de México

revista
mexicana de
astronomía
y astrofísica

ISSN en trámite

URL de DOI: https://doi.org/10.22201/ia.01851101p.2022.58.01

rmaa@astro.unam.mx

http://www.astroscu.unam.mx/RMxAA/

La *RMxAA* aparece indexada en Current Contents, Science Citation Index, Astronomy and Astrophysics Abstracts, Physics Briefs, Publicaciones Científicas en América Latina, Astronomy and Astrophysics Monthly Index, PERIODICA, RedALyC, Latindex y SciELO.

Revista Mexicana de Astronomía y Astrofísica, volumen 58, número 1, abril 2022, es una publicación semestral, editada y distribuida por el Instituto de Astronomía, UNAM, Circuito Exterior, Ciudad Universitaria, 04510, Alcaldía Coyoacán, Ciudad de México, Teléfono: 5556223906, Correo Electrónico: rmaa@astro.unam.mx, ISSN en trámite. Editora responsable: Christine Patricia Allen Armiño. Distribución: Bienes y Servicios del Instituto de Astronomía, UNAM. Impresa por Grupo Edición, S.A. de C.V., Xochicalco 619, Colonia Letrán Valle, 03650, Alcaldía Benito Juárez, Ciudad de México. Fecha de impresión: 27 de marzo de 2022. Número de ejemplares impresos: 500 en papel Couché de 100 gramos los interiores y en cartulina Couché de 250 gramos los forros. Precio de la publicación: gratuito.

Revista Mexicana de Astronomía y Astrofísica, **58**, 3–21 (2022)

https://doi.org/10.22201/ia.01851101p.2022.58.01.01

PRECISE MEASUREMENT OF ORBITAL AND PHYSICAL PARAMETERS OF BRIGHT DETACHED SOLAR ANALOG ECLIPSING BINARIES

Ömür Çakırlı[1], Barış Hoyman[1], Sara Bulut[1], Ahmet Dervişoğlu[2,3], and Cenk Kayhan[2]

Received April 12 2021; accepted September 17 2021

ABSTRACT

We combined photometry from the All Sky Automated Survey (ASAS) and the Transiting Exoplanet Survey Satellite (TESS) with high-resolution spectroscopy from the ESO public archive to obtain, for the first time, absolute physical and orbital parameters for six double-lined detached eclipsing binary systems with solar-type components. The atmospheric parameters of the stars have been determined from the individual spectra obtained with a disentangling method. One of the targets resulted in a triple system, and lines coming from three components in spectra show that each component's contribution to the total light is approximately equal. For the six systems the masses and radii of the components were obtained with a precision better than 3 %. A comparison of the observed stellar parameters with the prediction of stellar evolution based on the MESA stellar evolution code shows reasonable agreement.

RESUMEN

Combinamos datos fotométricos de los catálogos All Sky Automated Survey (ASAS) y Transiting Exoplanet Survey Satellite (TESS) con datos espectroscópicos de alta resolución del archivo público de ESO para obtener los parámetos físicos y orbitales absolutos de seis binarias eclipsantes separadas de doble línea, con componentes de tipo solar. Los parámetros atmosféricos se determinaron a partir de los espectros individuales obtenidos mediante un método para desenlazar. Una de las estrellas resultó ser un sistema triple; las líneas espectrales de las tres componentes muestran una contribución aproximadamente igual a la luz total. Se obtuvieron las masas y los radios de las componentes de los seis sistemas con una precisión mejor que 3 %. Los parámetros estelares observados concuerdan razonablemente bien con las predicciones del código de evolución estelar MESA.

Key Words: binaries: eclipsing — binaries: spectroscopic — stars: evolution — stars: fundamental parameters — stars: late-type

1. INTRODUCTION

One of the relevant goals in stellar astrophysics is understanding solar-type stars. The most direct way of studying them is when they are part of detached eclipsing binaries (DEBs). With these types of variable stars, it is possible to determine the fundamental stellar parameters (e.g. mass and radius) with a level of accuracy around 1 % (Southworth 2013). Specifically, it is assumed that both components in DEBs have not filled their Roche lobe yet, and thus evolve as single stars. Therefore, the two components of DEBs with well-determined parameters, through the application of very robust and simple mechanical principles, can provide a stringent test for the stellar evolutionary models. However, given that the current estimates of stellar masses and radii are still uncertain by as much as ten percent (e.g. Soderblom 2010; Valle et al. 2013), spectro-photometric studies of DEBs are of great importance.

Among these parameters, stellar mass plays an important role in stellar physics and the dynamics of stellar systems. It governs a star's entire evolution — determining which fuels it will burn and how long it will live. However, the vast majority of stellar masses are difficult to measure directly and are often estimated using the mass-luminosity relation. Determining this relation requires accurate and reliable data on stellar mass, mainly from binary star systems, especially detached eclipsing

[1]Ege University, Science Faculty, Astronomy and Space Science Dept., İzmir, Turkey.

[2]Department of Astronomy and Space Sciences, Erciyes University, 38039, Kayseri, Turkey.

[3]Department of Astronomy and Space Sciences, Atatürk University, Yakutiye, 25240, Erzurum, Turkey.

TABLE 1

LITERATURE INFORMATION ABOUT THE TARGETS OF THIS WORK

Common name	ASAS name	RA (h:m:s)	DEC (deg)	P (d)	T_0 (BJD-2450000)[a]	B (mag)	V (mag)
HD 142426	ASAS J155542-3306.7	15:55:42.52	−33:06:36.9	3.863103	51921.0736	10.16[c]	9.63[c]
HD 152451	ASAS J165354-1301.9	16:53:54.20	−13:01:57.5	2.207586	54804.5135	10.57[c]	10.13[c]
HD 197777	ASAS J204608-1120.6	20:46:08.19	−11:20:37.6	5.054638	52033.7675	10.31[c]	9.74[c]
HD 357932	ASAS J200522-0058.4	20:05:21.40	−00:58:27.2	2.880285	52384.1569	11.49[d]	10.89[d]
TYC 8726-1088-1	ASAS J170011-5316.0	17:00:10.54	−53:15:57.6	2.318830	51936.2813	11.20[c]	10.71[c]
CD −30 12958	ASAS J161409-3038.3	16:14:08.90	−30:38:15.6	3.904805	51924.1524	11.01[b]	10.54[b]

[a]For the eclipsing binary, where T_0 is the primary eclipse mid-time. [b] Munari et al. (2014). [c] Høg et al. (2000). [d] Henden et al. (2015).

binaries (Andersen 1991; Torres, Andersen, & Giménez 2010). The dependency of luminosity upon mass -the mass-luminosity relation- is one of the few stellar relations sufficiently fundamental to be applicable to many areas of astronomy.

This dependency is also quite important, both for single stars and for binary stars. For single objects, it allows astronomers to convert a relatively easily observed quantity, luminosity, to a more revealing characteristic, mass, that yields a better understanding of the object's nature. Besides, in searching for extrasolar planets, the mass-luminosity relation provides masses for the target primary stars and consequently allows us to derive the unseen companion's mass. In the broader context of the Galaxy, an accurate mass-luminosity relation permits a luminosity function to be converted to a mass function and provides estimates of the stellar contribution to the Galactic mass.

In this work, we focus on six known systems that have not yet been studied in detail. We chose them from the ASAS Catalog of Variable Stars[4] (ACVS, Pojmanski, Pilecki, & Szczygiel 2005) and photometric time series were retrieved from the All Sky Automated Survey (ASAS, Pojmanski 2002). For three of these systems, time series of the Transiting Exoplanet Survey Satellite (TESS, Ricker et al. 2015) were available and retrieved. Targets were also chosen based on the availability of high-resolution spectra in the ESO Science Archive Facility. We used these observations to determine for the first time accurate fundamental stellar parameters, i.e. effective temperature, surface gravity, radius, mass, luminosity, and age, for each component in the system. Some observational parameters of the six systems, as well as names, coordinates, ephemerides, and magnitudes are given in Table 1.

In § 2 and § 3, we describe how we acquired and processed the photometric and spectroscopic data and explain our radial velocity determination process, light curve analysis, and how we obtained atmospheric parameters from disentangled spectra, where we calculated each star's light contribution to the spectra, to perform the stellar atmosphere modeling. In § 4, we focus on the results of the combined photometric and spectroscopic analysis of the six double-lined eclipsing binaries, and provide a more extensive discussion of individual systems. We then present the evolutionary status of the systems in § 5. Finally, detailed conclusions are presented in § 6.

2. OBSERVATIONAL DATA

2.1. *Photometry*

All targets in our study have been explored as photometrically variable stars using data from the third phase of the ASAS (Pojmanski 2002). The third phase of the project, ASAS-3, which has produced a catalogue of about 50 000 variable stars (Pojmanski, Pilecki, & Szczygiel 2005), lasted from 2000 until 2009 (Pojmanski 2002) and has been monitoring the entire southern sky and part of the northern sky ($\delta < +28°$). The ASAS-3 system, which occupied the ten-inch astrograph dome of the Las Campanas Observatory (Chile), consisted of two wide-field telescopes equipped with $f/2.8$ 200 mm Minolta lenses and 2048×2048 AP 10 Apogee detectors, covering a sky field of $8.8° \times 8.8°$. Data collection was done through standard Johnson I and V filters during the ASAS-2 and ASAS-3 surveys, respectively. Around 10^7 sources brighter than about $V = 14$ mag were catalogued. With a CCD scale of about $14''.8$ per pixel, the astrometric accuracy is around 3-5$''$ for bright stars and up to 15$''$ for fainter stars. Thus, the photometry in crowded fields, such as in star clusters, is rather uncertain. The typical exposure time for ASAS-3 V-filter observations was three minutes, which resulted in reasonable photometry for stars in the magnitude range $7 \lesssim V \lesssim 14$. The data from ASAS-3 also provides accurate information about various parameters, once the mass ratios from the radial velocity measurements are available. Thus, for the preliminary light curve analysis, we used the ASAS V-band photometry.

We searched these variables in other photometric monitoring databases such as CoRoT (Convection, Rotation and planetary Transits, Auvergne et al. 2009), *Kepler* (Borucki et al. 2010), and TESS (The Transit-

[4]http://www.astrouw.edu.pl/asas/?page=acvs.

TABLE 2

LOG OF SPECTROSCOPIC OBSERVATION UTILISED IN THIS STUDY

Common name	Observatory/Instrument	Dates of observations	E.T.(s)	W. R.[Å]	N sp.	S/N
HD 142426	MPG/ESO-2.2-FEROS	21/06/2012 - 17/05/2013	420	3527 - 9216	10	76.8
HD 152451	MPG/ESO-2.2-FEROS	22/06/2012 - 01/06/2015	473	3520 - 9200	8	73.3
HD 197777	MPG/ESO-2.2-FEROS	22/06/2012 - 01/06/2015	702	3520 - 9210	16	67.7
HD 357932	MPG/ESO-2.2-FEROS	22/06/2012 - 01/06/2015	765	3530 - 9200	8	49.3
TYC 8726-1088-1	MPG/ESO-2.2-FEROS	21/06/2012 - 14/08/2013	503	3530 - 9150	8	60.3
CD −30 12958	MPG/ESO-2.2-FEROS	22/06/2012 - 01/06/2015	737	3550 - 9100	7	60.1

E.T.: Average Exposure Time; W.R.: Wavelength Ranges; N sp.: Number of spectra analysed; S/N: Average Signal-to-Noise.

ing Exoplanet Survey Satellite, Ricker et al. 2015). We found three targets observed by TESS: TYC 8726-1088-1, HD 142426, and CD −30 12958. These targets are also crossmatched with the TESS Input Catalog (TIC; Stassun et al. 2019): TIC 211832868, TIC 442829369, and TIC 95731445, respectively.

At the time this manuscript was written, TYC 8726-1088-1 and HD 142426 are observed in Sector 12 and only CD −30 12958 is observed in Sector 4. The rest of our targets in the study either do not have any reduced data available, or have not been observed by the telescope yet. We get target pixel files (TPF) for each target in related sectors from the Mikulski Archive for Space Telescopes (MAST[5]) database. The TPFs are subtracted for background and instrument noise, and cosmic rays. Then, the TPFs of each target are turned into a light curve using the aperture selected by the pipeline mask or creating a new custom mask that is contained within all fluxes of the star.

Only for CD −30 12958, the TPF file was not available. Therefore the TESS light curve was derived from the full-frame image (FFI) file of the sector, that was downloaded from TESSCut (Brasseur et al. 2019). We generated the light curve using an image subtraction pipeline optimized for use with FFIs. This pipeline is very similar to the one used to process ASAS-SN images and is also based on the ISIS package (Alard 2000). This method has become a standard technique for using TESS to study binary systems (Vallely et al. 2019).

In order to prepare the light curve for scientific analysis, we first converted the measured fluxes into TESS-band magnitudes using an instrumental zero point of 20.44 electrons per second from the TESS Instrument Handbook (Vanderspek et al. 2018). TESS observes in a single broad-band filter, spanning roughly 6 000 - 10 000 Å with an effective wavelength of ≈7 500 Å.

[5]https://archive.stsci.edu/index.html.

2.2. *Spectroscopy*

We queried the ESO Science Archive Facility looking for optical spectra with a resolution high enough to detect the lines of the binary components in the composite spectrum. Targets analysed in this study were observed multiple times in order to search for planets via radial velocity variation.[6] Therefore, we found a large number of spectra, which show good orbital phase distribution for each target. We retrieved FEROS archival data for our targets listed in Table 1. We preferred the FEROS instrument (attached to MPG/ESO 2.2m telescope located at the La Silla Observatory in Chile, Kaufer et al. 1999) motivated by its characteristics: large wavelength range (the complete optical spectral region from ≈3500 to ≈9200 Å in only one exposure), high resolution (R = 48 000), and high spectral stability, which makes it suitable for detecting narrow absorption features in a wide variety of spectral lines. We refer to Table 2 for a summary of the spectroscopic observations of the systems. There, in successive columns, we show the dates of observations, exposure times, wavelength ranges, number of spectra retrieved and analysed and the averaged signal to noise ratios.

3. DATA ANALYSIS

It is a well-known fact that physical parameters of binary stars derived from photometric light curve modeling are reliable only when the spectroscopically estimated mass ratio is utilized as an input in the photometric light curve modelling, and kept fixed. For the purposes of modeling the light curves of binary stars, among the parameters of the system, the mass ratio is the first and foremost parameter and should be acquired from precise spectroscopic radial velocity measurements. It has a significant contribution in deriving the precise masses and radii of the binary components, which are the essential parameters to understand the structure and evolution of binary stars.

[6]Based on spectra from observations made with ESO telescopes at La Silla Observatory under program 089.D-0097(A), 089.D-0097(B), 090.D-0061(B), 091.D-0145(A), 091.D-0145(B) by Helminiak, K., and 094.A-9029(R) by Gredel, R.

3.1. *Orbital Solutions*

Since none of the targets we have studied had published radial velocity measurements in the literature, we achieved our own estimates for all targets; in this, we aimed at a uniformly derived set of values and to determine the accuracy of our results.

For this reason, as a first attempt to measure the radial velocities of the components, we used our own templates for the implementation of the RAVESPAN technique (Pilecki et al. 2013, 2015). It is capable of working through three methods for velocity determination from the implemented spectra. These methods are: simple cross-correlation (CCF, Simkin 1974; Tonry & Davis 1979), two dimensional cross-correlation (TODCOR, Mazeh & Zucker 1994) and the broadening function technique (Rucinski 2002).

In order to identify the radial velocities of the components ($V_{1,2}$), we applied the cross-correlation technique for every epoch of each object; this technique is commonly used and implemented in the application. The spectra of the eclipsing binaries were cross-correlated against synthetic spectra (further information regarding generating synthetic spectra is given in § 3.4), which cover both optical and IR regions (3 800-12 000 Å). We used the spectra with well-separated lines to generate templates for both components in each system. We especially considered the absorption lines of O I (7772, 7774, and 7775 Å), Mg I (5167, 5173, and 5184 Å) and Mg II (4481 Å), Si II (4160 Å), Ti II (4300 Å), and Fe II (4508 and 4515 Å) for the primary, and Ca I (6192, 6439, and 6463 Å) and Fe I (6180, 6192, 6400, 6678, 6750, and 8824 Å) for the secondary components. To check the accuracy of the radial velocity measurements, we also calculated the Doppler shifts for each line by fitting Gaussian curves, and we calculated average radial velocities for each component. Although there are no high amplitude light variations seen in the light curves, we checked the Balmer lines for possible emission features caused by magnetic activity, which might affect the measured radial velocities. We checked the spectral lines for either dominant or shallow emission features.

Since the line cores seem clearly photospheric, we averaged the measured radial velocities over all lines of each epoch and calculated the standard deviation of the radial velocity means. However, we probably underrated the true uncertainties of the velocities because we did not take into account the signal-to-noise or the airmass values from the spectra file header. We found a velocity dispersion around $\approx$2 km s^{-1}per object.

With the radial velocity measurements of the systems at hand, we calculated the system mass ratio q, semi-major axis a, radial velocity semi-amplitudes K_1 and K_2, and the systemic velocity γ by using JKTEBOP (v40; Southworth, Maxted, & Smalley 2004; see Table 4). We present orbital solutions in Figures 1-5, and 8 with the radial velocities *O-C* diagrams which show that our residuals are phased to our solution. All individual measurements are also presented in Table 5 in the Appendix.

3.2. *Light Curve Modelling*

Mass, luminosity, and radius are fundamental parameters of any star. In order to determine fundamental parameters, we applied a global fitting of both the photometric data (TESS and ASAS) and radial velocities. This was performed using the JKTEBOP (v40: improvements to the calculation of proximity effects, Southworth, Maxted, & Smalley 2004), which is combined with the Monte Carlo sampler to find the best-fitting model. We note that this software is appropriate for detached EBs where tidal distortion is negligible. It is based on the EBOP code (Popper & Etzel 1981) originally written by Paul Etzel and based on the model of Nelson & Davis (1972). It is a quick procedure that analyses photometric data one set at a time, and in the version used for this paper did not allow for spots or pulsations. Prior to modelling, raw light curves were normalised by their median out-of-eclipse flux based on the ephemerides. Following this step, the final values of the orbital period P, inclination i, eccentricity e, longitude of periastron ω, surface brightness ratio J, and fractional radii of the components $r_{1,2}$ were calculated. For systems with several band light curves available (e.g. from ASAS and TESS) the dataset of better quality was used to determine the values of light curve–dependent parameters and to estimate their errors. For each light curve observed with each band, a 'synthetic' light curve was constructed by evaluating the best-fitting model at the phases of observation. As formal errors are underestimated, 10 000 iterations of a Monte Carlo algorithm were used to collect statistics on the parameters and yield the final errors.

During the synthesis, the gravitational darkening coefficients were set to $\beta = 0.32$ (Lucy 1967) and the limb darkening was modelled with the quadratic law of Kopal (1950) with coefficients taken from van Hamme (1993) and Claret (2017). For the systems in our samples, the third light (l_3) adjustment was not needed to obtain the convergence in most cases. For all systems, reasonable solutions were found assuming l_3=0. However, in the case of CD −30 12958 we expect that some amount of third light is present in the system. CD −30 12958 was a previously unknown eclipsing binary, and the presence of a third companion star was inferred from high-resolution spectra exhibiting signatures of strong third-body lines. The existence of a third-body in the system is explained in the following section.

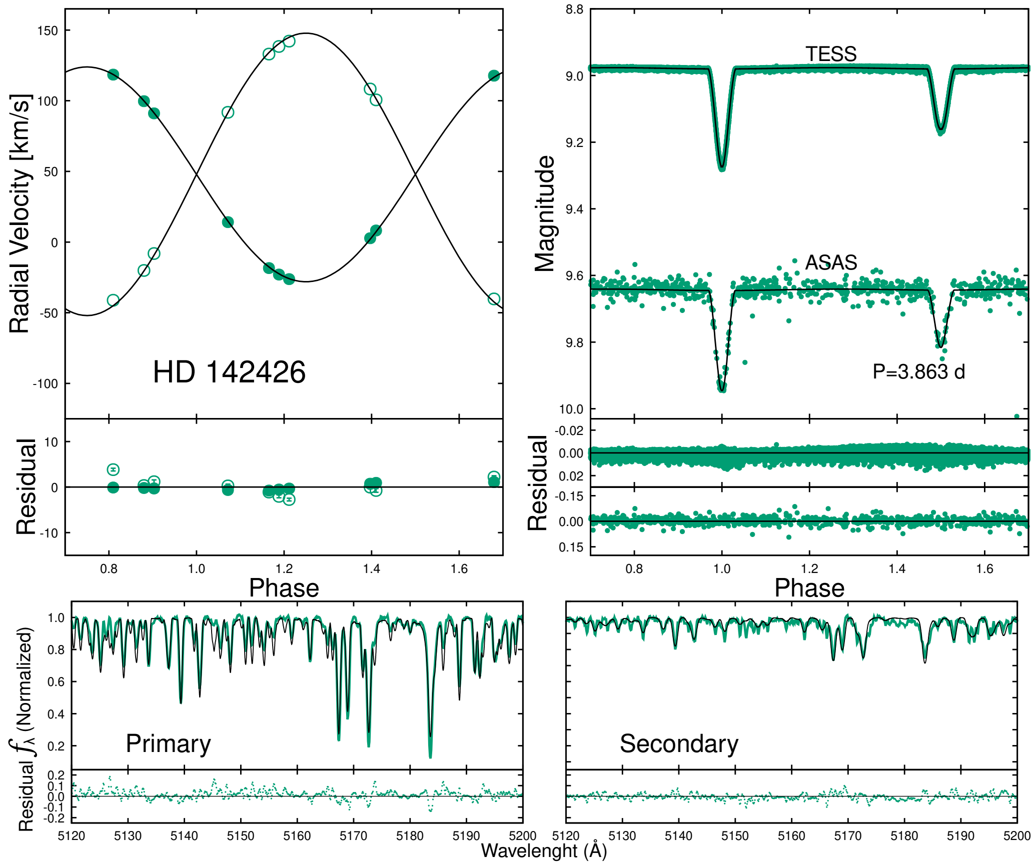

Fig. 1. Radial velocity (left) and light curves (right) of HD 142426. The best-fitting models are plotted with black lines. Filled circles on the radial velocity plot refer to high resolution data for the primary, and open ones for the secondary component. On both sides the phase zero is set for the deeper eclipse mid-time, according to the definition in JKTABSDIM. The color figure can be viewed online.

3.3. *Spectroscopic Light Ratio*

Since some binary systems are detached, they are good laboratories to derive their light contribution to composite spectra. Detached eclipsing binary stars also provide a robust one-step light ratio determination from their light curves. However, in eclipsing binaries with a partial eclipse, a strong degeneracy generally exists between the radii of the primary and secondary components; numerous light curve solutions exist having different radii r_1 and r_2 but a similar sum of their radii (Graczyk 2003). The degeneracy is breakable if we use proximity effects visible in the light curve. However, detached eclipsing double-lined spectroscopic binaries play pivotal roles in utilizing additional information obtained from the composite spectra of the systems, called the spectroscopic light ratio. The only non-trivial step is the need to determine the ratio of the absorption line strengths for the components. The measured value is a direct indicator of the exact light ratio of the components: a brighter component more strongly dilutes the lines of the fainter companion star and thus the lines of the primary appears deeper and stronger. Inspired by the work of Graczyk et al. (2018), we used the line intensity ratio of the increasing equivalent widths (EW) of metallic absorption lines with decreasing temperature for given chemical composition for the individual components.

Following the method of Graczyk et al. (2018), we first measured the line intensity ratio of the equivalent widths from the strength of the broadening function profiles by using a properly matched template spectrum in RAVESPAN over the wavelength regions 5000 – 6000 Å (ASAS; V-band) and 7000 – 9000 Å (TESS; TESS-band) using the advantage of the large wavelength and spectral stability that FEROS spectra offer, which makes them suitable for detecting narrow absorption features in a wide variety of spectral lines. The templates were calculated from a synthetic spectra library for the temperature and surface gravity of the components. The line intensity ratios I_2/I_1 are given in Table 3.

In order to convert I_2/I_1 into light ratios, we calculated the corrections k_{21} following the method of Graczyk et al. (2018). The final spectroscopic light ratios corre-

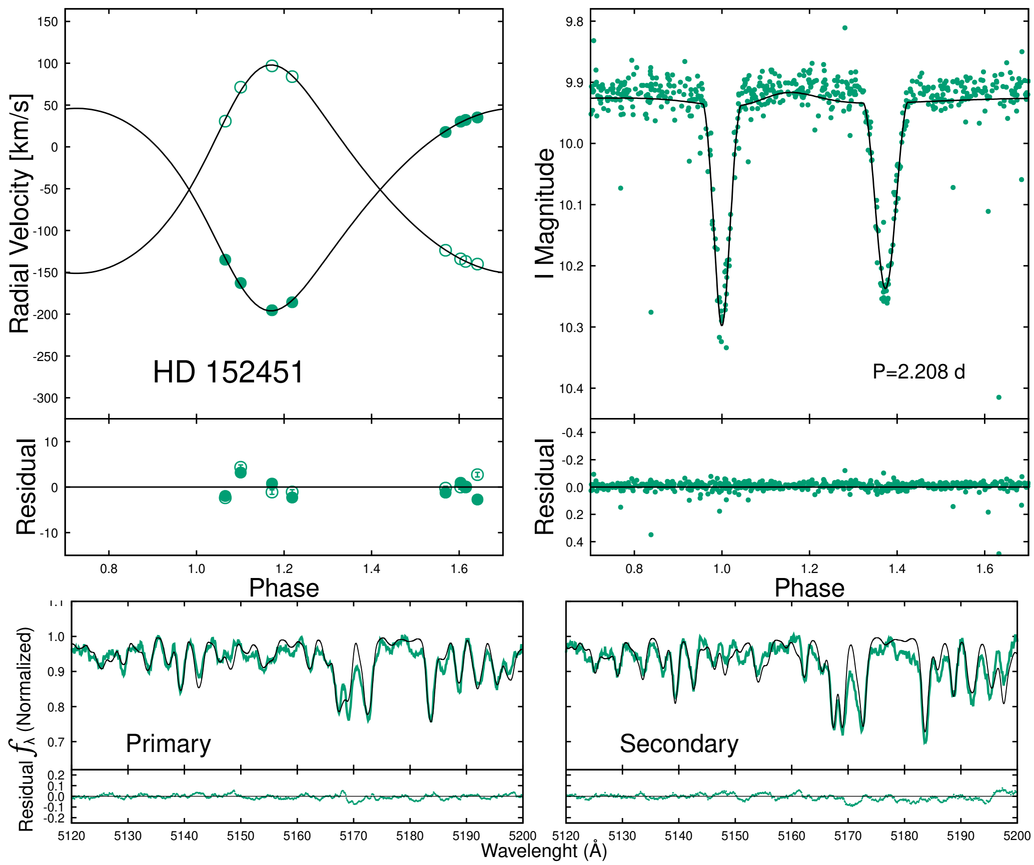

Fig. 2. Same as Figure 1, but for HD 152451. The color figure can be viewed online.

sponding to the true V-band and TESS-band light ratios were computed simply as the product $k_{21}\times(I_2/I_1)$, and these are also given in Table 3.

3.4. *Atmospheric Parameters From Disentangled Spectra*

Taking the findings above into consideration, and with an average of ten FEROS spectra for each target well distributed in the orbital phase, it was considered beneficial to carry out a spectral disentangling attempt. This way, we would understand the nature of the binaries and conduct a detailed spectroscopic analysis. We planned to determine the fundamental atmospheric parameters, abundances -which we would need in order to investigate the evolutionary status of the components- and the projected rotational velocity ($v \sin i$) values of the component stars of the systems. For the purpose of spectroscopic identification of the component spectra, spectral disentangling was performed on the time-series of the FEROS spectra, since only these spectra cover the complete optical spectral region on which the determination of the effective temperatures is based.

We used FDBINARY code[7] which performs spectral disentangling (Simon & Sturm 1994) formulated in the Fourier space according to the prescription of Hadrava (1995). The fundamental idea implemented in the code is that the most natural way to handle spectra for radial velocity measurements is to express them as a function of $x = \ln\lambda$ instead of as a function of λ (Hensberge, Ilijić, & Torres 2008).

The code is also capable of three-component disentangling, as well as light ratio variations by phase. As we have explained in § 3.3, the only basis in this study is the calculation of light ratio changes of the two components with respect to the orbital phase. The application of the procedure bypasses the step of radial velocity determination, but simultaneously optimizes orbital elements of the system and individual spectra of the binary components instead.

In the runs, we employed the disentangling of several (typically 2 or 3) spectral regions where the contributions from both binary components were clearly visible and we determined orbital elements from each of the considered

[7]http://sail.zpf.fer.hr/fdbinary/.

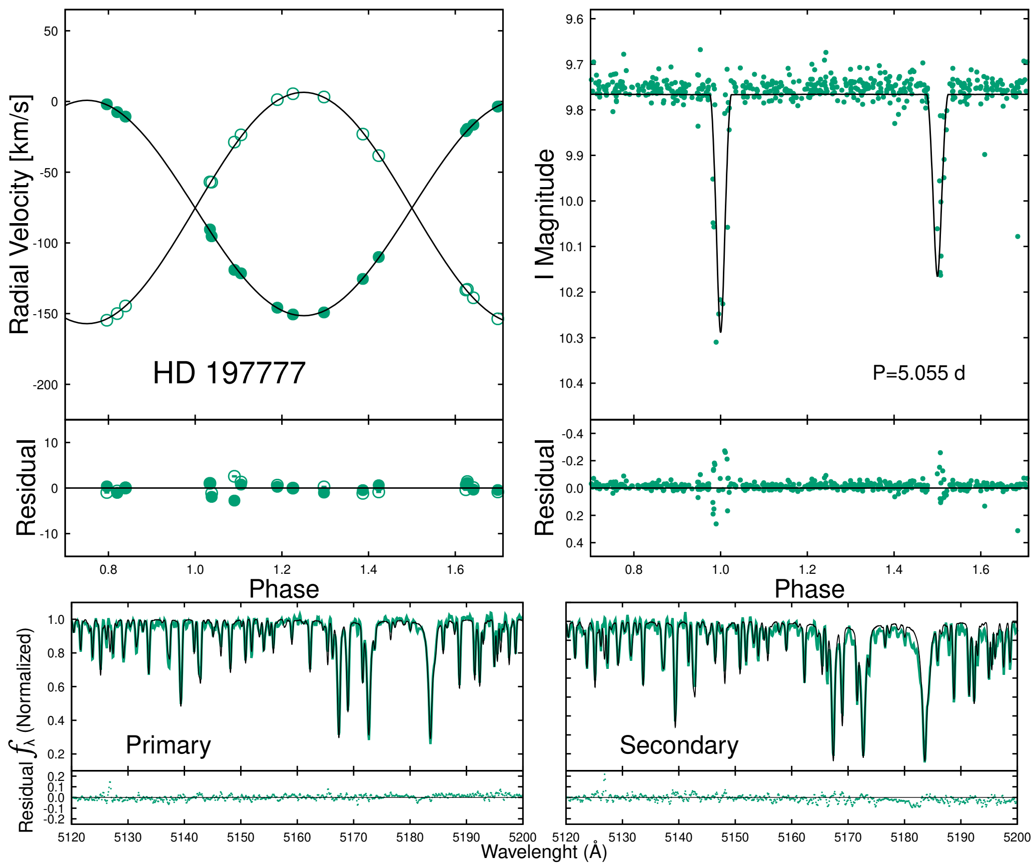

Fig. 3. Same as Figure 1, but for HD 197777. The color figure can be viewed online.

TABLE 3

THE SPECTROSCOPIC LIGHT RATIOS AT 5000 – 6000 Å (ASAS V-BAND) AND 7000 – 9000 Å (TESS TESS-BAND)

System	Line intensity		Correction	Light ratio	
Name	I_2/I_1(V-band)	I_2/I_1 (TESS-band)	k_{21}	L_2/L_1(V-band)	L_2/L_1(TESS-band)
HD 142426	0.589±0.033	0.274±0.033	0.95±0.01	0.56±0.08	0.26±0.01
HD 152451	0.309±0.041	0.479±0.085	0.94±0.01	0.29±0.05	0.45±0.02
HD 197777	0.448±0.056	0.604±0.109	0.96±0.01	0.43±0.02	0.58±0.01
HD 357932	0.494±0.088	0.618±0.089	1.00±0.01	0.49±0.06	0.61±0.03
TYC 8726-1088-1	0.505±0.039	0.536±0.079	0.97±0.02	0.49±0.03	0.52±0.02
CD −30 12958	0.604±0.077	0.344±0.142	0.96±0.02	0.58±0.05	0.33±0.01

regions separately. Among the several spectral regions, we focused on the spectral interval of 5 100 – 5 200 Å because it has been well-known for a long time that strong lines with marked wings can be useful tracers of the $\log g$ parameter (Gray 2005). We also did some trials to get robust effective temperatures and projected rotational velocities of the components. To get temperatures and projected velocities we chose three absorption lines present in their spectra; Fe I λ4046, Fe I λ4271, and Fe I λ4383. These lines are useful temperature indicators for the dwarf stars as noted in the Gray & Corbally (2009). We also used the initial input parameters (the epoch T_0, the orbital period P, the eccentricity e, the longitude of periastron ω and semi-amplitudes $K_{1,2}$) calculated from our orbital

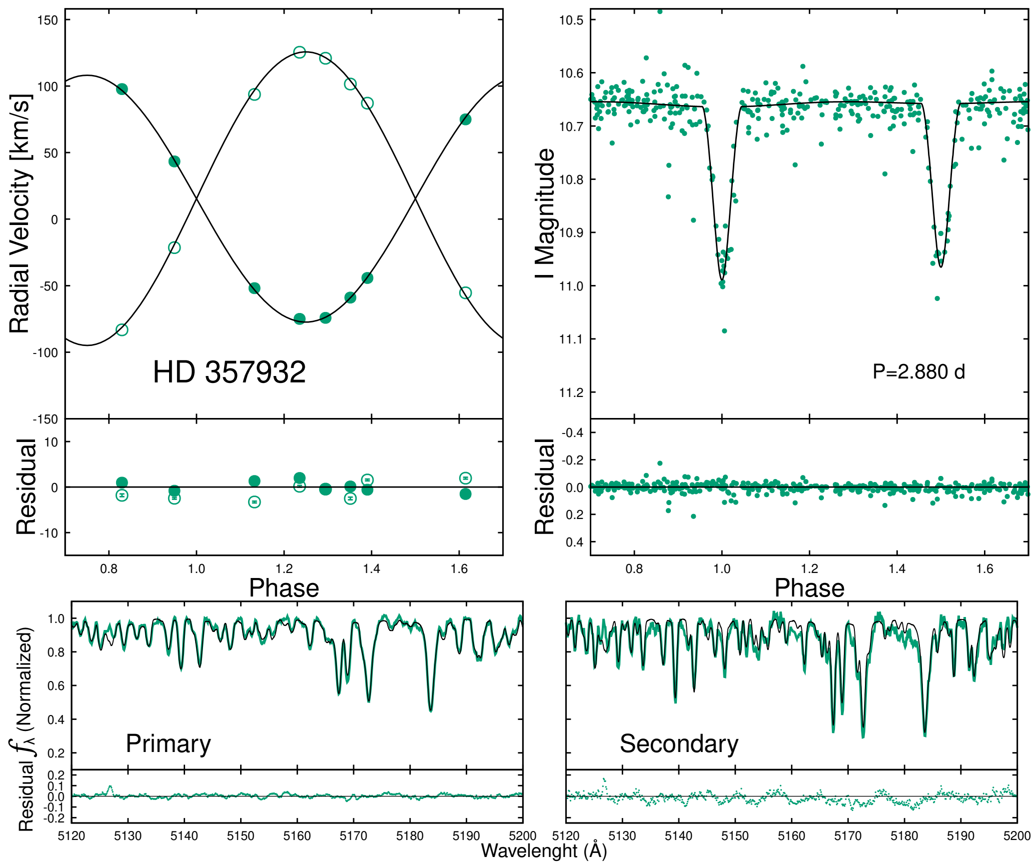

Fig. 4. Same as Figure 1, but for HD 357932. The color figure can be viewed online.

solution and light curve modelling in previous sections. The subscripts 1 and 2 denote the primary and secondary components, respectively. Then we applied the disentangling technique to the selected spectral regions to obtain the pure spectrum of each star to be used for the atmospheric analysis.

The resulting disentangled spectra of the primary and secondary components are plotted in Figures 1-5 and Figures 8. After the disentangled spectra of each spectral part were obtained, they were re-normalised considering the average light ratio of components obtained from the initial light curve analysis and the measured light contributions over spectral lines. In this process, the procedure given by Ilijic (2004) was used.

In order to corroborate the estimation of stellar parameters given in Table 4, we used the freely available, Python-based code ISPEC (the Integrated SPECtroscopic framework, Blanco-Cuaresma et al. 2014) to verify the primary and secondary stellar parameters. To maintain the atmospheric parameters we used the spectral synthesis approach, where the key drivers employ the code SPECTRUM (Gray & Corbally 1994), the MARCS grid of model atmospheres (Gustafsson et al. 2008), solar abundances from Grevesse, Asplund, & Sauval (2007), and the atomic line list provided by the third version of the Vienna Atomic Line Database (VALD3, Ryabchikova et al. 2015). ISPEC synthesizes spectra only in certain, user-defined ranges, called 'segments' which play an integral role in the analysis and are defined as regions of 100 Å around a certain line. We run the fit with the following parameters set free: effective temperature $T_{\rm eff}$, gravity $\log g$, metallicity [M/H], and rotational velocity $v \sin i$ using a set of spectra spread over the orbital period at known times. The resolution R was always fixed to 47 000. The lines are quite narrow, so macro- and microturbulence velocities v_{mic}, v_{mac} were automatically calculated by ISPEC from an empirical relation found by Sheminova (2019) and incorporated into the ISPEC program.

The full optimised parameters are listed in Table 4. The result of an application of this disentangling procedure is illustrated in Figures 1-5 and Figure 8 for the 5 150 – 5 200 Å region. The figures show separated spectra obtained by the disentangling code, and fitted synthetic spectra of the primary and secondary components.

TABLE 4: Binary parameters of systems[*]

Parameter	HD 142426		HD 152451		HD 197777		HD 357932		TYC 8726-1088-1		CD −30 12958	
	Primary	Secondary	Primary	Secondary	Primary	Secondary	Primary	Secondary	Primary	Secondary	Primary	Secondary
T_0 (HJD−2, 400, 000)[a]	51921.0759(1)		54804.5135(1)		52033.7675(1)		52384.1569(1)		51936.2814(6)		51924.1221(11)	
P (day)	3.863097(1)		2.207586(1)		5.054638(2)		2.880285(2)		2.318820(1)		3.904805(1)	
RV analysis												
$a\ sin\,i$ ($R_\odot$)	13.43(14)		10.46(7)		15.78(18)		11.57(11)		10.40(9)		14.33(14)	
γ (km s^{-1})	48.1(3)		-51.1(9)		-75.1(3)		14.4(2.1)		11.4(1)		-5.25(11)	
$M_{1,2}\ sin^3\ i$ ($M_\odot$)	1.239(39)	0.942(33)	1.602(37)	1.557(37)	1.069(39)	0.996(37)	1.396(38)	1.111(33)	1.404(35)	1403(36)	1.356(41)	1.234(40)
$K_{1,2}$ (km s^{-1})	76.3(1)	97.7(1)	121.1(6)	124.4(7)	76.2(5)	81.8(6)	90.1(1.1)	113.1(1.1)	113.4(1.0)	113.5(1.0)	88.5(1.3)	97.2(1.3)
e	0.000(1)		0.216(9)		0.000(1)		0.000(1)		0.000(1)		0.002(1)	
q	0.760(16)		0.972(15)		0.932(22)		0.795(15)		0.999(2)		0.910(18)	
w(°)	1(1)		171(4)		0(3)		0(1)		11(2)		44(2)	
$rms_{RV_{1,2}}$ (km s^{-1})	0.43	0.44	0.33	0.38	0.41	0.34	0.43	0.44	0.41	0.47	0.38	0.39
N_{RV}	10		8		15		8		9		7	
JKTEBOP analysis												
i(°)	85.6(1)		83.7(1)		87.5(1)		82.3(3)		88.7(1)		89.0(1)	
$r_{1,2}$	0.1103(7)	0.06600(9)	0.1885(2)	0.1715(2)	0.0805(1)	0.0776(1)	0.1514(2)	0.1350(2)	0.1481(2)	0.1400(3)	0.1039(1)	0.0950(2)
J	0.683(1)		0.551(9)		0.559(11)		0.555(33)		0.936(1)		1.023(1)	
$X^b_{1,2}$	0.1899	0.2099	0.2301	0.2704	0.2799	0.2901	0.2496	0.3136	0.2001	0.2201	0.2199	0.2598
$Y^b_{1,2}$	0.3302	0.3302	0.3271	0.3109	0.3109	0.3011	0.2902	0.2908	0.2779	0.3111	0.3281	0.3117
l_2/l_{tot}	0.209		0.388		0.435		0.502		0.524		0.34	
l_3/l_{tot}	—		—		—		—		—		0.33	
ISPEC analysis												
$T_{eff\ 1,2}$ (K)	6 390(150)	5 600(190)	7 210(150)	7 200(260)	6 035(150)	5 790(220)	6 685(130)	6 200(150)	6 870(130)	6 860(150)	6 750(150)	6 450(180)
log($g_{1,2}$) (cgs)	4.23(7)	4.51(12)	4.35(25)	4.37(29)	4.31(13)	4.41(23)	4.21(11)	4.36(4)	4.41(21)	4.47(22)	4.27(14)	4.29(15)
($v_{mic.}$) (km s^{-1})	1.66	1.38	1.88	1.21	1.41	1.23	1.33	1.43	1.98	1.96	1.7	1.7
($v_{mac.}$) (km s^{-1})	4.17	5.01	4.78	4.79	4.00	4.44	4.33	4.34	4.32	4.33	4.44	4.61
($v_{1,2}$ sin i)$_{obs}$ (km s^{-1})[c]	19.0(3)	18.1(1.1)	46.1(1.9)	33.2(2.4)	12.7(9)	12.1(9)	36.2(9)	26.1(1.1)	27.2(1.2)	25.5(1.1)	15.1(1.8)	13.1(2.0)
[M/H]	0.10(3)	0.05(7)	0.00(2)	0.0182)	0.00(1)	-0.05(3)	0.28(8)	0.33(9)	0.11(3)	0.18(9)	0.27(11)	0.31(14)
Reduced χ^2	0.0404	0.0419	0.0311	0.0312	0.0303	0.0301	0.0129	0.0144	0.0319	0.0399	0.0312	0.0416
Absolute parameters												
M ($M_\odot$)	1.26(3)	0.96(3)	1.63(4)	1.59(4)	1.07(3)	0.99(3)	1.39(3)	1.11(3)	1.41(3)	1.41(3)	1.36(3)	1.24(3)
R ($R_\odot$)	1.49(2)	1.26(2)	1.98(2)	1.81(2)	1.27(2)	1.23(2)	1.77(1)	1.58(2)	1.54(2)	1.46(2)	1.49(1)	1.36(2)
log (g) (cgs)	4.19(1)	4.52(1)	4.06(1)	4.13(1)	4.26(1)	4.26(1)	4.10(1)	4.36(1)	4.21(1)	4.26(1)	4.23(1)	4.26(1)
log (L) ($L_\odot$)	0.52(4)	0.18(7)	0.98(3)	0.90(4)	0.29(4)	0.18(4)	0.75(3)	0.49(4)	0.68(3)	0.63(3)	0.62(3)	0.46(3)
(v sin i)$_{calc}$ (km s^{-1})[d]	20.0(1.1)	16.5(1.2)	45.5(1.1)	41.4(1.3)	12.3(1)	12.3(1)	31.0(1)	27.7(6)	33.6(2)	31.8(2)	19.3(2)	17.6(2)
M_{bol} (mag)	3.44(10)	5.12(19)	2.29(9)	2.51(15)	4.03(11)	4.29(19)	2.87(9)	4.10(18)	3.05(15)	3.19(15)	3.20(9)	3.60(17)
(m–M)$_V$ (mag)	6.191(108)		7.840(98)		5.711(191)		8.020(111)		7.657(159)		7.341(111)	
$E(B-V)^e$ (mag)	0.066(1)		0.335(55)		0.011(7)		0.116(11)		0.112(23)		0.171(33)	
d (pc)[f]	171(8)		273(9)		179(9)		376(11)		291(5)		290(13)	
$d_{(Gaia)}$ (pc)[g]	$180.54^{+0.45}_{-0.52}$		$272.82^{+1.31}_{-1.69}$		$153.58^{+0.76}_{-0.87}$		$354.66^{+1.85}_{-2.36}$		$264.15^{+1.26}_{-1.05}$		$3047.11^{+1977.68}_{-3393.86}$ [h]	

[*] Errors in units of the last digits are given in parentheses. $l_1/(l_1+l_2)$, M_{bol}, (m-M)$_V$ and d denote luminosity ratio, absolute bolometric magnitude, distance modulus and distance, respectively

[a] Mid–time of the primary (deeper) eclipse, calculated from the complete light curve.

[b] X and Y, linear and non–linear coefficients of limb darkening, respectively.

[c] It is $v_{1,2}$ calculated with ISPEC .

[d] It is the velocity of (pseudo) synchronous given by JKTABSDIM.

[e] The average E(B-V) values derived from NaI (D_1, & D_2) and KI .

[f] The JKTABSDIM distance is calculated only when both values of T_{eff} were found with ISPEC .

[g] From Bailer-Jones et al. (2021). [h] From Bailer-Jones et al. (2018).

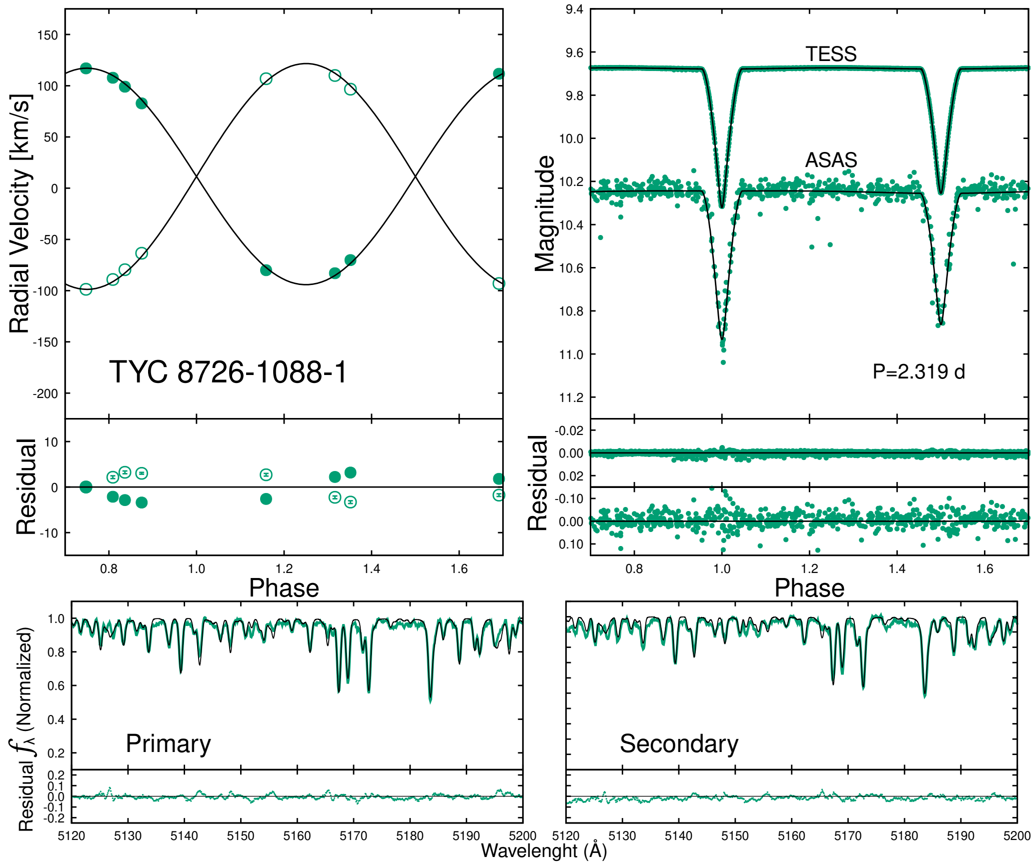

Fig. 5. Same as Figure 1, but for TYC 8726–1088–1. The color figure can be viewed online.

3.5. *Physical Properties and Distance*

Before discussing the comparison of the model predictions with observational data, we derived orbital and stellar parameters for all the studied systems. Not all systems have their parameters available in the literature. Therefore, we decided to analyse all of them in a uniform way, using photometric and spectroscopic results from the above sections. This was done using the JKTABSDIM code (Southworth, Maxted, & Smalley 2005), which propagates uncertainties via a perturbation analysis. In order to compute by code the absolute parameters of the systems, the necessary input parameters are orbital period (P), eccentricity (e), fractional radii ($r_{1,2}$), velocity semi–amplitudes ($K_{1,2}$) and inclination (i) (all with formal uncertainties), and the code returns absolute values of masses and radii (in solar units), $\log(g)$ and rotational velocities, assuming tidal locking and synchronization. JKTABSDIM can also estimate the distance to the targets, using the effective temperatures of two components, the measured metallicity, $E(B-V)$ and the apparent magnitudes via various calibrations. The analysis results and their errors are given in Table 4. These resulting parameters were used to place the components on the HR diagrams (Figure 10) for the purpose of examining their evolutionary status.

The distance to the systems is also straightforwardly measurable. For this, our favored method is via correlation of the reddening to the total equivalent width of the Na I and K I features.

The matter between the stars -the interstellar medium- manifests itself in unforeseen ways, and, as the detritus of stars, its fundamental properties and behavior hold clues to the history and future evolution of stars. Moreover, stars at large distances have been known to show peculiar absorption bands in their spectral analysis. These structures cannot be attributed to stellar lines because they do not follow the Doppler shift caused by the radial motion of the binary components (Merrill 1936). Today, one of best-known absorption features are the Na I (D_2 at 5889.951 Å, D_1 at 5895.924 Å) and K I (at 7699 Å) lines which are the most noticeable proxies for dust reddening, $E(B-V)$ (Munari & Zwitter 1997). As we know from the observations, the measurement of reddening value is an important milestone to determine the absolute temperature scale (and therefore the distance) of eclipsing binaries.

Munari & Zwitter (1997) empirically showed some evidence that the Na I D features are unique for tracing reddening for optically thin gas, but saturate for optically thick gas. In our study, we employed the method involved in the empirical relationship found by Munari & Zwitter (1997), which correlates reddening to the total equivalent width of the Na I D absorption lines. The equivalent width was accurately measured simultaneously with several best quality spectra at quadratures, where lines from both components are un-blended with the interstellar ones. The final value of $E(B-V)$ was then calculated as a sum of the reddenings of individual components of each system. The results for all our investigated binaries are shown in Table 4.

As an independent check on the reddening $E(B-V)$ we also measured the equivalent width of the interstellar K I (at 7699 Å) line in spectra in which the feature is well resolved from the stellar components. The strength of this line has been found to also correlate with the amount of extinction (Munari & Zwitter 1997), albeit with considerable scatter. Based on a mean equivalent width and on the calibration from the above authors we infer a value of $E(B-V)$, consistent with the results of Na I lines. The average values are given in Table 4.

Our samples are close neighbours of the Sun, with distances up to 376 pc, and are known as eclipsing binaries. To check the consistency of our estimated distances, we compared our values with the distances obtained from Bailer-Jones et al. (2018, 2021), which are calculated by using Gaia DR2 (Data Release 2; Gaia Collaboration et al. 2016, 2018) and eDR3 (early Data Release 3; Gaia Collaboration et al. 2021) parallaxes. All targets, except CD −30 12958, have accurate parallax measurements in Gaia eDR3. As shown in Table 4, all our calculated distances are compatible with Gaia distances. For the case of CD −30 12958, there is only the Gaia DR2 parallax measurement available and it is not reliable, due to very high uncertainties (≈70 %). Therefore our calculated distance for this target is more uncertain.

The reddening $E(B-V)$ values we derive from the optical spectroscopy are slightly higher than the predicted reddening from the Schlafly & Finkbeiner (2011) all-sky map. This discrepancy is due to the stars being in different galactic embedded regions. In the next section we will present a brief description of the systems due to their unusual features.

4. RESULTS

In this section, we focus on the results of the combined photometric and spectroscopic analysis of six double-lined eclipsing binaries, and a more extensive discussion of individual systems. Here we also present a brief description of CD −30 12958, which is the close pair in a triple-lined hierarchical system.

4.1. *HD 142426*

This system was relatively easy to model thanks to high quality photometric and spectroscopic data. First, we used the TESS light curve, which offers very good coverage in eclipses, and sufficient coverage out of them. With no third light contribution and no out-of-eclipse variation, we were able to derive a complete set of orbital and physical parameters, which are given in Table 4. We also analysed photometric data from the ASAS-3 archive (249 observations; a time base of ≈3300 d). HD 142426 turned out to be a double-lined binary (SB2), so we analysed a total of 10 FEROS spectra to cover the binary orbit. We checked the corresponding sky region of HD 142426 using the ALADIN interactive sky atlas (Bonnarel et al. 2000); no source sufficiently bright to affect the ASAS and TESS measurement is situated near our target.

4.2. *HD 152451*

HD 152451 is the most eccentric eclipsing binary in our sample. It has previously been identified as an eccentric binary with a period of 2.2076 d from the ASAS photometric data (Shivvers, Bloom, & Richards 2014). For the preliminary light curve analysis we used the ASAS V-band photometry, which contained 619 data points. We have also acquired 8 FEROS spectra, and using these, we derived the orbital parameters and the eccentricity of the system. Despite the small number of radial velocity and light curve measurements, the eccentricity precision is significantly better than that of Shivvers, Bloom, & Richards (2014).

The two effective temperatures derived from disentangled spectra were used in JKTABSDIM to calculate the distance. The result, 273(9) pc, is in reasonable agreement with the $272.82^{+1.31}_{-1.69}$ pc figure from Gaia eDR3 parallaxes. To ensure consistency we assumed $E(B-V) = 0.335$ mag. Without reddening, the values corresponding to bands B and V are ≈45 pc larger than those corresponding to J, H, K. The average equivalent width of the interstellar Na I D_1 and K I lines is 0.225 Å, and this correctly reproduces $E(B-V) \simeq 0.335$ mag, according to calibrations by Munari & Zwitter (1997).

The set of parameters given in Table 4 for HD 152451, their precision, and the fact that this system consists of a pair of "twins", make this target valuable for testing stellar formation and evolution models.

4.3. *HD 197777*

HD 197777 was initially classified as spectral type F1 in the Henry Draper Catalogue (Cannon & Pickering 1919).

The system was first noted as a double-lined spectroscopic binary in this study and was discovered to be an eclipsing binary by Pojmanski (2002) from ASAS photometry. This system has been observed with FEROS fifteen times, which makes it the most observed target in our sample (spectroscopically). We obtained the light curve of the system from the ASAS catalog and with a deeper primary minimum by folding with the orbital period given.

HD 197777 consists of two solar-mass stars of significant age (age > 9 Gyr) with nearly equal masses and radii. The inferred distance for the system is compared with the Gaia eDR3 results in Table 4. The estimated distance is in relatively good agreement with Gaia eDR3.

4.4. *HD 357932*

HD 357932 was initially classified as spectral type F0 in The Henry Draper Extension Charts (HDEC) (Nesterov et al. 1995); published in the form of finding charts, it contains spectral classifications for some 87 000 stars mostly between 10^{th} and 11^{th} magnitude. These data, while highly valuable, were unfortunately practically useless for modern computer-based astronomy.

A binary model for HD 357932 was obtained for the first time, using a combined analysis of ASAS light curve data and high-resolution FEROS spectra. We used an automated procedure to create the model, based on the JKTEBOP binary modelling code. In order to obtain the spectra of the components from the composite FEROS spectra of the system, we used the disentangling method, and we obtained a higher signal-to-noise mean component spectrum for both the primary and the secondary. From the joint fitting of the eclipse photometry, radial velocity analysis results and spectral disentangling results, we determined the masses of the HD 357932 binary with 3 % precision and the radii with 1 %-2 % precision. With such highly precise parameters, we were able to test stellar evolutionary models for solar-type stars, comparing the predictions of such models in the HR diagram.

4.5. *TYC 8726-1088-1*

TYC 8726-1088-1 is listed by Pojmanski (2002) as an eclipsing binary system with a period of ≈2.819 d. Aside from brightness (apparent V magnitude: $10^{m}.7$) and position measurements (Høg et al. 2000), no literature data are available and no light curve solutions or radial velocity studies have been attempted so far.

Comparison of the JKTABSDIM output showed that the two components of the system are indistinguishable, and as a result absolute parameters differ typically by 1-3 % of the obtained errors. We therefore adopted the derived results as the final ones and we accepted the system as a twin binary (mass ratio $q \simeq 1$); such systems are exceptional tools to provide information for probing the internal structure of stars.

For the distance determination, we adopted the interstellar reddening of $E(B-V)$ as derived from the correlation reddening of the total equivalent width of the Na I D absorption lines. The distance calculated with the trigonometric parallax from the Gaia eDR3 is about 90 % of the value found in our calculations.

TESS, ASAS I-band light curve, and radial velocity curve for the system are presented in Figure 5. Using our new precise analysis we classified the system as F3 type for the first time.

4.6. *CD* −30 12958

CD −30 12958 is the second longest-period system in this study. This star is listed in the ASAS-3 Catalogue (565 observations; a time base of ≈3200 d). Eclipse variations in the system light curves are noticeable. Except for the brightness (apparent V magnitude: $10^{m}.5$) and position measurements (Høg et al. 2000), no literature data are available and no light curve solutions or radial velocity studies have been attempted so far.

High-resolution spectra revealed that CD −30 12958 is likely a hierarchical triple, with the eclipsing binary components in a non-eccentric orbit and a third light contribution of over 30 %.

The eclipsing binary is composed of F5-type stars with masses: $M_p = 1.36(3)\,M_{\odot}$ and $M_s = 1.24(3)\,M_{\odot}$, and radii: $R_p = 1.49(1)\,R_{\odot}$ and $R_s = 1.36(2)\,R_{\odot}$. The third component has a similar spectral type (F3V) and is on a wide orbit. Its contribution to the total light from the light curve analysis is about 34 %, which is consistent with the value derived from spectral disentangling (35 %).

In the high-resolution FEROS optical spectra, CD −30 12958 appeared as triple-lined. The nearly equal peaks on the cross-correlation function (CCF) corresponding to the primary and secondary components are the strongest in this system, followed by a tertiary corresponding to a slightly weaker one (Figure 6 and 7). We measured the radial velocity of all components, denoted as a black cross in Figure 8, with the primary (filled circle) and the secondary (open circle) stars.

In order to calculate the random errors of the initial values of parameters (including l_3), we used the Monte Carlo simulation algorithm implemented in JKTEBOP , which was found to quantify the correlations between the parameters. For each ASAS I-band and TESS light curve, a 'synthetic' light curve was constructed by evaluating the best-fitting model at the phases of observation. This process was undertaken 10 000 times for each observed light curve of the system. The standard deviation of the distribution of values for each parameter has been calculated. A sample plot of the distributions of different parameter values for CD −30 12958 is shown in Figure 9.

From the predicted temperatures for the primary and secondary, we determined the distance as 290(13) pc with the $E(B-V)$ value derived from Na I D_1 given in Table 4. The resulting distance is inconsistent with the Gaia DR2 value of $3047.11^{+1977.68}_{-3393.86}$ pc; however, this value is significantly less precise. There is no measurement for this system in the Gaia eDR3. Notably, with its physical parameters and probable metallicity and age, the primary and secondary can be considered to be solar analogues. CD −30 12958 is interesting, as examples of such stars in eclipsing systems, particularly with well-measured absolute parameters, are very rare. In any case, eclipsing time variation (ETV) monitoring of such systems helps to identify their nature.

5. AGE AND EVOLUTIONARY STATUS

The accurate stellar fundamental parameters that can be derived from eclipsing binaries offer opportunities to confront our current stellar structure and evolution theories with observations.

In Figure 10, we show a comparison of the results of our analyses with theoretical MESA evolution tracks developed as part of the MESA Isochrones and Stellar Tracks project (MIST[8] v1.2, Dotter 2016; Choi et al. 2016). For each system, we determine the age at which the observed or calculated properties of both components are best represented. Because the stellar temperature $T_{\rm eff}$ is one of the most robust resulting parameters from the spectral analysis we compare our data on $T_{\rm eff}/\log g$ planes. One important caveat is that the measured $T_{\rm eff}$ values of the components are independent.

We located each component in the systems using the $T_{\rm eff}$ and $\log g$ determined by the JKTABSDIM code and compared them with the MESA tracks corresponding to the masses derived from the spectro-photometric analysis. This procedure allows us to infer the ages of each component in the binary systems. Each pair resulted to be nearly coeval, except for CD −30 12958. The ages of its components do not show agreement with each other. This may be caused by the contamination of the third component in the spectral disentangling procedure, which could affect the light curve modelling or radial velocity measurement.

6. SUMMARY AND CONCLUSIONS

In this study, we present physical parameters of six targets from our investigation, with the aim of characterizing interesting eclipsing binary systems by taking into account all available data. The orbital and physical parameters of the stars are shown in Table 4. The errors of the parameters, also given in Table 4, are calculated with

[8]http://waps.cfa.harvard.edu/MIST/interp_isos.html.

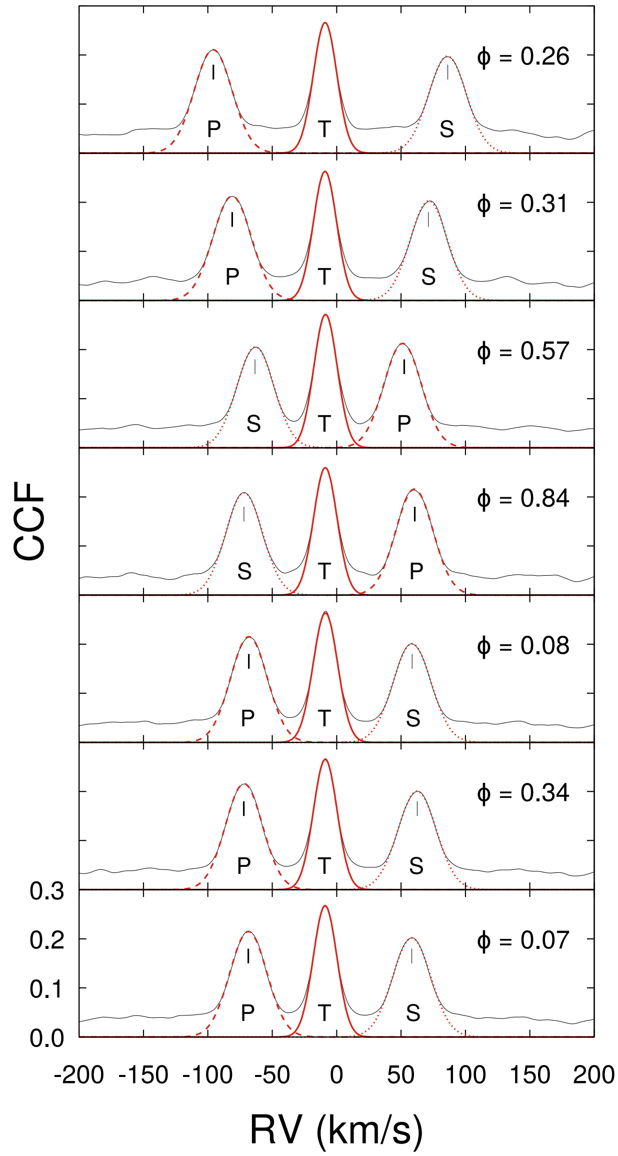

Fig. 6. Sample of cross correlation functions (CCFs) between CD −30 12958 and template spectra at different phases. The Gaussian fits to the two peaks are displayed with a dotted line for the secondary component (S) and with a dashed line for the primary one (P). Short vertical lines mark the centroid velocity of binary components. The tertiary component is indicated with a T. The color figure can be viewed online.

the JKTABSDIM procedure using the parameters and uncertainties from the radial velocity and light curve analysis described above.

High quality photometric (TESS + ASAS) and spectroscopic data (FEROS) allow us to obtain the masses and radii of the components with a precision better than 3 % for the systems, making them reliable test-beds for accurately understanding the origin and evolution of binaries.

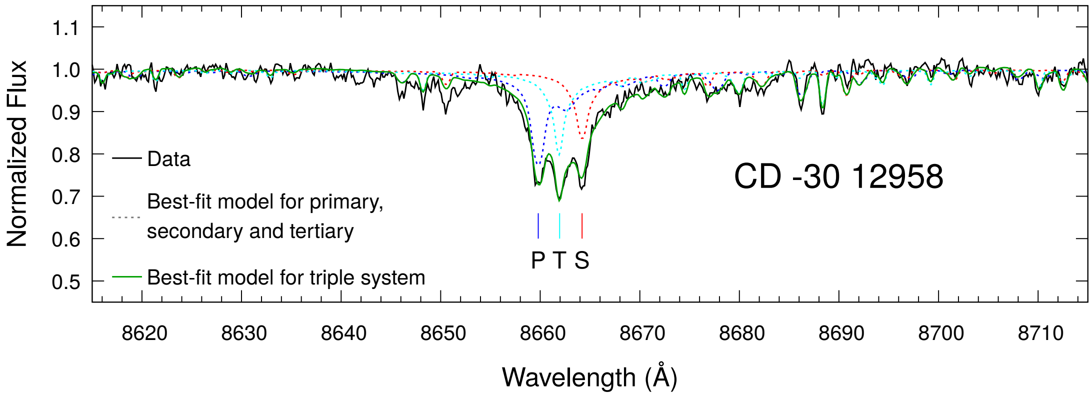

Fig. 7. FEROS spectra of the CD −30 12958 identified as a triple (SB3) system. The three components have different line-of-sight velocities, so many lines can be seen in triple form along the spectra. The SB3 model is overplotted with a good fit. The heliocentric velocity of the tertiary is $v_{\mathrm{helio},3} \approx 8.8\,\mathrm{km\,s^{-1}}$ at $\phi = 0.318$ (HJD 56101.6833). The color figure can be viewed online.

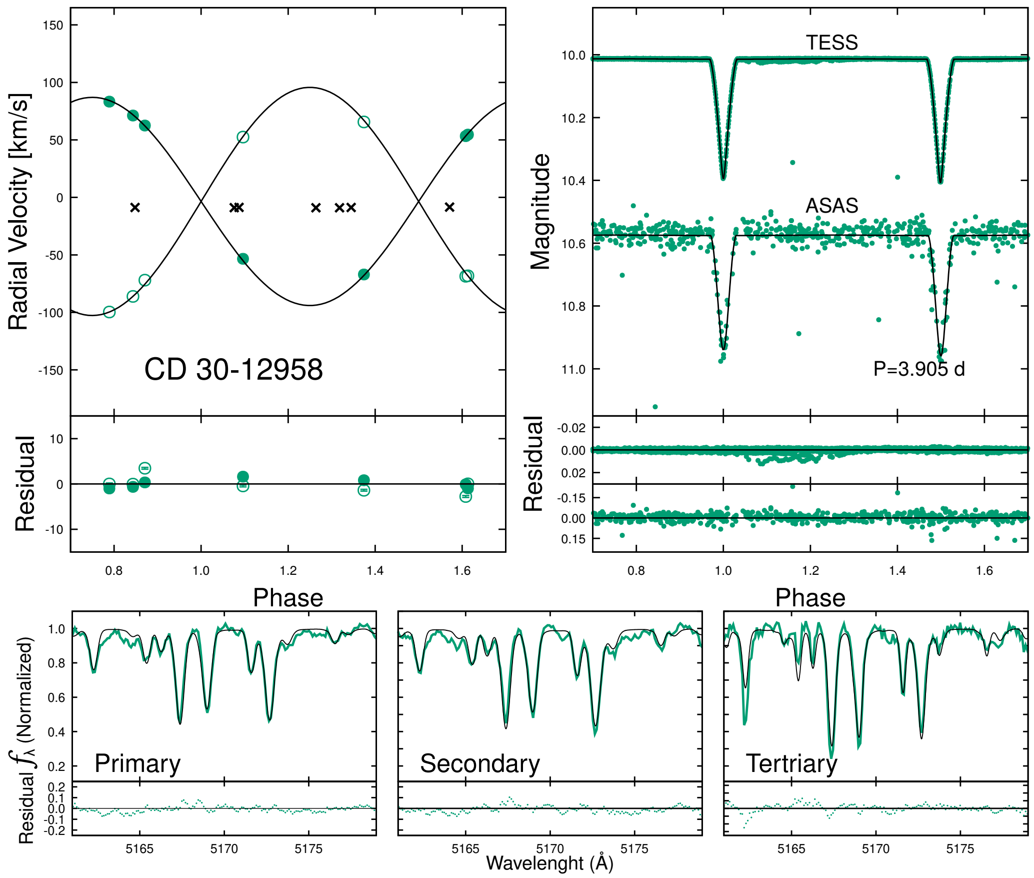

Fig. 8. Radial velocity (left) and light curves (right) of CD −30 12958. The best-fitting models are plotted with black lines. The filled circles on the radial velocity plot refer to high resolution data for the primary, the open ones for the secondary component, and the cross for the tertiary. On both sides phase zero is set for the deeper eclipse mid-time, according to the definition in JKTEBOP. The color figure can be viewed online.

We also emphasise that precise fundamental and orbital parameters of solar analogue type stars are vital for exoplanet studies (Allard, Homeier, & Freytag 2012; Huber et al. 2014; Johnson et al. 2007). Since the fundamental planet parameters are tightly bound to the host star properties, spectroscopic or photometric orbit solu-

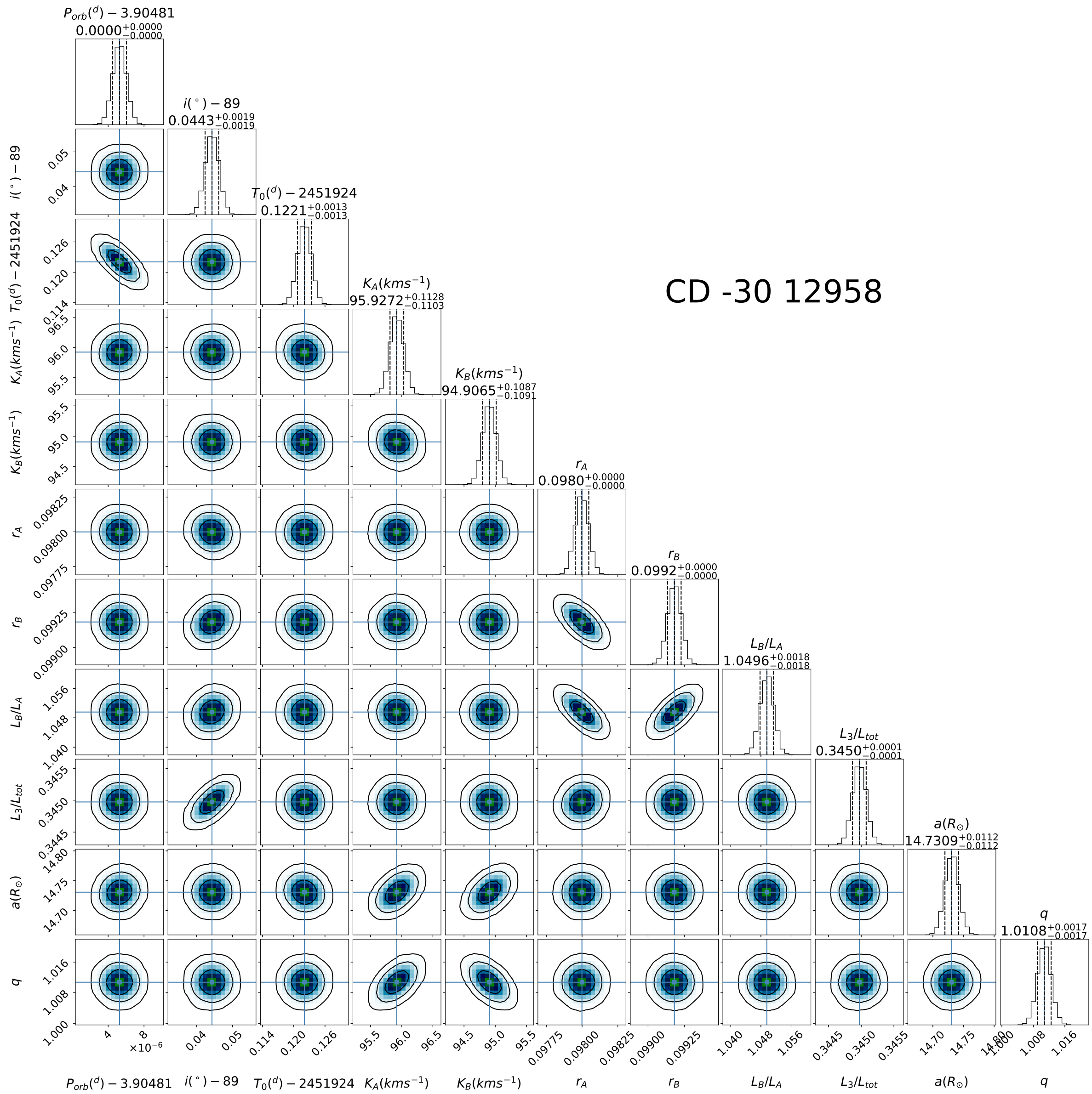

Fig. 9. "Corner plot" (Foreman-Mackey (2016); source code available at https://github.com/dfm/corner.py) for CD −30 12958, illustrating the correlations among the main fit parameters of our solution. Contour levels correspond to 1, 2, and 3σ, and the histograms on the diagonal represent the posterior distribution for each parameter, with the mode and internal 68 % confidence levels indicated. More realistic errors are discussed in the text. The color figure can be viewed online.

tions and estimation of fundamental parameters of the stars should be obtained with a precision better than 3 %, which we achieve in this study. For this reason, this study is also important to determine the fundamental parameters of candidate super Earth-mass planets that will be discovered as a result of ongoing observations of TESS.

One of the objects, CD −30 12958, shows lines coming from three components in its spectra. Further work on the object should focus on eclipse time variation analysis in order to independently determine orbital and physical parameters.

This work has been supported by Erciyes University Scientific Research Projects Coordination Unit under grant number DOSAP MAP-2020-9749. We are grateful to the anonymous referee for her/his valuable suggestions. This research made use of data collected at ESO under programmes 089.D-0097(A),

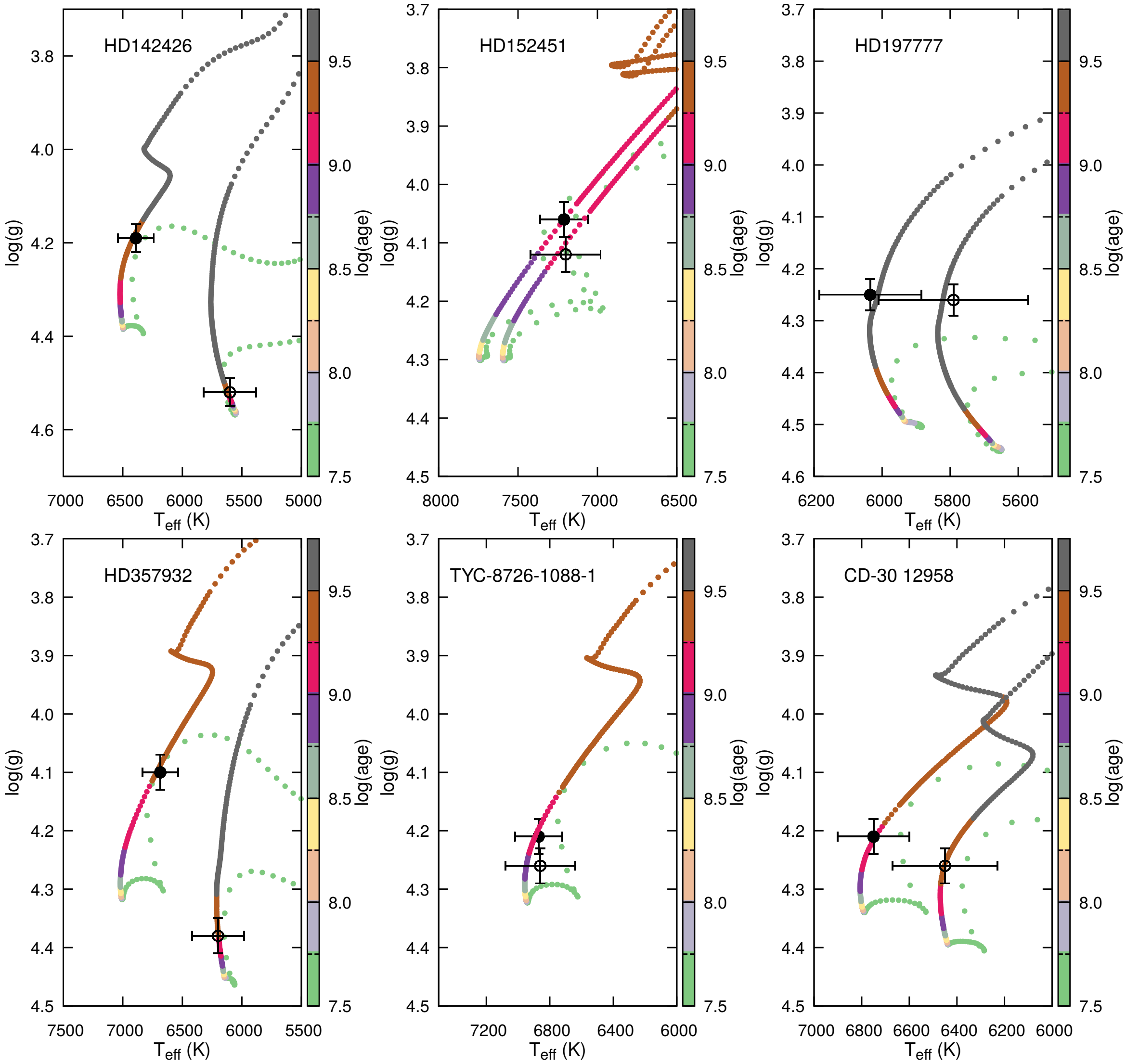

Fig. 10. Comparison of our results with MESA evolution tracks on $T_{\rm eff}$/log g planes. Primaries are shown with filled circle symbols, and secondaries with open circle symbols, both with error bars from Table 4. The colored points are the evolutionary tracks that best match the calculated component masses, and the colors indicate the stellar age with the color bars at the right side of the plots. The color figure can be viewed online.

089.D-0097(B), 090.D-0061(B), 091.D-0145(A), 091.D-0145(B) (by Helminiak, K.), and 094.A-9029(R) (by Gredel, R.). This paper includes data collected by the TESS mission. Funding for the TESS mission is provided by the NASA's Science Mission Directorate. The photometric data were obtained from the Mikulski Archive for Space Telescopes (MAST). This research has made use of the "Aladin Sky Atlas" developed at CDS, Strasbourg Observatory, France. The following internet-based resources were used in the research for this paper: the NASA Astrophysics Data System; the SIMBAD database operated at CDS, Strasbourg, France.

APPENDIX

JOURNAL OF THE RADIAL VELOCITY MEASUREMENTS OF THE TARGETS

System	BJD (+2400000)	v_1 ($\mathrm{km\,s^{-1}}$)	σ_1 ($\mathrm{km\,s^{-1}}$)	v_2 ($\mathrm{km\,s^{-1}}$)	σ_2 ($\mathrm{km\,s^{-1}}$)	S/N[a]	Instrument
HD 142426	56100.48817	99.7	0.1	-20.1	0.3	66.7	FEROS
	56100.57676	91.1	0.1	-8.1	0.4	78.1	FEROS
	56101.59107	-18.4	0.1	133.0	0.3	93.1	FEROS
	56101.67936	-23.0	0.1	138.4	0.3	91.0	FEROS
	56102.48378	2.7	0.1	108.3	0.4	88.5	FEROS
	56102.53602	8.2	0.1	100.6	0.4	87.9	FEROS
	56381.72036	117.7	0.1	-40.2	0.3	80.3	FEROS
	56383.77551	-26.2	0.1	142.2	0.3	97.3	FEROS
	56428.58030	118.5	0.1	-41.2	0.3	66.1	FEROS
	56429.59299	14.1	0.1	91.8	0.4	19.8	FEROS
HD 152451	56100.51148	-134.9	0.5	30.7	0.5	62.6	FEROS
	56100.74719	-195.3	0.4	96.9	0.5	70.5	FEROS
	56101.62227	17.8	0.4	-123.6	0.4	100.7	FEROS
	56101.69794	30.2	0.4	-133.9	0.5	94.4	FEROS
	56193.56731	-185.8	0.5	84.0	0.5	39.7	FEROS
	56195.51539	-162.8	0.5	71.4	0.5	66.4	FEROS
	57174.61018	32.2	0.4	-136.9	0.5	70.8	FEROS
	57174.66933	35.2	0.5	-140.1	0.5	81.6	FEROS
HD 197777	56100.87043	-19.4	0.1	-132.8	0.1	64.6	FEROS
	56100.94007	-16.5	0.1	-138.8	0.1	50.9	FEROS
	56101.84187	-7.5	0.1	-150.0	0.1	61.0	FEROS
	56101.93921	-10.7	0.1	-144.6	0.1	77.1	FEROS
	56102.92370	-90.5	0.1	-56.9	0.1	72.5	FEROS
	56102.94348	-95.3	0.1	-57.1	0.1	70.8	FEROS
	56192.70473	-2.0	0.1	-154.7	0.1	71.6	FEROS
	56194.69316	-145.8	0.1	1.3	0.1	78.4	FEROS
	56195.69009	-125.5	0.1	-23.1	0.1	79.3	FEROS
	56381.89630	-150.6	0.1	5.5	0.1	66.7	FEROS
	56382.89642	-110.0	0.1	-38.3	0.1	68.2	FEROS
	56383.91186	-21.0	0.1	-133.3	0.1	76.2	FEROS
	56517.76578	-121.5	0.1	-23.6	0.1	47.6	FEROS
	56518.73305	-149.2	0.1	3.2	0.1	57.2	FEROS
	56520.76058	-3.6	0.1	-153.7	0.1	66.4	FEROS
	57174.79210	-119.1	0.1	-28.7	0.1	74.3	FEROS
HD 357932	56100.73703	-59.0	0.1	101.5	0.3	53.8	FEROS
	56100.84868	-44.2	0.1	87.1	0.2	39.2	FEROS
	56193.66378	75.0	0.2	-55.4	0.2	47.2	FEROS
	56194.62898	43.4	0.1	-21.4	0.2	60.1	FEROS
	56195.62292	-74.2	0.1	120.9	0.3	60.9	FEROS
	56517.74754	-51.9	0.1	93.7	0.2	36.0	FEROS
	56519.75565	97.7	0.1	-83.2	0.3	42.9	FEROS
	57174.74906	-75.0	0.1	125.4	0.2	54.4	FEROS

[a]S/N values have been obtained from headers.

JOURNAL OF THE RADIAL VELOCITY MEASUREMENTS OF THE TARGETS
CONTINUED

System	BJD (+2400000)	v_1 (km s^{-1})	σ_1 (km s^{-1})	v_2 (km s^{-1})	σ_2 (km s^{-1})	S/N[a]	Instrument
TYC 8726-1088-1	56100.52124	99.0	0.2	-79.6	0.3	50.5	FEROS
	56100.61010	82.8	0.2	-63.5	0.2	53.9	FEROS
	56101.63328	-83.0	0.2	110.0	0.3	68.4	FEROS
	56101.71567	-70.2	0.2	96.6	0.3	69.0	FEROS
	56102.50223	111.7	0.2	-93.0	0.3	60.8	FEROS
	56102.63396	117.0	0.2	-98.7	0.3	70.1	FEROS
	56195.52928	107.8	0.2	-89.1	0.3	61.3	FEROS
	56518.65824	-80.0	0.2	106.8	0.3	52.4	FEROS
CD -30 12958	56101.47104	83.3	0.2	-99.7	0.2	63.1	FEROS
	56101.68325	71.2	0.2	-86.1	0.2	65.9	FEROS
	56102.67041	-53.4	0.2	52.5	0.2	71.1	FEROS
	56193.56602	-67.0	0.2	65.6	0.2	27.6	FEROS
	56194.49897	54.6	0.2	-68.2	0.2	65.7	FEROS
	56195.50516	62.5	0.2	-72.0	0.2	63.3	FEROS
	57174.58565	53.3	0.2	-68.6	0.2	63.1	FEROS

[a]S/N values have been obtained from headers.

REFERENCES

Alard, C. 2000, A&AS, 144, 363, https://doi.org/10.1051/aas:2000214

Allard, F., Homeier, D., & Freytag, B. 2012, RSPTA, 370, 2765, https://doi.org/10.1098/rsta.2011.0269

Andersen, J. 1991, A&ARv, 3, 91, https://doi.org/10.1007/BF00873538

Auvergne, M., Bodin, P., Boisnard, L., et al. 2009, A&A, 506, 411, https://doi.org/10.1051/0004-6361/200810860

Bailer-Jones, C. A. L., Rybizki, J., Fouesneau, M., Mantelet, G., & Andrae, R. 2018, AJ, 156, 58, https://doi.org/10.3847/1538-3881/aacb21

Bailer-Jones, C. A. L., Rybizki, J., Fouesneau, M., Demleitner, M., & Andrae, R. 2021, AJ, 161, 147, https://doi.org/10.3847/1538-3881/abd806

Blanco-Cuaresma, S., Soubiran, C., Heiter, U., & Jofré, P. 2014, A&A, 569, 111, https://doi.org/10.1051/0004-6361/201423945

Bonnarel, F., Fernique, P., Bienaymé, O., et al. 2000, A&AS, 143, 33, https://doi.org/10.1051/aas:2000331

Borucki, W. J., Koch, D., Basri, G., et al. 2010, Sci, 327, 977, https://doi.org/10.1126/science.1185402

Brasseur, C. E., Phillip, C., Fleming, S. W., Mullally, S. E., & White, R. L. 2019, ascl.soft05007

Cannon, A. J. & Pickering, E. C. 1919, AnHar, 94, 1

Choi, J., Dotter, A., Conroy, C., et al. 2016, ApJ, 823, 102, https://doi.org/10.3847/0004-637X/823/2/102

Claret, A. 2017, A&A, 600, 30, https://doi.org/10.1051/0004-6361/201629705

Dotter, A. 2016, ApJS, 222, 8, https://doi.org/10.3847/0067-0049/222/1/8

Duquennoy, A. & Mayor, M. 1991, A&A, 248, 485

Foreman-Mackey, D. 2016, JOSS, 1, 24, https://doi.org/10.21105/joss.00024

Gaia Collaboration, Brown, A. G. A., Vallenari, A., et al. 2018, A&A, 616, 1, https://doi.org/10.1051/0004-6361/201833051

Gaia Collaboration, Brown, A. G. A., Vallenari, A., et al., 2021, A&A, 649, 1, https://doi.org/10.1051/0004-6361/202039657

Gaia Collaboration, Prusti, T., de Bruijne, J. H. J., et al., 2016, A&A, 595, 1, https://doi.org/10.1051/0004-6361/201629272

Graczyk, D. 2003, MNRAS, 342, 1334, https://doi.org/10.1046/j.1365-8711.2003.06636.x

Graczyk, D., Pietrzyński, G., Thompson, I. B., et al. 2018, ApJ, 860, 1, https://doi.org/10.3847/1538-4357/aac2bf

Gray, D. F. 2005, The Observation and Analysis of Stellar Photospheres, 3rd ed. (Cambridge, MA: CUP)

Gray, R. O. & Corbally, C. J. 1994, AJ, 107, 742, https://doi.org/10.1086/116893

__________. 2009, Stellar Spectral Classification, (Princeton, NJ: PUP)

Grevesse, N., Asplund, M., & Sauval, A. J. 2007, SSRv, 130, 105, https://doi.org/10.1007/s11214-007-9173-7

Gustafsson, B., Edvardsson, B., Eriksson, K., et al. 2008, A&A, 486, 951, https://doi.org/10.1051/0004-6361:200809724

Hadrava, P. 1995, A&AS, 114, 393

Henden, A. A., Levine, S., Terrell, D., & Welch, D. L. 2015, AAS, 225, 336.16

Hensberge, H., Ilijić, S., & Torres, K. B. V. 2008, A&A, 482, 1031, https://doi.org/10.1051/0004-6361:20079038

Høg, E., Fabricius, C., Makarov, V. V., et al. 2000, A&A, 355, 27

Huber, D., Silva Aguirre, V., Matthews, J. M., et al. et al., 2014, ApJS, 211, 2, https://doi.org/10.1088/0067-0049/211/1/2

Ilijic, S. 2004, ASPC 318, Spectroscopically and Spatially Resolving the Components of the Close Binary Stars, ed. R. W. Hilditch, H. Hensberge, & K. Pavlovski K. (San Francisco, CA: ASP), 107
Jenkins, J. M., Twicken, J. D., McCauliff, S., et al. 2016, SPIE, 9913, 3, https://doi.org/10.1117/12.2233418
Johnson, J. A., Butler, R. P., Marcy, G. W., et al. 2007, ApJ, 670, 833, https://doi.org/10.1086/521720
Kaufer, A., Stahl, O., Tubbesing, S., et al. 1999, Msngr, 95, 8
Kopal, Z. 1950, HarCi, 454, 1
Lucy, L. B. 1967, ZA, 65, 89
Mazeh, T. & Zucker, S. 1994, Ap&SS, 212, 349, https://doi.org/10.1007/BF00984538
Merrill, P. W., 1936, ApJ, 83, 126, https://doi.org/10.1086/143707
Munari, U. & Zwitter, T. 1997, A&A, 318, 269
Munari, U., Henden, A., Frigo, A., et al. 2014, AJ, 148, 81, https://doi.org/10.1088/0004-6256/148/5/81
Nesterov, V. V., Kuzmin, A. V., Ashimbaeva, N. T., et al. 1995, A&AS, 110, 367
Nelson, B. & Davis, W. D. 1972, ApJ, 174, 617, https://doi.org/10.1086/151524
Pilecki, B., Graczyk, D., Pietrzyński, G., et al. 2013, MNRAS, 436, 953, https://doi.org/10.1093/mnras/stt1529
Pilecki, B., Graczyk, D., Gieren, W., et al. 2015, ApJ, 806, 29, https://doi.org/10.1088/0004-637X/806/1/29
Pojmanski, G. 2002, AcA, 52, 397
Pojmanski, G., Pilecki, B., & Szczygiel, D. 2005, AcA, 55, 275
Popper, D. M. & Etzel, P. B. 1981, AJ, 86, 102, https://doi.org/10.1086/112862
Raghavan, D., McAlister, H. A., Henry, T. J., et al. 2010, ApJS, 190, 1, https://doi.org/10.1088/0067-0049/190/1/1
Ricker, G. R., Winn, J. N., Vanderspek, R., et al. 2015, JATIS, 1, 014003, https://doi.org/10.1117/1.JATIS.1.1.014003
Rucinski, S. M. 2002, AJ, 124, 1746, https://doi.org/10.1086/342342
Ryabchikova, T., Piskunov, N., Kurucz, R. L., et al. 2015, PhyS, 90, 054005, https://doi.org/10.1088/0031-8949/90/5/054005
Schlafly, E. F. & Finkbeiner, D. P. 2011, ApJ, 737, 103, https://doi.org/10.1088/0004-637X/737/2/103
Sheminova, V. A. 2019, KPCB, 35, 129, https://doi.org/10.3103/S088459131903005X
Shivvers, I., Bloom, J. S., & Richards, J. W. 2014, MNRAS, 441, 343, https://doi.org/10.1093/mnras/stu578
Simkin, S. M. 1974, A&A, 31, 129
Simon, K. P. & Sturm, E. 1994, A&A, 281, 286
Soderblom, D. R. 2010, ARA&A, 48, 581, https://doi.org/10.1146/annurev-astro-081309-130806
Southworth, J., Maxted, P. F. L., & Smalley, B. 2004, MNRAS, 351, 1277, https://doi.org/10.1111/j.1365-2966.2004.07871.x
Southworth, J. 2013, A&A, 557, 119, https://doi.org/10.1051/0004-6361/201322195
__________. 2015, ASPC, 496, 164
Southworth, J., Maxted, P. F. L., & Smalley, B. 2005, A&A, 429, 645, https://doi.org/10.1051/0004-6361:20041867
Stassun, K. G., Oelkers, R. J., Paegert, M., et al. 2019, AJ, 158, 138, https://doi.org/10.3847/1538-3881/ab3467
Tokovinin, A. 2014, AJ, 147, 87, https://doi.org/10.1088/0004-6256/147/4/87
Tonry, J. & Davis, M. 1979, AJ, 84, 1511, https://doi.org/10.1086/112569
Torres, G., Andersen, J., & Giménez, A. 2010, A&ARv, 18, 67, https://doi.org/10.1007/s00159-009-0025-1
Valle, G., Dell'Omodarme, M., Prada Moroni, P. G., & Degl'Innocenti, S. 2013, A&A, 549, 50, https://doi.org/10.1051/0004-6361/201220069
Vallely, P. J., Fausnaugh, M., Jha, S. W., et al. 2019, MNRAS, 487, 2372, https://doi.org/10.1093/mnras/stz1445
van Hamme, W. 1993, AJ, 106, 2096, https://doi.org/10.1086/116788
Vanderspek, R., Doty, J., Fausnaugh, M., et al. 2018, TESS Instrument Handbook (Technical Report), Kavli Institute for Astrophysics (Boston, MA: MIT)
Vilardell, F., Ribas, I., Jordi, C., Fitzpatrick, E. L., & Guinan, E. F. 2010, A&A, 509, 70, https://doi.org/10.1051/0004-6361/200913299

Sara Bulut, Ömür Çakırlı, and Barış Hoyman: Ege University, Science Faculty, Astronomy and Space Science Dept., 35100 Bornova, İzmir, Turkey (e-mail: omur.cakirli@gmail.com).
Ahmet Dervişoğlu and Cenk Kayhan: Department of Astronomy and Space Sciences, Erciyes University, 38039, Kayseri, Turkey.
Ahmet Dervişoğlu: Department of Astronomy and Space Sciences, Atatürk University, Yakutiye, 25240, Erzurum, Turkey.

Revista Mexicana de Astronomía y Astrofísica, **58**, 23–35 (2022)

https://doi.org/10.22201/ia.01851101p.2022.58.01.02

A STUDY ON DIFFERENT ATTITUDE STRATEGIES AND MISSION PARAMETERS BASED ON LIGHTSAIL-2

L. G. Meireles[1], A. F. B. A. Prado[1], C. F. de Melo[2], and M. C. Pereira[2]

Received April 22 2021; accepted September 27 2021

ABSTRACT

The Planetary Society's LightSail-2 mission successfully validated the orbital maneuvering capability of a solar radiation pressure (SRP) propelled spacecraft. This paper presents a study on two alternative attitude strategies for the orientation of a solar sail. The goal is to increase the effect of the SRP acceleration over the spacecraft's orbital trajectory, with the intention of maintaining or even gaining altitude over time. Furthermore, one of these strategies was employed while varying a few of the mission's parameters to determine if it would be viable to maintain the spacecraft's average altitude. Results show that it is possible to increase the average altitude of the spacecraft over time while still reducing the number of maneuvers necessary to change the spacecraft's attitude. With that result in hand, it is also possible to change some of the mission parameters without compromising the solar sailing performance.

RESUMEN

La misión LightSail-2 de la Planetary Society validó con éxito la capacidad de maniobra orbital de una nave impulsada por la presión de la radiación solar (PRS). Presentamos un estudio sobre dos estrategias distintas para la orientación de una vela solar. El objetivo es aumentar el efecto de la aceleración por la PRS a lo largo de la trayectoria orbital de la nave, con la intención de mantener o incrementar con el tiempo la altitud. Además, una de las estrategias se usó para determinar la posibilidad de mantener la altitud promedio de la nave al variar algunos parámetros de la misión. Los resultados muestran que es posible aumentar con el tiempo la altitud promedio de la nave, mientras que se reduce el número de maniobras necesarias para cambiar la orientación de la nave. Con este resultado se ve que también es posible modificar algunos parámetros de la misión sin afectar el desempeño de la vela solar.

Key Words: celestial mechanics — methods: numerical — minor planets, asteroids: general — space vehicles

1. INTRODUCTION

Since the beginning of the space exploration age, space agencies and, most recently, private companies around the world, have faced the grand problem of vehicle autonomy and the limitations it imposes on a mission's duration. So far, the most traditional and reliable method of space vehicle's propulsion is chemical combustion. It requires that part of the overall space and total mass of the vehicle be reserved for the storage of fuel, which in turn will be used for required mission maneuvers. In this manner, it serves as a finite resource and is the main limiting factor of a mission's length over time. Alternative propulsion systems have long been of interest for agencies and organizations with the purpose of overcoming these problems. A method of propulsion which uses an abundant energy available throughout the whole space in the inner Solar System was conceived in the early 1920s by Soviet scientists Konstantin Tsiolkovsky and Friedrich Zander (McInnes 2004). This energy is called the solar radiation pressure (SRP) and is simply the momentum of the photons emitted by the Sun. In spite of its simple con-

[1]Space Mechanics and Control Division, National Institute for Space Research, Brazil.

[2]Mechanical Engineering Department, Federal University of Minas Gerais, Brazil.

cept, this technology requires a tremendous effort in materials engineering, in order to build structures large enough to absorb sufficient SRP while still having a limited total mass which facilitates its maneuverability (Vulpetti et al. 2015). These structures are denominated solar sails and have increasingly become target of studies (Forward 1990; Angrilli & Bortolami 1990; McInnes 1999; Wie 2007; Guerman et al. 2008; Zeng et al. 2015, 2016; Zhang & Zhou 2017; D'Ambrosio et al. 2019; Meireles 2019) and space missions (Johnson et al. 2011; Fernandez et al. 2014; Palla et al. 2017; Betts et al. 2017a; Viquerat et al. 2015; McNutt et al. 2014; Heiligers et al. 2019; Mori et al. 2020) from the 1990s until today, in order to validate and further explore their propelling concept and promising mission possibilities (McInnes 2003a,b). A special mention must be given to the Japan Aerospace Exploration Agency (JAXA), which has been responsible for significant contributions to the advances and validation of solar sailing and the first ever mission to employ a solar sail: IKAROS (Mori et al. 2010; Tsuda et al. 2011; Mori et al. 2012; Funase et al. 2012; Tsuda et al. 2013). Lastly, the most recent successful mission which employs a solar sail is LightSail-2, from The Planetary Society (Betts et al. 2017b, 2019; Mansell et al. 2020; Spencer et al. 2021). Despite the mission's successful demonstration of the solar sailing concept, its attitude configuration requires abrupt changes in the spacecraft's orientation. Considering the difficulty in maneuvering the large surface of the sail with a control system with components sufficiently small to be embarked in the mission, these attitude changes require a greater settling time than ideal for the employed strategy. This causes a SRP acceleration in unwanted directions and jeopardizes the solar sail's full potential (Plante et al. 2017). Based on this difficulty, this study proposes some alternative approaches, as presented in McInnes (2004), for the use of the solar sail by smoothing the attitude's rate of change during a maneuver, while still maintaining a similar solar sailing performance.

2. SYSTEM DYNAMICS

The LightSail-2 spacecraft has a total mass m of approximately 5 kg and its sail fully deployed has a surface area A of $32\,\mathrm{m}^2$. Its initial orbit is circular with an altitude of 720 km and an inclination of 24° (The Planetary Society 2020). Therefore, considering the Earth's mean radius as 6378 km, the initial osculating orbital elements are: semi-major axis of 7098 km, eccentricity of 0.0 and inclination of 24°. The three remaining orbital elements are considered to be zero, due to a lack of further information and their reduced importance for our study.

The dynamical model assumes a 4-body problem, including the Sun, the Earth and the Moon, besides the spacecraft. This means that some of the forces acting on the spacecraft are of gravitational nature, from the Sun, the Earth and the Moon. Nevertheless, a few other perturbation forces were considered in the dynamics. The gravitational potential of a non-spherical Earth was included by using up to the 4^{th} order zonal harmonics perturbation acceleration (Bate et al. 1971). Atmospheric effects were also included to determine the drag forces acting on the spacecraft by taking into account the 1976 U.S. Standard Atmosphere atmospheric model (National Oceanic and Atmospheric Administration (NOAA);National Aeronautics and Space Administration (NASA);United States Air Force (USAF) 1976). Furthermore, a solar radiation pressure (SRP) net force was also considered. It is the propelling force, whose model is presented in details in the next section (Vulpetti et al. 2015). Another widely used model for the SRP force can be found in McInnes (2004). This choice was made based on the existence of legacy codes from previous works developed with the format presented in Vulpetti et al. (2015). Finally, the Earth's shadow was considered as having a cylinder shaped umbra and no penumbra region to determine a light exposure coefficient for the SRP net force. The orbit was numerically integrated with the use of Cowell's method (Bate et al. 1971) and a RADAU integrator (Everhart 1985).

LightSail-2 mission's Attitude Determination and Control System (ADCS) is composed of 5 sun sensors, 4 magnetometers, 2 gyro sensors, 3 torque rods and 1 momentum wheel (Plante et al. 2017). However, this study does not take into consideration the delays from the actuators nor the errors from the sensors. The attitude values used in the orbital simulations are equal to the values proposed by the strategy, in order to compare the difference in their influence in the solar sailing performance.

2.1. *Solar Sail Dynamics*

To derive the dynamics of a solar sail propelled spacecraft it is convenient to define a Spacecraft Oriented Frame (SOF), as illustrated in Figure 1. The SOF's X axis points in the radial direction of a heliocentric inertial frame. It has the same direction of the incoming sunlight, which is indicated by the unit vector $\mathbf{u}$. The SOF's Z axis is defined as having

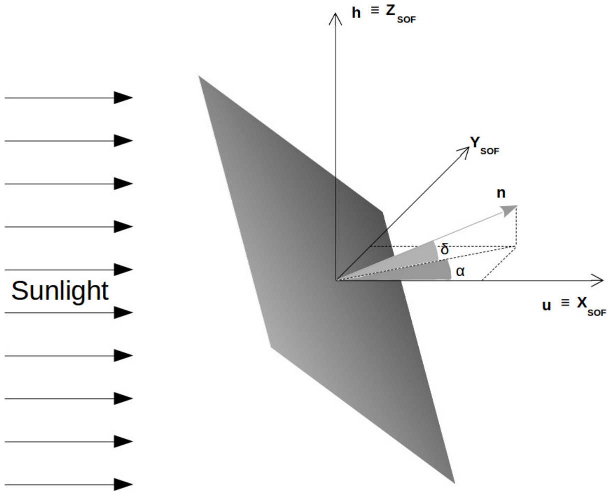

Fig. 1. Spacecraft oriented frame (SOF) referenced at the spacecraft's barycenter, adapted from Vulpetti et al. (2015).

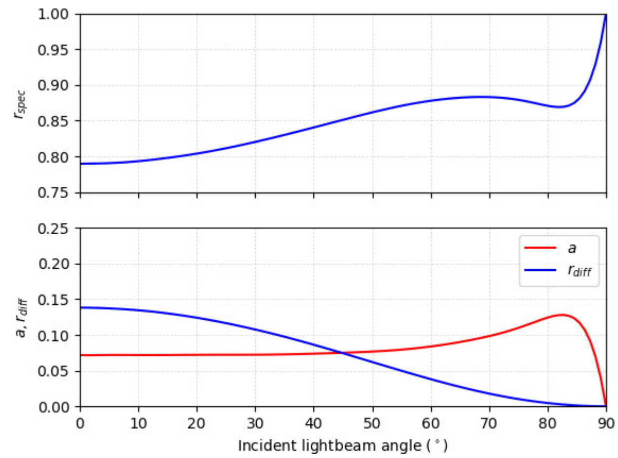

Fig. 2. Absorptivity a, diffuse reflectance r_{diff} and specular reflectance r_{spec} coefficients as a function of the incident light angle for an aluminium sail with a root mean square roughness equal to 20 nm (Vulpetti & Scaglione 1999). The color figure can be viewed online.

the same direction of the spacecraft's orbital angular momentum, indicated by the unit vector **h**. The Y axis is defined in agreement with a coordinate system in dextrorotation. The sail's orientation is represented by the unit vector **n** orthogonal to the solar sail surface. Two important angles are consequently defined, the azimuth α and the elevation δ, necessary to resolve **n** in the SOF. An important consideration is made: the **n** unit vector exists only in the opposite semi-space of the sunlight beam or, in other words, opposite to the sunlit layer of the solar sail. This limits both the azimuth and elevation angles to the interval $[-90, 90]^\circ$.

To determine the thrust **T** resulting from SRP, as a function of the sail's orientation, it is furthermore useful to define the lightness vector **L**, conceived in the SOF as the impulsive acceleration normalized by the Sun's local gravitational acceleration and defined as

$$\mathbf{L}=\left(\frac{1}{2}\frac{\sigma_{\mathrm{c}}}{\sigma}\right)n_{\mathrm{x}}[(2r_{\mathrm{spec}}n_{\mathrm{x}}+\chi_{\mathrm{f}}r_{\mathrm{diff}}+\kappa a)\mathbf{n}+(a+r_{\mathrm{diff}})\,\mathbf{u}]\,, \tag{1}$$

where σ_{c} is a constant referred to as critical loading (equation 2), σ is the sail loading (equation 3), n_{x} is the SOF's X axis **n** versor's component, r_{spec} is the specular reflectance coefficient, r_{diff} is the diffuse reflectance coefficient, χ is the emission/diffusion coefficient (the subscript f refers to the front side of the solar sail), κ is a net thrust dimensionless factor that results from the absorbed and re-emitted power on both sides of the sail (equation 4), and a is the absorptivity coefficient.

The previously mentioned critical loading σ_{c} (equation 2), sail loading σ (equation 3) and net thrust dimensionless factor κ (equation 4), are defined as

$$\sigma_{\mathrm{c}} \equiv 2\frac{I_{1\mathrm{AU}}}{c\; g_{1\mathrm{AU}}} \approx 1.5368\,\mathrm{g/m^2}, \tag{2}$$

$$\sigma \equiv \frac{m}{A}, \tag{3}$$

$$\kappa \equiv \frac{\chi_{\mathrm{f}}\epsilon_{\mathrm{f}}(T)-\chi_{\mathrm{b}}\epsilon_{\mathrm{b}}(T)}{\epsilon_{\mathrm{f}}(T)+\epsilon_{\mathrm{b}}(T)}, \tag{4}$$

where $I_{1\mathrm{AU}} = 1366\,\mathrm{W/m^2}$ is the energy flux emitted by the Sun at 1 Astronomic Unit, the average Sun-Earth distance, equal to 149 597 870 700 m, $c \approx 2,9979 \times 10^8$ m/s is the speed of light in a vacuum, $g_{1UA} \approx 5,930 \times 10^{-3}\,\mathrm{m/s^2}$ is the gravitational acceleration of the Sun at 1 Astronomical Unit, m is the spacecraft's total mass, A is the solar sail surface area, T is the solar sail's temperature and ϵ is the emittance coefficient as a function of T (again, the subscript f refers to the front side of the sail, while the subscript b refers to the back side). From equation 3 and LightSail-2 mission's specifications, the sail loading is $\sigma = 156.25\,\mathrm{g/m^2}$.

Further considerations are made in regard of the optical coefficients absorptivity a, diffuse reflectance r_{diff} and specular reflectance r_{spec}. They are all considered to be a function of the angle of the incident light beam, as portrayed in Figure 2.

An incidence angle of 0° represents the case where the unit vectors **u** and **n** are parallel. Since

TABLE 1

JPL'S MODEL SOLAR SAIL OPTICAL COEFFICIENTS

	r	r_{spec}/r	ϵ_{f}	ϵ_{b}	χ_{f}	χ_{b}
Ideal	1	1	0	0	2/3	2/3
Square	0,88	0,94	0,05	0,55	0,79	0,55

both the reflectance coefficients are also a function of the sail's reflective layer roughness, the worst case scenario for the graphs of a value of 20 nm root mean square roughness was considered for the simulations.

The Jet Propulsion Laboratory (JPL) published some of its solar sail models coefficients obtained from experimental studies developed in the early 2000's, which are presented in Table 1 (McInnes 2004). The values of ϵ and χ of a square solar sail were used for this study.

3. ATTITUDE STRATEGIES

This section serves the purpose of explaining in details each of the three different strategies, as presented in McInnes (2004) and used to simulate the solar sail's orientation and their consequences to the spacecraft's orbital trajectory. The results obtained from the Planetary Society strategy are used as a reference for comparison to the other two strategies analyzed by this study.

3.1. *Strategy 1: The Planetary Society*

The Planetary Society initial strategy consists of operating the solar sail at an "on-off" regime (Mansell et al. 2020). It consists of maintaining the solar sail at full exposure to the sunlight whenever the spacecraft is traveling away from the Sun. In other words, the unit vector orthogonal to the sail $\mathbf{n}$ is parallel to $\mathbf{u}$ and, consequently, both the azimuth and elevation angles α and δ are equal to zero. On the other hand, the "off" regime consists of maintaining the solar sail without any exposure to the sunlight whenever the spacecraft is traveling in the direction of the Sun. This means that the unit vectors $\mathbf{n}$ and $\mathbf{u}$ are orthogonal between themselves and α and/or δ are equal to 90°. The schematics of this strategy is illustrated in Figure 3.

In order to maximize the thrust component in the SOF XY-plane, δ is always equal to zero. Consequently, only the value of α changes. The first day of simulation (with the purpose of zooming in the X axis) for this strategy is illustrated in Figure 4.

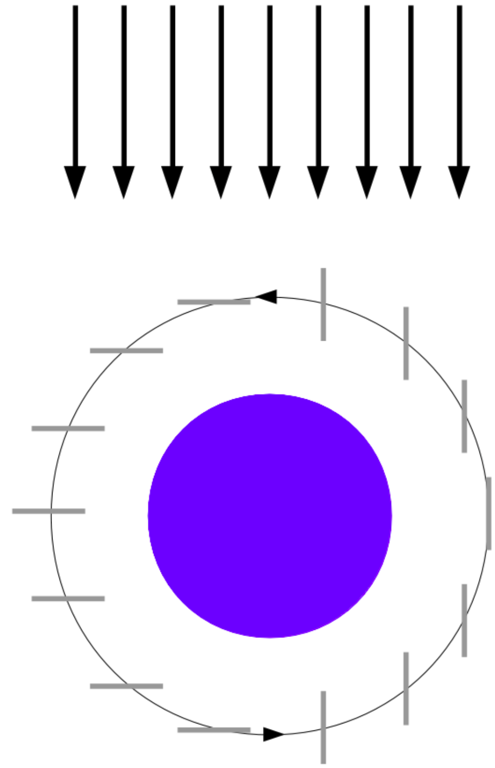

Fig. 3. LightSail-2 orientation schematics, adapted from Betts et al. (2017b). The color figure can be viewed online.

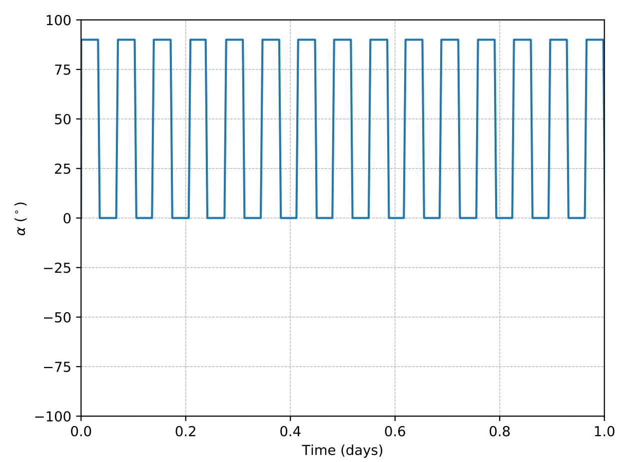

Fig. 4. Azimuth angle α as a function of time for Strategy 1. The color figure can be viewed online.

It is possible to observe that two attitude maneuvers are necessary at every orbital revolution.

The first 200 days of the orbital dynamics of this system were simulated using Strategy 1, as well as the spacecraft's altitude evolution, are presented in Figure 5.

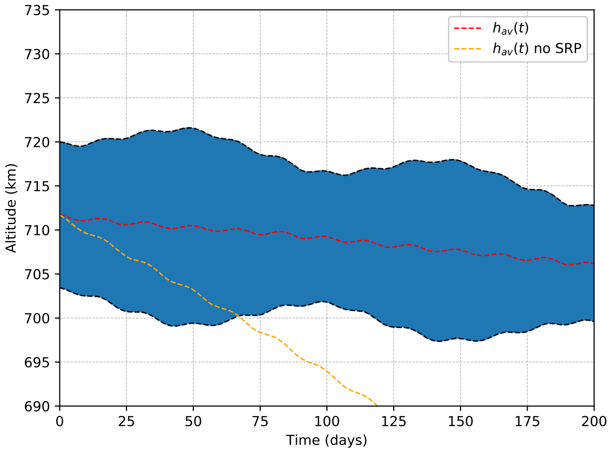

Fig. 5. Spacecraft's altitude as function of time for Strategy 1. The color figure can be viewed online.

The blue region of the plot is in fact the altitude over time. It is seen as a blur due to the large scale of time covered in the X axis. As expected, it behaves as a sinusoidal wave enveloped by two other curves of the maximum and minimum altitude reached at every revolution, which in turn are seen as the dashed black lines. The dashed red line is a simple average of the envelope curves and is considered to be the average altitude as a function of the simulation instant in days $h_{\rm av}(t[\text{days}])$. It starts at a value of 711.6867 km and decreases 5.5204 km to 706.1663 km after 200 days. The dashed orange line indicates $h_{\rm av}(t)$ for a simulation with disabled solar sailing, meaning a null SRP net force, to demonstrate the importance of solar sailing for maintaining the spacecraft's average altitude over time. After 200 days, $h_{\rm av}(200) = 671.6718$ km, having lost an extra 34.4945 km, or 7.25 times more, of average altitude in comparison with the situation where the solar sailing is active.

Figure 6 presents the actual highest and lowest points of the orbit's altitude values for the LightSail-2 mission, publicly made available and directly taken from The Planetary Society's link for the LightSail-2 Mission Control (The Planetary Society 2020). A similar chart can be seen in the same link. There are clear differences from the results seen in Figure 5, despite the fact that the general behavior of these figures are the same. This happens due to the simplified orbital model used in the simulation and to limited access to initial conditions information for the spacecraft. In addition, the model considered overestimates the solar radiation pressure net thrust in comparison to the drag force. Therefore, in order to approximate the simulation results to the

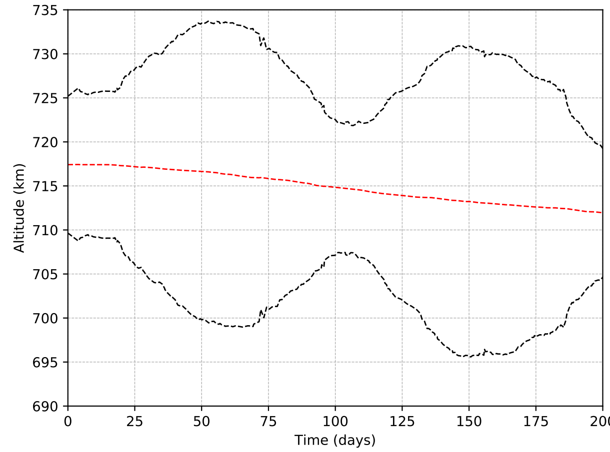

Fig. 6. LightSail-2's apogee, perigee and average altitude curves as a function of time from LightSail-2 Mission Control (https://www.planetary.org/explore/projects/lightsail-solar-sailing/lightsail-mission-control.html). The color figure can be viewed online.

LightSail-2's mission published data, the SRP net thrust had to be scaled down by a factor of 7×10^{-2}.

The initial average altitude of LightSail-2 mission's at sail's deployment, on 23 July 2019, is 717.4105 km. On 3 February 2020, 200 days after sail deployment, the average altitude is 711.6255 km, in contrast to the simulated value of 706.1663 km. Although a divergence from the simulated and actual trajectory data is not ideal, it is not a vital requirement for this study that they match in value. As is the case, the main result is a comparison from all the attitude strategies, and since they are all simulated using the same orbital models, the results from Strategy 1 serve mainly as a comparison reference for other strategies.

3.2. *Strategy 2: Maximum $\dot{\varepsilon}$*

Solar radiation pressure propulsion is a specific type of low-thrust. Therefore, the thrust is a function of the spacecraft's orientation, but for solar sails, its magnitude is also a function of the spacecraft's position. Therefore, an analysis of its trajectory as a function of its orientation is possible from a traditional approach (Keaton 1986) given this extra constraint $|\mathbf{T}| = f(\mathbf{n}, \mathbf{r})$, where $\mathbf{r}$ is the spacecraft's position in the heliocentric inertial frame (HIF).

From equation 5, it is known that the specific orbital energy's rate of change over time is maximized when the net thrust component in the direction of the spacecraft's velocity vector has its greatest magnitude. This does not necessarily mean (and often it

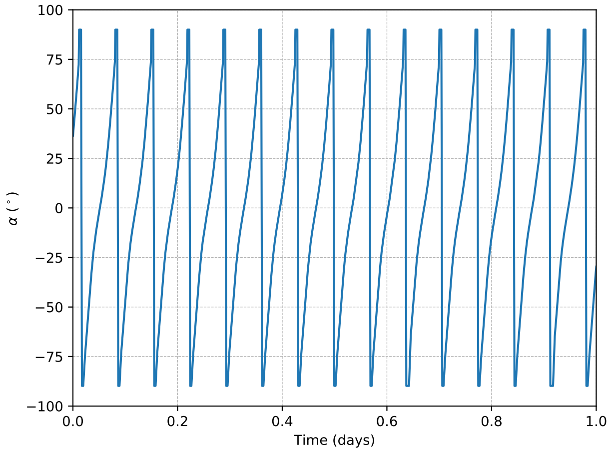

Fig. 7. Azimuth angle α as a function of time for Strategy 2. The color figure can be viewed online.

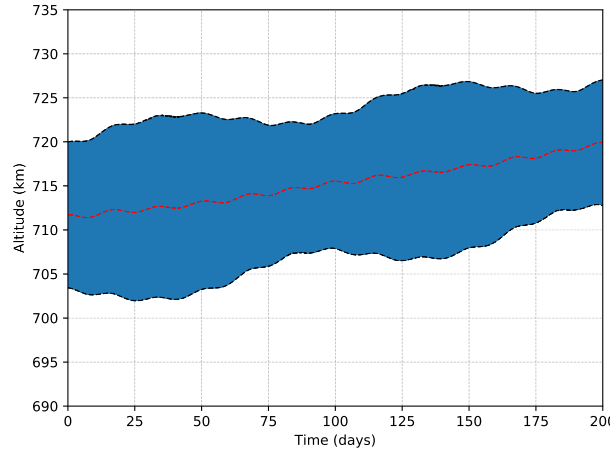

Fig. 8. Spacecraft's altitude as function of time for Strategy 2. The color figure can be viewed online.

is the case) that the sail and/or the net thrust vector should be pointed in the direction of travel. In equation 5 $\dot{\mathbf{r}}$ is the spacecraft's velocity vector in the HIF

$$\dot{\varepsilon} = \dot{\mathbf{r}} \cdot \mathbf{T}\frac{1}{m}. \tag{5}$$

To determine this optimal strategy, it is necessary to search for the orientation which gives the maximum component of $\mathbf{T}$ at the $\dot{\mathbf{r}}$ direction. Considering one point of the simulation at a time, that is to say, having a fixed position $\mathbf{r}$ and velocity $\dot{\mathbf{r}}$, this is a well bound one dimensional convex problem, with α constrained in the interval $[-90, 90]^\circ$. A simple hill climbing search algorithm is sufficient, and was used in this study to find the solutions. The first day of simulation (again, with the purpose of zooming in the X axis) for this strategy is illustrated in Figure 7.

In contrast to the limited number of attitude maneuvers per orbital revolution from Strategy 1, this approach requires a constant control over the sail's orientation. Nevertheless, it is possible to observe an interesting characteristic of this strategy's behavior: the sail completes half a rotation (the azimuth angle α rises from -90° to 90°) for every orbital revolution. This is a crucial information considered in the development of Strategy 3. It is also important to note that, from the definition of unit vector $\mathbf{n}$ (it exists in the semi-space opposite to the incoming sunbeam and, put differently, it always points away from the sail's side not exposed to the sunlight), the transition of value from $\alpha = 90^\circ$ to $\alpha = -90^\circ$ does not mean a change of 180° in the sail's orientation. In this situation, the unit vector $\mathbf{n}$ merely changes its side back to the one in the shadow. Furthermore, for this consideration to work with the simulations in this study, it is necessary for the solar sail to have equally reflective sides.

Figure 8 displays the same quantities presented in Figure 5, but this time, with the employment of Strategy 2.

There is a noticeable quantitative difference between the results of Strategies 1 and 2. The latter presents an average altitude after 200 days of 719.9000 km, which is 13.7337 km, or 1.94%, higher. But there is also a remarkable contrast between both simulations. While Strategy 1 decreases its average altitude over time, Strategy 2 actually increases its value. Starting from 711.7190 km, it gains 8.1810 km over the course of 200 days. This result is of great value given the objective of LightSail-2 mission in demonstrating the hidden potential of SRP in maneuvering a spacecraft. The more the solar sail is capable of increasing the average altitude of the spacecraft, the more the concept of solar sailing gains relevance.

3.3. *Strategy 3: Constant $\dot{\alpha}$*

From the desire of maintaining a performance in altitude gain close to the one obtained from Strategy 2 while trying to reduce the number of attitude maneuvers, in order to maintain a similarity to LightSail-2 mission's approach, a third strategy was analyzed. It consists of keeping the sail at a constant rate of change of its azimuth angle $\dot{\alpha}$, with a value that guarantees it completes half a rotation for every orbital revolution, as observed in Strategy 2. But there is a minor problem with this considera-

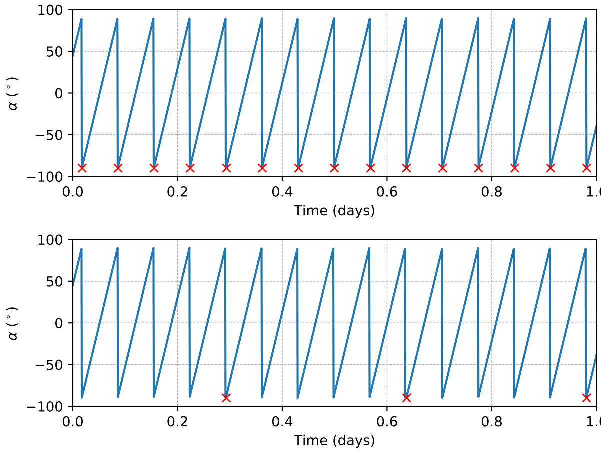

Fig. 9. Azimuth angle α as a function of time for Strategy 3. $N_{\text{rev}} = 1$ for the upper graph. $N_{\text{rev}} = 5$ for the lower graph. The color figure can be viewed online.

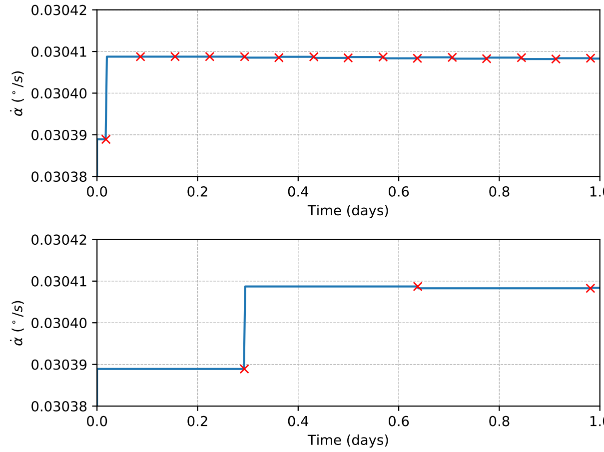

Fig. 10. Azimuth angle rate of change $\dot{\alpha}$ as a function of time for Strategy 3. $N_{\text{rev}} = 1$ for the upper graph. $N_{\text{rev}} = 5$ for the lower graph. The color figure can be viewed online.

tion. Since the goal is to increase the spacecraft's altitude and, consequently, its specific orbital energy, then the period of revolution will also increase. This would mean that the $\dot{\alpha}$ implemented is no longer able to maintain the half rotation per orbital revolution desired. Therefore, it is necessary to perform attitude maneuvers once in a while to correct $\dot{\alpha}$ and α. More specifically, an attitude maneuver will only be performed after a complete revolution, which means after an integer number of revolutions N_{rev}. As a reference, the maneuvers are performed at the point where the spacecraft is traveling directly in the direction of the Sun. In other words, when its velocity vector points in the opposite direction of its heliocentric position vector. At this instant, the desired value of α is always $-90°$.

Figure 9 illustrates some examples of the proposed strategy. Every instant of an attitude maneuver is indicated with a red cross in the graph. Once again, only the first day of simulation is presented with the intention of zooming on the X axis values and having a better view for further analysis. The top graph corresponds to an attitude maneuver once every orbital revolution ($N_{\text{rev}} = 1$). The bottom graph corresponds to an attitude maneuver once every five orbital revolutions ($N_{\text{rev}} = 5$).

Figure 10 presents the azimuth angle rate of change $\dot{\alpha}$ from the examples in Figure 9, in the same time interval. Once again, the instant of the maneuver is indicated by a red cross.

From the data presented in Figure 10, it is interesting to observe the general behavior of $\dot{\alpha}$ throughout the simulation (Figure 11).

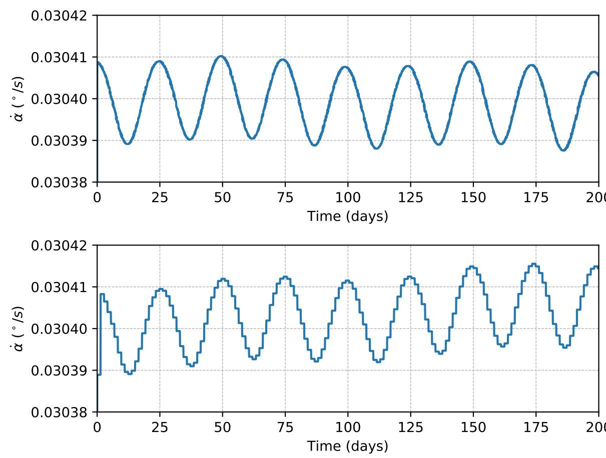

Fig. 11. Azimuth angle rate of change $\dot{\alpha}$ as a function of time for Strategy 3. $N_{\text{rev}} = 1$ for the upper graph. $N_{\text{rev}} = 20$ for the lower graph. The color figure can be viewed online.

As ε increases, so does the orbital period. Therefore, $\dot{\alpha}$ is supposed to decrease in this situation. The inverse is also true. As ε oscillates, so does $\dot{\alpha}$. In the case of $N_{\text{rev}} = 20$, is it possible to observe an overall increase in the average value of $\dot{\alpha}$, which is an indication of an overall loss of ε and, consequently, average altitude. An example of $N_{\text{rev}} = 20$ was considered instead of $N_{\text{rev}} = 5$ to make this even clearer in the graphical representation of the discrete range of values of $\dot{\alpha}$. As N_{rev} increases, the longer the sail maintains its azimuth angle rate of change.

It became interesting to simulate a range of N_{rev} to evaluate for how long the spacecraft can be left without any attitude maneuver and still have a bet-

TABLE 2

EVALUATION OF $H_{AV}(200)$ AS A FUNCTION OF N_{REV} FOR STRATEGY 3

N_{rev}	$h_{av}(200)$ (km)	$h_{gain}(200)$ (%)
1	711.9803	+0.0367
2	711.9994	+0.0394
3	712.0116	+0.0411
4	712.0119	+0.0412
5	712.0039	+0.0400
10	711.8236	+0.0147
15	711.3687	-0.0492
20	710.6479	-0.1505
25	709.6213	-0.2947
30	708.3483	-0.4736
35	706.7824	-0.6936
40	704.9903	-0.9454
45	702.9148	-1.2370
50	700.5899	-1.5637

ter performance than Strategy 1. The average altitude after 200 days of simulation $h_{av}(200)$ and its gain compared to the initial average altitude h_{gain} (equation 6) are presented in Table 2, as a function of N_{rev}

$$h_{gain}(t) = \left(\frac{h_{av}(t)}{h_{av}(0)} - 1 \right) \times 100. \qquad (6)$$

Remarkably, only values of N_{rev} greater than 35 resulted in $h_{av}(200)$ smaller than 706.1663 km, obtained by Strategy 1. This means that over 70 times fewer maneuvers could be performed without a loss in the solar sail's performance in keeping the spacecraft's average altitude. An unexpected result is having a maximum value for $N_{rev} = 4$. The expected maximum was found for $N_{rev} = 1$. Despite this fact, the whole range of N_{rev} from 1 up to 10 presents similar results for $h_{av}(200)$, all of which, as is the case of Strategy 2, show an increase of h_{av} over time. This indicates that other conditions are maybe more significant for this range of values.

Results from Table 2 are presented graphically in Figure 12.

The blue dashed line at the top is the result obtained from Strategy 2. It can be considered as a maximum, yet unattainable, goal for Strategy 3. On the other hand, the red dashed line at the bottom is the result obtained from Strategy 1. Since it was already implemented in the LightSail-2 mission, it can be considered as a minimum to overcome. For values of N_{rev} smaller than or equal to 35, Strategy 3 proved to be a successful attempt to improve the performance of a solar sail to gain altitude.

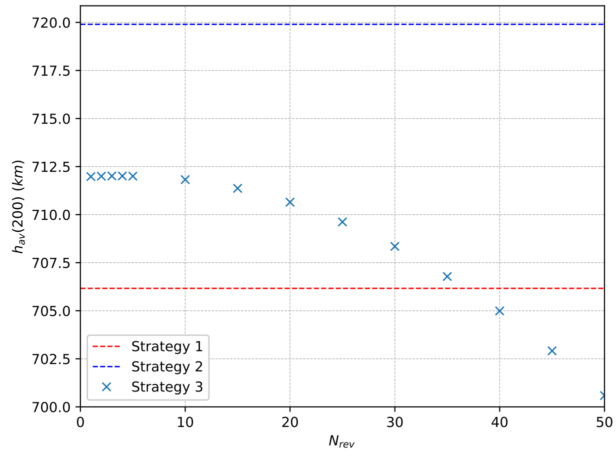

Fig. 12. Average altitude after 200 days as a function of N_{rev} for Strategy 3. The color figure can be viewed online.

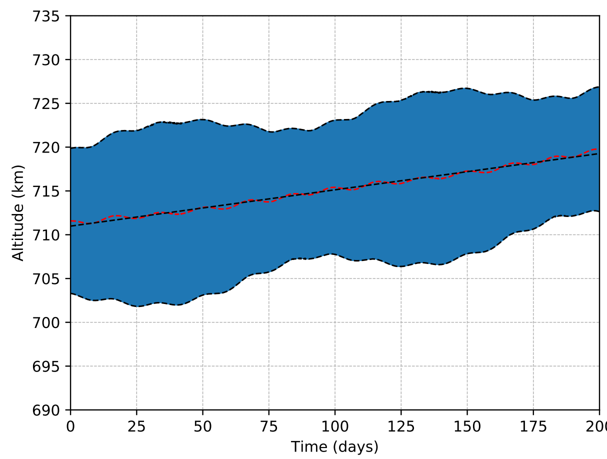

Fig. 13. The spacecraft altitude as a function of time for Strategy 2. The color figure can be viewed online.

4. MISSION PARAMETERS ANALYSIS

In this section, a set of mission parameter values were modified to investigate their general behavior. The use of Strategy 2 is justified as being a theoretical limit to the maneuvering potential of solar sailing. Namely, it is the best case scenario.

An important consideration is made for the average altitude's change of value over time. It is assumed to have a linear variation along the 200 days simulated. Therefore, it was possible to implement a linear least-squares regression for $h_{av}(t)$, as indicated in Figure 13 by the yellow dashed line. The

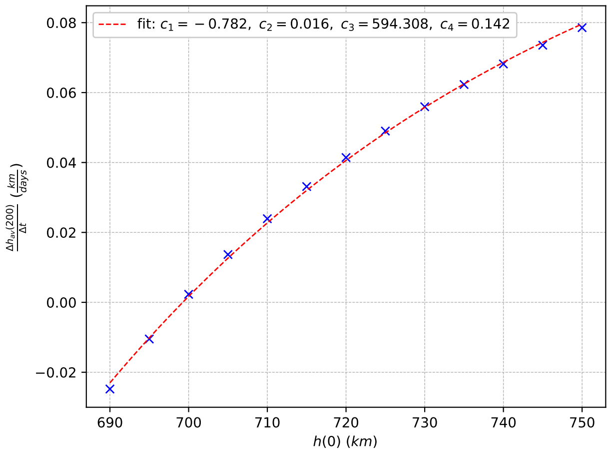

Fig. 14. Average altitude slope after 200 days as a function of the initial altitude $h(0)$ for Strategy 2. The parameters of equation 7 are also displayed. The color figure can be viewed online.

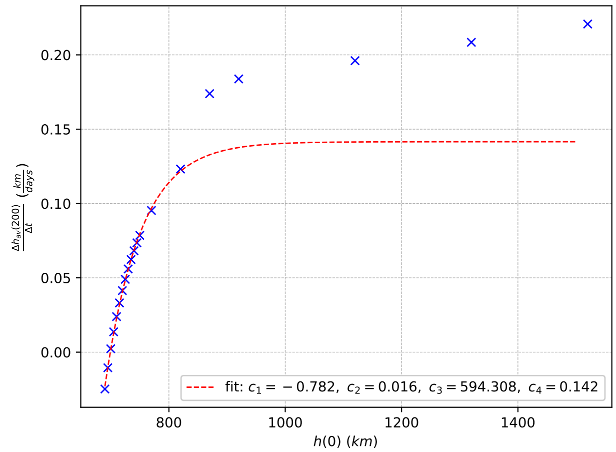

Fig. 15. Average altitude after 200 days as a function of the initial altitude $h(0)$ for Strategy 2 (extended view). Equation 7 function parameters are also displayed. The color figure can be viewed online.

slope of these regression lines is henceforth referred to as $\frac{\Delta h_{\mathrm{av}}(200)}{\Delta t}$. It is noted that this yellow line follows very closely the red line.

As final considerations, after each sweep of the mission parameters, the regression line's slope values are fitted to a given function, and are presented in the corresponding section.

4.1. *Initial Altitude Sweep*

An interesting analysis comes from the sweep of the mission's initial altitude $h(0)$. As indicated by Figure 5, the drag forces are greatly responsible for the spacecraft's altitude decay. An also known fact is that, as the altitude decreases, the drag forces increase in magnitude. In turn, this would decrease the slope of the regression line. The inverse is also expected to be true. Therefore, a sweep of values in the $[690, 750]$ km interval was made (Figure 14). In addition, given the exponential nature of the atmospheric model considered, the data is fitted to the function presented in equation 7

$$f(x) = c_1 \mathrm{e}^{-c_2(x-c_3)} + c_4, \tag{7}$$

where x is the independent variable from known data, y is the dependent variable for the fitted curve and c_{n} are the function's parameters.

Figure 14 shows that Strategy 2 can avoid the decay of the spacecraft for initial altitudes close to 700 km. Since the atmospheric model only considers that the atmosphere's density is not null up to an altitude of approximately 865 km, and therefore drag forces only exist until this altitude, it is interesting to extend the interval of analysis to verify that greater values of $h(0)$ do not fall near the fitted curve and behave in a different manner, closer to a linear behavior (Figure 15).

4.2. *Spacecraft Mass Sweep*

A fundamental parameter for solar sailing is the sail loading σ (equation 3). As the spacecraft's mass m increases, so does σ, and consequently the sail's capacity to maneuver the spacecraft decreases (equation 1). Given that Strategy 2 was able to increase $h_{\mathrm{av}}(t)$ over time, an effort was made to determine how much m could be increased while keeping a constant sail size (and surface area A) and still maintaining a positive slope for the average altitude regression line (Figure 16). Given the nature of equation 1, the data is fitted to the function presented in equation 8

$$f(x) = \frac{c_1}{x - c_2} + c_3. \tag{8}$$

The figure shows that, even for a massive spacecraft of nearly half a ton, the regression line's slope still maintains a positive value. Despite being a fitted parameter, the fact that c_3 is greater than zero indicates a limit, given this mission's initial conditions and the employment of Strategy 2, which would guarantee no decay for the spacecraft's average altitude. It means that, in theory, any spacecraft can use this technique.

In the search for negative $\frac{\Delta h_{\mathrm{av}}(200)}{\Delta t}$, the initial altitude was changed to smaller values and the same curve fit procedures were performed (Table 3). From Figure 17 it is possible to see that $\frac{\Delta h_{\mathrm{av}}(200)}{\Delta t}$ is more

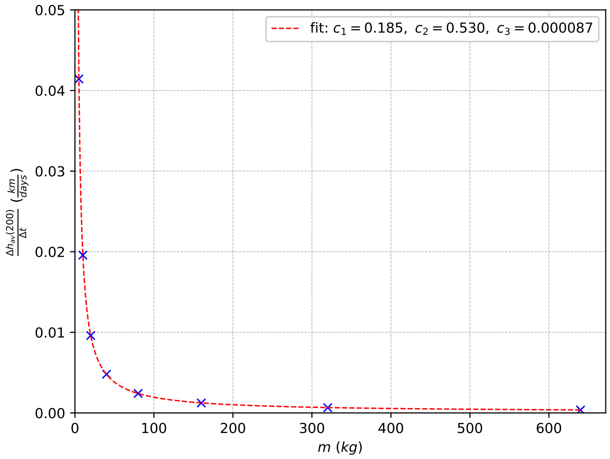

Fig. 16. Average altitude after 200 days as a function of the spacecraft's mass for Strategy 2. The parameters of equation 8 are also displayed. The color figure can be viewed online.

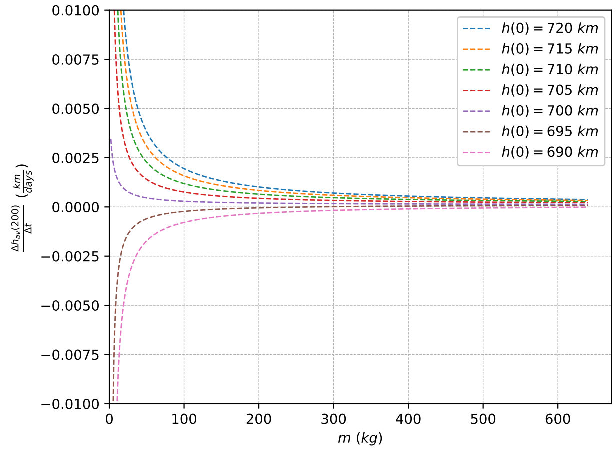

Fig. 17. Curve fit for the average altitude regression line's slope after 200 days as a function of the spacecraft's mass, for Strategy 2 and different initial altitudes $h(0)$. The color figure can be viewed online.

TABLE 3

CURVE FIT PARAMETERS FOR THE AVERAGE ALTITUDE*

$h(0)$	c_1	c_2	c_3
720	0.185	0.530	0.000087
715	0.147	0.538	0.000099
710	0.107	0.526	0.000112
705	0.063	0.330	0.000118
700	0.019	-3.681	0.000104
695	-0.035	1.671	0.000133
690	-0.090	1.398	0.000128

*Slope of the regression line after 200 days as a function of the initial altitude $h(0)$ for Strategy 2.

sensitive to variations of $h(0)$ for lower m, as expected. In fact, a negative $\frac{\Delta h_{\rm av}(200)}{\Delta t}$ starts to be observed for negative values of c_1, which happens with $h(0)$ lower than 700 km. This indicates a minimum altitude where Strategy 2 can be employed to keep a positive $\frac{\Delta h_{\rm av}(200)}{\Delta t}$ for a wide range of spacecraft masses. The present study showed that the initial altitude of the spacecraft is the determinant variable to allow this technique to be used to keep the spacecraft in orbit, and the mass does not influence the results.

4.3. *Orbital Plane Inclination Sweep*

Solar sails are an intriguing propelling method with a unique peculiarity. Considering an heliocentric inertial frame, their resulting thrust will always have a radially positive component. As long as a sail is open, it will reflect the incident sunlight, transfer linear momentum to or from the spacecraft to produce a resulting thrust with a positive radial component, whether this is a desired effect or not. The only alternative to avoid the aforementioned limitation is to reduce the sail's exposed surface area to zero. From a mission control perspective, this would mean increasing either the azimuth angle α or the elevation angle δ to 90°.

When considering a problem with the objective of increasing the average altitude over time, the desired direction in which the resulting SRP acceleration component needs to be maximized is different for various values of the orbital plane inclination. This results in slightly different desired azimuth angles over the span of an entire orbital revolution. In addition, it would be interesting to investigate different mission scenarios, considering whatever engineering limitations or obligations an organization might have in determining the orbital plane inclination of its mission. Inevitably, the variation of this orbital parameter is another interesting analysis to be made (Figure 18). Given the trigonometric relation of this parameter to the system's dynamics, the data is fitted to the form presented in equation 9

$$f(x) = c_1 \sin(c_2(x - c_3)) + c_4. \tag{9}$$

As is well known, a smaller exposed surface area results in a lower SRP net thrust. In turn, this means lower specific orbital energy gains or losses and, theoretically, a reduced solar sailing maneuverability. But this fact could be used to the mission

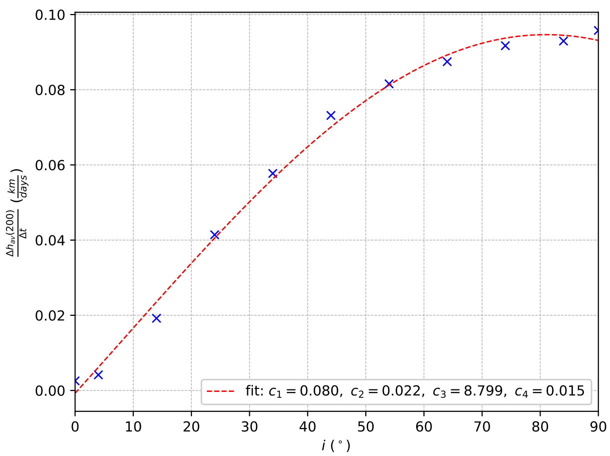

Fig. 18. Average altitude after 200 days as a function of the orbital plane inclination i for Strategy 2. The parameters of equation 9 are also displayed. The color figure can be viewed online.

advantage. In the situation of higher inclinations, the use of Strategy 2 is specially capable of making the best use of the minimization of losses. In other words, whenever the spacecraft is traveling in the direction of the Sun, the energy losses can be reduced even further, compensating the inferior energy gains. This justifies the increasing average altitude regression line slope, as seen in Figure 18. It also shows that the strategy works for all ranges of inclinations studied $[0, 90]°$ but, since $\frac{\Delta h_{\rm av}(200)}{\Delta t}$ increases with the inclination, higher inclinations can be used if the goal is to increase the altitude of the spacecraft. This is particularly interesting if an escape from the Earth is desired.

Once again, the initial altitude was changed to lower values, followed by the same curve fit procedures, in the search for a minimum orbital plane inclination where Strategy 2 is capable of maintaining a positive $\frac{\Delta h_{\rm av}(200)}{\Delta t}$ Table (4). These curves are displayed in Figure 19, which also indicates that, for each one, there is an interception point with the $\frac{\Delta h_{\rm av}(200)}{\Delta t} = 0$ axis, as well as an inclination value with a maximum $\frac{\Delta h_{\rm av}(200)}{\Delta t}$. In turn, these particular points are presented in Figure 20.

Figure 20 also displays a dashed red line that represents the mean value of i for $max\left(\frac{\Delta h_{\rm av}(200)}{\Delta t}\right)$ from the fitted curves, which is approximately 79.8°. In spite of this value, the verified best case scenario of i for the employment of Strategy 2 is an inclination of 90°. In the bottom graph, the blue area represents regions of $h(0)$ and i where Strategy 2 is able to maintain a positive $\frac{\Delta h_{\rm av}(200)}{\Delta t}$, while the

TABLE 4

CURVE FIT PARAMETERS FOR THE AVERAGE ALTITUDE*

$h(0)$	c_1	c_2	c_3	c_4
720	0.080	0.022	8.799	0.015
710	0.097	0.022	8.672	-0.009
700	0.118	0.022	8.982	-0.037
690	0.152	0.022	7.482	-0.079
680	0.208	0.021	4.076	-0.144
670	0.365	0.018	-9.752	-0.312
660	2.664	0.007	-132.831	-2.626

*Slope of the regression line after 200 days as a function of the initial altitude $h(0)$ for Strategy 2.

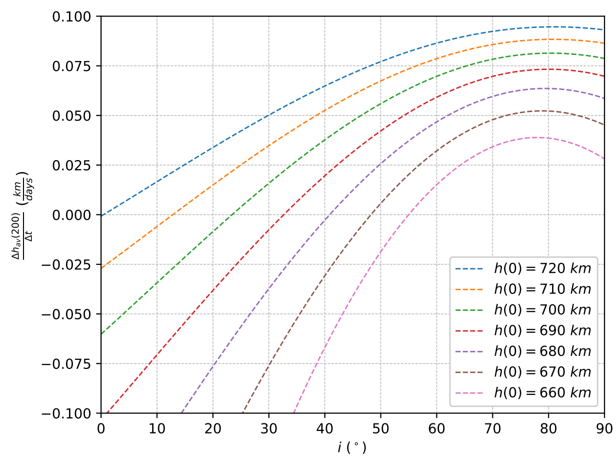

Fig. 19. Curve fit for the average altitude regression line's slope after 200 days as a function of the orbital plane inclination i for Strategy 2 and different initial altitudes $h(0)$. The color figure can be viewed online.

red area represents the opposite region, of negative $\frac{\Delta h_{\rm av}(200)}{\Delta t}$. Two remarks have to be made in this case scenario. First, for $h(0) > 720$ km, Strategy 2 is able to maintain an average altitude gain for any i, including equatorial orbits. Second, for lower $h(0)$, the drag forces are greatly superior, reducing the linear behavior of $h_{\rm av}(t)$ and making it very difficult to fit parameters into the same function used for the other $h(0)$ cases. This can already be verified with the parameter values of $h(0) = 660$ km in Table 4, which are different from the rest by an order of magnitude. Nevertheless, it was possible to verify that for $h(0) < 650$ km there are no positive $\frac{\Delta h_{\rm av}(200)}{\Delta t}$ for any i, which indicates that this is a limiting $h(0)$ where Strategy 2 cannot maintain an average altitude gain, even for the best value of the inclination.

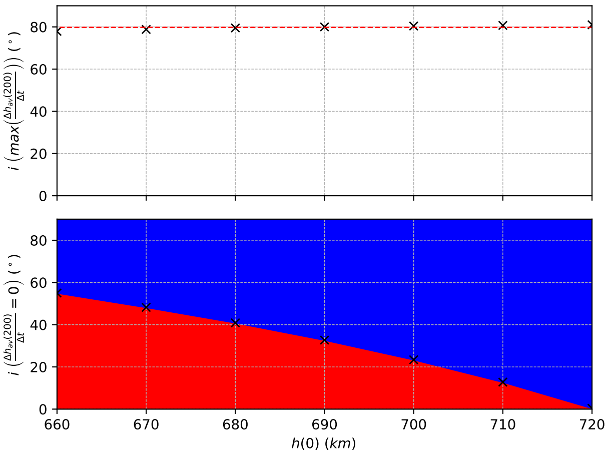

Fig. 20. Average altitude regression line's slope after 200 days maximum and null values as a function of the orbital plane inclination i and the initial altitude $h(0)$. The color figure can be viewed online.

5. CONCLUSION

This study had the purpose of investigating different attitude strategies for the LightSail-2 mission and how they affect the solar sail's capacity of maintaining the spacecraft's altitude over time. Strategy 1 effectively replicated the original approach from the LightSail-2 mission and its implementation served as a base of comparison. Strategy 2, as expected, achieved a maximum performance result, at the cost of constantly maneuvering the sail with small attitude corrections. This strategy made it even possible to increase the spacecraft's average altitude over time. Strategy 3 presents a simpler alternative to implement a smaller number of attitude maneuvers to keep the solar sail at a desired performance. Its implementation could mean a decrease of more than 70 times the number of attitude maneuvers implemented in LightSail-2's mission without losing its solar sail's maneuverability. For cases of up to one maneuver every 10 orbital revolutions, the sail also proved to be able to increase the spacecraft's average altitude over time.

Making use of Strategy 2's better performance, the values of the spacecraft's mass, initial altitude and orbital plane inclination were changed in desired intervals to investigate regions where the sail could still maintain an average altitude gain over time. It was determined that, for the same inclination and for a wide range of spacecraft's masses of up to half a ton, the initial altitude could be reduced by 20 km to a value of 700 km. In addition, the sail's performance could be increased with a raise in the inclination, with a best case scenario for the highest value of 90°. In turn, with this inclination, the initial altitude could be reduced a further 50 km to a value of 650 km.

Having examined the final results achieved and given the initial objectives, this study was successful in analyzing alternative attitude strategies able to keep a desired solar sail performance, while still keeping a simple enough implementation for the attitude control system employed in the LightSail-2 mission.

First and foremost, it is important to acknowledge the work and efforts of The Planetary Society, an organization concerned not only with the popularization of space technology and science, an already noble task, but also concerned with the practical advancements of the field, making missions such as LightSail-2 possible, which depend so much on the visionary collaboration of so many scientists, engineers and enthusiasts. The authors would also wish to express their appreciation for the support provided by Grants # 406841/2016-0 and 301338/2016-7 from the National Council for Scientific and Technological Development (CNPq), Grants # 2018/19959-0 and 2016/24561-0 from São Paulo Research Foundation (FAPESP) and to the financial support from the National Council for the Improvement of Higher Education (CAPES).

REFERENCES

Angrilli, F. & Bortolami, S. 1990, ESA Journal, 14, 431

Bate, R. R., Mueller, D. D., & White, J. E. 1971, Fundamentals of astrodynamics (New York, NY: Dover)

Betts, B., Nye, B., Vaughn, J., et al. 2017a, International Symposium on Solar Sailing, Kyoto, Japan

Betts, B., Spencer, D., Bellardo, J., et al. 2019, IAF Space Propulsion Symposium (Washington, DC: IAF), 709

Betts, B., Spencer, D., Nye, B., et al. 2017b, International Symposium on Solar Sailing, Kyoto, Japan

D'Ambrosio, A., Circi, C., & Zeng, X. 2019, AdSpR, 63, 3691

Everhart, E. 1985, IAUC 83, Dynamics of Comets: Their Origin and Evolution, ed. A. Carusi & G. B. Valsecchi (Dordrecht: ASSL), 115, 185 [LINK]

Fernandez, J. M., Visagie, L., Schenk, M., et al. 2014, AcAau, 103, 204

Forward, R. L. 1990, JSpRo, 27, 411

Funase, R., Kawaguchi, J., Mori, O., Sawada, H., & Tsuda, Y. 2012, 53rd AIAA/ASME/ASCE/AHS/ASC, Structures, Structural Dynamics and Materials Conference (Honolulu, HI: AIAA), https://doi.org/10.2514/6.2012-1748

Guerman, A., Smirnov, G., & Pereira, M. C. 2008, Advances in the Astronautical Sciences, 129, 607

Heiligers, J., Fernandez, J., Stohlman, O., & Wilkie, W. 2019, Astrodynamics, 3, 231

Johnson, L., Whorton, M., Heaton, A., et al. 2011, AcAau, 68, 571, https://doi.org/10.1016/j.actaastro.2010.02.008

Keaton, P. W. 1986, STIN 86 (Washington: NASA)

Mansell, J., Spencer, D. A., Plante, B., et al. 2020, AIAA Scitech 2020 Forum (Orlando, FL: AIAA), https://doi.org/10.2514/6.2020-2177

McInnes, C. R. 1999, AcAau, 45, 567, https://doi.org/10.1016/S0094-5765(99)00177-0

__________. 2003a, RSPTA, 361, 2989, https://doi.org/10.1098/rsta.2003.1280

__________. 2003b, AdSpR, 31, 1971, https://doi.org/10.1016/S0273-1177(03)00172-8

__________. 2004, Solar Sailing (Technology, Dynamics and Missions Applications) (London, UK: Praxis Publishing)

McNutt, L., Johnson, L., Kahn, P., Castillo-Rogez, J., & Frick, A. 2014, AIAA Space 2014 Conference and Exposition (San Diego, CA: AIAA), https://doi.org/10.2514/6.2014-4435

Meireles, L. G. 2019, Análise de modelos não-ideais da dinâmica de atitude de velas solares e seus efeitos no movimento orbita, Master Thesis, INPE, São José dos Campos, http://urlib.net/rep/8JMKD3MGP3W34R/3SUPEUS

Mori, O., Matsumoto, J., Chujo, T., et al. 2020, Astrodynamics, 4, 233

Mori, O., Sawada, H., Funase, R., et al. 2010, JSAST, 8, 4, https://doi.org/10.2322/tastj.8.To_4_25

Mori, O., Tsuda, Y., Sawada, H., et al. 2012, JSAST, 10, 413, https://doi.org/10.2322/tastj.10.Po_4_13

National Oceanic and Atmospheric Administration (NOAA), National Aeronautics and Space Administration (NASA), United States Air Force (USAF). 1976, US Standard Atmosphere, 1976 (Washington: NOAA-S/T 76-1562)

Palla, C., Kingston, J., & Hobbs, S. 2017, 7th European Conference on Space Debris (Darmstadt: ESA Space Debris Office)

Plante, B., Spencer, D., Betts, B., et al. 2017, Fourth International Symposium on Solar Sailing, Kyoto, Japan

Spencer, D. A., Betts, B., Bellardo, J. M., et al. 2021, AdSpR, 67, 2878, https://doi.org/10.1016/j.asr.2020.06.029

The Planetary Society. 2020, LightSail 2 Mission Control, https://www.planetary.org/explore/projects/lightsail-solar-sailing/lightsail-mission-control.html

Tsuda, Y., Mori, O., Funase, R., et al. 2011, AcAau, 69, 833, https://doi.org/10.1016/j.actaastro.2011.06.005

Tsuda, Y., Mori, O., Funase, R., et al. 2013, AcAau, 82, 183, https://doi.org/10.1016/j.actaastro.2012.03.032

Viquerat, A., Schenk, M., Lappas, V., & Sanders, B. 2015, 2nd AIAA Spacecraft Structures Conference (Kissimmee, FL: AIAA), https://doi.org/10.2514/6.2015-1627

Vulpetti, G. & Scaglione, S. 1999, AcAau, 44, 123, https://doi.org/10.1016/S0094-5765(99)00038-7

Vulpetti, G., Johnson, L., & Matloff, G. L. 2015, Solar sails (New York, NY: Copernicus Books)

Wie, B. 2007, JSpRo, 44, 545, https://doi.org/10.2514/1.23084

Zeng, X., Gong, S., Li, J., & Alfriend, K. T. 2016, JGCD, 39, 1223, https://doi.org/10.2514/1.G001061

Zeng, X., Jiang, F., & Junfeng, L. 2015, RAA, 15, 597, https://doi.org/10.1088/1674-4527/15/4/011

Zhang, X. & Zhou, C. 2017, ChJA, 30, 1719, https://doi.org/10.1016/j.cja.2017.08.006

Cristiano F. de Melo and Maria Cecília Pereira: Federal University of Minas Gerais, Av. Presidente Antônio Carlos, 6627 - Pampulha, Belo Horizonte, Minas Gerais, 31270-901, Brazil (cristiano.fiorilo@demec.ufmg.br, cecilia@demec.ufmg.br).

Lucas G. Meireles and Antônio F. B. A. Prado: National Institute for Space Research, Av. dos Astronautas, 1758 - Jardim da Granja, São José dos Campos, São Paulo, 12227-010, Brazil (meireleslg@gmail.com, antonio.prado@inpe.br).

Revista Mexicana de Astronomía y Astrofísica, **58**, 37–45 (2022)

https://doi.org/10.22201/ia.01851101p.2022.58.01.03

OFF-AXIS EXACT RAY TRACING ALGORITHM FOR ZERO COMA POINT DETERMINATION IN CLASSICAL AND NON-CLASSICAL REFLECTIVE TELESCOPES

J. Herrera, M. R. Najera, and C. A. Guerrero

Instituto de Astronomía, Universidad Nacional Autónoma de México, A.P. 106, Ensenada 22860, B. C., México.

Received July 9 2021; accepted September 29 2021

ABSTRACT

In this work we present a general algorithm to calculate the zero coma point for classical and non-classical reflecting telescopes with aspherical surfaces. We programmed a general ray tracing function applicable to conical surfaces with asphericity, displacements, and inclinations that can be modified by the users, according to their specifications. This function is used to evaluate the transverse coma and determine the optimal conjunction of shift and tilt of the secondary mirror that prevents the introduction of axial coma during the collimation process. We present the calculation of the zero coma point for the classical telescopes of the National Astronomical Observatory, San Pedro Mártir, Mexico. Furthermore, we show an example of a wide-field telescope with aspherical surfaces, as will be the case of the TAOS-II telescopes, for which the classical analytical expression cannot be used.

RESUMEN

En este trabajo presentamos un algoritmo general para calcular el punto de coma cero para telescopios reflectores clásicos y no clásicos con superficies asféricas. Programamos una función de trazado de rayos general aplicable a superficies cónicas con asfericidad, desplazamientos e inclinaciones, que puede ser modificada por los usuarios, según sus especificaciones. Esta función se utiliza para evaluar la coma transversal y determinar la conjunción óptima de desplazamiento e inclinación del espejo secundario que evita la introducción de coma axial durante el proceso de colimación. Presentamos el cálculo del punto de coma cero para los telescopios clásicos del Observatorio Astronómico Nacional, San Pedro Mártir, México. Además, mostramos el ejemplo de un telescopio de campo amplio con superficies asféricas, como será el caso de los telescopios TAOS-II, para los que no se puede utilizar la expresión analítica clásica.

Key Words: instrumentation: miscellaneous — methods: analytical — methods: data analysis — methods: numerical — telescopes

1. INTRODUCTION

For telescopes composed of two mirrors, the zero coma point (ZCP) determines a physical point over the optical axis of the primary mirror, M_1, where the secondary mirror, M_2, can rotate during the collimation process, without introducing transverse coma in the resulting image. The analytical expression for the ZCP in aplanatic reflector telescopes is well known and it is of great importance in the alignment of classical telescopes, such as the Cassegrain, Gregorian or Ritchey-Chretien type (Schroeder & Inc 2000; Schechter & Levinson 2011); however, this equation is not directly applicable to some variants of wide-field reflector telescopes, composed not only of conical surfaces but also containing asphericity terms in the secondary mirror, or telescopes coupled with aspherical corrective lenses.

In the present work, we developed an exact-ray-tracing algorithm for off-axis aspherical surfaces, which we applied to the numerical determination of the ZCP for classical and non-classical telescopes. As an example of the application of this algorithm, we show the calculation of the ZCP for every telescope of the Observatorio Astronómico Nacional (OAN-SPM), which is located in the Sierra San Pedro Mártir, Baja California, México.

The content of this article is divided as follows: in § 2 we describe the analytical solution and how it is used in the collimation process; in addition, the concept of the ZCP is described. § 3 describes the concept of non-classical design for a telescopes with asphericity terms in one or more surfaces of the system. In § 4 we describe the transverse coma aberration by means of three rays traveling through the surfaces of the telescope, given that this process will be the basis for the function to be minimized using our proposed algorithm. In § 5 we describe the approach required for programming the general ray tracing function, using off-axis arbitrary surfaces. We include flowcharts representing the complete algorithm procedure in § 6, while in § 7 we discuss the spot diagrams and output plots for a theoretical wide-field telescope used as an example of the aplication of our algorithm. In § 8 we present the values of the ZCPs for the telescopes of the OAN-SPM and future projects under development. Finally, we present our conclusions in § 9.

2. CLASSICAL ANALYTIC SOLUTION

An aplanatic telescope composed of two mirrors with conical surfaces enables the possibility to correct the spherical aberration in an exact form or, at least, a correction to third order. While the powers of both surfaces allow us to balance and control the Petzval field curvature and define the system's power, the conic constants allow us to control the spherical aberration, in the case of a Cassegrain telescope. However, with the improvement in the construction precision of conical surfaces of revolution, we have been able to reduce an additional optical aberration, typically, the coma.

A reflector telescope with a laterally misaligned or inclined element becomes an optical system without symmetry of revolution; this means that the optical axis is no longer coaxial with the mechanical axis, which in turn produces a displacement of the exit pupil that originates coma arising from misalignment. The nature of this induced aberration has been widely studied, for example by Schroeder & Inc (2000) and Schechter & Levinson (2011); the latter present an exhaustive analysis of the patterns generated by misalignment. The understanding of these effects is of special relevance, since real-world telescopes are opto-mechanical systems subject to mechanical bending and misalignment.

A problem associated with the misalignment of reflecting telescopes is that it is impossible to unequivocally determine the origin of axial coma, as it can be originated due to lateral displacement, inclination of the secondary mirror, or a combination of both. The misalignment produced by displacement and inclination can even be of the same magnitude and of the opposite sign (Schroeder & Inc 2000), which allows the effect to be compensated and eliminated. In a misaligned system, astigmatism is asymmetric and linear in the field; this is added to the natural astigmatism due to optical design or astigmatism produced by the shape of the elements, either by construction or by errors in the support of the optical components.

In the collimation process of a telescope we look for the coaxiality of all the optical elements. A very useful collimation procedure is described by McLeod (1996). Prior to achieving an optimal collimation, the image plane of a slightly out-of-focus telescope exhibits donut-shaped images, which will be defocused and will display astigmatism and coma.

Typically the aberration of astigmatism is not a problem in nearly collimated telescopes, where the coma dominates the image quality. In this case, it may be sufficient to correct the coma by means of only lateral displacement or tilt of the secondary mirror. However, our main interest in this work is the collimation of wide-field telescopes, for which the astigmatism at the edges of the wide field will be more relevant than in small-field telescopes.

In the first collimation stage, we compensate the axial coma aberration by means of lateral displacements of the secondary mirror, until the image plane is dominated only by astigmatism. When the optical systems are aligned, the astigmatism is distributed with symmetry of revolution over the entire field, or it can be zero depending on the design of the system. There are strategies to measure the wavefront around the field to estimate the tilt or shift of the secondary mirror required to correct the astigmatism (McLeod 1996). However, this correction should not introduce coma aberration again.

For this reason, it is important to perform continuous compensation of astigmatism, by simultaneously moving and tilting the secondary mirror. This combination is homologous to move the secondary mirror, with its optical axis pivoting around a single point on the optical axis of the primary mirror. This point is known as the "zero coma point", also called "neutral point", which has been calculated in different ways by several authors; one of the most cited works is that of Schroeder & Inc (2000). Thus, by moving the secondary mirror with respect to this point, we avoid inducing axial coma in the image plane, when trying to compensate for astigmatism.

It is important to point out that, before starting any movement with respect to the ZCP, we must first reach the compensation of coma during the first collimation stage, as described before. Once this is achieved, we guarantee that the optical axes of the secondary and primary mirrors are aligned. Then, the analytical equation to calculate the position of the ZCP is determined for the third order correction, according to equation 1 (Wetherell & Rimmer 1972):

$$ZCP = \frac{1}{C_{M_2}} \frac{m+1}{(m+1) - (K_{M_2} - 1)(m-1)}, \quad (1)$$

where ZCP is the distance to the zero coma point measured from the secondary mirror, C_{M_2} and K_{M_2} are the secondary mirror's curvature and conic constant, and $m = F/F_p$ is the amplification of the system.

3. NON-CLASSICAL TELESCOPES

There is, however, a caveat to the previously described procedure. There are telescopes that are composed of conical surfaces plus an asphericity polynomial term α_j. Other telescopes also contemplate one or more correcting aspherical lenses, whose sagittae are defined according to equation 2:

$$z_1 = \frac{cs^2}{1 + \sqrt{1 - (K+1)c^2 s^2}} + \sum_{j=1}^{n} \alpha_j s^{2j}, \quad (2)$$

where z is the sagitta of the surface, $s^2 = x^2 + y^2$ is the distance of the optical axis to a point over the surface, K is the conic constant and $c = 1/R_c$ is the paraxial curvature, with R_c the radius of curvature of the surface.

As expected, equation 1 for the ZCP is not appropriate for telescopes with these aspheric components. The objective of this work is to numerically determine the position of the ZCP in the most general way, given that corrective lenses can have different contributions in the correction of aberrations and an analytical estimation of the ZCP can rapidly grow in complexity, as we increase the number of surfaces to be considered.

4. COMA-INDUCED CHANGE IN AMPLIFICATION

There are several procedures to evaluate and compensate the axial coma, such as the Abbe sine condition and the offense against the sine condition (OSC) (Smith 2000). There are also general forms for Abbe's sine condition that contemplate systems without symmetry of revolution (Elazhary et al. 2015). However, the transverse coma aberration does not require the calculation of the position of the system's exit pupil, which is defined as the change in amplification as a function of the aperture (see Figure 1), expressed as:

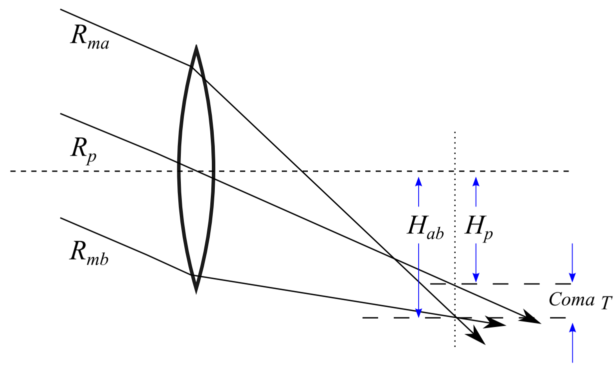

Fig. 1. Transverse coma produces a different amplification for the same object with a dependence on the system's aperture. The color figure can be viewed online.

$$Coma_T = H_{ab} - H_p. \quad (3)$$

In Figure 1 we can see three rays arriving on a meridional plane, two of them, R_{ma} and R_{mb}, are passing through the edges of the pupil of the system and the third ray is passing through the center of the pupil, called the principal ray R_p. From the exact ray tracing we can find the direction cosines of these three rays and the intersection point on the surfaces. With this information we can determine the point of intersection between rays R_{ma} and R_{mb}, we can find the distance from this point to the optical axis, the position of the perpendicular plane to the optical axis passing through this point and, finally, the point of intersection of the principal ray R_p and its distance from the optical axis.

5. COMA COMPENSATION FUNCTION

The evaluation of the aberrations of an optical system can be done based on the exact ray tracing procedure, which determines the optical path of a ray passing through a set of surfaces. The exact ray tracing, is also known as "skew ray tracing" (Spencer & Murty 1962).

Taking advantage of the procedure for calculating the ZCP and using the exact ray tracing described

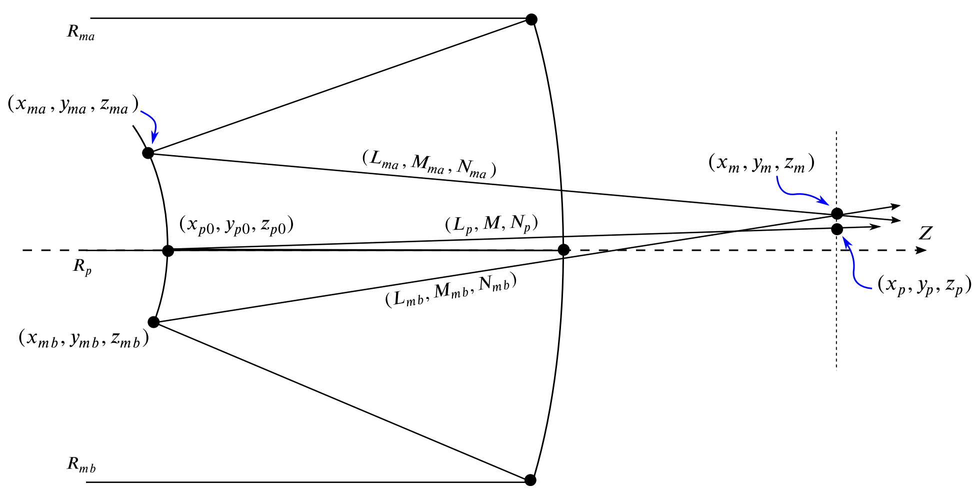

Fig. 2. Output ray parameters used in the evaluations of equations 4, 5 and 6, that help us to compute the transverse coma. The color figure can be viewed online.

in § 4, we programmed a function in Python for calculating the exact ray tracing through a telescope that has a correcting lens. In this program it is possible to define the conic and asphericity parameters as constants. With this routine, it is also possible to introduce lateral displacements on the secondary mirror. As a result of this program, we can calculate the parameters of the three rays at the output of the system, as schematically described in Figure 1 and Figure 2.

With the parameters of the marginal rays R_{ma} and R_{mb} we can calculate the point y_m, where the vectors intersect, and also the height of the chief ray y_p:

$$y_m = \left(\frac{M_{ma}M_{mb}}{N_{ma}M_{mb}-N_{mb}M_{ma}}\right) \times \times \left(z_{mb} - z_{ma} - y_{mb}\frac{N_{mb}}{M_{mb}} + y_{ma}\frac{N_{ma}}{M_{ma}}\right), \tag{4}$$

$$z_m = (y_m - y_{mb})\frac{N_{mb}}{M_{mb}} + z_{mb}, \tag{5}$$

$$y_p = y_{p0} + \frac{M_p}{N_p}(z_m - z_{p0}). \tag{6}$$

With these parameters we are able to calculate the transverse aberration, described by equation 3. Solving by the Newton-Raphson method for the tilt value of the secondary mirror that minimizes the transverse aberration, we have:

$$y_m - y_p = 0. \tag{7}$$

6. SOS-ZCP ALGORITHM

The SoS-ZCP (*Serpent of Stars-Zero Coma Point*) is an algorithm written in Python, divided into three sections in terms of its functionality. The first section incorporates the thorough General ray tracing function for a three-dimensional continuous surface. In this script the user provides the surface properties and position (tip/tilt and shift) in space; therefore, this part of the algorithm can be used as an operator that is supplied with a ray and then returns the ray parameters through the entire system. The ray is provided as a data set with the origin coordinates and direction cosines, the returned data are in the same format. The function is configured with all the telescope parameters, surface by surface, including corrector lenses if they are required.

The second section of the algorithm invokes the first function to trace the three rays presented in Figure 2. Using equations 4, 5 and 6 the coma aberration is calculated, by means of equation 3. It is important to mention that, in this second part of the algorithm, the user can modify the properties of the system, such as the tilt and shift of an element.

The third section of the algorithm (schematically described in Figure 3) takes the output of the second section and uses it as a function of two variables, T_x and θ_y, which are the secondary mirror M_2 lateral translation and tilt angle, respectively.

Our algorithm applies the Newton-Raphson method in an optimization process, in order to calculate the value of θ_y that minimizes the amount of coma, then setting a criterion near to zero (1e-7 mm), for a proposed translation T_x of M_2. The

TABLE 1

TELESCOPE ϕ 2.1 m $f/3$ (THEORETICAL EXAMPLE)

Element	Radius (mm)	Thickness (mm)	Glass	Semi-Diameter (mm)	k	α_1	α_2	α_3
M_1	−7670.112	−227241	Mirror	1005.0	−1.597			
M_2	−7670.112	227241	Mirror	465.0	−37.027			5.940e−19
M_1 Vertex		56.538	Air					
Corrector Front		7.0	Silica Schott	191.0		3.955e−5	−1.021e−9	
Corrector Back		300.0	Air	191.0				
Image Plane				78.4				

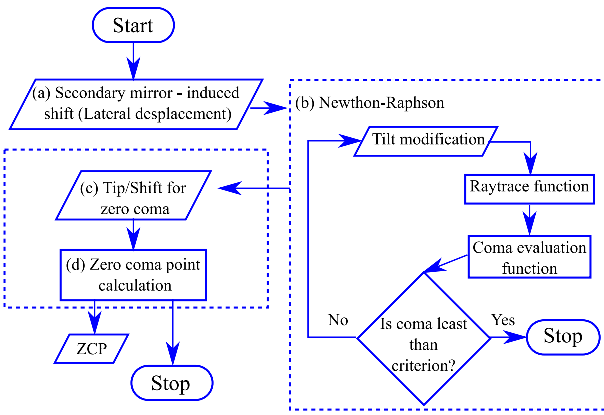

Fig. 3. *ZCP* function flowchart. The color figure can be viewed online.

projection of the resulting compensated M_2 optical axis on the M_1 axis is calculated directly from the triangle defined by the lateral translation and tilt; thus, the *ZCP* is calculated as:

$$ZCP = \frac{T_x}{\tan(\theta_y)}. \tag{8}$$

The source code of the SoS-ZCP is available at https://github.com/MNajeraR/SoS-ZCP (Nájera et al. 2021). It is implemented in Python 2.7 under the MIT License. Version v2.0.0 is used in this paper and is archived at http://doi.org/10.5281/zenodo.4929555.

7. WIDE-FIELD TELESCOPE EXEMPLIFICATION

We are especially interested in calculating the *ZCP* for a telescope similar to those of the TAOS-II project, given that they will have an aspheric secondary mirror and a very wide field of view ($FOV = 1.7°$), which is the ideal scenario for this implementation. The parameters of the TAOS-II telescopes are not yet public. However, the manufacturer has provided all the information for the commercial telescopes (Melsheimer & MacFarlane 2000; Bowen & Vaughan 1973), which we have used to design our example telescope.

We have designed a theoretical $f/3$ telescope, whose primary mirror is 2.1 m in diameter and has a $FOV = 1.4°$. The primary and secondary mirrors have the same radius of curvature to decrease the Petzval curvature, the system has an aspherical correction plate and the secondary mirror also has an asphericity term. The parameters of the design data are listed in Table 1.

In order to calculate the zero coma point for this telescope, we introduced its parameters in our algorithm. We calculated the position of the *ZCP* at a distance of 564.8 mm, behind the secondary mirror. In Figure 4 we show an schematic diagram of the telescope, with the secondary mirror rotated by 0.1°, pivoted around the *ZCP*. In Figure 4 we only show the two marginal rays and the principal ray; they are parallel to the optical axis. At the image space these rays converge to the same off-axis point, minimizing the coma. For rays arriving in a meridional plane (x, z) the convergence occurs at a point on the chief ray; for rays incident on the sagittal plane (y, z) the converging point on the chief ray is different, which is the physical origin of the astigmatism.

Figure 5 (left) shows a set of 9 spot diagrams for different fields on the image plane of our wide-field telescope, in this case the telescope is perfectly aligned and focused. The wavelength used for the present example is 600 nm. The spot diagrams were made with a polar-array ray pattern (Malacara-Hernández & Malacara-Hernández 2013) in the entrance pupil M_1, where a slight astigmatism aberration is perceived, especially in the corner images, which is not related to the scale of the plots. In Fig-

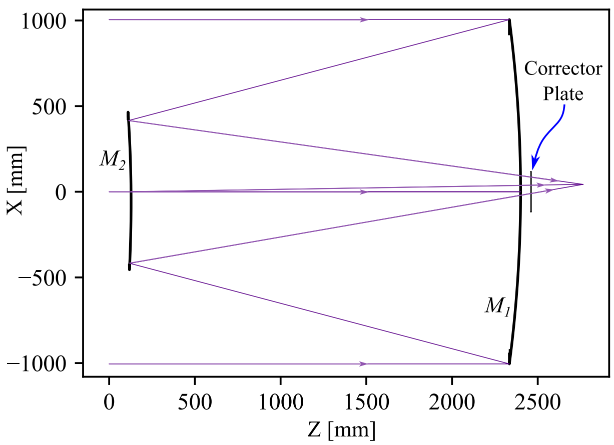

Fig. 4. Wide-field telescope example. The three parallel rays converge to the same point, when M_2 is pivoting around the telescope's ZCP, located at 564.8 mm behind the secondary mirror. The color figure can be viewed online.

ure 5 (right), coma aberration can be clearly seen over the entire field. In this example the secondary mirror M_2 is laterally displaced by 1 mm outside of the optical axis, without adding tilt.

Figure 6 (left) shows the spot diagram produced by the same system as Figure 5, but this time a pivoting movement has been made with respect to the ZCP. The image plane has been slightly put out of focus to allow the images to display the typical annular shape produced by out-of-focus telescopes. These spot diagrams display astigmatism aberration (Z_{22} from Zernike polynomials) that can be estimated using equation 9 (Luna et al. 2007), which is not symmetrical in the field:

$$Z_{22} = (A - B)\,\frac{1}{4\sqrt{6}f/\#}, \tag{9}$$

where A and B are the major and minor axes of the ellipse produced by astigmatism. It is important to stress that, when pivoting around the ZCP, coma aberration is not added to the field.

Figure 6 (right) shows the same spot diagrams as those on the left, but with the correct focus; we can see from the scale that, even when using focused images, it is not possible for us to accurately evaluate the amount of astigmatism when performing collimation, specially under bad seeing conditions. Therefore, the correction of astigmatism must be done in fine alignment using a wave-front sensor.

In Figure 6, the small proportion of spherical aberration is due to the presence of spherical aberration in the design of the primary mirror, because it was not completely corrected. The aberrations produced by misalignment are only coma and astigmatism, where the proportion of induced astigmatism depends on the particular design, which must be considered in each case.

It should be noted that the spot diagrams were made with the same function programmed for the exact ray tracing (General ray tracing function). This is a by-product of the present work, which can be used, modified and applied to various other academic problems, such as the optimization of the parameters of an optical design, by direct use of a particular ray aberration as a merit function.

8. OAN-SPM TELESCOPES

We calculated the ZCP for every one of the classical telescopes of the OAN-SPM, using the analytical expression, together with the numerical results obtained with our algorithm for comparison. Additionally, we have included the 2.12 m telescope of the Observatorio Astrofísico Guillermo Haro located in Cananea, Sonora, México. In order to perform this calculation, we need the construction parameters of the telescopes, which are presented in Table 2, where the SAINT-EX and TAOS-II telescopes have been omitted, because their parameters are not yet public.

The results of the ZCP are presented in Table 3, where the first column list the respective telescope (the 2.1 m telescope of the OAN-SPM can be coupled to three different secondary mirrors), the second column contains the focal ratio of each telescope, the third column displays the calculation of the ZCP using the analytical equation, while the fourth column contains the calculation of the ZCP using our algorithm. The last column shows the percentage error between the neutral point equations and the numerical value calculated from ray tracing.

The most relevant result shown in Table 3 is the fact that the value calculated using the classical and the numerical solution are very different for telescopes with aspherical surfaces, as can be seen in the case of the TAOS-II telescope. This is to be expected because the classical solution does not take asphericity terms into account. Ignoring the asphericity terms undoubtedly produces a systematic error during collimation.

Three of the telescopes shown in the Table 3 (1.5 m, SAINT-EX (Sabin et al. 2018) and TAOS-II) have secondary mirrors with an electromechanical positioning system that allows all degrees of freedom; however, the movement of the mirror may not occur

TABLE 2

CONSTRUCTION PARAMETERS FOR OAN-SPM TELESCOPES

Telescope (m)	Focal ratio $f/\#$	Mirror	R_c (mm)	Thickness (mm)	k	Diameter (mm)	M_1 Vertex to Image plane (mm)
0.84	15	M_1	−5287.0	2029.7	−1.0049	840.0	
		M_2	−1555.0	877.1	−2.6990		250.0
1.5	13	M_1	−5975.0	2475.7	−1.0049	1540.0	
		M_2	−1208.0	877.1	−1.8970		275.0
2.1	7.5	M_1	−9638.0	3452.2	−1.0773	2118.0	
		M_2	−3930.0	1037.5	−4.3281		673.0
2.1	13.5	M_1	−9638.0	3974.7	−1.0773	2118.0	
		M_2	−2028.0	1069.1	−2.7284		406.0
2.1	30	M_1	−9638.0	4366.7	−1.0773	2118.0	
		M_2	−981.0	1449.5	−2.3947		185.0
6.5 (TSPM)	5.1	M_1	−16256.0	6178.0	−1.0000	6502.4	
		M_2	−5150.9	1851.3	−2.6946		1714.5
2.12 (INAOE[a])	11.9	M_1	−11340.0	4463.3	−1.0274	2118.0	
		M_2	−3114.1	900.063	−2.7747		330.0

[a]The INAOE 2.12 m telescope is not part of the OAN-SPM. However, it is in Mexican territory and part of the Mexican astronomical community.

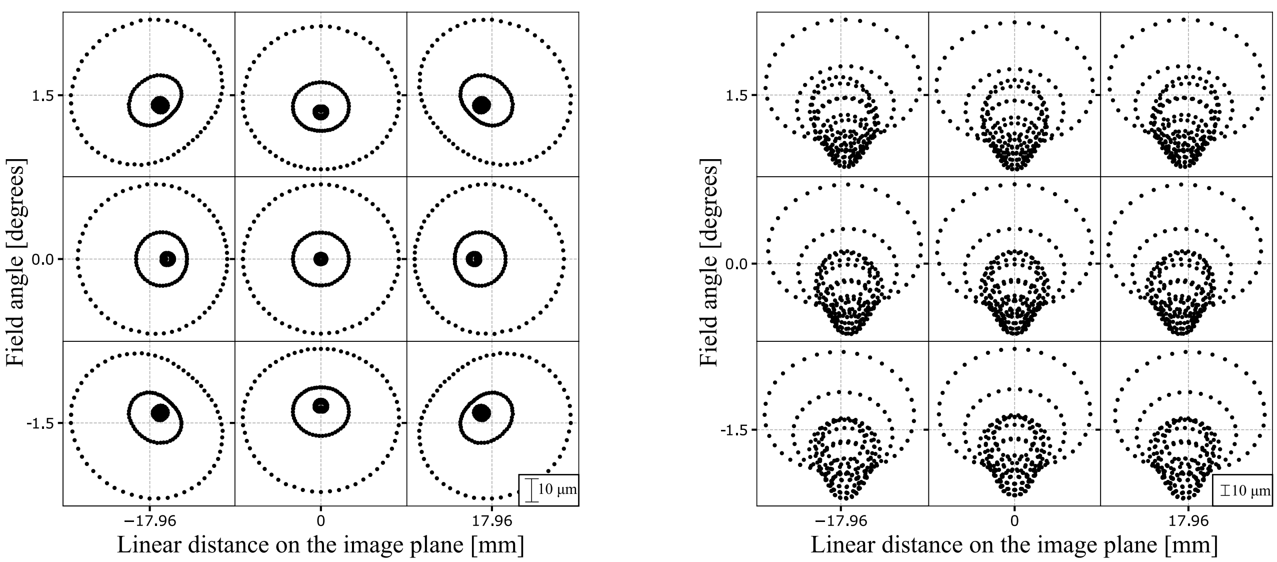

Fig. 5. Spot diagrams for a wide-field telescope, (left) aligned telescope, (right) with introduction of a 1 mm lateral displacement in the secondary mirror, where the coma aberration is evident.

with respect to the vertex of the secondary mirror or the ZCP. To take advantage of these mechanisms, we must study the vector components of the movements in order to obtain a geometric operator that allows us to perform a combination of steps that, together, are equivalent to a movement pivoting at the ZCP.

9. CONCLUSIONS

We presented the SoS-ZCP general algorithm that performs the exact ray tracing computation for surfaces defined by a sagitta function, to calculate the ZCP, even though the telescope may have aspheric surfaces. The algorithm has been implemented to

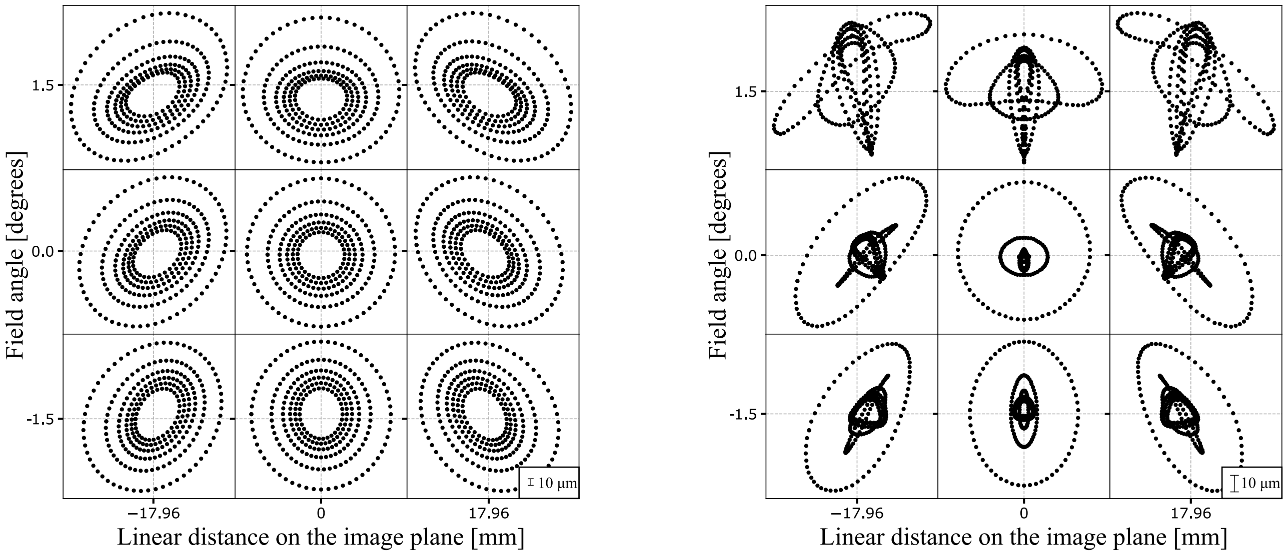

Fig. 6. Spot diagrams for a wide field telescope. (Left) with pivoting of the secondary mirror with respect to its ZCP. The images are out of focus to show annular images. (Right) spot diagrams at the correct focus. In both diagrams we can see the presence of astigmatism and very little coma contribution, given that the original design has a small coma aberration.

TABLE 3

ZERO COMA POINT FOR OAN-SPM TELESCOPES

Telescope (m)	Focal ratio $f/\#$	Classical solution (mm)	Exact ray tracing (mm)	Percentage error (%)
0.84	15	563.37	563.51	0.02
1.0 (SAINT-EX)	7.8	535.87	538.54	0.50
1.3 (TAOS-2)	4	591.00[a]	380.64	35.59
1.5	13	504.46	504.25	0.04
2.1	7.5	1188.06	1186.32	0.15
2.1	13.5	688.38	686.68	0.25
2.1	30.5	321.75	320.10	0.51
6.5 (TSPM)	5.1	1950.15	1953.58	0.18
2.12 (INAOE)	11.9	1130.17	1129.78	0.35

[a]The classical solution is actually not applicable to the TAOS-II telescopes.

calculate the ZCP numerically, which is very relevant, especially in the case of non-classical telescopes, such as those of the TAOS-II project, which will employ a secondary mirror with an asphericity term. In these circumstances, the classical solution is unable to produce a correct result, as expected.

We applied the calculation of the ZCP using the exact ray tracing for every telescope of the OAN-SPM with which we are involved, and the results are reported in this document. This information is relevant for the OAN-SPM technical staff, given that the Observatory is actively working on integrating real-time image quality metrology by means of wavefront sensing for a deterministic collimation process. After the determination of the ZCP, the next step is to evaluate the astigmatism over the field and to find a solution to correct it in the optical axis.

The work presented in this article could have been carried out with commercial software. However, many tasks do not merit the acquisition of a license. There are other open source packages, but we decided to use our own implementation because, in the future, we will consider ray tracing through surfaces with arbitrary shapes.

The SoS-ZCP algorithm has been released for other users to take advantage of it. The exact ray tracing might seem complex, but the algorithm was written in the simplest way possible, thus allowing every section of the code to easily be reused in other academic problems, where a sophisticated optical design program can be avoided.

We would like to thank the thorough revision of the referee, whose comments helped us to improve the quality of our work. M. R. Nájera acknowledges financial support from CONACyT through a master's grant.

REFERENCES

Bowen, I. S. & Vaughan, A. H., Jr. 1973, ApOpt, 12, 1430, https://doi.org/10.1364/AO.12.001430

Elazhary, T. T., Zhou, P., Zhao, Ch., & Burge, J. H. 2015, ApOpt, 54, 5037, https://doi.org/10.1364/AO.54.005037

Luna, E., Salas, L., Gutiérrez, L., & Nuñez, J. M. 2007, ApOpt, 46, 3439, https://doi.org/10.1364/AO.46.003439

Malacara-Hernández, D. & Malacara-Hernández, Z. 2013, Handbook of Optical Design (3rd ed.; Taylor & Francis Group)

McLeod, B. A. 1996, PASP, 108, 217, https://doi.org/10.1086/133712

Melsheimer, F. M. & MacFarlane, M. J. 2000, SPIE 4003, Optical Design, Materials, Fabrication, and Maintenance, ed. P. Dierickx, https://doi.org/10.1117/12.391539

Nájera, M. R., Herrera, J., & Guerrero, C. A. 2021, MNajeraR/SoS-ZCP: SoS-ZCP, https://doi.org/10.5281/zenodo.4968507

Sabin, L., Gómez Maqueo, Ch. Y., Demory, B. O., Petrucci, R., & SAINT-EX Consortium. 2018, SAINT-EX: Searching for exoplanets from the San Pedro Mártir Observatory, The 20th Cambridge Workshop on Cool Stars, Stellar System and the Sun, https://doi.org/10.5281/zenodo.1479857

Schechter, P. L. & Sobel Levinson, R. 2011, PASP, 123, 812, https://doi.org/10.1086/661111

Schroeder, D. J. 2000, Astronomical Optics (San Diego, CA: Academic Press)

Smith, W. J. 2000, Modern Optical Engineering: The Design of Optical Systems (3rd ed.; New York, NY: McGraw-Hill)

Spencer, G. H. & Murty, M. V. R. K. 1962, JOSA, 52, 672

Wetherell, W. B. & Rimmer, M. P. 1972, ApOpt, 11, 2817, https://doi.org/10.1364/AO.11.002817

Carlos A. Guerrero, Joel Herrera, and Morgan R. Najera: Instituto de Astronomía, Universidad Nacional Autónoma de México, A.P. 106, Ensenada 22860, B. C., México (cguerrero, joel, mnajera@astro.unam.mx).

Revista Mexicana de Astronomía y Astrofísica, **58**, 47–60 (2022)

https://doi.org/10.22201/ia.01851101p.2022.58.01.04

NEW PHOTOMETRY AND SPECTROSCOPY OF DW CANCRI

S. H. Ramírez[1], O. Segura Montero[1], R. Michel[2], and J. Echevarría[1]

Received June 30 2021; accepted November 17 2021

ABSTRACT

We present new observations of the cataclysmic variable DW Cancri, after the system recovered from a low state. We performed a power spectrum analysis that reveals a clear signal of the 38 min spin period in our photometric data. Our spectroscopic power spectrum search was consistent with studies performed before the low state, showing the orbital and spin modulations. Our Doppler Tomography study exhibits a disc structure and an enhanced asymmetric region, possibly related to a hot spot component. Furthermore, a wavelet transform analysis reveals the 70 min spin-orbit beat period. We interpret these results as an indication of a partial recovery of the system. However, DW Cnc does not yet show all the original photometric modulations reported before the low state. Thus, we propose further observations to elucidate if such original signals require more time to reactivate.

RESUMEN

Presentamos nuevas observaciones de la variable cataclísmica DW Cancri después de que se ha recobrado de un estado bajo. Un análisis de espectro de potencias revela clara señal del período de espín de 38 minutos en nuestra fotometría. Nuestro espectro de potencias espectroscópico concuerda con estudios anteriores al estado bajo, mostrando los períodos orbital y de espín. Nuestro estudio de Tomografía Doppler exhibe una estructura de disco y una asimetría intensa, posiblemente causada por una zona de impacto. Un análisis de ondículas revela la presencia localizada del período de batimiento de 70 minutos. Interpretamos estos resultados como una recuperación parcial del sistema. Sin embargo, DW Cnc no muestra todas las señales reportadas, previo al estado bajo, en la fotometría. Proponemos observaciones adicionales para dilucidar si dichas señales requieren mayor tiempo para reactivarse.

Key Words: binaries: spectroscopic — novae, cataclysmic variables — stars: individual: DW Cnc — techniques: photometric — techniques: spectroscopic

1. INTRODUCTION

As described by the standard model (e.g. Warner & Nather 1971) cataclysmic variables (CVs) are semi-detached binary systems consisting of a late-type secondary star filling its critical Roche surface, that transfers matter into a white dwarf (WD) via an accretion disk (see Warner 1995, for a comprehensive review on CVs). CVs can be divided into systems with outbursts, like dwarf novae, and non-outburst systems, like intermediate and polar systems (e.g. Hellier 2001). Intermediate polar systems (IPs) are a class of CVs whose primary component is a magnetic white dwarf. The presence of a moderate magnetic field (0.1-10 MG) in these systems is strong enough to inhibit the formation of the innermost regions of the accretion disk, but is not sufficiently strong to synchronise the rotation of the white dwarf with the orbit (e.g. Hameury & Lasota 2017). The number of intermediate polars is small (about one percent) compared with the total population of CVs (Warner 1995).

DW Cancri (hereafter DW Cnc) was identified as a CV by Stepanyan (1982). Rodríguez-Gil et al. (2004) performed its first time-resolved spectroscopic study. Their analysis led them to suggest that the system is a short-period intermediate polar below

[1]Instituto de Astronomía, Universidad Nacional Autónoma de México, Ciudad Universitaria, Ciudad de México, México.
[2]Instituto de Astronomía, Universidad Nacional Autónoma de México, Ensenada, Baja California, México.

the period-gap, whose photometric data resemble the behaviour of VY Scl stars. They found the Balmer and He I lines to be modulated with two periods: 86.10±0.05 min, associated with the orbital period; and 38.58±0.02 min, likely corresponding to the WD spin period. Patterson et al. (2004) confirmed the intermediate polar nature of DW Cnc. A radial velocity search performed by these authors detected the 86 and 38 min periods. Additionally, in a photometric power search they found a 70 min signal, consistent with the beat period of the binary (compelling evidence of its IP nature), and also a weak periodic signal at 110 min, which was left as an unsolved problem. Nucita et al. (2019) reported positive *XMM-Newton* observations in 2012 in the range 0.3 - 10 Kev; their light curves show evidence of a period around 38 min and also a signature around 75 min, both consistent within the errors to the spin and beat periods, respectively.

In a previous publication (Segura Montero et al. 2020), a radial velocity study of DW Cnc was presented, with observations performed during a low state in 2018-2019. Through a power spectrum analysis they found the 86 min signal associated with the orbital period and two much weaker modulations associated with the 70 min beat period and the 38 min spin period. Particularly, the 38 min signal was significantly weaker than that previously published by Rodríguez-Gil et al. (2004) and Patterson et al. (2004). To explain this substantial change Segura Montero et al. (2020) suggested that the sudden drop into a low state – caused by an episode of low mass transfer from the companion– inhibited the lighthouse effect produced by the rebound emission, thus rendering the spin period of the WD difficult to detect. Such variability in the behaviour of DW Cnc exemplifies the importance of pursuing follow-up observations of the system.

Hence, in § 2 of this paper we present new photometric and spectroscopic observations of DW Cnc. In § 3 we show a radial velocity study of the Hα and He I 5876 Å emission lines. We performed a power spectrum search of our photometric and spectroscopic data, which is shown in § 4, followed by a wavelet transform analysis in § 5. We also carried out a Doppler tomography study in § 6. We close the article with a discussion of our results and our conclusions in § 7 and § 8, respectively.

2. OBSERVATIONS AND REDUCTION

2.1. *Photometry*

CCD photometry was obtained on 2020 March 8-9 and 15-16, with the 0.84m telescope at the Observatorio Astronómico Nacional at San Pedro Mártir, located in Baja California, Mexico. V and R images were obtained sequentially during the four nights with an e2vm E2V-4240 2048×2048 CCD using 2×2 binning. The exposure times were of 30s and 20s for the V and R filters, respectively. Data reduction was carried out with the IRAF[3] software system. After bias and flat field corrections, aperture photometry of DW Cnc and some field stars was obtained with the PHOT routine. The same comparison star (RA=7:58:58, DEC=+16:15:07) used by Patterson et al. (2004) was adopted, assuming the reported magnitudes of B=15.89, V=15.21, and R=14.82. The log of photometric observations is shown in Table 1.

TABLE 1

LOG OF PHOTOMETRIC OBSERVATIONS FOR DW CNC

Date	Julian Date (2450000 +)	No. of exposures V	No. of exposures R
08 March 2020	8916	201	210
09 March 2020	8917	201	219
15 March 2020	8923	197	191
16 March 2020	8924	131	133

2.2. *Spectroscopy*

Spectra were obtained with the 2.1m telescope of the Observatorio Astronómico Nacional at San Pedro Mártir, using the Boller and Chivens spectrograph and a Spectral Instrument CCD detector in the 5500 - 6500 Å range (resolution ≈ 1200), on the nights of 2020 March 15 and 16. The exposure time for each spectrum was 300 s. Standard IRAF procedures were used to reduce the data. The log of spectroscopic observations is shown in Table 2. The spectra show strong Hα λ6563 Å and He I λ5876 Å emission lines. The typical S/N ratio of the individual spectrum is of ≈20 for the emission lines. The spectra were not normalized.

3. RADIAL VELOCITIES

The radial velocity of the emission lines in each spectrum were computed using the RVSAO package in IRAF, with the CONVRV function, constructed by J. Thorstensen (2008, private communication). This

[3] IRAF is distributed by the National Optical Astronomy Observatories, which are operated by the Association of Universities for Research in Astronomy, Inc. (AURA), under cooperative agreement with the National Science Foundation (NSF).

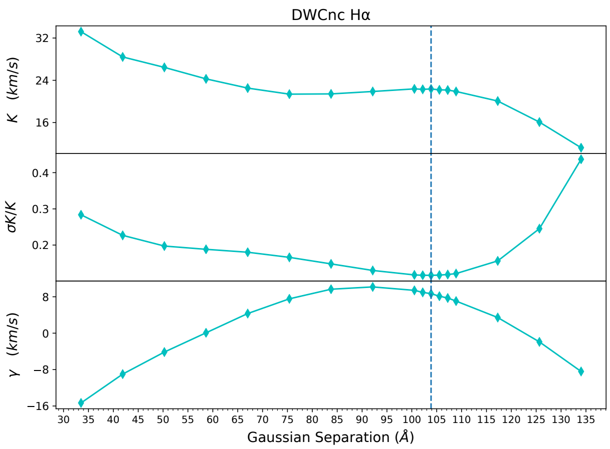

Fig. 1. Diagnostic diagram of the Hα emission line. The vertical blue dashed line indicates an optimal separation of 103.9 Å (62 pixels). The used width for the Gaussians was 16.8 Å (10 pixels). See text for further discussion. The colour figure can be viewed online.

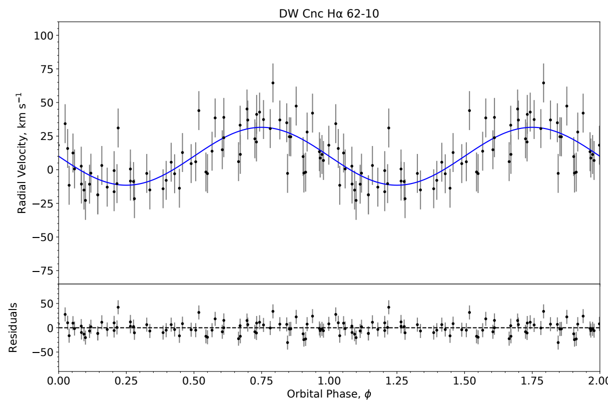

Fig. 2. Radial velocity curve for the best solution of the Hα emission line. The best fit is shown as the blue line, and the 1σ error bars have been scaled so that the goodness-of-fit parameter $\chi^2_\nu = 1$. The colour figure can be viewed online.

TABLE 2

LOG OF SPECTROSCOPIC OBSERVATIONS FOR DW CNC

Date	Julian Date (2450000 +)	No. of spectra
15 March 2020	8923	28
16 March 2020	8924	51

TABLE 3

ORBITAL PARAMETERS OBTAINED FROM Hα AND He I λ 5876[1]

Parameter	Hα	He I λ5876
γ (km s^{-1})	10 ±2	40 ±2
K_1 (km s^{-1})	21.5 ±2.5	27.3 ±2.9
HJD_0*	0.803 ±0.001	0.833 ±0.001
P_{orb} (min)	Fixed**	Fixed**

[1]Using the wings of the lines.
*(24558923+ days).
**86.10169 ± 0.00031 min.

routine follows the algorithm described by Schneider & Young (1980), convolving the emission line with an antisymmetric function, and assigning the zero value of this convolution as the midpoint of the line profile. As in Segura Montero et al. (2020), we initially used the GAU2 option, available in the routine, which uses a negative and a positive Gaussian to convolve the emission line, and needs the input of the width and separation of the Gaussians. This method traces the emission of the wings of the line profile, presumably arising from the inner parts of the accretion disc.

Following the methodology described by Shafter et al. (1986), we made a diagnostic diagram to find the optimal Gaussian separation, by performing a non-linear least-squares fit (Newville et al. 2014) of a simple circular orbit to each trial:

$$V(t) = \gamma + K_1 \sin\left(2\pi \frac{t - t_0}{P_{orb}}\right), \qquad (1)$$

where γ is the systemic velocity, K_1 the semi-amplitude, t_0 the time of inferior conjunction of the donor and P_{orb} is the orbital period. We employed χ^2_ν as our goodness-of-fit parameter. Note that we have fixed the orbital period, as derived in Segura Montero et al. (2020), and therefore we only fit the other three parameters.

In particular, a control parameter is defined in this diagnostic, σ_K/K, whose minimum is a very good indicator of the optimal fit. The diagnostic diagram for Hα is displayed in Figure 1, while the orbital fit for its best solution is exhibited in Figure 2. The diagnostic diagram of the He I λ 5876 Å emission line is shown in Figure 3, and its orbital fit appears in Figure 4. The 1σ error bars of the radial velocity fits were scaled so that the goodness-of-fit χ^2_ν=1. The parameters for the optimal orbital fit of both emission lines are shown in Table 3, with the respective estimated standard errors for the best-fit values.

Furthermore, as explained in § 4.2, following Patterson et al. (2004), we also implemented the DGAU convolution option to perform an additional power

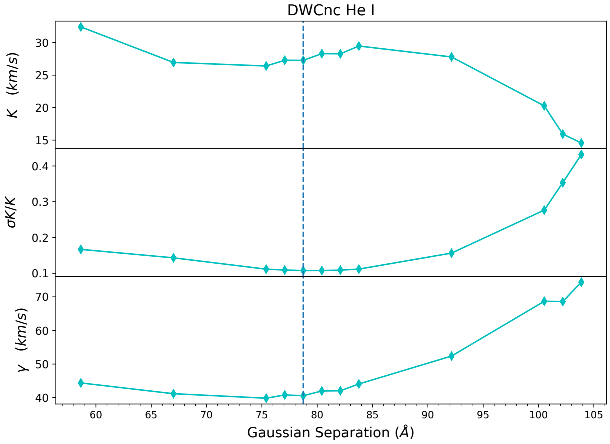

Fig. 3. Diagnostic diagram of the He I λ 5876 Å emission line. The vertical blue dashed line indicates an optimal separation of 78.7 Å (47 pixels). The used width for the Gaussians was 11.7 Å (7 pixels). See text for further discussion. The colour figure can be viewed online.

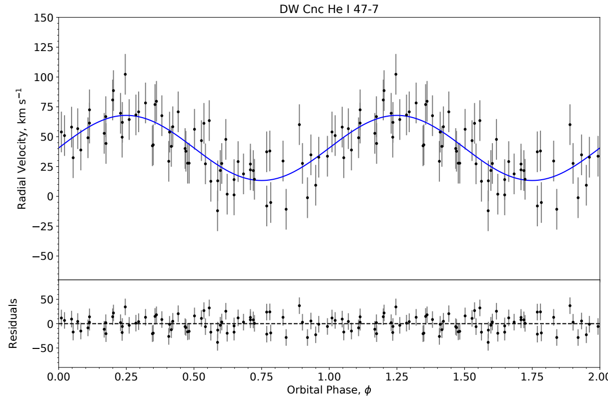

Fig. 4. Radial velocity curve for the best solution of the HeI emission line. The best fit is shown as the blue line, and the 1σ error bars have been scaled so that the goodness-of-fit parameter $\chi^2_\nu = 1$. The colour figure can be viewed online.

spectrum. This option uses the derivative of a single Gaussian, and only requires the input of the Gaussian width.

4. POWER SPECTRUM SEARCH

We made a power spectrum analysis of the V and R photometric bands, and a power search of the measured radial velocities of the Hα and the He I λ5876 Å emission lines, using a Lomb-Scargle algorithm (Scargle 1982) in both cases.

For each periodogram, we computed the false-alarm-probability (hereafter FAP), using a function included in Astropy Collaboration et al. (2013). As explained by VanderPlas (2018), the FAP quantifies the significance of a peak by calculating the probability that the random variations in the data lead to a peak of similar magnitude, conditioned on the assumption of the null hypothesis of having no periodic signal present in the data. Following de Lira et al. (2019), we identified as significant peaks those whose FAP was less than 0.01, i.e., with a significance level greater than 99 percent.

4.1. *Photometric Data*

In Figure 5 we show the results of the photometric frequency analysis. The results from the V band are in the upper panel, where we observe a prominent peak at a frequency of 37.47 cycles/day (associated with the 38 min spin period). Two other weak signals are also present: 13.26 and 23.25 cycles/day, which correspond to periods of 108 min and 62 min, respectively. We do not find the orbital period, and contrary to Patterson et al. (2004) and Nucita et al. (2019), our periodogram does not detect the 70 min spin-orbit beat period.

The results from the R band (middle panel) show the same signals as the V band. In the bottom panel, we show the combined analysis using both the V and R bands. The results are the same as before, where no significant power signals are found for the orbital and beat periods. We note here that the 23.25 signal did not yield a FAP below the 0.01 threshold. To probe for its legitimacy and make an attempt to unmask new signals, we followed Patterson et al. (2004), by fitting a sine wave with a periodicity corresponding to the predominant 37.47 cycles/day signal, and then subtracting the fitted sinusoid from the photometric time series. We proceeded to make a new Lomb-Scargle search of the residuals as exhibited in Figure 6. It can be observed that after subtracting the spin cycle, both of the 13.26 and 23.25 signals remain present, with their recalculated FAPs below the 0.01 cutoff value. This result is different from that obtained by (Patterson et al. 2004), whose power search yields a weak bump at 16 cycles/day after subtracting the spin and beat modulations; however, this detection weakens when they study the long-term behaviour of their data.

Before folding the photometric time series by the modulations found in the power spectra, we made an analysis to check whether the V and R data are correlated. For this purpose we used a code[4] developed by Figueira et al. (2016), which implements a

[4]See https://bitbucket.org/pedrofigueira/bayesiancorrelation/src/master/.

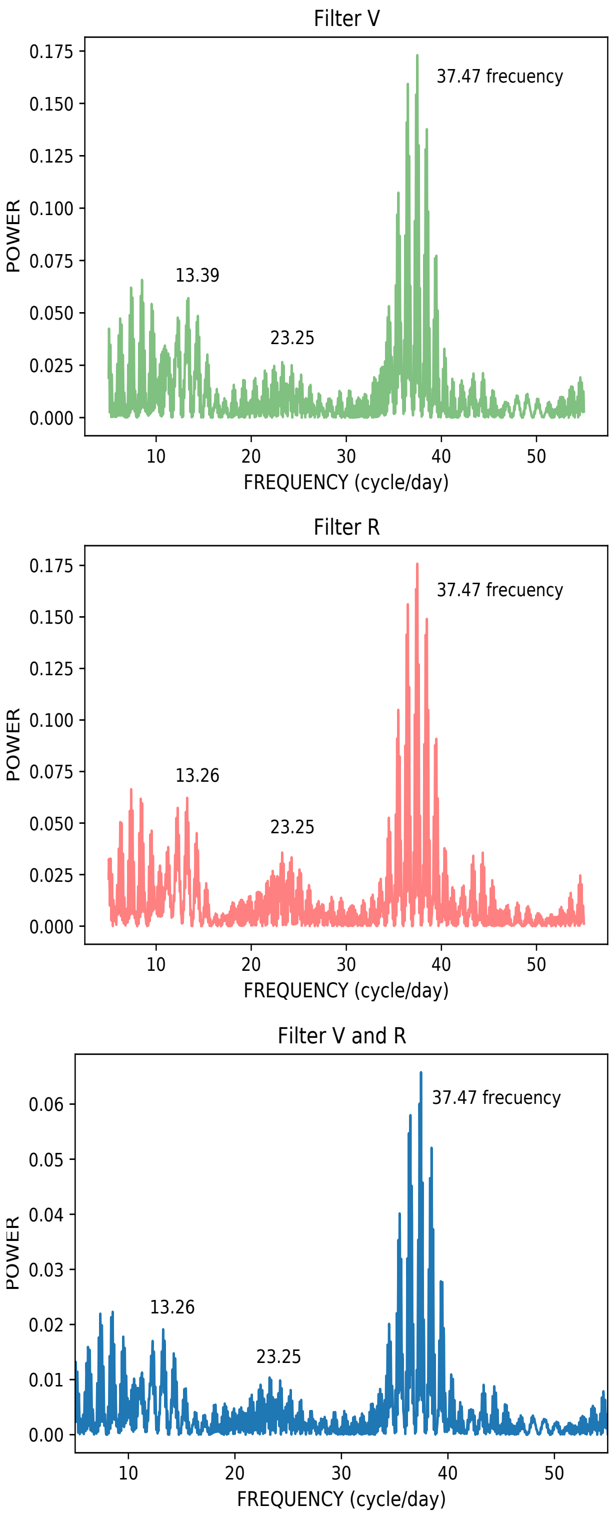

Fig. 5. Power spectra of the photometric observations. From top to bottom the panels depict the power spectra of the V band, the R band and of the combined data. See text for further discussion. The colour figure can be viewed online.

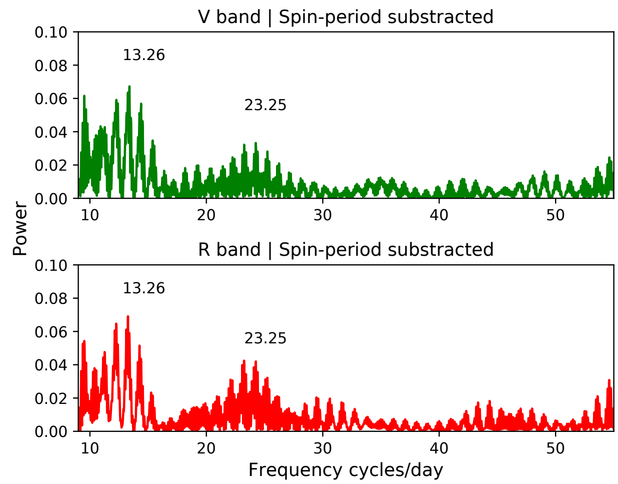

Fig. 6. Power spectrum of the residuals, after removing the spin period signal from the photometric data. The colour figure can be viewed online.

Bayesian approach to produce the probability distribution of the correlation coefficient ρ. The V and R data yielded a distribution with a mean value of 0.367, a standard deviation of 0.034, and with a 95% credible interval of [0.298,0.431]. The lower limit of the 95% credible interval is well above $\rho = 0$, which establishes sufficient confidence in the correlation.

In Figure 7 we show, from top to bottom, the photometric data folded by the associated spin period, the 62-min period, the associated orbital period and the 108-min period. To reduce the influence of noise we averaged the data into 60 phase bins. Folding by the spin period clearly depicts a strong modulation, as expected from the power spectrum analysis. The 62-min and 108-min folded data show a slightly noisier, yet clearly perceptible, sinusoidal oscillation. It is worth noting that the 62 min signal corresponds to the beat period between the spin and 108-min periods. Finally, as expected from the lack of signal in the power search, folding by the orbital period yields no sinusoidal modulation for the photometry.

4.2. *Spectroscopic Data*

4.2.1. GAU2 *Option*

As described in § 3, we performed the measurement of the radial velocities using the GAU2 convolution option. We then proceeded to implement the Lomb-Scargle power search on the convolved data, which is shown in Figure 8. The upper panel is the analysis of Hα, which shows a peak frequency at 16.82 cycles/day, corresponding to the 86 min orbital period.

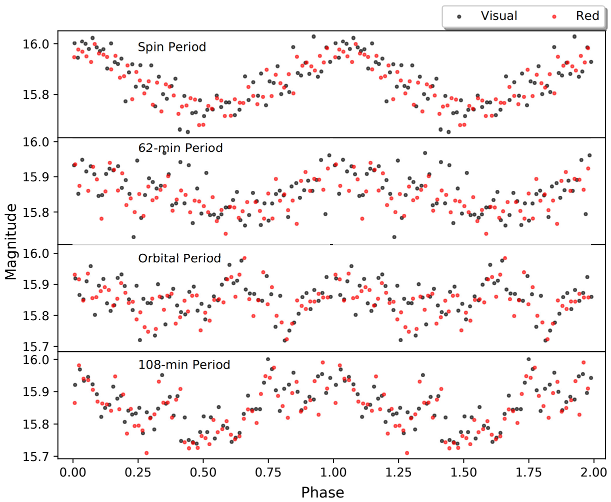

Fig. 7. Photometric data folded by the period signals found in the power spectrum search. The data have been averaged into 60 phase bins. The HJD_0 was selected manually to begin each modulation at its highest value, except for the orbital period for which we used the HJD_0 found in Segura Montero et al. (2020). The colour figure can be viewed online.

No significant power signals for the spin and beat periods were found. In the lower panel we repeated the analysis for He I λ5876 Å, which shows a peak frequency at 16.76 cycles/day, associated also with the 86 min orbital period. Again, the spin and beat period signals are not present. The mean value of the orbital period for both lines is 85.76 $\pm$ 0.15 min. This value is, within the errors, compatible with that measured by Segura Montero et al. (2020). Since we observed a smaller number of spectra than the previous authors, we have a larger error. Therefore we will adopt their value of $P_{orb} = 86.10169 \pm 0.00031$ min, throughout this paper.

Following the methodology used for the photometric data described in § 4.1, we subtracted the conspicuous orbital signal from both the Hα and He I λ 5876 Å data sets and performed a power search on the residuals (shown in Figure 9). The subtracted data of Hα (top panel), as with the DGAU option (see § 4.2.2), show the appearance of a weak picket fence around 20.70 cycles/day, with an overly high FAP value of 0.92. On the other hand, the residuals from the He I λ 5876 Å data (bottom panel) show a signal at 36.39 cycles/day, a frequency comparable to the spin modulation, but its 0.97 FAP value puts its legitimacy in doubt.

We folded the data by the orbital and spin periods, as shown in Figure 10. The upper panel exhibits a clear modulation when the data is folded by the orbital period. However, folding by the spin period (bottom panel) shows no evident indication of a periodic signal.

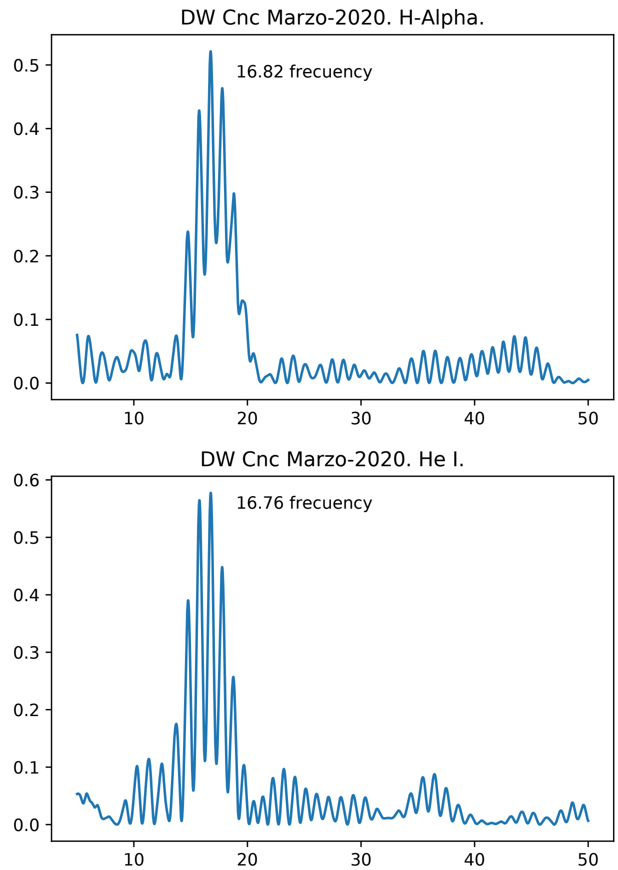

Fig. 8. Top: Power spectra of Hα using GAU2. Bottom: Power spectra of the He I λ5876 Å emission line using GAU2. See text for further discussion. The colour figure can be viewed online.

4.2.2. DGAU *Option*

Following Patterson et al. (2004) we measured the radial velocities by convolving the emission lines with the derivative of a Gaussian (DGAU option) of 83.8 Å(50 pixels) of width. As can be observed in Figure 11, performing a power search on the data yielded the spin and orbital periods for Hα (top panel). The He I λ5876 Å emission line (bottom panel) shows a clear signal of the orbital period and a weak power peak at the spin period. The computed FAP for this weaker spin peak yielded 0.94, rendering it as a questionable signal for He I λ5876 Å. This results are in agreement with those obtained by Patterson et al. (2004) in their spectroscopic power search, where they found the orbital and spin periods.

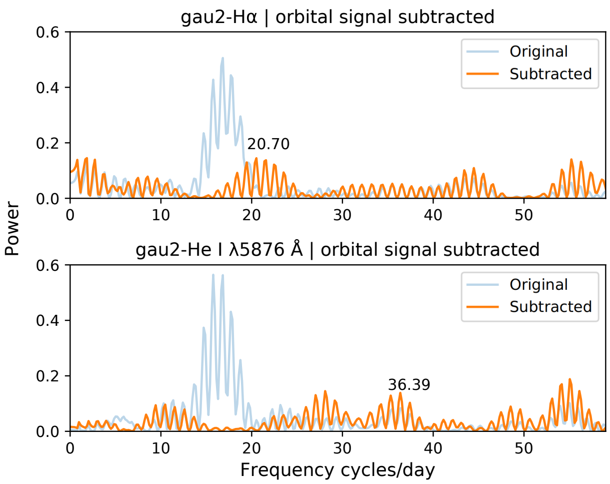

Fig. 9. The upper panel shows the power spectrum of the residuals of the GAU2 Hα radial velocity data, after removing the orbital period signal. The lower panel shows the same for He I λ5876 Å. On each panel, the solid orange line represents the power search performed on the residuals. For comparison, we superposed the power spectrum of the original data, plotted as the faint solid blue line. The colour figure can be viewed online.

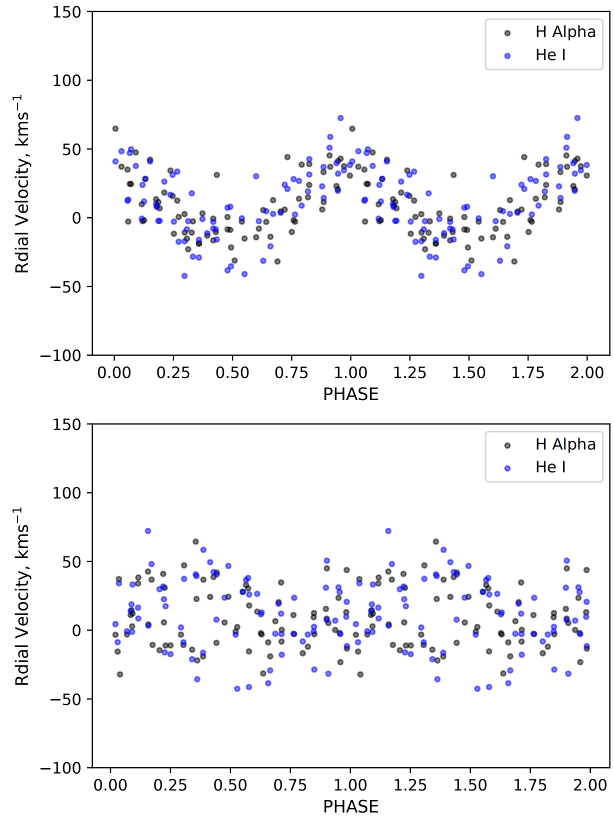

Fig. 10. Folded spectroscopic data. The top panel is folded by the orbital period. The bottom panel is folded by the spin period. The colour figure can be viewed online.

As before, we subtracted the strong modulations from the DGAU radial velocity data sets of both emission lines, and performed a new Lomb-Scargle search on the residuals. After subtracting the orbital signal from the He I λ 5876 Å data (bottom panel of Figure 12), the spin signal peak in the power search of its residuals shows a considerable increase, showing a new FAP value of 0.01 and establishing a better reliability upon this modulation. After subtracting both the orbital and spin signals from the Hα data (top panel of Figure 12), its residuals hint at a weak surge of the 20.70 cycles/day signal, consistent with the GAU2 option in § 4.2.1. However, the FAP of this signal yields 0.93, a value far too high. Nonetheless, we also detected this signature in the wavelet analysis in § 5, indicating that its presence could be real.

In Figure 13 we folded the data by the spin and orbital periods, where both signals show clear modulations of the DGAU radial velocities.

5. WAVELET TRANSFORM ANALYSIS

The wavelet transform is a method that applies the convolution of the signal with a set of wavelets to map the variations occurring in both the time and frequency domains (See Bravo et al. 2014, and references therein for a detailed formulation of the method.). The wavelet map, otherwise known as the scalogram, is a useful tool that allows the detection of the scales (or frequencies) that contribute most to the total energy of the signal (e.g. Benítez et al. 2010).

Following Bravo et al. (2014) and de Lira et al. (2019), we performed a wavelet transform analysis of the photometric lightcurve and the spectroscopic radial velocity data. We applied the continuous 6th order Morlet wavelet transform, implemented from the Python ObsPy package[5] (Krischer et al. 2015). In Figures 14–19 we show the local and global power spectra of our data sets. As explained by Bravo et al. (2014), the local spectrum depicts the energy distribution in time-frequency space, and the global spectrum is obtained by time integration of the local map.

5.1. *Photometry*

The scalogram of the V-band (Figure 14) shows a predominant signal at 15.4 cycles/day. This signal is detected in all four nights, and its relative intensity increases on the third (HJD +2458923) and fourth

[5]Available at: https://github.com/obspy/obspy/wiki/.

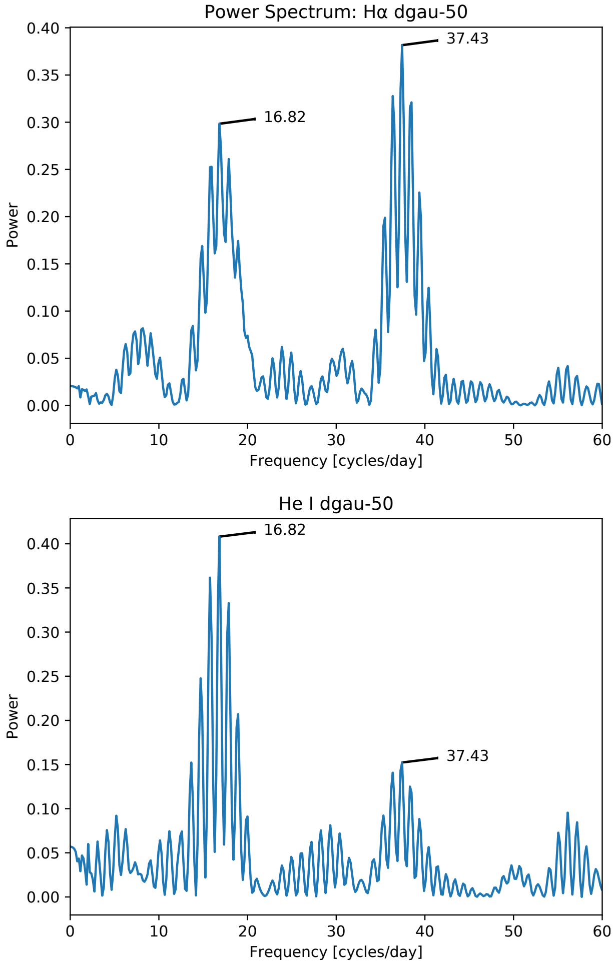

Fig. 11. Power spectra of the Hα (top) and He I λ 5876 Å (bottom) emission lines, using the dgau option with a Gaussian width of 50 pixels (see text). The colour figure can be viewed online.

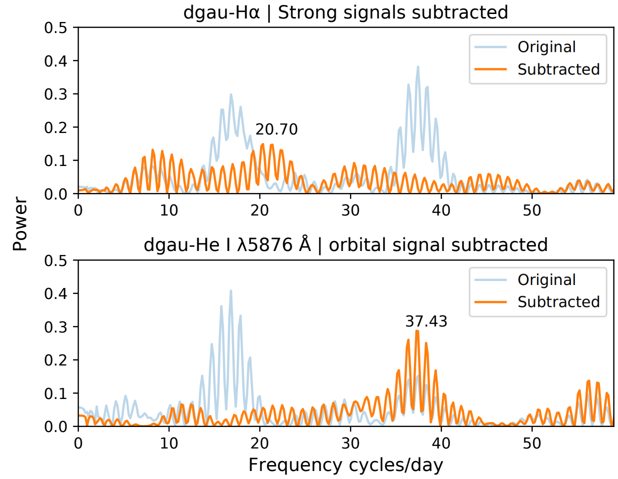

Fig. 12. The upper panel shows the power spectrum of the residuals of the DGAU Hα radial velocity data, after removing the spin period and orbital period signals. The lower panel shows the same for He I λ5876 Å, after subtracting the orbital period. On each panel, the solid orange line represents the power search performed on the residuals. For comparison, we superposed the power spectrum of the original data, plotted as the faint solid blue line. The colour figure can be viewed online.

night (HJD +2458924). This signature is consistent with the orbital cycle, which was absent in the Lomb-Scargle power spectrum.

The *R*-Band analysis (Figure 15) shows a similar structure to that exhibited by the *V*-band scalogram, except for the second night (HJD +2458917), which yields a strong signal at ≈21 cycles/day; this frequency is comparable to the 20.60 cycles/day modulation found by Patterson et al. (2004), corresponding to the beat period between the spin and orbital cycles. We note that we did not detect this signal in the photometric power Lomb-Scargle analysis (see § 4.1), but it did appear after subtracting the stronger signals in the spectroscopic data in § 4.2. A secondary signal peaking at ≈35 cycles/day (possibly associated with the spin period) is also visible during the second night (HJD +2458917).

5.2. *Spectroscopy*

We performed the wavelet analysis on the radial velocity data sets obtained both from the GAU2 and DGAU convolution methods. We now proceed to describe this results.

5.2.1. GAU2 *Option*

The Hα GAU2 scalogram in Figure 16, shows a broad power peak extending from ≈20 to ≈39 cycles/day at the outset of the first night (HJD +2458923.0). Such broad power peak narrows down into two localized peaks, of which the most prominent and persistent shows a midpoint at a frequency of ≈22 cycles/day; a signal consistent with that also found in the photometric Lomb-Scargle analysis of ≈23 cycles/day. The second night of this scalogram (HJD +245894) displays a strong signal at ≈33 cycles/day, which we consider to be a possible alias of the spin modulation. The ≈22 cycles/day signature is also present during the second night but with a decrease in relative intensity.

The He I λ 5876 Å GAU2 scalogram, exhibited in Figure 17, shows a prominent signal that persists throughout the first night (HJD +2458923) at ≈22 cycles/day, in agreement with the Hα GAU2 data. During this first night a secondary signal appears at ≈40 cycles/day, which gradually shifts to ≈37 cycles/day (related to the spin period) as the

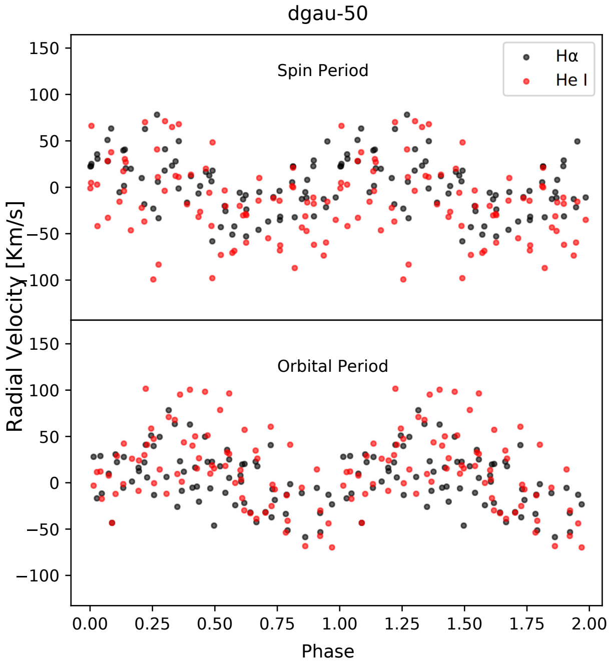

Fig. 13. Radial Velocity data of Hα and and He I λ 5876 Å, folded by the spin (top panel) and orbital (bottom panel) periods found in the power spectrum search. The colour figure can be viewed online.

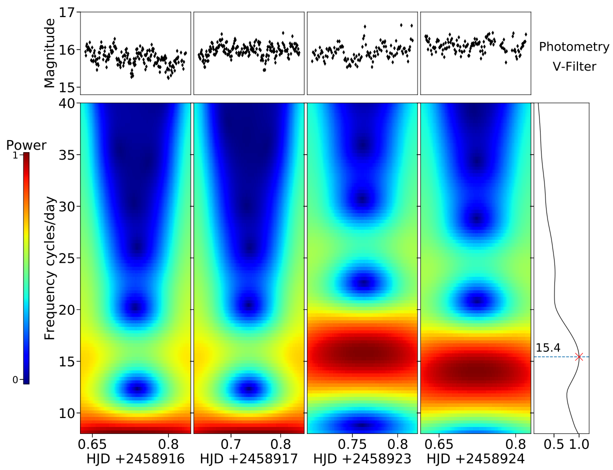

Fig. 14. Scalogram of the V-band photometric data. The global spectrum is exhibited in the utmost right panel, while the local spectrum appears in the panels below the data of each night. An orbital cycle signal ($\approx$16 cycles/day) is present throughout all 4 nights of observations. See text for further discussion. The colour figure can be viewed online.

night progresses. During the second night (HJD +2458924) we see an overall shift towards smaller frequency values, displaying a strong signal at $\approx$33 cycles/day and a slightly milder yet very persistent signal at $\approx$16 cycles/day (consistent with the orbital period).

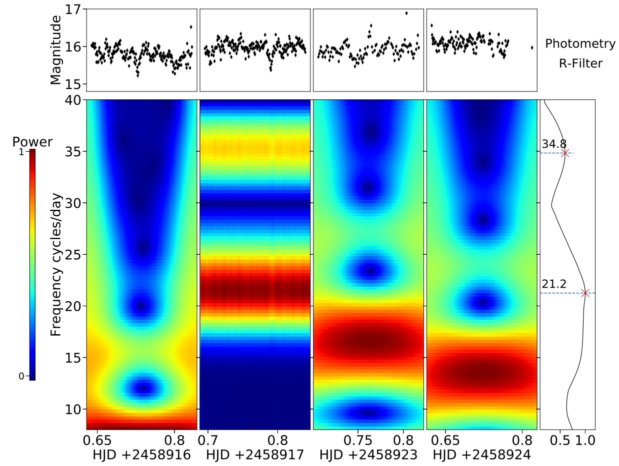

Fig. 15. Scalogram of the R-band photometric data. The global spectrum is exhibited in the utmost right panel, while the local spectrum appears in the panels below the data of each night. The second night shows the presence of the spin period and a $\approx$21 cycles/day signal (consistent with the spin-orbit beat period). The rest of the nights are dominated by the orbital cycle. See text for further discussion. The colour figure can be viewed online.

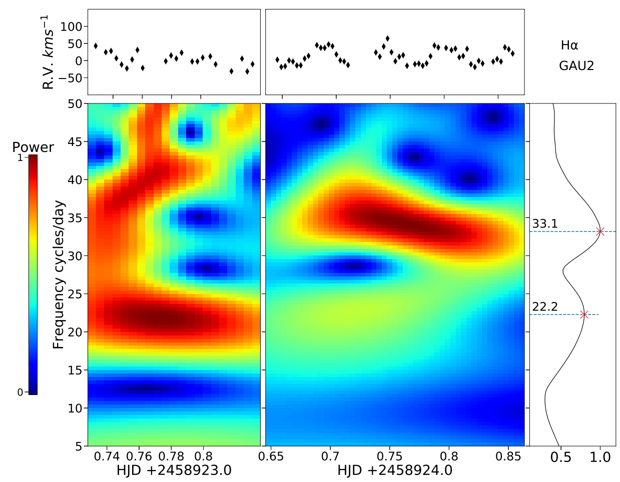

Fig. 16. Scalogram of the Hα GAU2 spectroscopic data. The global spectrum is exhibited in the utmost right panel, while the local spectrum appears in the panels below the data of each night. The first night shows prominent signals at $\approx$37 cycles/day and $\approx$22 cycles/day. The latter signal also appears during the second night but is surpassed in intensity by a $\approx$33 cycles/day signature. See text for further discussion. The colour figure can be viewed online.

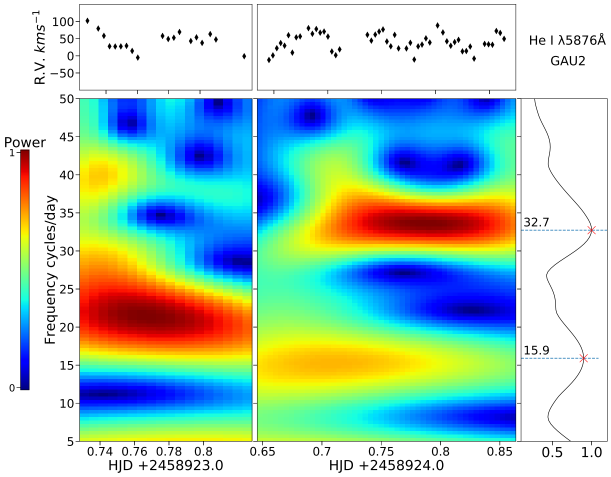

Fig. 17. Scalogram of the He I λ5876Å GAU2 spectroscopic data. The global spectrum is exhibited in the utmost right panel, while the local spectrum appears in the panels below the data of each night. The first night shows a dominant signal at ≈22 cycles/day and a second one at ≈40 cycles/day. The second night is dominated by a ≈33 cycles/day signature, accompanied by a persistent secondary signal at ≈16 cycles/day. See text for further discussion. The colour figure can be viewed online.

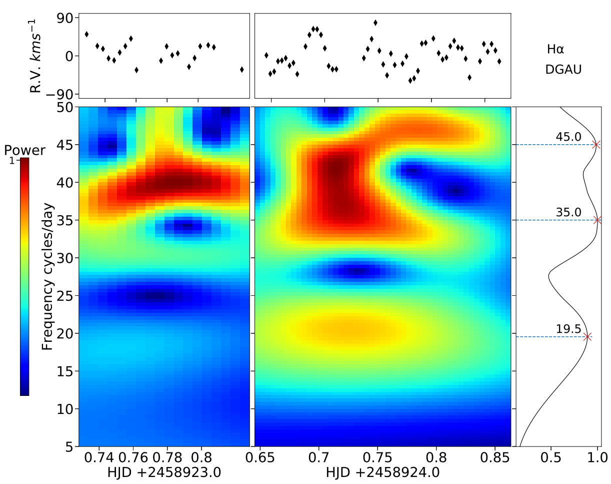

Fig. 18. Scalogram of the Hα DGAU spectroscopic data. The global spectrum is exhibited in the utmost right panel, while the local spectrum appears in the panels below the data of each night. The first night shows a strong signal, consistent with the spin cycle, at ≈38 cycles/day. During the second night the spin cycle signal is also present although with a broader structure; a secondary signature also appears this night at ≈20 cycles/day, which is consistent with the spin-orbit beat period. See text for further discussion. The colour figure can be viewed online.

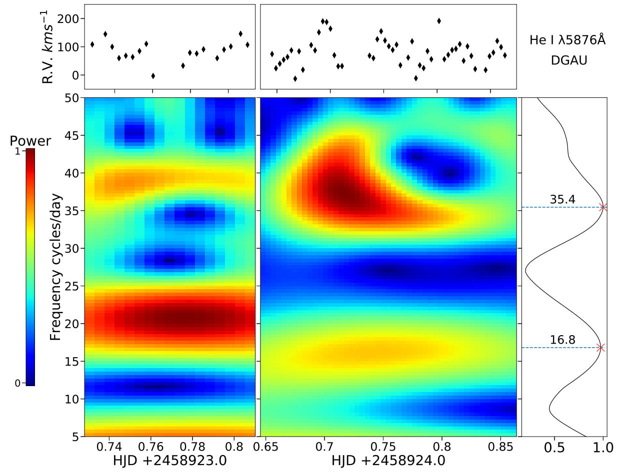

Fig. 19. Scalogram of the He I λ5876Å DGAU spectroscopic data. The global spectrum is exhibited in the utmost right panel, while the local spectrum appears in the panels below the data of each night. The first night shows a strong and persistent detection at the ≈20 cycles/day beat signal. Another signature is evident at the ≈38 cycles/day spin signal. The latter is also present during the second night, although its structure considerably broadens. The second night shows also the appearance of a persistent signal of the orbital cycle at ≈16 cycles/day. See text for further discussion. The colour figure can be viewed online.

5.2.2. DGAU *Option*

Figure 18 depicts the Hα DGAU scalogram, showing during the first night (HJD +2458923), a conspicuous signal at the expected spin period of ≈38 cycles/day. In the second night (HJD +2458924), the signal observed the previous night is still visible, but its structure considerably broadens in frequency, eventually adopting a two-pronged shape, whose contribution reflects on the loss of the 38 cycles/day signal in the global spectrum. The second night also shows a clear signal at ≈20 cycles/day, related to the 70 min beat period.

The He I λ 5876 Å DGAU scalogram, in Figure 19, displays a strong signal at ≈20 cycles/day that persists all throughout the first night (HJD +2458923), and a weaker signature at ≈38 cycles/day, consistent with the spin modulation. On the second night (HJD +2458924) the spin cycle signal becomes enhanced and its structure considerably broadens. This night also shows the appearance of a secondary detection at ≈16 cycles/day, related to the spin modulation, which persists over the whole night.

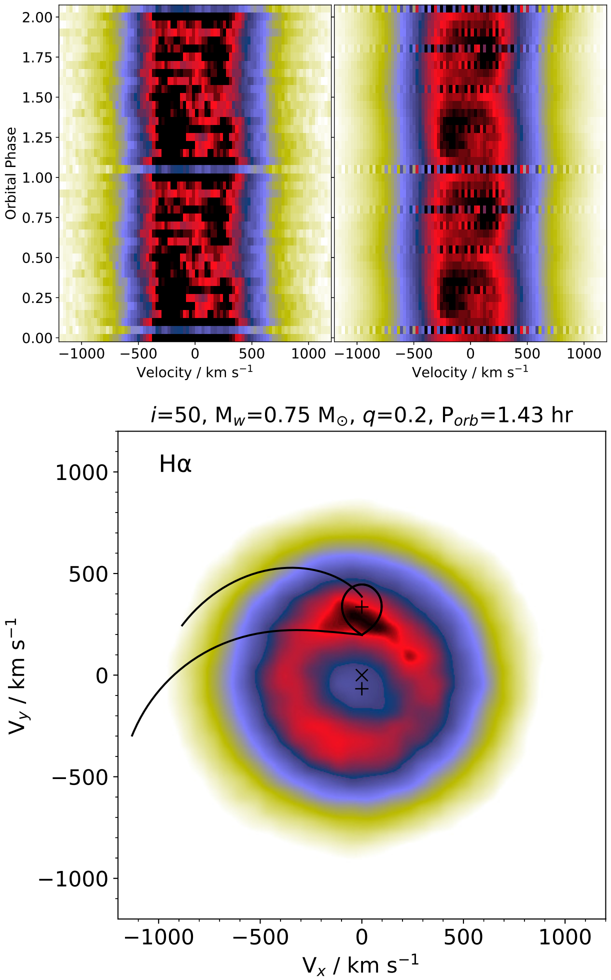

Fig. 20. Trail spectra and Doppler tomography of the Hα emission line. The relative emission intensity is shown in a scale of colours, where the strongest intensity is represented by black, followed by red, then blue, and finally yellow. The cross marks represent (from top to bottom) the position of the secondary, the centre of mass and the primary component. The Roche lobe of the secondary is depicted around its cross. The Keplerian and ballistic trajectories of the gas stream are marked as the upper and lower curves, respectively. The colour figure can be viewed online.

6. DOPPLER TOMOGRAPHY

Doppler tomography is an indirect imaging technique developed by Marsh & Horne (1988). It produces two-dimensional mappings of the emission intensity in velocity space of the accretion disc, using the phase-resolved profiles of the spectral emission lines. We obtained the Doppler tomography of the Hα and of the He I λ 5876 Å emission lines, using a Python wrapper[6] (Hernandez Santisteban 2021) of the original FORTRAN routines published by Spruit (1998) within an IDL environment. In the top left panel of Figure 20 we show the observed trailed spectra of Hα, while the reconstructed trailed spectra appears in the top right panel; the tomogram is displayed in the bottom panel. With the same layout, the trailed spectra and tomography of He I λ 5876 Å are exhibited in Figure 21. The parameters used to plot the features in the tomograms are as follows: an inclination of $i = 50°$; a value of the mass of the primary star of M_w=0.75 M$_\odot$, consistent with the average mass for white dwarfs in CVs below the period gap (Knigge 2006); a mass ratio $q = 0.2$, estimated following Echevarria (1983); and an orbital period of $P_{orb} = 86.10$ minutes (Patterson et al. 2004; Rodríguez-Gil et al. 2004; Segura Montero et al. 2020). We now proceed to describe the results obtained for each emission line.

6.1. Hα

The Hα observed trailed spectra display a complex behaviour. From orbital phase 0.0 to ≈0.10 they show a single peaked structure. In the interval from 0.10 to 0.30, the trailed spectra display a double-peaked profile. After this interval, the profile briefly becomes single peaked, and from 0.35 to 0.55 the blue shifted peak becomes more intense than the red shifted peak. From 0.55 onward the line profile again displays a symmetric double-peaked structure with a brief single-peaked intrusion at ≈ 0.8.

The tomography shows a disc signal in red colour (Marsh & Horne 1988) with a superimposed intense region (in black) at the position of the Roche Lobe of the secondary, which could be caused by emission from a hot spot component (e.g. Echevarría et al. 2007). The disc structure was not detected in the tomography by Segura Montero et al. (2020), but this finding is in good agreement with the dominant double-peaked structure, characteristic of discs in systems of high inclination (Horne & Marsh 1986), exhibited by the Hα line profiles reported by Rodríguez-Gil et al. (2004).

6.2. *He I 5876 Å*

The He I λ 5876 Å trailed spectra show the oscillation of a broad single-peaked profile, consistent with the line profiles of this emission line put forward by Rodríguez-Gil et al. (2004). The tomography shows a blob-like region of high intensity in the upper quadrants that overlays the position of the Roche Lobe

[6] Available at https://github.com/Alymantara/pydoppler.

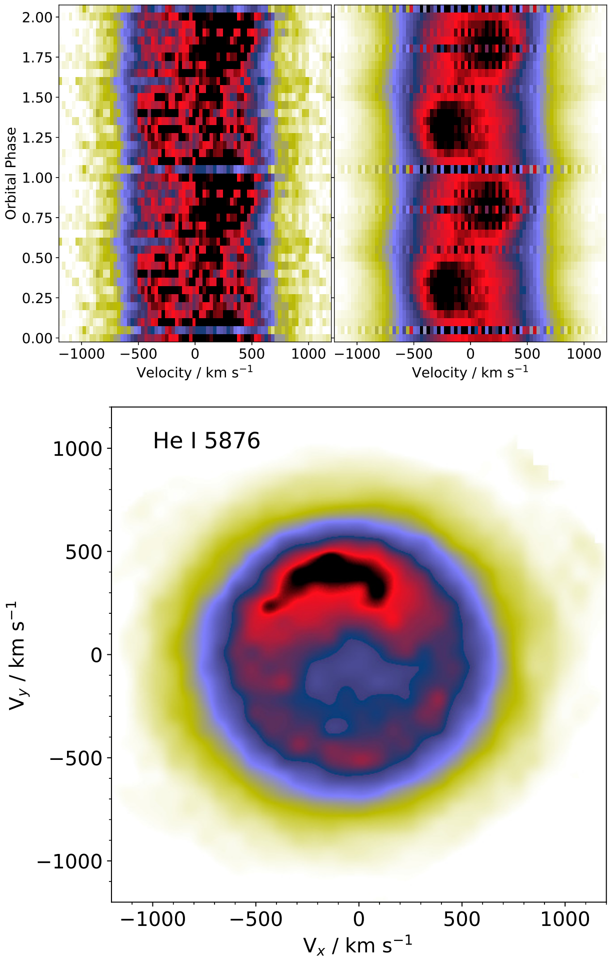

Fig. 21. Trail spectra and Doppler tomography of the He I λ 5876 Å emission line. The relative emission intensity is shown in a scale of colours, where the strongest intensity is represented by black, followed by red, then blue, and finally yellow. The cross marks represent (from top to bottom) the position of the secondary, the centre of mass and the primary component. The Roche lobe of the secondary is depicted around its cross. The Keplerian and ballistic trajectories of the gas stream are marked as the upper and lower curves, respectively. The colour figure can be viewed online.

of the secondary, and further extends towards negative velocities, covering the position where the emission coming from the hotspot is expected in velocity space. Note that the position of the blob in the He I λ 5876 Å tomography is consistent with that of the region of maximum intensity observed for Hα.

7. DISCUSSION

We performed a study of new photometric and spectroscopic observations of DW Cnc, after the system recovered from a low state, presumably caused by an episode of low mass transfer from the secondary that inhibited the lighthouse effect (Segura Montero et al. 2020). Photometry from the AAVSO shows that at the time of our observations, DW Cnc had already reached a state comparable to that from 1999-2003 reported by Patterson et al. (2004) and Rodríguez-Gil et al. (2004). With this in mind, we performed various analyses to compare the behaviour displayed by DW Cnc before and after experiencing the low state.

Our photometric power search analysis (see § 4.1) shows a clear spin-cycle modulation, in agreement with Patterson et al. (2004) and Rodríguez-Gil et al. (2004). Our photometry also exhibits a moderate signal at 108 min. Patterson et al. (2004) found evidence of a similar weak signal at 110.85(9) min; they left this finding as an unsolved problem, which as they put it, *does not seem related to any other clocks in the binary.* Furthermore, we have also detected a new 62 min period signal which, although weak, corresponds to the beat period of the spin and the 108 min signatures. Finding this beat signal suggests that the 108 min period is not caused by spurious effects. Still, the origin of these modulations remains unknown. However, we did not find the 70 min beat period signal, nor the 86 min orbital period after the subtraction of the main spin modulation; the lack of signals is the main contrast in our photometric results from those by Patterson et al. (2004). We find the same contrast with the modulations found in the X-ray observations of Nucita et al. (2019), who also detected the spin-orbit beat period and a spin modulation signal.

We also conducted two different power spectrum analyses of the radial velocities of the Hα and He I λ 5876 Å emission lines (see § 4.2): the first one by convolving the lines with two antisymmetric Gaussians (GAU2), and the second one by employing the derivative of a Gaussian (DGAU) as the convolution function. When employing the same method as Patterson et al. (2004), i.e. DGAU, we obtain signals consistent with these authors, detecting both the orbital and spin modulations. On the other hand, the power search in the GAU2 option (which traces the inner regions of the disc) yielded only a strong signal for the orbital period. This, in a way, is also similar to the results reported by Rodríguez-Gil et al. (2004), who find both signals when using a *broad* Gaussian but obtain exclusively the orbital signature when the correlation of the emission line is made with a *narrow* Gaussian.

In § 5, we conducted a wavelet transform analysis which confirmed the presence of some of the signals found in the Lomb-Scargle periodograms. However, and perhaps more remarkably, this analysis also detected a localized signature of the 70 min beat period in the DGAU scalograms. We note that a weak hint of the beat modulation also appeared in the Hα periodograms after subtracting the dominant signals from the spectroscopic data, but we regard this detection with caution, given the high FAP yielded by the signature (see § 4.2).

We implemented a Doppler tomography study of the binary in § 6. The trailed spectrum of Hα exhibits a double-peaked structure that becomes single-peaked in short intervals, and with a changing relative intensity of the peaks. On the other hand, the He I λ 5876 Å trailed spectrum shows a broad single-peaked profile. Both of these trailed spectra are consistent with the structure of the profiles of the same emission lines reported by Rodríguez-Gil et al. (2004). Moreover, our Hα Doppler tomogram displays the presence of the accretion disc, a structure not detected in the tomograms by Segura Montero et al. (2020), hinting at a possible replenishing of the disc. Our tomography also shows what appears to be a hot spot component for both emission lines, in good agreement with the S-wave, presumably originated at the location of the bright spot, exhibited in the trailed spectra diagrams from Rodríguez-Gil et al. (2004).

The similarities with previous studies, listed above, lead us to believe that the system has undergone at least a partial recovery from the low state. In particular, finding a clear indication of the spin period both in our photometry and in the DGAU option, a signal which avoided detection in Segura Montero et al. (2020), suggests that the outer disc has undergone enough replenishing to provoke a detectable lighthouse beacon. This is further supported by the tomography showing a clear indication of the accretion disc and a hot spot emission.

Nonetheless, the main differences regarding the signals found (and not found) in the Lomb-Scargle power search of the photometry prevent us from declaring complete recovery of the previous state of DW Cnc. It remains to be seen if the system will fully recover to the condition reported in Patterson et al. (2004). The results in the present article show some progress, but further observations are still required to see whether if the mechanisms causing the behaviour reported in 2004 require more time to get kick-started and allow detection.

8. CONCLUSIONS

Photometric and spectroscopic observations of DW Cnc show, to some extent, a behaviour that agrees with that exhibited before experiencing a low state; pointing at a partial recovery of the system. Namely, our photometry yields a strong modulation of the spin period, which eluded detection by Segura Montero et al. (2020), indicating the reactivation of the lighthouse effect; our analysis also showed a weak unresolved signal at 108 min. Furthermore, when implementing the same methodology as Patterson et al. (2004) to measure the radial velocities of the emission lines, we obtained a result consistent with these authors in the periodogram, where we detect both the orbital and spin periods. Furthermore, in agreement with Rodríguez-Gil et al. (2004), we find evidence of the disc structure and hot spot emission in our Doppler tomography study. Finally, our wavelet transform analysis displays a localized detection of the 70 min beat period.

However, the signatures in the photometric periodograms do not completely match those reported before the low state by Nucita et al. (2019) and Patterson et al. (2004), who find not only the spin cycle, but also a signal corresponding to the spin-orbit beat period, and even a weak detection of the orbital signal after further treatment of their data. Instead we found a new 62 min period which corresponds to the beat between the spin and 108 min periods.

We could not find public data that would enable us to replicate our analyses. Therefore, we propose additional observations of the system to assess if it is possible that the mechanisms that gave rise to the signatures exhibited before the low state, require more time to completely rekindle.

The authors are indebted to DGAPA (Universidad Nacional Autónoma de México) support, PAPIIT projects IN114917 and IN103120. We thank the staff at the OAN-SPM for facilitating and helping us to obtain our observations. This research made extensive use of ASTROPY, a community-developed core Python package for Astronomy (Astropy Collaboration et al. 2013); Python's SciPy signal processing library (Virtanen et al. 2020) and MATPLOTLIB (Hunter 2007). We also thank the anonymous referee, whose comments substantially helped to improve the content of this paper.

REFERENCES

Astropy Collaboration, Robitaille, T. P., Tollerud, E. J., et al. 2013, A&A, 558, 33, https://doi.org/10.1051/0004-6361/201322068

Benítez, R., Bolós, V. J., & Ramírez, M. E. 2010, CMwA, 60, 634, https://doi.org/10.1016/j.camwa.2010.05.010

Bravo, J. P., Roque, S., Estrela, R., Leão, I. C., & De Medeiros, J. R. 2014, A&A, 568, 34, https://doi.org/10.1051/0004-6361/201323032

de Lira, S. R., Bravo, J. P., Leão, I. C., et al. 2019, MNRAS, 484, 3935, https://doi.org/10.1093/mnras/stz122

Echevarria, J. 1983, RMxAA, 8, 109

Echevarría, J., de la Fuente, E., & Costero, R. 2007, AJ, 134, 262, https://doi.org/10.1086/518562

Figueira, P., Faria, J. P., Adibekyan, V. Zh., Oshagh, M., & Santos, N. C. 2016, OLEB, 46, 385, https://doi.org/10.1007/s11084-016-9490-5

Hameury, J.-M. & Lasota, J.-P. 2017, A&A, 602, 102, https://doi.org/10.1051/0004-6361/201730760

Hellier, C. 2001, Cataclysmic Variable Stars - How and Why They Vary (London, UK: Springer)

Hernández Santisteban, J. V. 2021, Astrophysics Source Code Library, ascl:2106.003

Horne, K. & Marsh, T. R. 1986, MNRAS, 218, 761, https://doi.org/10.1093/mnras/218.4.761

Hunter, J. D. 2007, CSE, 9, 90, https://doi.org/10.1109/MCSE.2007.55

Knigge, C. 2006, MNRAS, 373, 484, https://doi.org/10.1111/j.1365-2966.2006.11096.x

Krischer, L., Megies, T., Barsch, R., et al. 2015, CS&D, 8, 014003, https://doi.org/10.1088/1749-4699/8/1/014003

Marsh, T. R., Horne, K. 1988, MNRAS, 235, 269, https://doi.org/10.1093/mnras/235.1.269

Newville, M., Stensitzki, T., Allen, D. B., & Ingargiola, A. 2014, zndo, 11813, https://doi.org/10.5281/zenodo.11813

Nucita, A. A., Conversi, L., & Licchelli, D. 2019, MNRAS, 484, 3119, https://doi.org/10.1093/mnras/stz118

Patterson, J., Thorstensen, J. R., Vanmunster, T., et al. 2004, PASP, 116, 516, https://doi.org/10.1086/421034

Rodríguez-Gil, P., Gänsicke, B. T., Araujo-Betancor, S., & Casares, J. 2004, MNRAS, 349, 367, https://doi.org/10.1111/j.1365-2966.2004.07512.x

Scargle, J. D. 1982, ApJ, 263, 835, https://doi.org/10.1086/160554

Schneider, D. P. & Young, P. 1980, ApJ, 238, 946, https://doi.org/10.1086/158059

Segura Montero, O., Ramírez, S. H., & Echevarría, J. 2020, MNRAS, 494, 4110, https://doi.org/10.1093/mnras/staa856

Shafter, A. W., Szkody, P., & Thorstensen, J. R. 1986, ApJ, 308, 765, https://doi.org/10.1086/164549

Spruit, H. C. 1998, arXiv: astro-ph/9806141

Stepanyan, D. A. 1982, PZ, 21, 691

VanderPlas, J. T. 2018, ApJS, 236, 16, https://doi.org/10.3847/1538-4365/aab766

Virtanen, P., Gommers, R., Oliphant, T. E., et al. 2020, NatMe, 17, 261, https://doi.org/10.1038/s41592-019-0686-2

Warner, B. 1995, Cataclysmic, Variable Stars (Cambridge, UK: CUP)

Warner, B. & Nather, R. E. 1971, MNRAS, 152, 219, https://doi.org/10.1093/mnras/152.2.219

J. Echevarría, S. H. Ramírez, and O. Segura Montero: Instituto de Astronomía, Universidad Nacional Autónoma de México, Apartado Postal 70-264, Ciudad Universitaria, Ciudad de México, C. P. 04510, México.

R. Michel: Instituto de Astronomía, Universidad Nacional Autónoma de México, Apartado Postal 877, Ensenada, Baja California, C. P. 22830, México.

Revista Mexicana de Astronomía y Astrofísica, **58**, 61–72 (2022)

https://doi.org/10.22201/ia.01851101p.2022.58.01.05

MORPHOLOGICAL STUDY OF A SAMPLE OF DWARF TIDAL GALAXIES USING THE *C*-*A* PLANE

I. Vega-Acevedo[1,2,3] and A. M. Hidalgo-Gámez[2]

Received February 22 2021; accepted November 22 2021

ABSTRACT

In this investigation, we determined the Concentration (C) and Asymmetry (A) parameters in a sample of tidal dwarf galaxies (TDG) or candidate galaxies. Most of the galaxies in the sample were found to be in a very precise region of the C-A plane, which clearly separates them from other galaxies. In addition, the stellar mass (M_{star}) and the star formation rate (SFR) in the sample were determined using optical images and GALEX observations. The main results are: the M_{star} and the SFR in the TDG sample do not follow a linear correlation with the C and A respectively, as observed in the rest of galaxies, and the M_{star} and the SFR have a linear correlation similar to that followed by galaxies at high redshift. Then, we can conclude that the C-A plane can be a useful method for the morphological identification of candidates for TDG or dwarf objects from very turbulent environments.

RESUMEN

Los parámetros morfológicos Concentración, C, y Asimetría, A, pueden ayudar a identificar si una galaxia enana es candidata a ser una *tidal dwarf galaxy* (TDG). Se calcularon los valores de C y A en el óptico de una muestra de galaxias que son TDG o candidatas a serlo. Se encontró que la muestra se identifica fácilmente de otros tipos de galaxias. Además, se determinó la masa estelar M_{star}, y la tasa de formación estelar, SFR, de la muestra empleando imágenes en el óptico y de GALEX. Encontramos que: la M_{star} y SFR no siguen una correlación lineal respecto a la C y la A, tal como se observa para el resto de las galaxias y que la M_{star} y la SFR siguen una correlación linear similar a la que siguen las galaxias muy corridas al rojo. Por lo tanto, el uso del plano C-A puede ser un método para la identificación morfológica de candidatos a TDG u objetos enanos de ambientes muy turbulentos.

Key Words: galaxies: dwarf — galaxies: fundamental parameters — galaxies: interactions — galaxies: irregular — galaxies: star formation — galaxies: structure

1. INTRODUCTION

A tidal dwarf galaxy (TDG) can be defined as a massive (around $10^8 M_\odot$ baryonic mass) gravitationally bound, self-rotational object of gas, dust, and stars, that is formed during a merger or interaction between massive galaxies (Duc et al. 2000). The first time the idea of small galaxies being formed from the debris of interaction between galaxies was proposed by Schweizer (1978). Since then, this topic has been very active, identifying these galaxies and studying their main properties e.g. (Schechtman-Rook & Hess 2012; Smith et al. 2010; Bournaud et al. 2004; Duc & Mirabel 1999; Duc et al. 1997; Duc & Mirabel 1994; Mirabel, Dottori, & Lutz 1992). These objects typically have an average radius of 6 kpc, an average SFR of $8 \times 10^{-2} M_\odot \mathrm{yr}^{-1}$, and a metallicity of 8.5 dex (Duc & Mirabel 1999). Some authors, such as Duc & Mirabel (1999), even mention that TDGs have an average (B-V) color index of 0.3. However, this result is somewhat difficult to establish since

[1]Departamento de Matemáticas, ESIME, Instituto Politécnico Nacional, México.

[2]Departamento de Física, ESFM, Instituto Politécnico Nacional, México.

[3]Planetario Luis Enrique Erro, Instituto Politécnico Nacional, México.

Smith et al. (2010) find very dispersed values for the color index (g-r), as well as for the (FUV-g) index, the latter having a very large range of values for all TDGs. Also, they might be relatively long-lived objects, more than 1 Gyr, since after their formation at the interaction, they remain orbiting the parent system, or they are expelled from it. However, not all of the objects in the tidal tails of the interacting systems are real galaxies. Some are just gas condensations too small to form a gravitationally bound object (a galaxy) and will dissipate after a few Myr (Bournaud et al. 2004). Others are the result of something called the "whip effect", which is a phenomenon that occurs when different parts of the tidal tail are superimposed on the line of sight. Using only direct images, it is difficult to differentiate between real tidal dwarf galaxies, gas condensations, and whip-effect objects. Only spectroscopy and, particularly, HI dynamic and position-velocity diagrams, can help to tell them apart. In this sense, the number of real or genuine TDGs is very small, although there are many more tidal objects which cannot be classified as real TDG, but only as TDG candidates. Also, there are some objects which are in the outermost part of the tidal tails, which have low metallicity and mass. The difficulty here is to determine if these dwarf galaxies are tidal objects or original dwarf galaxies, as in the case of NGC4656 UV (Schechtman-Rook & Hess 2012). Then, it can be seen that the identification and classification of tidal galaxies is a difficult task, and it takes quite a long time to obtain a definitive classification.

In this investigation, we used the C-A-S system (Conselice et al. 2003) to separate tidal objects from other types of galaxies, and we checked if it is possible to differentiate between the genuine TDGs candidate TDGs and other tidal objects. The C-A-S system, (Concentration, Asymmetry, and Clumpiness) has recently been used to differentiate morphological types of galaxies (Conselice 2003). It has been found that the C-A-S space, or just the C-A plane, is a powerful tool to distinguish between elliptical, spiral, irregular, and starburst galaxies, where each type of galaxy occupies a different region of the C-A-S space (Conselice 2003; Conselice et al. 2003). Moreover, dwarf elliptical galaxies have different values of concentration and asymmetry than their larger counterparts (Yagi et al. 2006; Conselice et al. 2002; Conselice 2003). Therefore, our goal is to verify if TDGs are located in a separate place in the C-A plane, so they can be easily traced, and if the C and A parameters are different from those of genuine TDGs as well as for the rest of tidal objects.

This paper is structured as follows; § 2 is a description of the sample, the data acquisition, and the determination of parameters. § 3 presents the result of the C-A plane study for the TDGs and dwarf galaxies. We investigate the possible correlation of C and A with the stellar mass and star formation in § 4, along with a discussion of the results, and finally, our conclusions are listed in § 5.

2. SAMPLE, DATA ACQUISITION, AND DETERMINATION OF THE PARAMETERS

As we said, the main goal of this investigation is to study if there are differences in the concentration, C, and asymmetry, A, between tidal dwarf galaxies, candidates, and the rest of the dwarf galaxies. In addition, we can check if the C-A plane can be used to identify TDGs from other types of tidal objects, like projection effects in the tidal tails.

2.1. *Sample Selection*

In order to verify how useful the C-A plane is to identify TDGs, we selected a sample of tidal objects, which includes confirmed TDGs as well as candidates, which are those objects whose self-rotation has not been confirmed yet. We selected 17 objects that come from pre-merger binary pairs with optical tails, merger systems, and interacting galaxies.

In order to choose the objects of our sample we followed five criteria: (a) only objects classified previously in the literature, as TDGs or TDG candidates, (b) objects with a radius strictly less than 6 kpc, in order to be considered as dwarf galaxies, (c) objects in the tidal tails or in the vicinity of galaxies that show evidence of interactions, (d) objects with images in the optical from SDSS and (e) with images in the UV by GALEX.

The final sample was reduced to a total of 17 objects, eight of which were confirmed TDGs, five TDG candidates, and four were objects with a very low probability of being TDG. However, there was not enough evidence to affirm the opposite. Due to the criteria imposed for the selection of the sample, the distance, magnitude, as well as other properties of the objects, are very different.

In the following, we summarize some of the properties of the selected objects, and some others are listed in Table 1.

The main properties of the sample are listed in Table 1. An ID number is given in Column 1, while the name is given in Column 2. This name is that of the parent system along with a letter that describes the location of the TDG. The right ascension

TABLE 1

SAMPLE OF TIDAL DWARF GALAXIES

ID[a] (1)	Name (2)	RA [$J2000$] (3)	Dec [$J2000$] (3)	Dis[Mpc] (4)	Radii[b][kpc] (5)
1	Arp 105N[3]	11:11:12.8	28:45:57.14	134.25	4.71
2	Arp 105S[2]	11:11:13.4	28:41:15.96	134.25	4.71
3	Arp 112E[3]	00:01:34.5	31:26:33.70	66.09	5.31
4	Arp 181W[1]	10:27:26.3	79:49:12.79	143.56	5.30
5	Arp 181E[1]	10:27:40.1	79:49:45.3	143.56	3.88
6	Arp 202W[1]	09:00:09.3	35:43:40.26	48.70	2.63
7	Arp 226NW[1]	22:20:33.5	-24:37:22.07	66.14	3.85
8	Arp 226E[1]	22:20:55.7	-24:41:10.21	66.14	4.47
9	Arp 242N[2]	12:46:10.4	30:45:11.31	101.44	4.15
10	Arp242S[3]	12:46:12.0	30:42:02.34	101.44	5.62
11	Arp244S[1]	12:01:26.6	-19:00:49.33	30.38	3.95
12	Arp245N[1]	09:45:44.1	-14:17:34.55	39.15	5.81
13	Arp305E[1]	11:58:41.5	27:29:34.90	55.12	4.86
14	NGC4656N[3]	12:44:14.4	32:16:43.88	13.41	5.40
15	Arp270S[2]	10:49:34.5	32:52:38.31	28.14	1.91
16	Arp270N[2]	10:49:44.2	33:00:42.40	28.14	0.76
17	HolmbergIX[2]	09:57:31.5	69:02:43.69	1.90	0.86

[a]Column (1) is the identification number in each object of our sample.

[b]The radii in Column (6) are the r(80%), obtained as described in § 2.2.

[1]Tidal dwarf galaxies confirmed, TDG.

[2]Tidal dwarf galaxies candidates, TDGc.

[3]Non-likely tidal dwarf galaxies, nlTDG.

and declination are listed in Column 3, while the distance to the system (aka, the interacting parent galaxies) is presented in Column 4. This distance is important, because the farther the system is the more difficult it is to distinguish tidal features, and the more easily the low surface brightness structure is lost in the images. In Column 5 are listed the radii of the TDGs, as the r_{80} described in § 2.2.

Smith et al. (2010) proposed that Arp 181N, Arp 181S, and Arp 202W could be TDGs. This was confirmed later by Sengupta et al. (2013). Moreover, Scott et al. (2018) found evidence that Arp 202W lacked a significant old stellar population, so they concluded that it might have been formed in the extended dark matter halo of one of its parent galaxies. Also, both systems in Arp 226, Arp 226NW, and Arp 226E, have been confirmed as TDGs by their metallicity and HI gas dynamics (Lelli et al. 2015). The Arp 244 system was the first where the existence of TDG candidates (Arp 244W and Arp 244E) was reported (Schweizer 1978; Mirabel, Dottori, & Lutz 1992). The high-resolution mapping of HI made by Hibbard et al. (2001) and Gordon, Koribalski, & Jones (2001) corroborated the neutral gas counterpart of these two objects. More recent authors have confirmed that these objects are TDG (Smith et al. 2010; Hibbard et al. 2005). Finally, there are two other systems with genuine tidal objects: Arp 245N, which has been proposed as a tidal galaxy still in formation (Smith et al. 2010; Brinks et al. 2001; Duc et al. 2000), and Arp 305E, which Hancock et al. (2009) proposed as a TDG after studying its star formation and age, all of which was later confirmed by Sengupta et al. (2017).

However, there are some other galaxies the nature of which has aroused some doubts. Duc & Mirabel (1994), Duc et al. (1997), and Smith et al. (2010) suggested that Arp 105N and Arp 105S might be tidal objects. However, Bournaud et al. (2004) showed that Arp 105N is a "whip effect" object, but confirmed that Arp 105S could be a TDG at an early state. Anyhow, we will keep Arp 105N in our sample in order to see if such a kind of object can be distinguished from a real TDG in the C-A plane. A similar situation applies for Arp 242, where Arp 242N is considered as a TDG (Smith et al. 2010), but Bournaud et al. (2004) did not get any conclusion on Arp 242S. Therefore, it will be considered as a TDG candidate in this investigation. Arp 112E, also called KUG 2359+311, was considered as one of the reddest TDG candidates by Smith et al. (2010). However, Fu et al. (2020) could not observe HI gas in this object, nor any bridge of gas between it and Arp 112. This could indicate two things: it is a normal dwarf galaxy in the vicinity of Arp 112, or KUG 2359+311 is a TDG that has run out of gas. Only Smith et al. (2010) proposed Arp 270N as TDGc, and we will consider it as such in this investigation. Sabbi et al. (2008) found that Holmberg IX is a stronger TDG candidate. Moreover, Schechtman-Rook & Hess (2012), using a photometric analysis, also found evidence that Holmberg IX could be a TDGc, although it was not a definitive conclusion. Finally, according to Schechtman-Rook & Hess (2012), NGC 4656 might have, at least, two tidal objects: NGC 4656N and NGC 4656UV. Although Zasov et al. (2017) concluded that NGC4656UV is rather an LSB-dwarf galaxy with dark matter, which agrees with Muñoz-Elgueta et al. (2018), where it is proposed that NGC 4656 and 4656UV are a pair of interacting galaxies and NGC 4656UV does not have a tidal origin.

In conclusion, in our sample, there are 8 confirmed TDG, 4 candidates, and 5 objects which might not be TDG, which we call non-likely tidal dwarf galaxy (nlTDG). Although there are a few more TDGs and candidates, these are the ones with good resolution in their optical images, deep enough to allow a good determination of C and A. They also have UV images, in order to get the SFR. Therefore, they are the only ones included in this investigation.

The images used in this work for the determination of C and A were selected from the SDSS in the g filter (Blanton et al. 2017; Doi et al. 2010), except for Arp 244, where an image from the DSS in the V filter was used. For the determination of the parameters C and A, the MIDAS software was used. The images used for the star formation in the ultraviolet are from the GALEX space observatory database (Bianchi, Shiao, & Thilker 2017).

2.2. *Determination of the C and A Indexes*

The concentration index, C, quantifies the concentration of the light in a galaxy, and it is defined as

$$C = 5 \times \log \left(\frac{r\,(80\%)}{r\,(20\%)} \right), \tag{1}$$

where $r(80\%)$ and $r(20\%)$ represent the radius that encloses, respectively, 80% and 20% of the light curve of the source in units of 1.5 Petrosian reverse radii (Bershady et al. 2000). This index has been used extensively to classify galaxies into two broad classes, early and late (Doi et al. 2010; Bell et al. 2003). The correlation between the C index and the stellar mass is very interesting, in the sense that massive galaxies have a higher C index (Conselice 2006a).

In order to determine C, we followed the methodology described below. First, from a two-dimensional Gaussian fitting the optical center of the galaxy was determined. This point will be the center of elliptical rings, from which the intensity against the radius can be plotted for each object. This can be integrated to get the flux vs. radius plot. Then, we selected those radii which contain 80% and 20% of the total flux of the object, respectively. The distance from the center of the galaxy to these points is the r_{80} and r_{20}, respectively. These values are the values we used in Section 2.1. The software MIDAS was used. For a more detailed process, the reader should refer to Vega-Acevedo (2013).

The definition of the asymmetry index A used in this paper is

$$A = \frac{\sum |I - R|}{\sum |I|}, \tag{2}$$

where I is the original image and R is that same image rotated by 180 degrees around the optical center (determined as previously said). The rotated image was created with the software as well as the $|I - R|$ one. Both parts of the equation were obtained with the addition of the flux of all the pixels inside the r_{80}, and a subsequent division of these two quantities, the total flux in the $|I - R|$ image and in the I image. The MIDAS software was also used for this procedure (Vega-Acevedo 2013).

The asymmetry index takes values from 0, for galaxies completely symmetrical, to 1 where the galaxy is completely asymmetrical (Conselice et al. 2003, 2000).

The A index has been used to identify recent merger systems that are very distorted. Based on asymmetry measurements on images of nearby merger remnants, it can be considered that a galaxy is a merger remnant if its asymmetry index is larger than a certain value $A > A_m$, with $A_m = 0.35$ (Conselice et al. 2003). Note that this criterion applies to disk-disk mergers only. Spheroid-dominated mergers suffer much weaker morphological distortions, hence this asymmetry criterion cannot be used.

The final values of A and C for this sample of tidal dwarf galaxies are listed in Columns 2 and 3 of Table 2, while the stellar mass and the star formation rates are listed in Columns 4 and 5, respectively.

TABLE 2

SAMPLE VALUES

ID[a]	A	C	$M_*\ [M_\odot]\ 10^8$	SFR $\left[M_\odot \mathrm{yr}^{-1}\right]\ 10^{-2}$
1	0.5 ± 0.1	1.7 ± 0.3	3.3 ± 0.5	61.9 ± 0.5
2	0.4 ± 0.1	1.7 ± 0.3	6.1 ± 0.5	38.5 ± 0.5
3	0.6 ± 0.1	2.1 ± 0.3	1.6 ± 0.5	28.8 ± 0.5
4	0.8 ± 0.1	1.7 ± 0.3	0.4 ± 0.5	8.0 ± 0.5
5	0.7 ± 0.1	1.6 ± 0.2	1.0 ± 0.5	7.9 ± 0.5
6	0.6 ± 0.1	2.1 ± 0.3	0.2 ± 0.5	3.9 ± 0.5
7	0.2 ± 0.1	1.5 ± 0.2	3.5 ± 0.5	17.9 ± 0.5
8	0.7 ± 0.1	1.6 ± 0.2	8.3 ± 0.5	10.8 ± 0.5
9	0.3 ± 0.1	1.7 ± 0.3	1.7 ± 0.5	39.2 ± 0.5
10	0.6 ± 0.1	1.8 ± 0.3	0.8 ± 0.5	20.2 ± 0.5
11	0.1 ± 0.1	1.5 ± 0.2	1.2 ± 0.5	29.9 ± 0.5
12	0.1 ± 0.1	1.6 ± 0.2	1.2 ± 0.5	11.1 ± 0.5
13[a]	0.5 ± 0.1	2.4 ± 0.4	–	2.5 ± 0.5
14	0.5 ± 0.1	2.0 ± 0.3	0.40 ± 0.5	2.7 ± 0.5
15[a]	0.5 ± 0.1	1.5 ± 0.2	–	0.7 ± 0.5
16	0.6 ± 0.1	1.9 ± 0.3	1.4 ± 0.5	5.0 ± 0.5
17[a]	0.4 ± 0.1	2.0 ± 0.3	–	0.8 ± 0.5

[a]The stellar mass obtained for these objects is smaller than $0.1 \times 10^8 M_\odot$.

TABLE 3

AVERAGES AND $1\,\sigma$ VARIATIONS OF C AND A FOR GALAXY TYPES

Type	C	A
TDGs	1.7 ± 0.2	0.5 ± 0.2
Ellipticals[a]	4.4 ± 0.3	0.0 ± 0.1
Dwarf ellipticals[a]	2.5 ± 0.3	0.0 ± 0.1
Spiral[a]	3.3 ± 0.6	0.1 ± 0.1
Dwarf Spiral[b]	2.4 ± 0.6	0.2 ± 0.1
Irregulars[a]	3.3 ± 0.5	0.3 ± 0.2
Dwarf irregulars[a]	2.9 ± 0.3	0.2 ± 0.1

The error for C and A corresponds to a $1\,\sigma$ variation from the average.

[a]Data taken from Conselice (2003).

[b]Data taken from Vega-Acevedo & Hidalgo-Gámez (2014).

3. THE C AND A PLANE

Many researchers have used the position in the concentration−asymmetry plane (C-A) to classify galaxies by their morphology (Bershady et al. 2000; Lauger et al. 2005; Menanteau et al. 2006; Yagi et al. 2006; Huertas-Company et al. 2008; Neichel et al. 2008). Based on their results we checked if tidal dwarf galaxies were in a separate place in this plane and, therefore, easily spotted.

The A parameter, listed in Table 2, ranges between 0 and 1, the smaller the values the more symmetric the galaxy. Only three of our galaxies have low A values (< 0.2), but also only three have very high asymmetry values (> 0.7). Therefore, most of the TDGs, about 60% of the galaxies, have intermediate A values. Also, it can be seen that most of the TDG are more asymmetric than the average dwarf galaxies, as can be seen in Table 2 and Figure 1, where the histogram distribution of the A values for the TDGs in our sample is shown in (d) panel. In the other panels the distribution for elliptical (a), spiral (b) and irregular galaxies (c) are shown for comparison. These values have been obtained from Conselice (2006a) and Vega-Acevedo & Hidalgo-Gámez (2014). There are large differences between TDGs and elliptical and spiral, the latter having small A values, no larger than 0.3. On the contrary, irregulars and TDGs show a broad range of asymmetry values, although the peak for Irr (including dwarf) is at lower values than for TDGs. This is also seen in Table 3, where the average values of the asymmetry index are shown for some of the galaxies types. TDGs have the largest one, while Irr and dIrr have a smaller average A value (in this investigation we separated between dwarf and normal irregular galaxies).

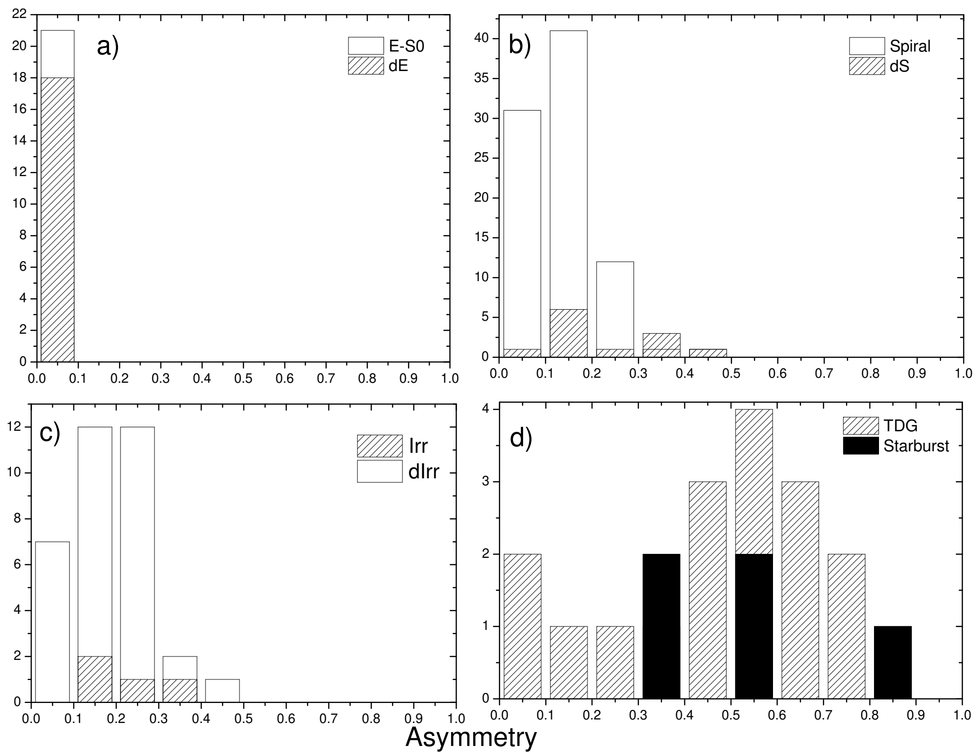

Fig. 1. Histogram of asymmetries for Conselice (2003) and Vega-Acevedo & Hidalgo-Gámez (2014).

Another interesting aspect to notice is those TDGs with very small asymmetry indexes. As can be seen in Table 2, at least two of them have A values lower than 0.1 (Arp 244S and Arp 245N). We think there are two reasons for such unexpected values: one is that these are not TDGs but some other tidal features, more symmetric, which might not be the case based on the large number of investigations that confirmed the tidal nature of these particular objects (Smith et al. 2010; Hibbard et al. 2005; Smith et al. 2010; Brinks et al. 2001; Duc et al. 2000). The second one is the lack of low surface brightness structure in the images used for the A determination. This might lead to a lower value of the asymmetry because only the central part of the galaxies was used, which are always more symmetric than the outer parts (Vega-Acevedo 2013). Therefore, it is important to use the deepest images for the A determination (Vega-Acevedo 2013). However, as this investigation used archive data, such a requirement could not always be fulfilled.

Concerning the asymmetry for the different types of tidal objects, the TDGc have the lowest average value (0.38) while the nlTDGs have the highest (0.52), although the differences are of the same order of the dispersion.

Low values of the C parameter indicate a low concentration of light at the center of the galaxy, which is more common in late-type galaxies (spiral and irregular galaxies). Therefore, Bell et al. (2003) differentiated late and early galaxies based on this parameter. Actually, according to them, a value of C higher than 2.6 indicates an early galaxy. Only one of the galaxies (Arp 305N) in our sample has C close to this value, while the other 16 are well into the late-type values. Figure 2 shows the histogram distribution of the C values for different morphological types of galaxies. It is clear that TDGs have the narrowest distribution and the lowest C values. Only some of the dS and dE have similar C values, but the average values (listed in Column 1 of Table 3) are very different. The concentration average value is very similar for the three types of dwarf galaxies. Moreover, it is also interesting to notice that dwarf galaxies always have lower concentration values than their larger counterparts, although all dwarf galaxies have larger C values than the TDGs. Again, the nlTDG have the highest average concentration values (1.9), while the TDGc have the lowest ones (1.7). In any case, it can be concluded that TDGs have different values of the A and C index than any other types of galaxies, including dwarf ones.

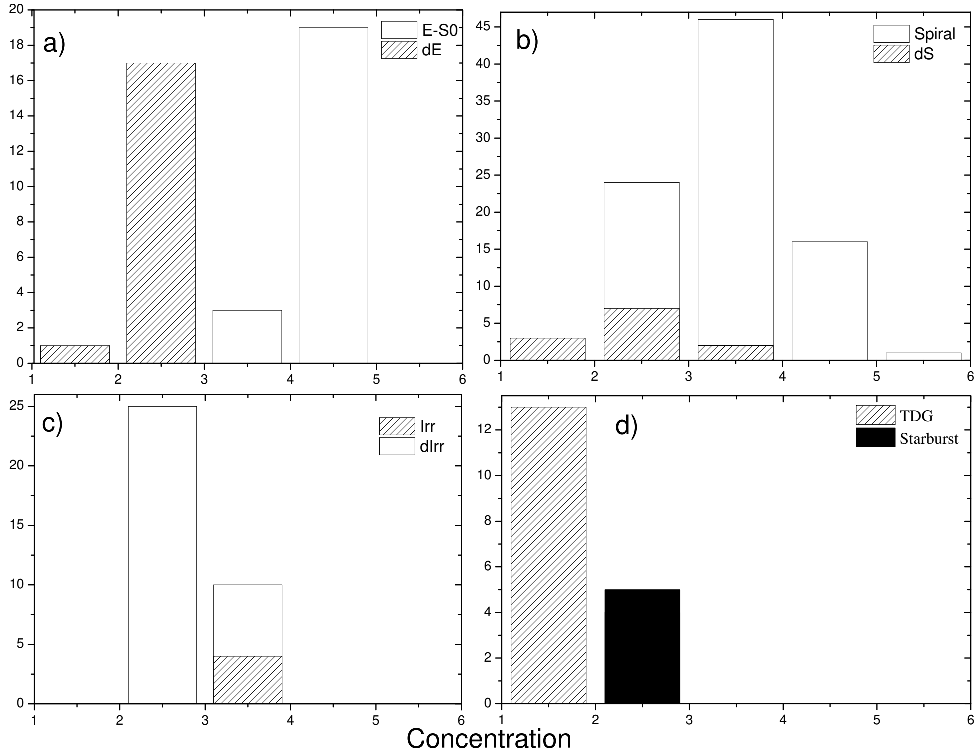

Fig. 2. Concentrations histogram for Conselice (2003) and Vega-Acevedo & Hidalgo-Gámez (2014).

3.1. *C-A Plane*

As seen so far, tidal dwarf galaxies might have particular values of the A and, especially, the C indexes. As pointed out by several investigations (Conselice et al. 2000; Conselice 2003; Vega-Acevedo & Hidalgo-Gámez 2014), galaxies with different morphologies have different positions in the C-A plane, and they can be differentiated very easily. This is one of the advantages of the CA system. Therefore, we have plotted the TDG of our sample in the C-A plane along with the elliptical, irregular, spiral and starburst galaxies, in Figure 3. There are two interesting conclusions from this figure. Firstly, TDGs are not located near the starburst galaxies. However, both groups of galaxies have a broad range of A values. Secondly, the C indexes for TDGs are very low. They are the lowest values for all the types of galaxies, despite the low concentration that dwarf galaxies have, as already noted. Therefore, the identification of TDGs can be done very easily using the C-A plane because they are located in a specific strip in this plane, at C values smaller than 2.

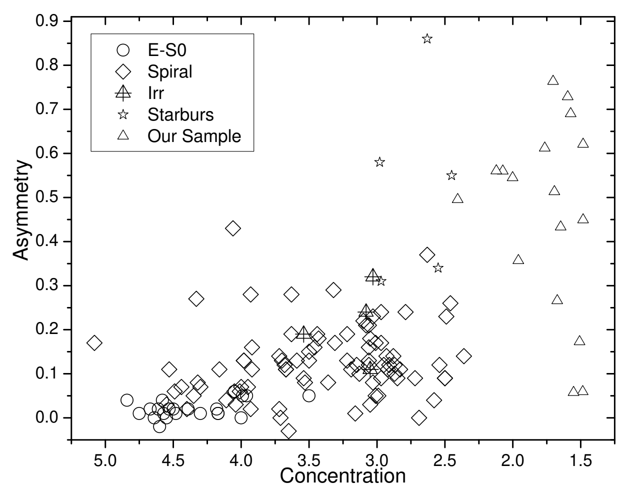

Fig. 3. This figure shows the C-A plane for the different morphological types of galaxies. Circles correspond to elliptical or spheroidal galaxies (E, S0), diamonds to spiral galaxies, cross triangles to irregular galaxies, five-pointed stars to starburst galaxies, and triangles to the objects in our sample. All the data not in our sample were taken from Conselice et al. (2003).

In Figure 4 we show the C-A plane again, but for dwarf galaxies only. Along with the data points of dE, dS, dI, and TDG, there are the regions of early, and late-type proposed by several authors (Bershady et al. 2000; Conselice et al. 2003), separated by a dotted line. One of the most striking aspects is that more than 90% of the dwarf galaxies have a concentration index lower than 3, including dE, but no specific value of A. This is contrary to what happens to large galaxies, where more than 75% of them have $C > 3$. Both dS and TDG are located in the late-type region, while dE are located at the bottom of the plane (early region), with very low A indexes and intermediate C values. Previous investigations proposed that the structure of dS can be explained by minor interactions (Vega-Acevedo & Hidalgo-Gámez 2014). This might explain the similarities in the C index between dS and TDG's (see Figure 4). The main caveat is the low number of dS galaxies analyzed so far. On the contrary, the dIrr galaxies are distributed at large C indexes (> 2.5) and from early to late-type, although almost 70% of the dI are in the late-type regions.

In this figure, it can be seen that TDGs have the same characteristics as other kinds of dwarf galaxies, but they are separated from both dI and dS. They have the smallest C indexes of all the dwarf galaxies, $1.5 < C < 2.5$, and can be localized in a region over the dashed line in Figure 4, which is given by:

$$\log{(A)} = 1.21C - 3.37. \tag{3}$$

No other dwarf galaxy is located to the right of this line except for one dS. Although more data on late-type dwarf galaxies are needed to reinforce this conclusion, this might indicate the TDGs to be morphologically different from the rest of the dwarf galaxies, with a different origin and evolution.

It is interesting to notice that there is no real difference in the position in the C-A plane between genuine TDG, candidate TDG, and the nlTDG objects.

4. DISCUSSION

Although the C parameter values are very similar for most of the galaxies in our sample of tidal dwarf galaxies, the asymmetry parameter is spread all over the whole range. The relationship between the asymmetry parameter and the star formation rate (Vega-Acevedo & Hidalgo-Gámez, in preparation) is well known, so we would like to study the influence of the SFR on the C-A plane, if any. We will also explore how the stellar mass might affect the position of the galaxies in this plane.

The star formation rate for the galaxies in our sample is listed in Table 2, Column 4, and it was determined from the UV flux from GALEX with the calibration proposed by Hunter, Elmegreen & Ludka (2010),

$$SFR\left[M_{\odot}\mathrm{yr}^{-1}\right] = 1.27\times10^{-28}L\left[\mathrm{erg\ s^{-1}Hz^{-1}}\right]. \tag{4}$$

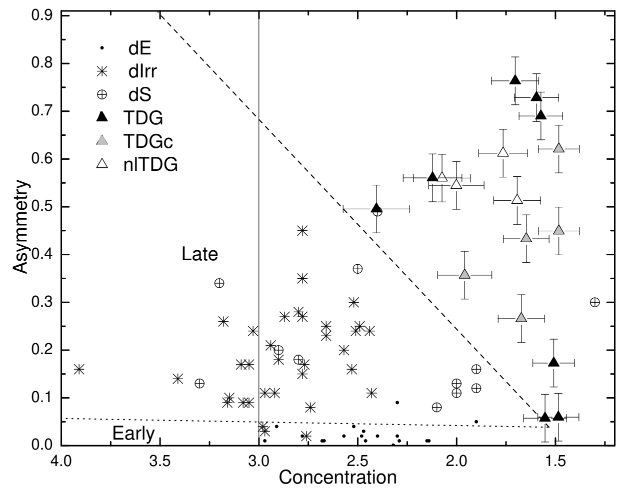

Fig. 4. Asymmetry vs concentration for dwarf galaxies only. This figure shows the C-A plane with different types of dwarf galaxies. Black dots correspond to dwarf elliptical galaxies (dE), stars to dwarf irregular galaxies (dIrr), crossed circles to dwarf spirals (dS), black triangles to tidal dwarf galaxies confirmed (TDG), grey triangles to tidal dwarf galaxies candidates (TDGc), and white triangles represent the non-likely tidal dwarf galaxies, (nlTDG). The dotted lines separate the early from the late galaxies, and the late from TDGs, while the vertical line represents the maximum value usual for dwarf galaxies. The data for dE and dIrr are from Conselice et al. (2003), while the data for dS are from Vega-Acevedo & Hidalgo-Gámez (2014).

The main caveat is the lack of an extinction correction, which could systematically overestimate the SFR. Although it is possible to use IR flux to correct the UV flux from extinction (Rosa-González, Terlevich & Terlevich 2002), the small resolution of the infrared images does not allow to obtain the precise IR fluxes of the tidal dwarf galaxies.

The stellar masses, listed in Table 2, Column 3, were determined with the calibrations by Bell et al. (2003). In particular, we used the following relation

$$\log\left[\frac{M_*}{L_g}\right] = a_g + b_g\,(g-r)\,, \tag{5}$$

where the stellar luminosity is given in solar units, and where $a_g = -0.499$ and $b_g = 1.519$ (Bell et al. 2003); and the (g-r) were obtained using the g and r images inside the r_{80}. From the values listed in Table 2, it is clear that most of the TDG's in our sample have stellar masses smaller than $2\times10^8 M_{\odot}$, with a median value of $2.4\times10^8\ M_{\odot}$, which is very similar to the one determined by Kaviraj et al. (2012) for a sample of 407 TDGc, of $1.9\times10^8\ M_{\odot}$.

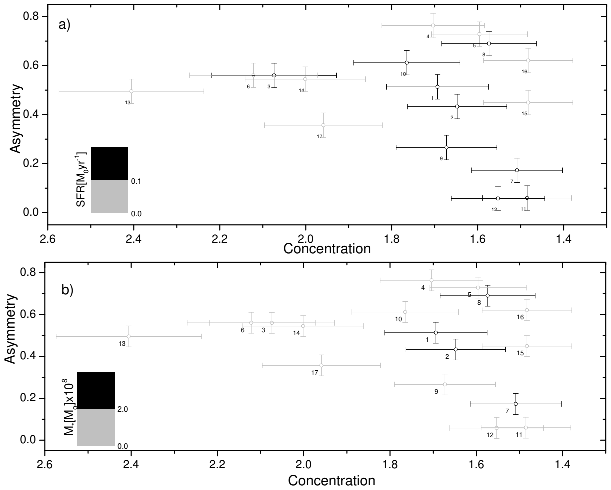

Fig. 5. C-A plane. In the top panel, the black points represent objects with SFR over $0.1M_{\odot}$ yr^{-1}, while the grey points represent objects with SFR lower than $0.1M_{\odot}$ yr^{-1}. In the bottom panel, the black points represent objects with stellar mass larger than $2 \times 10^8 M_{\odot}$, and the grey points represent those with stellar mass smaller $2 \times 10^8 M_{\odot}$.

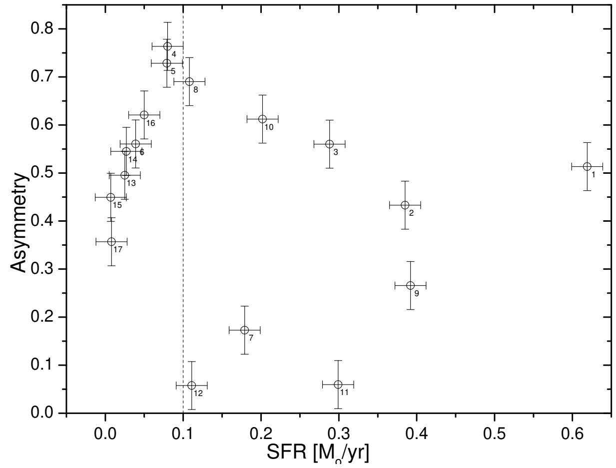

Fig. 6. Asymmetry vs the star formation rate. The vertical dash line represents the average value of star formation for dwarf galaxies.

Similarly, the SFR is very low ($< 0.1M_{\odot}$ yr^{-1}) for half of the sample with an average value of $0.17M_{\odot}$ yr^{-1}. These values are similar to the typical values in a sample of late-type galaxies (Magaña-Serrano et al. 2020), although it is very small compared to the SFR of interacting galaxies, which is of the order of 1-3.5$M_{\odot}$ yr^{-1} (Pearson et al. 2019).

We can explore again the C-A plane adding these two parameters. They are shown in Figure 5, where the different colors indicate different stellar masses in the top panel, and different SFRs in the bottom one. No clear differences can be seen; galaxies with large and small stellar mass are located at the same place in the C-A plane, although all the galaxies with high SFR but one (Arp 112) have C values smaller than 1.8.

In Vega-Acevedo (2013), as well as in other authors (Conselice et al. 2003; Mayya & Romano 2001), a relationship between the asymmetry parameter and the SFR was obtained for normal galaxies. We can see that the TDG in Figure 6 can be grouped into two categories: those with a SFR lower than $0.1M_{\odot}$ yr^{-1} seem to follow a linear correlation, while TDGs with a higher SFR do not show a clear correlation, only a dispersion diagram, with no particular value of the asymmetry. Moreover, there are no real differences between the candidates, the confirmed TDGs, and the nlTDG in the diagram, although three out of five of the latter are located at the high SFR locus. More data are needed to confirm the lack of trend for galaxies with high SFR. We must notice that the SFR determined in Vega-Acevedo & Hidalgo-Gámez (2014) used the H$_{\alpha}$ flux, which gives smaller values than the UV flux, so small differences are expected.

We can also check if there is any relationship between C and the stellar mass as proposed for normal galaxies (Conselice 2006a). Figure 7 shows that there is a logarithmic relationship,

$$C = ax^b, \tag{6}$$

where $a = 2.28 \pm 0.68$ and $b = -0.01 \pm 0.01$ (see solid line in Figure 7). Despite this possible correlation, it is clear that the TDG can be divided into two groups, with approximately 76% of the sample having a stellar-mass of less than $2 \times 10^8 M_{\odot}$.

In a recent study of galaxies in chaotic environments at high redshift (Cosmic Assembly Near-infrared Deep Extragalactic Legacy Survey, CANDELS) by Salmon et al. (2015), a linear correlation between the SFR and the stellar mass was found. Although CANDELS galaxies are early-type at z between 4 and 6, it is assumed that their gas is very turbulent. In such a way, they are very similar to TDGs, which are being formed in a very turbulent environment. Therefore, a similar correlation might be expected for the latter. As can be seen in Figure 8, there is a linear correlation

$$SFR\ (M_{\odot}\mathrm{yr}^{-1}) = \alpha\ M_*\ (M_{\odot}) + \beta, \tag{7}$$

where $\alpha = (5 \pm 1) \times 10^{-10}$ and $\beta = 0.02 \pm 0.01$. These values are very similar to those of CANDELS

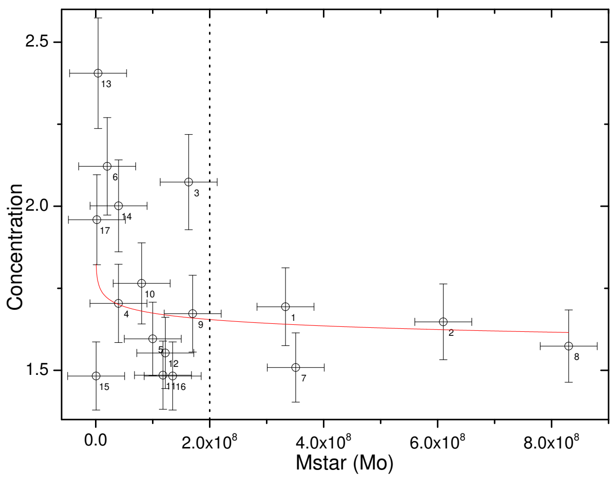

Fig. 7. Concentration vs stellar mass, M_{star}. The vertical dash line represents the average value of stellar mass for dwarf galaxies, while the solid line is a fit to the data-points. The color figure can be viewed online.

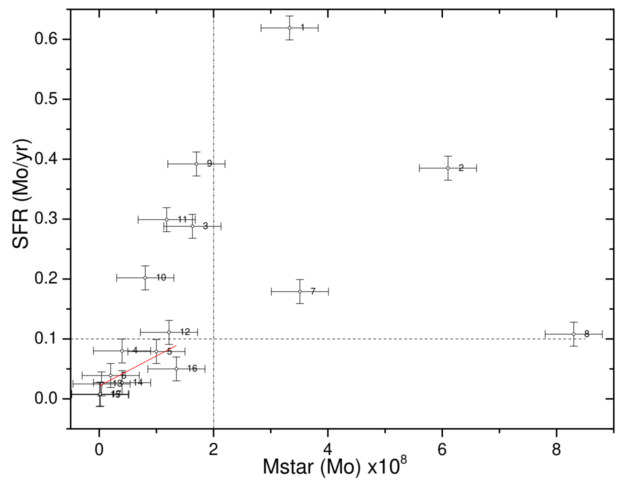

Fig. 8. Star formation rate, SFR vs stellar mass, M_{star}. The horizontal dash line represents the average value of star formation for dwarf galaxies, and the vertical dash line represents the average value of stellar mass for dwarf galaxies. The solid line is a fit to the data-points. The color figure can be viewed online.

galaxies for $z = 4$. It is very interesting to note that those galaxies with a stellar mass of less than $2M_{\odot}$ and a stellar formation of less than 0.1 $M_{\odot}\mathrm{yr}^{-1}$ are those reinforcing such relationship, while only two galaxies outside this "box" follow it. Galaxies with low M_* but high SFR seem to follow a linear correlation but with a different slope. More data are needed to understand the reason why these galaxies do not follow a single correlation between the SFR and the stellar mass.

5. CONCLUSIONS

In this investigation, we determined the C and A parameters for a sample of TDGs in order to know if they have similar values to the rest of the galaxies. In our sample, we included five tidal objects, which might not be TDGs, just to check if there are any differences between genuine, real TDGs and any other tidal object.

We noticed that the TDGs have the lowest C values than any other group of galaxies. This indicates that they are the loosest of the galaxies, which is quite expected if these objects are still in the assembling stage. Moreover, the exact value of the C parameters does not depend on the stellar mass or the SFR. Also, TDG are the galaxies with the largest values of the A parameter, except for starburst galaxies. This is quite expected because they are just assembling and the asymmetry might be larger.

With these values, it is clear that TDGs are located in a separated, well defined region in the C-A plane. No other galaxies, including dwarf galaxies, fall in this part of the plane. This might indicate that TDGs have a very different origin than the rest of the galaxies. Or, the other way around, dwarf galaxies (dE, dS, and dI) may not be formed from the debris of interacting systems. The main caveat is that there is no difference between the confirmed TDGs, the TDG candidates, and the non-likely TDG objects with very similar average values of both A and C for the three subsamples.

Contrary to what was obtained for large galaxies, there is no correlation between the A parameter and SFR, except for galaxies with SFR smaller than $0.1M_{\odot}$ yr^{-1}. Moreover, the relationship between C and stellar mass is exponential, but with a large dispersion.

On the other hand, we obtained a relationship between SFR and the stellar mass for the galaxies in our sample. This correlation is very similar to the one obtained for CANDELS galaxies, which are early-type galaxies at $z > 4$ with a turbulent environment. This is interesting because TDGs, as they are being formed during an interaction of galaxies, also have a very turbulent environment. This suggests that the environment and turbulence are crucial parameters for understanding galaxy formation. However, for a thorough conclusion on this subject, more TDGs are needed.

This research was supported by the Instituto Politécnico Nacional (México) under the research projects SIP-20210556, and SIP-20200822. This work is part of M. en C. I. Vega Acevedo's Ph.D. thesis, sponsored by CONACyT. This investigation has made use of the NASA/IPAC Extragalactic Database (NED), which is operated by the Jet Propulsion Laboratory, California Institute of Technology, under contract with the National Aeronautics and Space Administration (NASA). This work is based in part on observations made with the GALEX Space Telescope, which is operated by the Jet Propulsion Laboratory with the National Aeronautics and Space Administration (NASA). The SDSS-III web site is http://www.sdss3.org/. SDSS-III is managed by the Astrophysical Research Consortium for the Participating Institutions of the SDSS-III Collaboration including the University of Arizona, the Brazilian Participation Group, Brookhaven National Laboratory, Carnegie Mellon University, University of Florida, the French Participation Group, the German Participation Group, Harvard University, the Instituto de Astrofisica de Canarias, the Michigan State/Notre Dame/JINA Participation Group, Johns Hopkins University, Lawrence Berkeley National Laboratory, Max Planck Institute for Astrophysics, Max Planck Institute for Extraterrestrial Physics, New Mexico State University, New York University, Ohio State University, Pennsylvania State University, University of Portsmouth, Princeton University, the Spanish Participation Group, University of Tokyo, University of Utah, Vanderbilt University, University of Virginia, University of Washington, and Yale University. The authors wish to thank Mr. P. Gómez-Garcés and Lic. A. Romo-González for a careful revision of the English grammar.

REFERENCES

Bell, E. F., McIntosh, D. H., Katz, N., & Weinberg, M. D. 2003, ApJS, 149, 289, https://doi.org/10.1086/378847

Bershady, M. A., Jangren, A., & Conselice, C. J. 2000, AJ, 119, 2645, https://doi.org/10.1086/301386

Bianchi, L., Shiao, B., & Thilker, D. 2017, ApJS, 230, 24, https://doi.org/10.3847/1538-4365/aa7053

Blanton, M. R., Bershady, M. A., Abolfathi, B., et al. 2017, AJ, 154, 28, https://doi.org/10.3847/1538-3881/aa7567

Bournaud, F., Duc, P.-A., Amram, P., Combes, F., & Gach, J.-L. 2004, A&A, 425, 813, https://doi.org/10.1051/0004-6361:20040394

Brinks, E., Duc, P.-A., Springel, V., et al. 2001, ApSSS, 277, 405, https://doi.org/10.1023/A:1012719910476

Conselice, C. J. 2003, ApJS, 147, 1, https://doi.org/10.1086/375001

________. 2006, MNRAS, 373, 1389, https://doi.org/10.1111/j.1365-2966.2006.11114.x

Conselice, C. J., Bershady, M. A., & Gallagher, J. S. III. 2000, A&A, 354, 21, https://arxiv.org/abs/astro-ph/0001195v1

Conselice, C. J., Bershady, M. A., & Jangren, A. 2000, ApJ, 529, 886, https://doi.org/10.1086/308300

Conselice, C. J., Bershady, M. A., Dickinson, M., & Papovich, C. 2003, AJ, 126, 1183, https://doi.org/10.1086/377318

Conselice, C. J., Gallagher, J. S. III, Calzetti, D., Homeier, N., & Kinney, A. 2000, AJ, 119, 79, https://doi.org/10.1086/301174

Conselice, C. J., Gallagher, J. S. III, & Wyse, R. F. G. 2002, AJ, 123, 2246, https://doi.org/10.1086/340081

Conselice, C. J., Rajgor, S., & Myers, R. 2008, MNRAS, 386, 909, https://doi.org/10.1111/j.1365-2966.2008.13069.x

Doi, M., Tanaka, M., Fukugita, M., et al. 2010, AJ, 139, 1628, https://doi.org/10.1088/0004-6256/139/4/1628

Duc, P.-A., Brinks, E., Wink, J. E., & Mirabel, I. F. 1997, A&A, 326, 537

Duc, P.-A., Brinks, E., Springel, V., et al. 2000, AJ, 120, 1238, https://doi.org/10.1086/301516

Duc, P.-A. & Mirabel, I. F. 1994, A&A, 289, 83

Duc, P.-A. & Mirabel, I. F. 1999, IAUS 186, Galaxy Interactions at Low and High Redshift, ed. J. E. Barnes & D. B. Sanders, 61

Fu, Z., Sengupta, C., Sethuram, R., et al. 2020, arXiv: 2011.06368v1, https://doi.org/10.1088/1674-4527/21/2/43

Gordon, S., Koribalski, B., & Jones, K. 2001, MNRAS, 326, 578, https://doi.org/10.1046/j.1365-8711.2001.04588.x

Hancock, M., Smith, B. J., Struck, C., Giroux, M. L., & Hurlock S. 2009, AJ, 137, 4643, https://doi.org/10.1088/0004-6256/137/6/4643

Hibbard, J. E., Bianchi, L., Thilker, D. A., et al. 2005, ApJL, 619, 87, https://doi.org/10.1086/423244

Hibbard, J. E., van der Hulst, J. M., Barnes, J. E., & Rich, R. M. 2001, AJ, 122, 2969, https://doi.org/10.1086/324102

Huertas-Company, M., Rouan, D., Tasca, L., Soucail, G., & Le Fèvre, O. 2008, A&A, 478, 971, https://doi.org/10.1051/0004-6361:20078625

Hunter, D. A., Elmegreen, B. G., & Ludka, B. C. 2010, AJ, 139, 447, https://doi.org/10.1088/0004-6256/139/2/447

Kaviraj, S., Darg, D., Lintott, C., Schawinski, K., & Silk, J. 2012, MNRAS, 419, 70, https://doi.org/10.1111/j.1365-2966.2011.19673.x

Kennicutt, R. C. Jr. 1998, ARA&A, 36, 189, https://doi.org/10.1146/annurev.astro.36.1.189

Lauger, S., Burgarella, D., & Buat, V. 2005, A&A, 434, 77, https://doi.org/10.1051/0004-6361:200400138

Lelli, F., Duc, P.-A., Brinks, E., et al., 2015, A&A, 584, 113, https://doi.org/10.1051/0004-6361/201526613
Lisenfeld, U., Braine, J., Duc, P.-A., et al. 2001, Dwarf Galaxies and their Environment, ed. K. S. de Boer, R. J. Dettmar, & U. Klein (Shaker Verlag), 273, https://astro.uni-bonn.de/~deboer/webgk/dgeconf/dgeproc/dge273.ps.gz
Madau, P., Pozzetti, L., & Dickinson, M. 1998, ApJ, 498, 106, https://doi.org/10.1086/305523
Magaña-Serrano, M. A., Hidalgo-Gámez, A. M., Vega-Acevedo, I., & Castañeda, H. O. 2020, RMxAA, 56, 39, https://doi.org/10.22201/ia.01851101p.2020.56.01.06
Mirabel, I. F., Dottori, H., & Lutz, D. 1992, A&A, 256, 19
Mayya, Y. D. & Romano R. 2001, RMxAC, 11, 115
Menanteau, F., Ford, H. C., Motta, V., et al. 2006, AJ, 131, 208, https://doi.org/10.1086/498344
Meurer, G. R., Wong, O. I., Kim, J. H., et al. 2009, ApJ, 695, 765, https://doi.org/10.1088/0004-637X/695/1/765
Muñoz-Elgueta, N., Torres-Flores, S., Amram, P., et al. 2018, MNRAS, 480, 3257, https://doi.org/10.1093/mnras/sty1934
Neichel, B., Hammer, F., Puech, M., et al. 2008, A&A, 484, 159, https://doi.org/10.1051/0004-6361:20079226
Pearson, W. J., Wang, L., Alpaslan, M., et al. 2019, A&A, 631, 51, https://doi.org/10.1051/0004-6361/201936337
Rosa-González, D., Terlevich, E., & Terlevich, R. 2002, MNRAS, 332, 283, https://doi.org/10.1046/j.1365-8711.2002.05285.x
Sabbi, E., Gallagher, J. S., Smith, L. J., de Mello, D. F., & Mountain, M. 2008, ApJ, 676, 113, https://doi.org/10.1086/587548
Salmon, B., Papovich, C., Finkelstein, S. L., et al. 2015, ApJ, 799, 183, https://doi.org/10.1088/0004-637X/799/2/183
Salpeter, E. E. 1955, ApJ, 121, 161
Schweizer, F. 1978, IAUS 77, Structure and Properties of Nearby Galaxies, ed. E. M. Berkhuijsen & R. Wielebinski (Dordrecht, Reidel Publishing), 279
Scott, T. C., Lagos, P., Ramya, S., et al. 2018, MNRAS, 475, 1148, https://doi.org/10.1093/mnras/stx3248
Schechtman-Rook, A. & Hess, K. M. 2012, ApJ, 750, 171, https://doi.org/10.1088/0004-637X/750/2/171
Sengupta, C., Dwarakanath, K. S., Saikia, D. J., & Scott, T. C. 2013, MNRAS, 431, 1, https://doi.org/10.1093/mnrasl/sls039
Sengupta, C., Scott, T. C., Dwarakanath, K. S., Saikia, D. J. & Sohn, B. W. 2014, MNRAS, 444, 558, https://doi.org/10.1093/mnras/stu1463
Sengupta, C., Scott, T. C., Paudel, S., et al. 2017, MNRAS, 469, 3629, https://doi.org/10.1093/mnras/stx885
Smith, B. J., Giroux, M. L., Struck, C., & Hancock, M. 2010, AJ, 139, 1212, https://doi.org/10.1088/0004-6256/139/3/1212
Vega-Acevedo, I. & Hidalgo-Gámez, A. M. 2014, ASPC 480, Structure and Dynamics of Disk Galaxies, ed. M. S. Seigar & P. Treuthardt (Arkansas, AK: ASP), 239
Vega-Acevedo, I., 2013, Estudio del parámetro de asimetría en galaxias espirales enanas, Master Thesis, Escuela Superior de Física y Matemáticas, Instituto Politécnico Nacional, Mexico City
Yagi, M., Nakamura, Y., Doi, M., Shimasaku, K., & Okamura, S. 2006, MNRAS, 368, 211, https://doi.org/10.1111/j.1365-2966.2006.10144.x
Zasov, A. V., Saburova, A. S., Egorov, O. V., & Uklein, R. I. 2017, MNRAS, 469, 4370, https://doi.org/10.1093/mnras/stx1158

A. M. Hidalgo-Gámez: Departamento de Física, Escuela Superior de Física y Matemáticas, Instituto Politénico Nacional, U. P. Adolfo López Mateos, C. P. 07738, Ciudad de México, Mexico (amhidalgog@ipn.mx).
I. Vega-Acevedo: Escuela Superior de Ingeniereía Mecánica y Eléctrica, Instituto Politénico Nacional, U. P. Adolfo López Mateos, C. P. 07738, Ciudad de México, Mexico (ivegaa@ipn.mx).

Revista Mexicana de Astronomía y Astrofísica, **58**, 73–82 (2022)

https://doi.org/10.22201/ia.01851101p.2022.58.01.06

FIRST LIGHT CURVE ANALYSIS OF THE MODERATE FILL-OUT CONTACT BINARY SYSTEMS TYC 2402-643-1, TYC 2703-1235-1 AND TYC 2913-2145-1

Carlo Barani[1], Francesco Acerbi[2], and Velimir Popov[3]

Received April 25 2021; accepted November 23 2021

ABSTRACT

We present the results of our study of the W Ursae Majoris eclipsing binary systems (EW) TYC 2402-643-1, TYC 2703-1235-1 and TYC 2913-2145-1 based on CCD observations obtained using Sloan *g'* and *i'* filters. The light curves were analysed using the latest version of the Wilson-Devinney code, and the obtained data were used to estimate the physical parameters of the systems. TYC 2402-643-1 and TYC 2913-2145-1, having mass ratio < 0.25, can be classified as Extreme Mass Ratio Binary (EMRBs) systems and belong to the A-subtype class of the EW. The third one, TYC 2703-1235-1, having mass ratio q about 3 ($1/q = 0.33$) belongs to W-subtype class of the EW. The absolute dimensions of the primaries and secondaries were estimated and investigated using different evolutionary diagrams.The parameters of the progenitors of the components of the systems were calculated and the results are consistent with the determination of the subtypes.

RESUMEN

Presentamos los resultados de nuestro estudio de tres binarias eclipsantes de tipo W Ursae Majoris: TYC 2402-643-1, TYC 2703-1235-1 y TYC 2913-2145-1, basado en observaciones CCD con los filtros Sloan *g'* e *i'*. Se analizaron las curvas de luz con la última versión del código Wilson-Devinney, y con los datos obtenidos se estimaron los parámetros físicos de los sistemas. TYC 2402-643-1 y TYC 2913-2145-1, con un cociente de masas de < 0.25, pueden ser clasificadas como binarias con cociente de masas extremo (EMRBs) y pertenecen al subtipo A de las EW. TYC 2703-1235-1, con un cociente de masas q de aproximadamente 3 ($1/q = 0.33$) pertenece al subtipo W de las EW. Se investigaron las dimensiones absolutas de las primarias y de las secundarias con distintos diagramas evolutivos. Se calcularon los parámetros de las progenitoras de las componentes de los sistemas. Los resultados concuerdan con las determinaciones de los subtipos.

Key Words: binaries: eclipsing — stars: fundamental parameters — stars: individual: TYC 2402-643-1, TYC 2703-1235-1, TYC 2913-2145-1

1. INTRODUCTION

The eclipsing binary star TYC 2402-643-1 (NSVS 6868895 = GSC 02402-00643 = UCAC4 635-024089) was proposed as a variable star in the list provided by Gettel et al. (2006) which suggested a period of variability of 0.399579 days.

Based on the four values of the new times of minima (ToM's), listed in Table 1, we propose the new ephemeris as:

$$\mathrm{HJD(MinI)} = 2458865.3253(5) + 0.3992342(2) \times \mathrm{E}. \quad (1)$$

TYC 2703-1235-1 (NSVS 8702136 = GSC 02703-01235 = UCAC4 604-123844) was found to be a variable star by Woźniak et al. (2004) from the Northern Sky Variability Survey.

The first period was indicated by J. S. Shaw and collaborators in their online list (https://www.

[1]Via Molinetto 35, 26845 Triulza di Codogno (LO), Italy.
[2]Via Zoncada 51, 26845 Codogno (LO), Italy.
[3]Department of Physics and Astronomy, Shumen University, Shumen, Bulgaria.

TABLE 1

CCD TIMES OF MINIMA FOR TYC 2402-643-1

HJD	$Epoch_{(1)}$	$O-C_{(1)}$	Error	Source
2458865.3249	0.0	0.0001	0.0021	This paper
2458865.5256	0.5	0.0010	0.0029	This paper
2458866.3232	2.5	-0.0006	0.0028	This paper
2458866.5232	3.0	-0.0004	0.0025	This paper

physast.uga.edu/~jss/nsvs/) as $P = 0.393128$ days and the type of variability was suggested as the W UMa system. Using two ToM's as obtained from literature Hoňkova et al. (2013) and three ToM's as observed by us (Table 2) we can propose a new ephemeris as follows:

$$\text{HJD (MinI)} = 2459088.4634(9) + 0.3931349(3) \times \text{E}. \quad (2)$$

TYC 2913-2145-1 also identified STARE aur0 1201 = GSC 02913-02145 = UCAC4 654-032034, was suggested as a variable, with a period of 0.54634 days, during the observations of the STellar Astrophysics and Research on Exoplanets (STARE) operating in the Canary Islands, Spain (http://www.hao.ucar.edu/research/stare/lc_database.html). The proposed variability was EB type.

During our observations we obtained two ToM's (Table 3) and the new ephemeris:

$$\text{HJD (MinI)} = 2458870.4821(3) + 0.5460860(2) \times \text{E}. \quad (3)$$

2. OBSERVATIONS AND DATA REDUCTION

The preliminary available information about the targets was taken from the AAVSO Variable Star Index database (VSX) and is presented in Table 4.

To investigate the absolute parameters, the eclipsing binary stars TYC 2402-643-1, TYC 2703-1235-1 and TYC 2913-2145-1 have been observed in 2020 with the 30-cm Ritchey Chretien Astrograph located into the *IRIDA South* dome of the NAO Rozhen - Bulgaria.

The astrograph was equipped with a focal reducer to work at f/5 and a CCD camera ATIK 4000M (2048 × 2048 pixels, 7.4 μm/pixel, pixel-scale of the optical system of 1.04 arcsec/pixel and a field of view of 35 × 35 arcmin).

The photometric observations were carried out with Sloan type filters in the *g', i'* bands and the log of CCD photometric observations is presented in Table 5.

TABLE 2

CCD TIMES OF MINIMA FOR TYC 2703-1235-1

HJD	$Epoch_{(2)}$	$O-C_{(2)}$	Error	Source
2455799.4988	-8366.0	0.0020	0.0005	OEJV 160
2455800.4776	-8363.5	-0.0020	0.0010	OEJV 160
2459088.4634	0.0	0.0000	0.0034	This paper
2459089.4463	2.5	0.0001	0.0009	This paper
2459090.4289	5.0	-0.0001	0.0012	This paper

TABLE 3

CCD TIMES OF MINIMA FOR TYC 2913-2145-1

HJD	$Epoch_{(3)}$	$O-C_{(3)}$	Error	Source
2458867.4786	-5.5	0.0000	0.0052	This paper
2458870.4821	0.0	0.0000	0.0036	This paper

The standard sequence (de-biasing, dark frame subtraction and flat-fielding) was applied for photometric data reduction by the software AIP4WIN2.0 Berry & Burnell (2006). The aperture ensemble photometry was carried out with the automatic photometry tool LesvePhotometry[4] de Ponthire (2010).

The color transformation was applied along with the previously estimated transformation coefficients of the optical system. To obtain the magnitudes in the respective color bands for the comparison and check stars we used the catalogue APASS DR9 Henden et al. (2015) (Table 6).

3. PHOTOMETRIC SOLUTIONS WITH THE W-D METHOD

No published photometric solutions have been found for all three systems. The latest version of the Wison-Devinney code, (Wilson & Devinney 1971, Wilson 1990, Wilson & van Hamme 2015) was used to perform a simultaneous analysis of the available light curves. The effective temperatures determined in different ways are shown in Table 7 where T_{g-i} is determined by the measured index $(g' - i')$ at quadrature while T^{der}_{g-i} is determined after dereddening, both by means of the relations from Covey et al. (2007); T_G is the Gaia DR2 temperature from Gaia Collaboration (Brown et al. 2018); T^{der}_{J-K} is determined by the 2MASS index $(J-K)$ from Skrutskie et al. (2006) while T^{der}_{B-V} is determined by the APASS DR10 index $(B - V)$, both after dereddening and by means of the relations from Pecaut & Mamajek (2013); T_{Lamost} are taken from the LAMOST DR5

[4]www.dppobservatory.net.

TABLE 4

PARAMETERS OF THE TARGETS FROM THE VSX DATABASE

Target	RA(2000)	Dec(2000)	Period, d	Mag.	Ampl.	Reference
TYC 2402-643-1	05:18:58.08	+36:58:05.96	0.399579	11.373(R1)	0.442	Gettel et al. (2006)
TYC 2703-1235-1	21:21:40.47	+30:36:07.02	0.393128	11.94(R1)	0.75	Hoffman et al. (2009)
TYC 2913-2145-1	05:21:42.98	+40:41:00.71	0.54634	10.61(R)	0.40	Brown & Charbonneau (2000)

TABLE 5

LOG OF PHOTOMETRIC OBSERVATIONS

Target	UT Date [yyyymmdd]	Exposures (g', i') [s]	Number (g', i')	Mean error (g', i') [mag]
TYC 2402-643-1	2020 Jan 16	30, 90	237, 237	0.011, 0.009
	2020 Jan 17	30, 90	204, 204	0.009, 0.008
TYC 2703-1235-1	2020 Aug 26	60, 90	106, 106	0.008, 0.009
	2020 Aug 27	60, 90	167, 167	0.004, 0.005
	2020 Aug 28	60, 90	86, 86	0.004, 0.005
TYC 2913-2145-1	2020 Jan 18	30, 90	240, 240	0.007, 0.006
	2020 Jan 20	30, 90	98, 98	0.009, 0.009
	2020 Jan 21	30, 90	223, 223	0.006, 0.006
	2020 Jan 23	30, 90	113, 113	0.006, 0.007

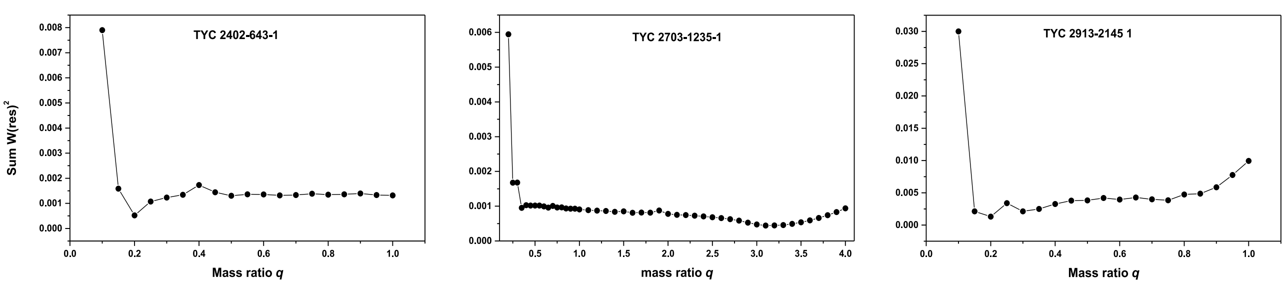

Fig. 1. The relation $\Sigma(res)^2$ versus mass ratio q in Mode 3 for the three systems in the WD code.

catalog (Luo et al. 2019). The last column indicates the mean effective temperatures of the targets T_m, adopted here for the procedures of the light curves solutions.

The shape of the light curves of these systems is similar to the most frequent light curve shapes of the W UMa type binary stars, so the classical Mode 3 (overcontact configuration) of the W-D code was used.

The q-search procedure was used, leaving as free parameters the temperature of the secondary components T_2, the inclination i of the systems, the non-dimensional surface potentials ($\Omega_{1=2}$) and the monochromatic luminosities of the primary components L_1. Other parameters such as g_2, A_2, L_2, x_2 and y_2 are not free but fixed to their theoretical values.

As soon as the $\Sigma(res)^2$ showed a minimum value we also added the value of the mass-ratio q to the set of the free parameters and ran a new W-D working session that only stopped when the corrections to the parameters became smaller than their probable errors (Figure 1).

The mass-ratio converged to a value of $q = 0.210$ for TYC 2402-643-1, $q = 3.05$ ($1/q = 0.327$) for TYC 2703-1235-1 and $q = 0.193$ for TYC 2913-2145-1 in the final solution. The value of the mass ratios for the first and the third systems corresponds to a transit at the primary minima inherent to the A-subtype contact binaries, while for

TABLE 6

MAGNITUDES OF THE COMPARISON AND CHECK STARS

Label	Star ID	RA(2000)	Dec(2000)	g'	i'
Target	TYC 2402-643-1	05 18 58.10	+36 58 05.2	11.349	10.797
Chk	UCAC4 636-024573	05 19 01.87	37 02 53.48	12.973	11.620
C1	UCAC4 636-024658	05 19 21.61	37 02 27.18	13.639	12.624
C2	UCAC4 636-024637	05 19 15.80	37 01 23.13	13.006	12.393
C3	UCAC4 635-024132	05 19 08.76	36 58 06.84	12.222	11.689
C4	UCAC4 636-024521	05 18 48.57	37 05 08.70	12.560	11.966
C5	UCAC4 636-024485	05 18 39.27	37 06 07.67	11.680	11.514
C6	UCAC4 635-024236	05 19 35.14	36 50 25.01	11.455	10.924
Target	TYC 2703-1235-1	21 21 40.52	+30 36 08.1	11.745	11.043
Chk	UCAC4 604-123798	21 21 23.20	30 36 01.70	12.897	11.945
C1	UCAC4 604-123970	21 22 24.04	30 45 07.66	12.889	11.076
C2	UCAC4 604-123988	21 22 28.49	30 42 26.83	13.124	12.607
C3	UCAC4 604-123848	21 21 41.68	30 39 27.15	12.409	12.245
C4	UCAC4 604-123814	21 21 28.51	30 41 03.43	11.854	10.543
C5	UCAC4 603-128892	21 21 45.45	30 33 40.65	12.735	12.606
C6	UCAC4 604-123956	21 22 19.14	30 36 55.52	12.170	10.988
C7	UCAC4 604-123756	21 21 04.98	30 37 11.64	12.252	12.052
Target	TYC 2913-2145-1	05 21 42.90	+40 40 58.0	10.972	10.580
Chk	UCAC4 654-031899	05 20 56.36	40 38 49.86	12.606	11.747
C1	UCAC4 654-032144	05 22 23.34	40 41 51.84	12.089	11.489
C2	UCAC4 654-031940	05 21 10.50	40 47 17.45	12.483	11.898
C3	UCAC4 654-032070	05 21 54.82	40 42 32.33	12.351	11.873
C4	UCAC4 653-032388	05 21 46.72	40 32 29.57	11.919	11.528
C5	UCAC4 655-033047	05 21 32.40	40 48 41.47	10.969	11.063
C6	UCAC4 654-032142	05 22 22.81	40 47 31.99	10.229	10.138

TABLE 7

TARGET TEMPERATURES

Target	T_{g-i}	T_G	T_{Lamost}	T_m
TYC 2402-643-1	5899	6429	6511	6280
Target	T^{der}_{g-i}	T^{der}_{J-K}	T^{der}_{B-V}	T_m
TYC 2703-1235-1	6180	5884	5736	5930
Target	T_{g-i}	T_G	T^{der}_{J-K}	T_m
TYC 2913-2145-1	6254	6694	6530	6470

TYC 2703-1235-1 the value corresponds to an occultation at primary minima, a typical W-subtype contact binary in the Binnendijk (1965) classification.

The light curve of TYC 2703-1235-1 shows asymmetries between the two maxima with Max II higher than Max I by 0.02 mag in the *g'* filter, the well known inverse O'Connell effect (O'Connell 1951), while in the *i'* filter this effect is not detectable. To justify this asymmetry, a small 25° hot spot has been placed on the surface of the primary component of the system.

The fact that the presence of a hot spot tends to be less noticeable at longer wavelengths is already known and it is an indication of a wavelength-dependent hot spot activity, probably due to an impact from a mass transfer between the components.

It is well known that in the Wilson-Devinney program the errors of the adjustable parameters are unrealistically small. The problem of unrealistically small errors is not intrinsic to the WD method nor related only to parameter correlations. In fact the WD code provides the "probable" errors, which are derived by the differential correction routine and are related to the standard errors of the linearized least-squares algorithm, and the errors can be used as a measure of the uncertainties only for normal distributions of the photometric errors.

Many strategies are possible to obtain an independent estimate of the uncertainties in a light curve analysis. One of these is to approach the problem

TABLE 8

VALUES OF THE FITTED PARAMETERS

Target	q	i [°]	$\Omega_{1,2}$	T_1 [K]	T_2 [K]	θ [°]	φ [°]	γ [°]	Ts/T$_*$
TYC 2402-643-1	0.210(6)	86.79(43)	2.2216(12)	6280(fxd)	6088(43)	-	-	-	-
TYC 2703-1235-1	3.054(30)	81.77(44)	6.5507(29)	5930(fxd)	5725(86)	91.2(9)	20.7(1.1)	25.1(7)	1.05(2)
TYC 2913-2145-1	0.194(5)	88.61(58)	2.1870(23)	6470(fxd)	5740(86)	-	-	-	-

TABLE 9

CALCULATED PARAMETERS

Target	r_1	r_2	f	l_1	l_2	$\Sigma(res)^2$
TYC 2402-643-1	0.530(10)	0.266(2)	0.273	0.798(23)	0.177(3)	0.000469
TYC 2703-1235-1	0.299(2)	0.491(2)	0.238	0.286(34)	0.665(5)	0.000455
TYC 2913-2145-1	0.535(2)	0.258(2)	0.221	0.861(23)	0.122(1)	0.001232

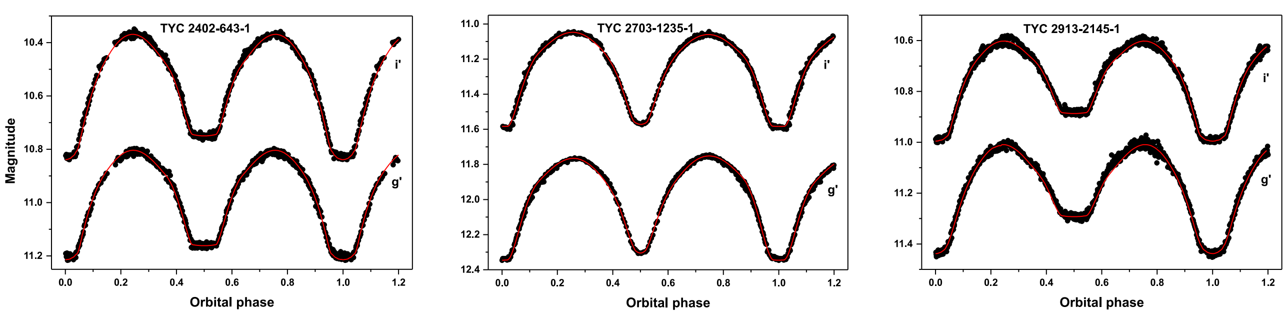

Fig. 2. CCD light curves of the systems. The points are the original CCD observations and the full lines are the theoretical fits with the surface spot contribution. The color figure can be viewed online.

through the bootstrap technique (Efron & Tibshirani 1986, Esmer et al. 2021), that allows to estimate parameter confidence levels of least squares solutions.

For this purpose we have generated many different data samples of free parameters(i, $\Omega_{1,2}$, T_2, l_1 and q) by random resampling with repetitions (bootstrapping), performing the minimization procedure for each sample and deriving confidence intervals from the resulting distribution of parameters.

The full set of parameters from our solutions is listed in Tables 8 and 9. The results of our modeling and the obtained fitted curves are shown in Figure 2, while graphic representations of the three systems are shown in Figure 3, using the Binary Maker 3.0 software (Bradstreet & Steelman 2002).

4. ESTIMATE OF THE ABSOLUTE RELATIVE ELEMENTS

Since no spectroscopic measurements of the orbital elements are available at present, the absolute parameters of the systems cannot be determined directly. Therefore, these results should be considered "relative" rather than "absolute" parameters and regarded as preliminary. The low galactic latitude of the systems implies that interstellar reddening E(B-V) may be large. Therefore, we have preferred to use a statistical method for the estimation of the absolute elements instead of a method based on the Gaia distance.

The empirically three-dimensional correlations from Gazeas (2009) $M(P,q)$, $R(P,q)$, given below,

$$\log M_1 = 0.725(59)\log P - 0.076(32)\log q + 0.365(32),$$

$$\log M_2 = 0.725(59)\log P + 0.924(33)\log q + 0.365(32),$$

$$\log R_1 = 0.930(27)\log P - 0.141(14)\log q + 0.434(14),$$

$$\log R_2 = 0.930(29)\log P + 0.287(15)\log q + 0.434(16),$$

and the Stefan-Boltzmann law

$$L_{1,2} = R_{1,2}^2 * (T_{1,2}/T_\odot)^4,$$

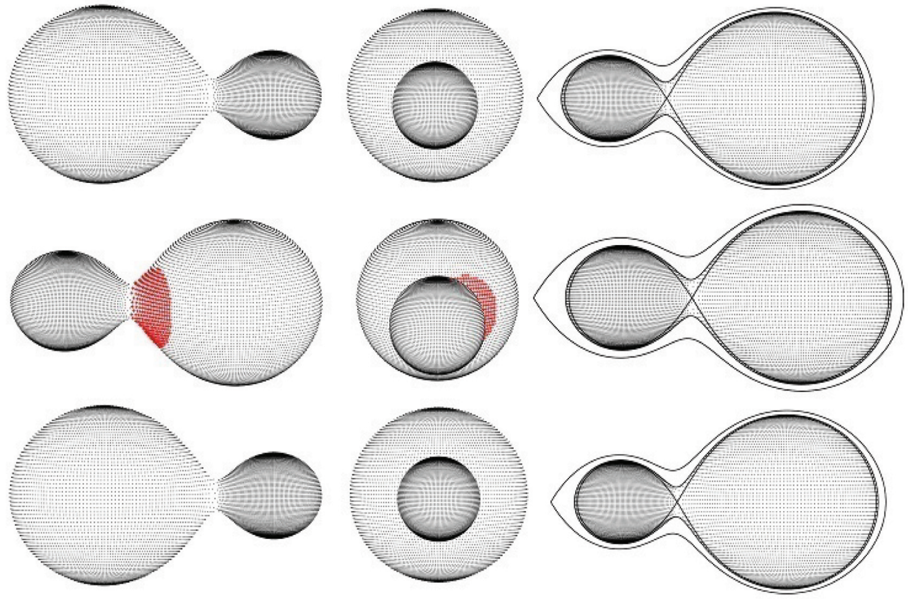

Fig. 3. Graphic representation of TYC 2402-643-1 (top), TYC 2703-1235-1 (middle) and TYC 2913-2145-1 (bottom) according to our solution, at quadrature (left) and at the primary minimum (center). Right: the configuration of the components of the systems in the orbital plane is shown. The color figure can be viewed online.

TABLE 10

RELATIVE PARAMETERS

Target	L_1 $[L_\odot]$	L_2 $[L_\odot]$	R_1 $[R_\odot]$	R_2 $[R_\odot]$	a $[R_\odot]$	M_1 $[M_\odot]$	M_2 $[M_\odot]$	Sp.type
TYC 2402-643-1	2.91(76)	0.68(20)	1.44(7)	0.74(5)	2.68(12)	1.34(17)	0.28(4)	F7V+F9V
TYC 2703-1235-1	0.66(20)	1.99(52)	0.83(6)	1.33(7)	2.70(12)	0.42(6)	1.28(17)	G0V+G3V
TYC 2913-2145-1	6.00(1.6)	0.91(28)	1.95(10)	0.97(7)	3.55(16)	1.69(22)	0.33(5)	F5V+G3V

Note: Spectral types are according to Pecaut & Mamajek (2013).

allowed us to have a preliminary estimate of the relative parameters of the systems under study. It is important to note that the empirical law does not give the full solution but an approximation of their physical parameters, as the single quantities are affected by errors of 13% and 14% for M_1 and M_2, 5% and 7% for R_1 and R_2.

In the article by Gazeas (2009) it is stated that the empirical laws relating to the 3D domain are affected by an error of less than 5%. In order to verify whether this statement is a under or overestimated value, we have applied the above relations to the catalog of contact binaries reported in the article by Gazeas & Stępień (2008) thus calculating masses, radii and luminosity of all systems. Comparing the difference between the calculated parameters and those reported in the catalog, we found that the RMS of the residuals is much higher than 5%. This procedure has therefore allowed us to obtain more realistic values of the uncertainties of the estimated values of the absolute elements reported in Table 10.

We used the estimated relative elements of the systems as reported in Table 10 to investigate the evolutionary states of our targets by comparing the location of their components on the main sequence (MS) diagrams expressed as $\log T$-$\log L$, $\log M$-$\log L$, $\log M$-$\log R$, and $\log M$-$\log T$. We built the isochrone tracks for the zero age main sequence (ZAMS) and the terminal age main sequence (TAMS) according to the PARSEC models (Bressan et al. 2012), as shown in Figure 4. As the PARSEC models extend up to 30 Gyr we limited the TAMS evolutionary tracks to stars with masses larger than $0.7M_\odot$.

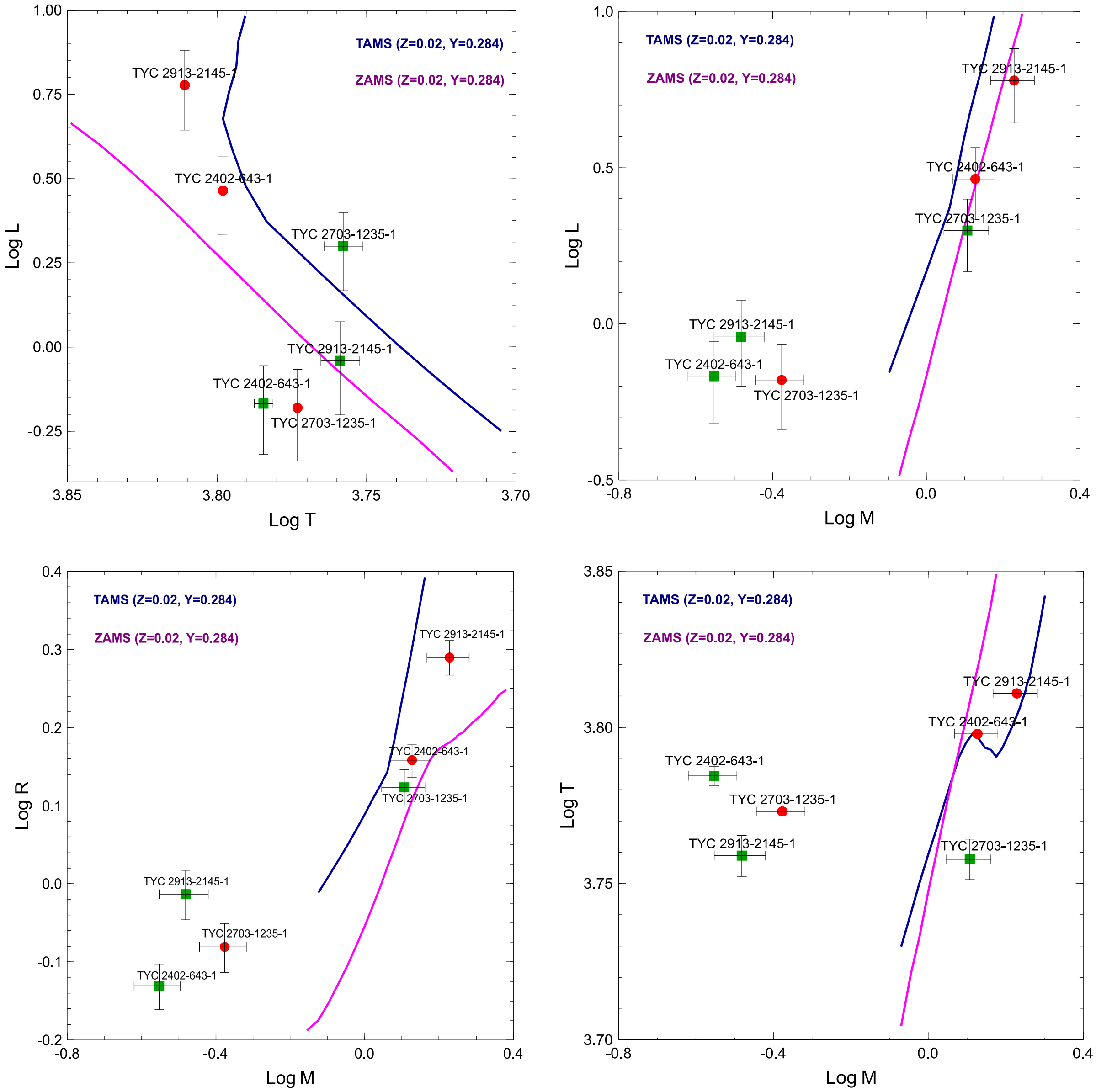

Fig. 4. Properties of our targets shown against evolutionary tracks of $\log T - \log L$, $\log M - \log L$, $\log M - \log R$, and $\log M - \log T$ (Bressan et al. 2012). The primaries are marked with red circles and the secondaries with green squares. The color figure can be viewed online.

The correlations between the absolute parameters of our targets (W UMa stars) differ from the correlations between the parameters of the stars belonging to MS. The evolutionary states of the binary components of our targets are similar. The more massive components are near the ZAMS, meaning that they are little evolved stars, while the less massive components are located above the TAMS, implying that they have evolved away from the main sequence. These results are due to the mass and energy exchange between the binary components and their internal evolutionary transformations.

The three targets do not differ from the general cases of the EW type stars, where the less massive components of the binary systems have a luminosity larger than that of a main sequence star with the same mass and radius, (Yakut & Eggleton 2005, Yildiz & Doğan 2013). For the W subtype this phenomenon can be due to the energy transfer from the primary to the secondary star that changes the sec-

TABLE 11

PARAMETERS OF THE PROGENITORS OF THE SYSTEMS

Target	Subtype	M_{1i} [$M_\odot$]	M_{2i} [$M_\odot$]	a_{fof} [$R_\odot$]	P_{fof} [Days]
TYC 2402-643-1	A	0.82	1.84	5.43	0.8996
TYC 2703-1235-1	W	2.18	0.39	5.39	0.8569
TYC 2913-2145-1	A	1.16	1.92	5.94	0.9575

ondary and makes it over-sized and over-luminous for its mass (Webbink 2003, Li et al. 2008). The secondary components of the A-subtype are thought to have evolved from initially more massive stars (Zhang et al. 2020).

5. FROM DETACHED TO CONTACT PHASE

The formation of the W UMa type contact binaries is a complex process in which different mechanisms are combined.

Yildiz & Doğan (2013) developed a method for the computation of the initial masses of contact binaries. Their main assumption is that the mass transfer starts near or after the TAMS phase of the initially massive component, which is the progenitor of the currently less massive components. They discovered that binary systems with an initial mass larger than $1.8 \pm 0.1\ M_\odot$ become A-subtype, while systems with initial masses smaller than this become W-subtype.

By applying their method to our systems we derived the masses of the progenitors of the systems M_{2i} and M_{1i} with the semi-major axis a_{fof} and the orbital periods P_{fof} at the time of the first overflow (i.e fof).

These parameters are computed from equations from Yildiz & Doğan (2013) as developed by Kriwattanawong & Kriwattanawong (2019) and are reported in our Table 11.

6. CONCLUSIONS

We have derived, for the first time, a photometric solution for the eclipsing binary systems TYC 2402-643-1, TYC 2703-1235-1 and TYC 2913-2145-1.

TYC 2402-643-1 and TYC 2913-2145-1 are found to be A-type contact binaries and, having mass ratios < 0.25, can be classified as extreme mass ratio binary systems (EMRBs) (Samec et al. 2015). The discovery of binaries with extremely low mass ratios as our targets and other similar, such as USNO-B1.0 1452-0049820 and ASAS J102556+2049.3 from Kjurkchieva et al. (2018a) and NSVS 2569022 with $q = 0.077$ and of some others as were pointed out in Table 3 of Kjurkchieva et al. (2018b) provoke future theoretical investigations to establish the lower mass ratio limit of the W UMa type stars.

TYC 2703-1235-1 was found to be a W-subtype with a mass ratio of $q = 3.054$ ($q_{inv} = 0.327$) and a shallow fill-out parameter of $f = 22.1\%$. These characteristics agree with those of most W-subtype contact systems.

Our systems have high orbital inclination, between 81 and 88 degrees, displaying total eclipses, so the photometric parameters obtained here are reliable (Terrell & Wilson 2005).

W UMa systems generally show an almost equal temperature for the components, and this is the case for two of the three systems. In contrast, TYC 2913-2145-1 is in a relatively poor thermal contact with $\Delta T = 730$K. The relatively large difference in temperature and the shallow fill-out value could indicate that TYC 2913-2145-1 may be at a key evolutionary stage, as predicted by the thermal relaxation oscillation theory (TRO) (Lucy 1967, Lucy & Wilson 1979, Flannery 1976, Robertson & Eggleton 1977, Eggleton 1996, Qian & Ma 2001, Yakut & Eggleton 2005, Li et al. 2005, and Li et al. 2008).

From our observed ToM's as well as from those obtained from the literature we cannot say much about the period variation of the systems, but we used the data in our analysis for refining the ephemeris.

Following the work of Qian et al. (2020) it is possible to see that the position of TYC 2913-2145-1 in the period-temperature correlation graph is just on the outer edge of the lower boundary, confirming that it is at the beginning of the evolutionary stage of contact binary evolution (Figure 5), as assumed by us due to both its relatively large temperature difference and the low value of contact between the components.

The other two systems show a good thermal contact with difference in temperatures between the components of a couple of hundred K, and are well inside the boundaries for normal EW; they will approach the final evolutionary stage of the contact binary evolution (Figure 5).

Absolute parameters were estimated for the components. The overluminosity of the secondaries in the W UMa systems can be due to the energy transfer from the primary to the secondary for the

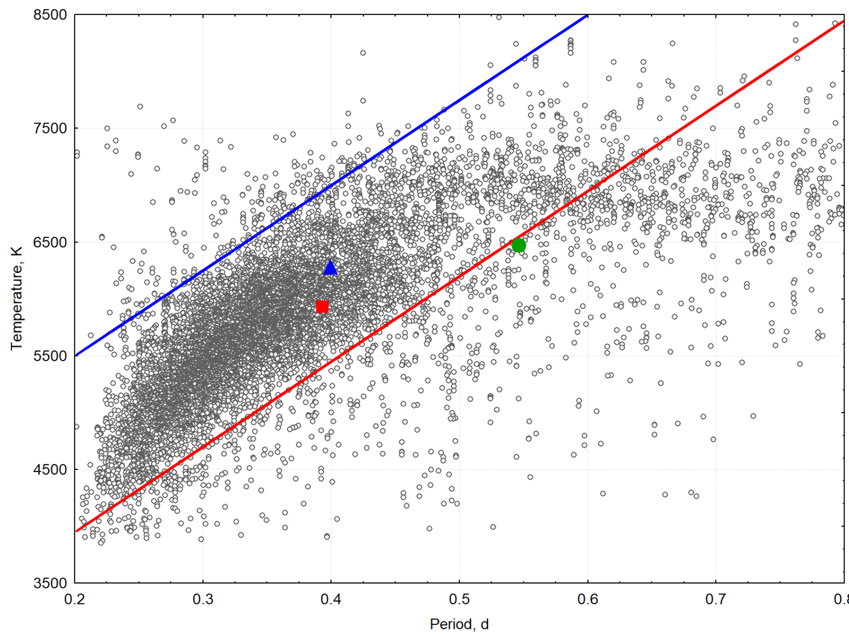

Fig. 5. Correlation between orbital period and temperature based on parameters of 8510 contact binaries from Qian et al. (2020). The position of TYC 2402-643-1 is marked in blue, the one of TYC 2703-1235-1 in red and the one of TYC 2913-2145-1 in green. The red and blue lines are the boundaries of normal EWs. Systems near the red border are marginal contact systems, while those close to the blue border are deep contact ones. The color figure can be viewed online.

W-subtype, and to the evolution of the secondary component from an initial more massive star of A-subtype.

The study of Yildiz & Doğan (2013) shows that the W UMa binary systems with an initial mass of the secondary component of the system ($M2_i$, the actual primary component) larger than 1.8±0.1M$_\odot$ become A subtype, while the systems with initial masses smaller than this become W subtype.

By applying the method to our systems we are able to estimate the absolute relative parameters of the detached system, the progenitor of the contact system, as shown in Table 11. We found that the initial mass of the secondary component of the two A-subtypes would be greater than 1.8 solar masses, while for the W-subtype system it would be smaller than that value, as predicted.

The results show that the angular momentum of the three systems has decreased; consequently, the orbital period and the semi-major axis have decreased too. To verify the reliability of our results we used the relationship between masses and ratios as specified in Qian (2001). We found that our systems do not deviate from these correlations.

The research was supported in part by project D01-383/20 of the Scientific Fund of the Bulgarian Ministry of Education and Science. The research was made with the support of the private IRIDA OBSERVATORY.[5] This work has used data from the European Space Agency (ESA) mission GAIA, processed by the GAIA Data Processing and Analysis Consortium (DPAC). Funding for the DPAC has been provided by national institutions, in particular the institutions participating in the GAIA Multilateral Agreement. This research has used the SIMBAD database, operated at CDS, Strasbourg, France, NASA Astrophysics Data System Abstract Service. We are thankful to Svetla Potter for the English language corrections. We would like to thank the anonymous referee for all her/his very useful comments and corrections which have improved the quality of this paper.

REFERENCES

Berry, R. & Burnell, J. 2006, The Handbook of Astronomical Image Processing with AIP4WIN2 software, (Willmann-Bell. Inc. WEB.)

Binnendijk, L. 1965, VeBam 27, The Position of Variable Stars in the Hertzsprung-Rusell Diagram, 36

Bradstreet, D. H. & Steelman, D. P. 2002, AAS, 201, 7502

[5]http://www.irida-observatory.org.

Bressan, A., Marigo, P., Girardi, L., et al. 2012, MNRAS, 427, 127, https://doi.org/10.1111/j.1365-2966.2012.21948.x

Brown T. M. & Charbonneau, D. 2000, ASPC 219, Disks, Planetesimals, and Planets, ed. F. Garzón, C. Eiroa, D. de Winter, and T. J. Mahoney (ASP), 584

Covey, K. R., Ivezić, Ž, Schlegel, D., et al. 2007, AJ, 134, 2398, https://doi.org/10.1086/522052

de Ponthire, P. 2010, LESVEPHOTOMETRY, automatic photometry software (http://www.dppobservatory.net)

Efron, B. & Tibshirani, R., 1986, StaSc, 1, 54, https://doi.org/10.1214/ss/1177013815

Eggleton, P. P. 1996, ASPC 90, The origins, evolution, and destinies of binary stars in clusters, ed. E. F. Milone & J. -C. Mermilliod (San Francisco, CA: ASP), 257

Esmer, B. M., Baştürk, Ö., Hinse, T. C., Selam, S. O., & Correia, A. C. M. 2021, A&A, 648, A85, https://doi.org/10.1051/0004-6361/202038640

Flannery, B. P. 1976, ApJ, 205, 217, https://doi.org/10.1086/154266

Gaia Collaboration, Brown, A. G. A., Vallenari, A., et. al. 2018, A&A, 616, 1, https://doi.org/10.1051/0004-6361/201833051

Gazeas, K. D. 2009, CoAst, 159, 129,

Gazeas, K. D. & Stępień, K. 2008, MNRAS, 390, 1577, https://doi.org/10.1111/j.1365-2966.2008.13844.x

Gettel, S. J., Geske, M. T., & McKay, T. A. 2006, AJ, 131, 621, https://doi.org/10.1086/498016

Henden, A. A., Levine, S., Terrell, D., & Welch, D. L. 2015, AAS, 225, 336.16

Hoffman, D. I., Harrison, T. E., & McNamara, B. J. 2009, AJ, 138, 466, https://doi.org/10.1088/0004-6256/138/2/466

Hoňková, K., Juryšek, J., Lehký, M., et al. 2013, OEJV, 160, 1

Kjurkchieva, D. P., Popov, V. A., & Petrov, N. I. 2018, AJ, 156, 77, https://doi.org/10.3847/1538-3881/aace5e

_________. 2018, RAA, 18, 129, https://doi.org/10.1088/1674-4527/18/10/129

Kriwattanawong, W. & Kriwattanawong, K. 2019, RAA, 19, 143, https://doi.org/10.1088/1674-4527/19/10/143

Li, L., Han, Z., & Zhang, F. 2005, MNRAS, 360, 272, https://doi.org/10.1111/j.1365-2966.2005.09024.x

Li, L., Zhang, F., Han, Z., Jiang, D., & Jiang, T. 2008, MNRAS, 387, 97, https://doi.org/10.1111/j.1365-2966.2008.12736.x

Lucy, L. B. 1967, ZA, 65, 89

Lucy, L. B. & Wilson, R. E. 1979, ApJ, 231, 502

Luo, A.-L., Zhao, Y.-H., Zhao, G., et al. 2019, yCat, 5164, 0

O'Connell, D. J. K. 1951, PRCO, 2, 85

Pecaut, M. J. & Mamajek, E. E. 2013, ApJS, 208, 9, https://doi.org/10.1088/0067-0049/208/1/9

Qian, S.-B. 2001, MNRAS, 328, 914, https://doi.org/10.1046/j.1365-8711.2001.04921.x

Qian, S.-B. & Ma, Y. 2001, PASP, 113, 754

Qian, S.-B., Zhu, L.-Y., L. Liang, et al. 2020, RAA, 20, 163

Robertson, J. A. & Eggleton, P. P. 1977, MNRAS, 179, 359, https://doi.org/10.1093/mnras/179.3.359

Samec, R. G., Benkendorf, B., Dignan, J. B., et al. 2015, AJ, 149, 146, https://doi.org/10.1088/0004-6256/149/4/146

Skrutskie, M. F., Cutri, R. M., Stiening, R., et al. 2006, AJ, 131, 1163, https://doi.org/10.1086/498708

Terrell, D. & Wilson, R. E. 2005, Ap&SS, 296, 221, https://doi.org/10.1007/s10509-005-4449-4

Webbink, R. F. 2003, ASPC 293, 3D Stellar Evolution, ed. S. Turcotte, S., S. C. Keller, & R. M. Cavallo (ASP), 76

Wilson, R. E. & Devinney, E. J. 1971, ApJ, 166, 605, https://doi.org/10.1086/150986

Wilson, R. E. 1990, ApJ, 356, 613, https://doi.org/10.1086/168867

Wilson, R. E. & van Hamme, W. 2015, Computing binary stars observables, ftp.astro.ufl.edu, directory pub/wilson/lcdc2015

Woźniak, P. R., Vestrand, W. T., Akerlof, C. W., et al. 2004, AJ, 127, 2436, https://doi.org/10.1086/382719

Yakut, K. & Eggleton, P. P. 2005, ApJ, 629, 1055, https://doi.org/10.1086/431300

Yildiz, M. & Doğan, T. 2013, MNRAS, 430, 2029, https://doi.org/10.1093/mnras/stt028

Zhang, X.-D., Qian, S.-B., & Liao, W. P. 2020, MNRAS, 492, 4112, https://doi.org/10.1093/mnras/staa079

Zhang, X.-D. & Qian, S.-B. 2020, MNRAS, 497, 3493, https://doi.org/10.1093/mnras/staa2166

Francesco Acerbi: Via Zoncada 51, 26845 Codogno (LO), Italy (acerbifr@tin.it).
Carlo Barani: Via Molinetto 35, 26845 Triulza di Codogno (LO), Italy (cvbarani@alice.it).
Velimir Popov: Department of Physics and Astronomy, Shumen University, 115 Universitetska str., 9700 Shumen, Bulgaria (velimir.popov@elateobservatory.com, v.popov@shu.bg).

Revista Mexicana de Astronomía y Astrofísica, **58**, 83–97 (2022)

https://doi.org/10.22201/ia.01851101p.2022.58.01.07

THE PROPERTIES OF HIGH REDSHIFT GALAXIES

Luz Ángela García

Grupo de Simulación, Análisis y Modelado (SiAMo), Vicerrectoría de Investigación, Universidad ECCI, Bogotá, Colombia.

Received May 31 2021; accepted December 10 2021

ABSTRACT

This work studies the connection between the first galaxies and their hosting dark matter halos in the early Universe when reionization is concluding. Our numerical models (already presented in an earlier study) trace the star formation history at $z = 4$ - 8, the galaxy stellar mass function, the stellar-to-halo mass distribution, and other high redshift galaxies statistics. All these predictions are consistent with observations to date and with other high-resolution cosmological simulations. A key finding of this work is the robust estimate of the cosmic star formation history (through the implementation of galaxy and supernova winds and atomic and molecular cooling processes) and self-consistent chemical pollution of the intergalactic medium. The theoretical models are compatible with a faint-end slope of the galaxy luminosity function of $\alpha = -2$ at the end of reionization.

RESUMEN

Este trabajo estudia la conexión entre las primeras galaxias y sus halos de materia oscura en el Universo temprano, cuando la reionización está concluyendo. Nuestros modelos teóricos (presentados en un trabajo previo) trazan la historia de formación estelar en $z = 4$ - 8, la función de masa estelar, la distribución de masa estelar a masa de halo, y otras estadísticas de las galaxias a alto corrimiento al rojo. Todas estas predicciones concuerdan con las observaciones actuales y con otras simulaciones numéricas de alta resolución. Un hallazgo crucial de este trabajo es la sólida estimación de la historia cósmica de formación estelar (a través de la implementación de vientos galácticos y de supernovas y procesos de enfriamiento atómico y molecular), y un esquema autoconsistente para el enriquecimiento químico en el medio intergaláctico. Además, los modelos teóricos son compatibles con una pendiente en el límite débil de la función de luminosidad de las galaxias con $\alpha = -2$ al final de la reionización.

Key Words: cosmology: theory — dark ages, reionization, first stars — galaxies: star formation

1. INTRODUCTION

The formation and evolution of galaxies at high redshift strongly determined the progression of the epoch of reionization (EoR). The hierarchical model for structure formation provides a scenario where small dark matter halos ($\approx 10^6 M_\odot$) at $z \approx 30$ reached a critical temperature to agglomerate baryons, and formed stars (Tegmark et al. 1997), initially metal-free (POP III). However, these first stars evolved and consumed their fuel quickly and produced the first supernova explosions. With them, the chemical pollution of the intergalactic medium (IGM) began (Matteucci & Calura 2005). Consequently, a new generation of stars (POP II) formed the first black holes in the Universe. Interestingly, metals in POP II stars supplied an additional cooling source; therefore, these structures were less massive and had longer lives than metal-free stars. The interaction of the collapsed systems in the Universe and the IGM is described through feedback models that account for winds that spread out chemical elements and vary the ionization state of free hydrogen.

Using Hubble Space Telescope imaging, Robertson et al. (2015) measured the abundance and luminosity distribution of early galaxies and provided a constraint for the observed star formation rate (SFR). However, the largest compilation to date for the SFR was presented by Madau & Dickinson (2014). Later works by Oesch et al. (2015); McLeod et al. (2015); Finkelstein et al. (2015); Song et al. (2016); Oesch et al. (2018); Ishigaki et al. (2018); Bhatawdekar et al. (2019); among others, have complemented our survey of galaxies at early times, pushing the detections to very faint objects at higher redshifts ($z \approx 11$; Robertson 2021).

On the other hand, theoretical models have a threefold purpose: (i) match the observations available for the synthetic galaxies and their environment; (ii) provide a physical description of the star formation process at all times, and (iii) interpolate -when possible- the progression of galaxies and their properties in time. There are multiple models that reproduce the star formation history of galaxies at early times, focusing on specific physical processes, among them: Angus (*AustraliaN* Gadget-3 *early Universe Simulations*, Tescari et al. 2014); the Renaissance suite (with the AMR code Enzo, O'Shea et al. 2015); Eagle (Evolution and Assembly of GaLaxies and their Environments, Crain et al. 2015; Schaye et al. 2015); CROC (Cosmic Reionization on Computers, Zhu et al. 2020); the Obelisk simulation (Trebitsch et al. 2020); L-Galaxies 2020 (Henriques et al. 2020; Yates et al. 2021a); Flares (First Light And Reionisation Epoch Simulations, Lovell et al. 2021; Vijayan et al. 2021); Astraeus (semi-numerical rAdiative tranSfer coupling of galaxy formaTion and Reionization in N-body dArk mattEr simUlationS, Hutter et al. 2021).

With the advent of the James Webb Space Telescope (JWST) shortly, we will reach an unprecedented understanding of the first light and the reionization, as well as the assembly of galaxies (Gardner et al. 2006). The expectation is that JWST will observe galaxies out to $z > 12$ and even at $z \approx 15$ (depending on their brightness). It will provide a uniform census of galaxies in the redshift range of 7 - 12 and extend the observed cosmic star formation evolution at a level not achievable by Hubble (Finkelstein 2016). In addition, JWST will: detect stars with very low metallicity ($10^{-3} Z_{\odot}$), set constraints of the top-heavy IMF, provide an estimate of the escape fraction of ionizing photons of galaxies, and allow for a robust investigation of the UV luminosity function at high redshift (Atek et al. 2015 found a steep faint-end slope at $z \approx 7$). Theoretical works such as UniverseMachine by Behroozi et al. (2020), IllustrisTNG with dust modeling (Vogelsberger et al. 2020) or Williams et al. (2018) -that creates a mock catalog of galaxy populations from the UV to the near-infrared- anticipate future observations from the instrument and provide a realistic (yet conservative) forecast of the galaxy assembly at redshifts up to 15.

The paper is presented as follows: § 2 gives an overview of our numerical simulations and the physical modules implemented to recreate the structure formation at high redshift. Also, we briefly present a description of other numerical simulations considered to evaluate the performance of our models. § 3 shows a series of statistics for galaxy and halo properties in the simulations at $4 < z < 8$. We also compare our theoretical predictions with observational data available to-date and to the largest compilation of high-resolution cosmological models in this redshift range. We establish a connection between the galaxy properties and their hosting dark matter halo and show a self-consistent chemical enrichment in the models. § 4 discusses future scenarios where our conclusions can be tested, as well as the strengths and caveats of our models. Finally, § 5 summarizes the findings and conclusions of this study.

2. THE NUMERICAL SIMULATIONS

This work relies on a set of high-resolution hydrodynamical simulations at high redshift ($4 < z < 8$), initially presented in García et al. (2017b). The model is based on a customized version of the smoothed particle hydrodynamics (SPH) code Gadget-3 (Springel 2005), with a spatially flat cosmology ΛCDM model and cosmological parameters $\Omega_{0m} = 0.307$, $\Omega_{0b} = 0.049$, $\Omega_{\Lambda} = 0.693$, $n_s = 0.967$, $H_0 = 67.74$ km s^{-1}Mpc^{-1} (or $h = 0.6774$) and $\sigma_8 = 0.816$. A summary of the numerical simulations is shown in Table 1.

The numerical models are complemented with an algorithm that identifies collapsed structures, so-called parallel Friends-of-Friends (FoF), and a parallel SUBFIND algorithm to identify substructures within FoF halos.

The mechanism for which star-forming gas particles turn into star-type particles by a stochastic process was first proposed by Katz et al. (1996) and later discussed in Springel & Hernquist (2003); Tornatore et al. (2007).

Thus, our model produces self-consistently chemical enrichment based on the stochastic scheme for star formation. The module follows the evolution of hydrogen, helium, and nine elements up to iron, delivered from SNIa and SNII and intermediate-mass stars. Importantly, stars with masses $m \leq 40 M_{\odot}$ explode as supernovae before turning into a black hole. Conversely, stars above such threshold collapse into a black hole without experiencing the supernova stage, contributing to the feedback process, but not to the chemical evolution in the simulations. The overall state of a simple stellar population depends on the lifetime function (Padovani & Matteucci 1993), the stellar yields, and the initial mass function (IMF).

The stellar yields account for the amount of metals released by each source during the stellar evolution: SNIa (Thielemann et al. 2003), SNII (Woosley & Weaver 1995) and low- and intermediate-mass stars. Moreover, the solar metallicity layers follow results from Asplund et al. (2009).

The cooling processes that allow the gas to form stars include atomic, metal-line cooling (Wiersma et al. 2009), as well as low-temperature cooling by molecules and metals (Maio et al. 2007; Maio & Tescari 2015).

TABLE 1

OVERVIEW OF THE SIMULATIONS USED IN THE PAPER*

Simulation	Box size (cMpc/h)	Comoving softening (ckpc/h)	$M_{\rm gas}$ ($\times 10^5 {\rm M}_\odot/h$)	$M_{\rm DM}$ ($\times 10^6 {\rm M}_\odot/h$)
Ch 18 512 MDW	18	1.5	5.86	3.12
Ch 18 512 MDW mol	18	1.5	5.86	3.12
Ch 18 512 EDW	18	1.5	5.86	3.12
Ch 18 512 EDW mol	18	1.5	5.86	3.12
Ch 12 512 MDW mol	12	1.0	1.74	0.925
Ch 25 512 MDW mol	25	2.0	15.73	8.48

*The first column corresponds to the name of the run, the second one to the box size. The third column lists the comoving gravitational softening length. Columns 4 and 5: the gas and DM particle masses. Note that all runs have the same initial number of gas and DM particles (2×512^3). The acronyms MDW and EDW stand for momentum- and energy-driven winds feedback prescriptions, and mol at the end of the run's name indicates the presence of low-temperature metal and molecular cooling. The fiducial model is highlighted in bold in the first row: Ch 18 512 MDW.

On the other hand, this work builds on a multi-sloped IMF (Chabrier 2003) that accounts for massive POP II and, to some extent, to POP III stars, which significantly contribute to the first stages of the star formation processes and the hydrogen reionization.

Our numerical simulations implement galactic winds to regulate the star formation process, the dispersion of metals from galaxies to the intergalactic medium (IGM), and prevent overcooling of the gas (Springel & Hernquist 2003). Such feedback mechanisms expel material and balance the temperature among neighbor gas particles, allowing physical processes to occur. There are two kinetic supernova–driven winds considered in this work: energy- (EDW; Springel & Hernquist 2003) and momentum-driven winds (MDW; Puchwein et al. 2013), and AGN feedback (Springel et al. 2005; Fabjan et al. 2010; Planelles et al. 2013). The latter type of feedback is essential at low redshift ($z \approx 2$) when massive halos are more numerous and massive.

In this work, both EDW and MDW supernova outflows are implemented, with a fixed fiducial velocity $v_{\rm fid} = 600$ km/s. The main assumption in the former prescription for the winds is the proportionality between the star formation rate $\dot{M}_\star$ and the mass-loss rate due to winds $\dot{M}_w$, through the relation $\dot{M}_w = \eta \dot{M}_\star$. The factor η is defined as the wind mass loading factor and quantifies the efficiency of the wind to expel material out of the source cell.

The kinetic energy of the wind and the halo circular velocity allow us to establish a numerical relation between wind mass–loading factor η and v_w [1]:

$$\eta = 2 \times \left(\frac{v_{\rm fid}}{v_w} \right)^2 . \quad (1)$$

[1]See García et al. (2017b) for the complete derivation of this expression.

Nonetheless, Puchwein et al. (2013) show that the star formation rate $\dot{M}_\star$ and the mass expelled by supernova winds $\dot{M}_w$ do not necessarily have a linear relation. Instead, a more natural assumption would be a mathematical relationship for the star formation rate of the galaxy and the winds' momentum flux. In such case, $\eta \propto v_w^{-1}$:

$$\eta = 2 \times \frac{v_{\rm fid}}{v_w} . \quad (2)$$

It is worth mentioning that the wind velocity v_w has the same functional form as in the energy-driven winds feedback. Yet, their efficiencies η behave in distinctive ways because of the scaling with v_w.

On the other hand, different authors have shown that AGN feedback is critical to regulate the star formation rate history, gas accretion, stellar evolution, and metal enrichment when the Universe has evolved for 10 billion years (i.e., $z \approx 2$), at the peak of the star formation and consequently, the most significant quasar activity in the history of the Universe.

Nevertheless, Tescari et al. (2014) present an extensive discussion of the negligible effect of AGN feedback at the redshifts of interest of this work. Two main factors determine that AGNs do not play an essential role at high redshift: (i) the galaxies are still experiencing their first stages of star formation; hence, very few super-massive black holes have formed at this time; (ii) dark matter halos are still growing by mergers; thus, AGNs (if existing) are rare, and so are their feedback mechanisms.

Other Numerical Simulations

In order to convey a successful comparison of the predictions from this set of simulations with current theoretical models, we briefly summarize the main features of each of the mock cosmological boxes, highlighting their resolution and box sizes.

- UNIVERSEMACHINE

  As described in Behroozi et al. (2020), the UNIVERSEMACHINE is based on the Very Small MultiDark-Planck (VSMDPL) simulation, a modified version of GADGET- 2 with a flat ΛCDM model and $h = 0.68$. This model was run from $z = 150$ to 0, in a cube size of 160 cMpc/h with 3840^3 particles, allowing it to reach a gas mass of $9.1 \times 10^6 M_\odot$, a numerical resolution of 2 ckpc/h at $z > 1$ and resolved dark matter halos with 100 particles (i.e., above $10^9 M_\odot$). The latter property of the UNIVERSEMACHINE makes it suitable to appropriately describe halos at high redshift and to foresee the characteristics of undetected galaxies at the epoch of reionization.

- L-Galaxies 2020

  This semianalytical model of galaxy evolution (Henriques et al. 2020) is run on the MILLENNIUM-II simulations in a box of ≈ 96.1 Mpc/h side. It only contains dark matter particles (the baryonic physics is implemented through effective modules that are easily adapted), reaching a broad coverage at the cosmological level. The dark matter particles have a mass resolution of $7.7 \times 10^6 M_\odot/h$. The model is scaled to the Planck 2013 cosmology with $h = 0.673$. L-Galaxies 2020 currently has two distributions: **Default model** or **DM**, first described in Henriques et al. (2020), assumes that 70% of the metal content is released by supernova is instantly mixed with the local interstellar medium (ISM) before being expelled out of galaxies via SN winds. Instead, the **Modified model -MM-** (Yates et al. 2021a) adopts a chemical pollution prescription where up to 90% of metals produced in supernova explosions are moved directly to the circumgalactic medium (CGM) without passing by the ISM. These two complementary scenarios cover a wide range of CGM enrichment schemes, likely to occur in real galaxies.

- EAGLE

  Evolution and Assembly of GaLaxies and their Environments (EAGLE) is a hydrodynamical suite of cosmological simulations run in a modified version of GADGET- 3 (Crain et al. 2015; Schaye et al. 2015). The model's main strength is the galaxy growth and evolution, and it includes similar prescriptions and modules as the ones implemented in our numerical simulations. For this paper, we will only focus on their largest volume 'L100N1504' cube, with 67 (Mpc/h)^3 box-size and 2×1504^3 particles (dark matter + gas). The initial mass is $1.2\,(6.6)\times 10^6 M_\odot/h$ for baryons (and dark matter). The assumed cosmology is Planck 2013 with $h = 0.6777$, and their supernova feedback is EDW.

- TNG100

  IllustrisTNG is a set of gravo-magnetohydrodynamical simulations based on the Illustris project (Nelson et al. 2018; Pillepich et al. 2018; Naiman et al. 2018; Marinacci et al. 2018; Springel et al. 2018). TNG (The Next Generation) has a standard configuration for three different volumes: 35, 75, and 205 cMpc/h of side length -TNG50, TNG100, and TNG300, respectively-. The first box size involves the largest resolution, instead of TNG300, which covers a more vast cosmological region at the expense of reducing the gravitational softening. Each simulated box has different levels of resolution (moving from 1 to 3-4, with decreasing numerical resolution and lighter simulation outputs). The assumed cosmology is Planck 2015 with $h = 0.6774$. In particular, for the comparison intended in this work, we only consider the TNG100-1 run, with 2×1820^3 particles, and average cell masses of $7.5 \times 10^6 M_\odot$ and $1.4 \times 10^6 M_\odot$ for dark matter and gas, respectively.

- FLARES

  First Light and Reionisation Epoch Simulations (FLARES) is a suite of zoom simulations that focuses on the typical overdensities reached during the epoch of reionization. The models are presented and discussed in Lovell et al. (2021); Vijayan et al. (2021), and they are a re-simulated version of EAGLE with a total volume of (3.2 cGpc)^3 -dark matter only-. The dark matter particles have a mass of $8.01 \times 10^{10} M_\odot/h$. Smaller regions of 15 Mpc/h in radius are re-computed with a full hydrodynamical treatment (about our boxes in size) from $z = 10$ down to $z = 4.67$ with the EAGLE galaxy formation scheme. FLARES assumes Planck 2014 cosmological parameters with $h = 0.6777$, and the same configuration as the EAGLE reference run (100 cMpc) with 9.7 and $1.6 \times 10^6 M_\odot$ initial masses for dark matter and gas particles, respectively, leading to a numerical resolution of 2.66 ckpc (between the gravitational softening reached by our synthetic boxes with 18 and 25 cMpc/h).

3. GALAXY PROPERTIES IN OUR SIMULATIONS

Following the assumptions from previous section, AGN feedback is not implemented in our simulations (Tescari et al. 2014). The simulations were anchored at $z = 8$, and observables such as the cosmic star formation rate and the galaxy stellar mass function were used to calibrate the mass loading factor for the winds

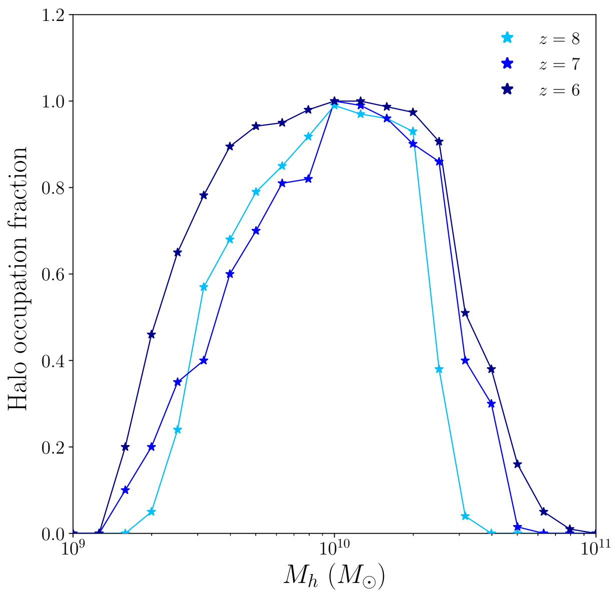

Fig. 1. Halo occupation fraction in the simulation Ch 18 512 MDW (our fiducial run). The distributions show the percentage of dark matter halos containing formed stars at z = 8, 7, and 6 (light, navy, and dark blue lines, respectively). The color figure can be viewed online.

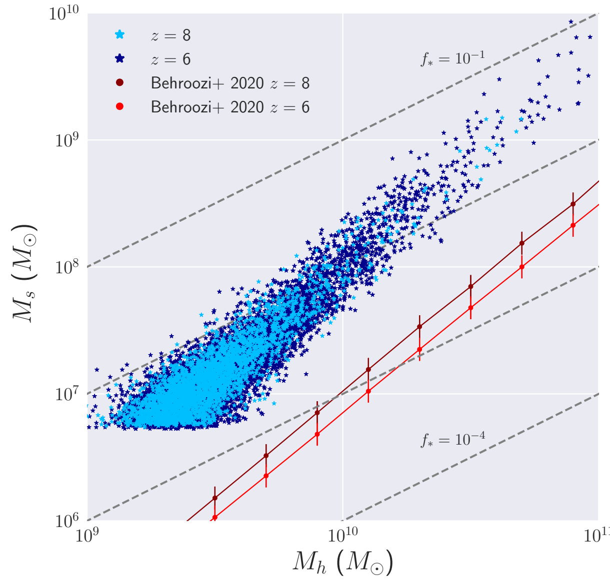

Fig. 2. Galaxy stellar-to-halo virial mass function in our reference model Ch 18 512 MDW. The graph displays the distribution of masses above the threshold for this simulation box-size at redshifts z = 8 and 6 (corresponding to light and dark blue stars, respectively). For comparison, the predicted trends from UniverseMachine (Behroozi et al. 2020) are shown at z = 8 (dark red circles) and z = 6 (red dots). Grey dashed lines indicate constant stellar functions $f_* = M_*/M_h$, ranging from 10^{-4} (bottom) to 10^{-1} (top). The color figure can be viewed online.

$v_{\rm fid}$ = 600 km/s, and match the observations at the time when García et al. (2017b) was published. Hence, the SFR (z = 8) and the stellar mass function are not predictions of the model.

3.1. *Halo Occupation Fraction*

The halo occupation fraction presents the distribution of dark matter halos with chemically enriched star-particles at a particular redshift, as a function of the halo mass. We present the halo occupation fraction in the fiducial model Ch 18 512 MDW in Figure 1, including mass bins of $\log(M_h/\mathrm{M}_\odot) = 0.1$. It is worth noting that we only take into account halos above the mass resolution $M_{h,min} = 1.48 \times 10^9 \mathrm{M}_\odot$.

The distribution in Figure 1 reaches its maximum occupation at $M_h \approx 1 \approx 10^{10}\mathrm{M}_\odot$ for z = 8, 7, and 6, which is consistent with the hierarchical model of structure formation. Dark matter halos with masses below $10^9\mathrm{M}_\odot$ contain less than 470 dark matter particles, then they cannot be considered virialized, and the star formation in such regions is disfavoured for two reasons: first, they are unresolved, and they do not efficiently experience atomic cooling; hence, gas is collisionally excited and less likely to form structure in the dark matter wells until it cools down. On the contrary, halos with large masses ($\geq 10^{10}\mathrm{M}_\odot$) preferentially form stars, but they are rare on the simulations at high redshift. Although scarce, dark matter halos with large masses present a non-negligible occupation of chemically enriched stellar populations.

At z = 6 (dark blue line), when the Universe has evolved for ≈ 360 Myr from the start of the simulations (z = 8), the highest probability of finding fully occupied halos occurs at $M_h \approx 1 \times 10^{10}\mathrm{M}_\odot$. The latter result indicates that halos in the simulation have grown in mass during this period and, consequently, also the cosmic star formation rate.

3.2. *Stellar-to-Halo Mass Function*

Another observable that we check in our models is known as the galaxy stellar-to-halo virial mass function, presented in Figure 2 for the fiducial run Ch 18 512 MDW, at z = 8 and 6.

Figure 2 presents the distribution of the stellar-to-halo mass for each galaxy in the fiducial simulation above the mass resolution threshold (> $10^9\mathrm{M}_\odot$ or equivalently, more than 470 dark matter particles). Simulated galaxies follow a trend of 10^{-2}, and at the high mass end, f_* moves to 10^{-1}. f_* grows with redshift, with more galaxies with large stellar masses at z = 6. This result is also seen in numerical simulations such as Astraeus (Hutter et al. 2021), with $M_h = 10^{9.5-10}\mathrm{M}_\odot$ corresponding to stellar masses ≈ $10^{7.5-8}\mathrm{M}_\odot$ during the epoch of reionization. Moreover, O'Shea et al. (2015) display this distribution (Figure 2, left), but they stack all the galaxies in their realizations up to their final redshifts. The Renaissance simulations describe galaxies that are evolving during the progress of reionization; therefore, they account for halo masses down to $7 \times 10^6 \mathrm{M}_\odot$ (halos with formed stars). Their plot is not directly comparable with Figure 2 because the mass range covered by their simulations differs from ours. Still, galaxies around $10^9 \mathrm{M}_\odot$ in their work show the same difference of two orders of magnitude in M_h/M_s. Recent observations by Stefanon et al. (2021) reveal the same ratio of two orders of magnitude for stellar-to-halo mass ratios (see Table 7 in their work). They emphasize that there is no significant evolution in the observed stellar-to-halo mass function for galaxies in the first Gyr of cosmic time. The latter conclusion is consistent with Figure 2. Instead, predictions by Behroozi et al. (2020) are an order of magnitude below the trend of our fiducial simulation, at $z = 8$ and 6. However, we cannot provide a clear explanation for this discrepancy since UniverseMachine is calibrated to resolve virialized halos up to $z \approx 15$, but the ratio predicted by their simulation is off compared with other simulations at $z = 6$ - 8 (including ours).

It is worth mentioning that we only calculate the stellar-to-halo mass function for the fiducial model Ch 18 512 MDW because there is minimal variation in the range of masses resolved by our simulations due to our small boxes (12, 18, and 25 cMpc/h). Thus, the trend shown in Figure 2 is barely affected by changes in the box size.

3.3. *Galaxy Stellar Mass Function*

One can also count the number density of galaxies formed inside the virialized halos per unit volume V per stellar mass bin ΔM (Weigel et al. 2016). This observable is known as the galaxy stellar mass function, and it is given by:

$$\Phi(z) = \frac{\#_{\mathrm{gal}}(\Delta M)}{V \cdot \Delta M}. \tag{3}$$

The analytical form that describes the galaxy stellar mass function is commonly described using a Schechter function (Schechter 1976), as follows:

$$\Phi(M) = \ln(10)\Phi^{*}\mathrm{e}^{-10(M-M_{*})}10^{(M-M_{*})(\alpha+1)}. \tag{4}$$

The exponential term in the expression above shows the evolution for the high- and low-mass and the fore-most right term a power-law behavior as a function of the stellar mass.

We present the best fit parameters and corresponding errors for the galaxy stellar mass functions at $z = 8$, 7, and 6 for three of our models with same configuration (MDW and no molecular cooling) with box sizes of 12, 18, and

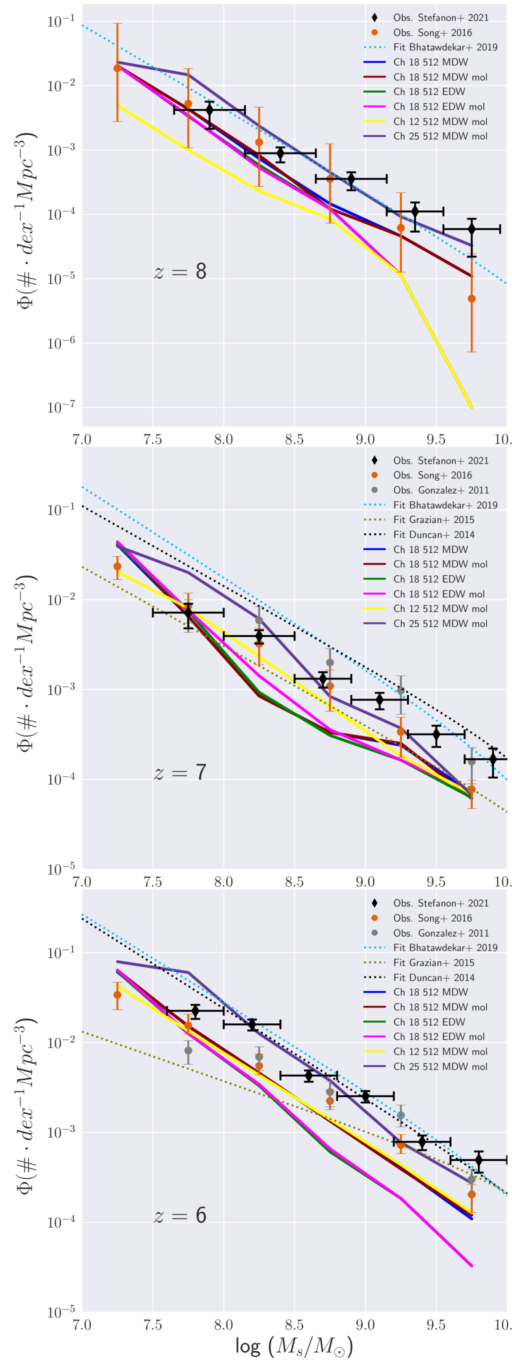

Fig. 3. Simulated galaxy stellar mass function at $z = 8$, 7 and 6 in the top, middle and bottom panels. Theoretical predictions from our models are compared with observations by Stefanon et al. (2021) as black diamonds, Song et al. (2016) as orange circles and González et al. (2011) as grey circles, and the best fits proposed Bhatawdekar et al. (2019), Grazian et al. (2015) and Duncan et al. (2014) as light blue, olive and black dotted lines, respectively. The parameters of the Schechter function (4) for each model are presented in Table 2. The color figure can be viewed online.

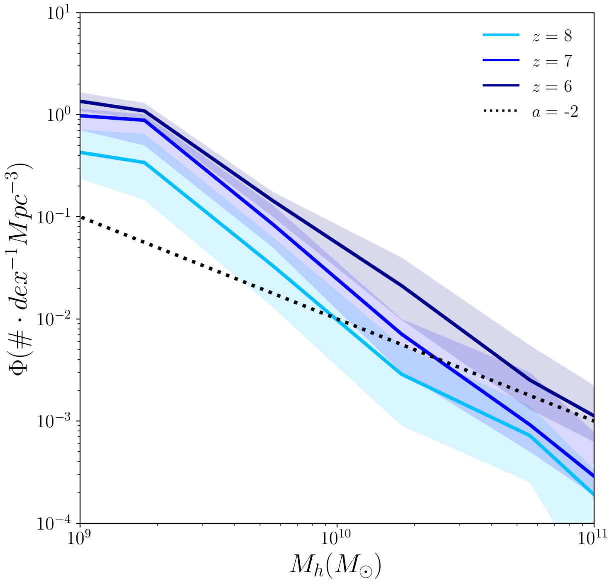

Fig. 4. Halo mass functions at z = 6, 7, and 8 in dark, navy, and light blue. We include shaded regions corresponding to Poisson errors for the fiducial run Ch 18 512 MDW. As a reference, we show a constant power-law slope $\alpha = -2$ for galaxies at high redshift, as a dotted black line. The color figure can be viewed online.

25 cMpc/h, in Table 2. We derive these parameters with an adapted version from python routine EMCEE. Table 2 also shows the Schechter function parameters from Duncan et al. (2014), Grazian et al. (2015), Bhatawdekar et al. (2019) and Stefanon et al. (2021).

One highlight from Table 2 is that the slope of the galaxy stellar mass function at z = 6 - 8 remains constant, and in all the cases presented, is close to the value −2. These findings are consistent with the observational constraints also shown in Table 2.

The evolution of the galaxy stellar mass function from z = 8 to 6 is displayed in Figure 3. Remarkably, the galaxy stellar mass function Φ at z = 8 was set to match observations by Song et al. (2016) and to calibrate the mass loading factor of the simulations $\nu_{\rm fid}$. However, the theoretical trends agree well with the best fit at z = 8 by Bhatawdekar et al. (2019) and with the most recent Spitzer/IRAC observations by Stefanon et al. (2021), which is quite reassuring since the observational detections came after our simulations.

The predicted galaxy stellar mass functions at z = 8, 7, and 6 are compatible with the observational data at high z. Nonetheless, the simulations slightly differ from the galaxy stellar mass function reported by Song et al. (2016) and González et al. (2011) in the high mass end at z = 6, mainly because massive galactic halos are scarce in the simulations at these redshifts; thus, high-mass galaxies are rare. Larger synthetic boxes could alleviate this mass bias (for instance, FLARES or UNIVERSEMACHINE).

On the other hand, results with FLARES (Lovell et al. 2021; Vijayan et al. 2021, supported by a vast cosmological box, that at z = 5 and 6, reach stellar masses up to 10^{11}M$_\odot$), claim that the galaxy stellar mass function must be fitted with a double-slope Schechter function with a knee at $M_s = 10^{10}$M$_\odot$. They back the latter argument with recent observational constrains from Stefanon et al. (2021). Nevertheless, our small boxes do not allow us to test this range of mass ($M_{s,\max} \approx 10^{9.8}M_\odot$ in our largest realization; hence, we keep a single-slope fit). One of the motivations for the Lovell et al. (2021) work was to extend the range of stellar masses and the number of resolved galaxies reached by the EAGLE simulation. Our cosmological runs have similar modules, box sizes, and an analogous configuration as EAGLE; therefore, tests related to galaxy observables must be done with EAGLE -or equivalent hydrodynamical simulations. Instead, this particular conclusion derived by Lovell et al. (2021) is out of the reach of our simulations.

3.4. *Halo Mass Function*

In order to characterize the galaxies in the simulations, the halo mass functions at redshifts z = 8, 7, and 6 are presented in Figure 4, in light, navy, and dark blue lines, respectively. This quantity is computed with systems above the mass resolution limit (a resolved halo in the simulation contains ≈ 470 dark matter particles, or equivalently, a minimum mass $M_{h,min} = 1.48 \times 10^9M_\odot$ for boxes of 18 Mpc/h side length). Whenever a galactic halo is below this mass threshold, the object is considered unresolved and is excluded from the statistics.

The evolution of the mass function for dark matter halos is computed only with the fiducial model Ch 18 512 MDW since the number of resolved galaxies is almost independent of the feedback mechanisms or the cooling processes implemented in the simulations. As a reference, a dotted black line is presented on top of our predictions in Figure 4, indicating a constant faint-end slope $\alpha = -2$.

Theoretically, the number density of halos follows the relations $\frac{d(\log N)}{d(\log M_h)} = -1$, as shown in Figure 4, and $N \propto M_h^{\alpha+1}$, leading to a faint-end slope $\alpha = -2$[2]. Although the set of simulations presented in this work is unable to provide a direct prediction of the power slope due to the narrow range of halo masses and the small box sizes of the simulations, the curves in Figure 4 show a trend consistent with a power-law slope of −2 at $z \approx$ 6-8.

We support the latter claim based on the results described in previous sections. The stellar-to-halo mass

[2]See a similar discussion in Behroozi et al. (2020).

TABLE 2

BEST FIT SCHECHTER FUNCTION PARAMETERS AND UNCERTAINTIES FOR THE GALAXY STELLAR MASS FUNCTION $\Phi(M)^*$

	$\log_{10} M_*$	α	Φ^* (10^{-5}Mpc^{-3})
$z \approx 8$			
Stefanon et al. (2021)	$9.98^{+0.44}_{-0.24}$	$-1.82^{+0.20}_{-0.21}$	$2.04^{+0.35}_{-0.78}$
Bhatawdekar et al. (2019)	$10.54^{+1.00}_{-0.94}$	$-2.30^{+0.51}_{-0.46}$	$0.095^{+0.56}_{-0.08}$
Ch 18 512 MDW	10.34 ± 0.02	-2.20 ± 0.05	0.092 ± 0.005
Ch 12 512 MDW	9.25 ± 0.02	-2.15 ± 0.06	0.870 ± 0.005
Ch 25 512 MDW	10.55 ± 0.02	-2.30 ± 0.07	0.098 ± 0.005
$z \approx 7$			
Stefanon et al. (2021)	$10.04^{+0.15}_{-0.13}$	$-1.73^{+0.08}_{-0.08}$	$7.24^{+0.62}_{-0.71}$
Bhatawdekar et al. (2019)	$10.27^{+0.60}_{-0.67}$	$-2.01^{+0.17}_{-0.13}$	$3.9^{+9.2}_{-2.85}$
Grazian et al. (2015)	$10.69^{+1.58}_{-1.58}$	$-1.88^{+0.36}_{-0.36}$	$0.57^{+59.68}_{-0.56}$
Duncan et al. (2014)	$10.51^{+0.36}_{-0.32}$	$-1.89^{+1.39}_{-0.61}$	$3.60^{+3.01}_{-0.35}$
Ch 18 512 MDW	10.61 ± 0.02	-1.95 ± 0.04	0.67 ± 0.03
Ch 12 512 MDW	10.72 ± 0.02	-1.92 ± 0.04	0.60 ± 0.03
Ch 25 512 MDW	10.51 ± 0.02	-2.10 ± 0.05	0.72 ± 0.03
$z \approx 6$			
Stefanon et al. (2021)	$10.24^{+0.08}_{-0.11}$	$-1.88^{+0.06}_{-0.03}$	$8.13^{+0.52}_{-0.35}$
Bhatawdekar et al. (2019)	$10.35^{+0.50}_{-0.50}$	$-1.98^{+0.07}_{-0.07}$	$6.05^{+8.96}_{-3.49}$
Grazian et al. (2015)	$10.49^{+0.32}_{-0.32}$	$-1.55^{+0.19}_{-0.19}$	$6.91^{+13.5}_{-4.57}$
Duncan et al. (2014)	$10.87^{+1.13}_{-0.54}$	$-2.00^{+0.57}_{-0.40}$	$1.4^{+41.1}_{-1.4}$
Ch 18 512 MDW	10.41 ± 0.02	-2.01 ± 0.05	1.20 ± 0.03
Ch 12 512 MDW	10.42 ± 0.02	-2.02 ± 0.05	1.15 ± 0.03
Ch 25 512 MDW	10.40 ± 0.02	-2.05 ± 0.05	3.20 ± 0.03

*For each redshift, we find the best parameters for the fiducial model and two equivalent runs with the same setup, but 12 and 25 cMpc/h box side.

ratio (Figure 2) shows little evolution of the mass ratio at $z = 8$ to 6 (regardless of the increasing number of halos that form galaxies with time). On the other hand, the galaxy stellar mass function (Table 2 and Figure 3) indicates that the slope is close to -2 during the time frame described by the simulations. Since the halo masses, M_h are two orders of magnitude larger than the stellar masses M_s -this ratio stays constant at the tail of the reionization- and the slope for the stellar mass function is -2, with almost no variation in time, the value of the slope of the halo mass function is consistent with -2.

3.5. *Star Formation Rate Density*

The star formation rate is the mass of the new stars in the simulation, measured in the total volume per year. It is commonly assessed by galaxy surveys or derived from studies with luminosity functions. There are two ways to compute the cosmic star formation rate in the numerical runs: (i) adding up the star formation of each gas particle, per comoving volume V; or (ii) recovering the SFR estimate for galaxy groups from the FoF catalog.

Figure 5 shows the cosmic star formation rate in our simulations at $4 < z < 8$. The left panel shows the total SFR (including contributions from all the collapsed objects inside the box). Conversely, the right panel displays the same observable, but this time, applying a cut in mass; thus, only the most luminous galaxies are taken into account in the calculation. This mass threshold responds to the resolution achieved by our telescopes that only detect the most luminous galaxies (in particular, at high redshift). Current instruments do not detect the faintest objects; therefore, their SFR cannot be inferred with that method. Consequently, there is an excess in the star formation rate predicted by the simulations -on the left- to observational data. The discrepancy between the calculated and the observed SFR is corrected in the right panel by imposing a luminosity cut $M_{UV} < -17$ (corresponding to a minimum SFR > 0.331 $M_\odot$/yr and the absolute magnitude set by Hubble observations). When we impose

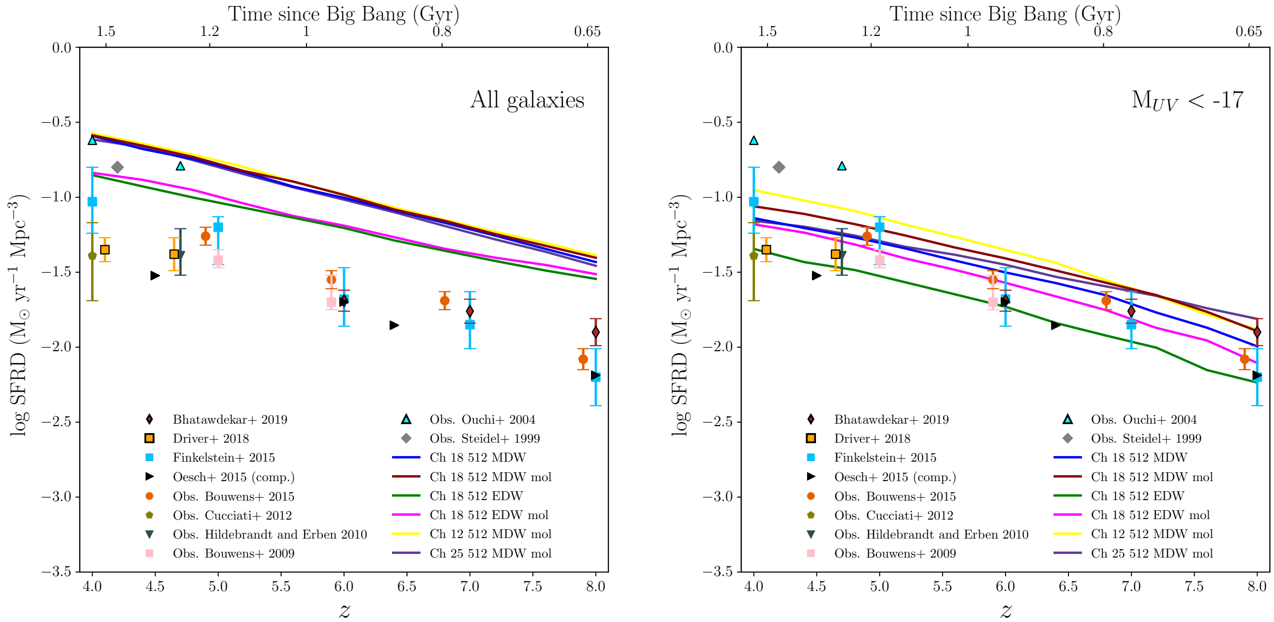

Fig. 5. Cosmic star formation rate density in the redshift range of $4 < z < 8$. The predictions from the simulations are compared with observations from Bhatawdekar et al. (2019) shown as brown diamonts, Driver et al. (2018) as yellow squares, Bouwens et al. (2015) as orange circles (with dust corrections), Cucciati et al. (2012) as an olive pentagon, Hildebrandt et al. (2010) as a green inverted triangle, Bouwens et al. (2009) as a pink square, Ouchi et al. (2004) as cyan triangles and Steidel et al. (1999) as a grey diamond. In the left panel, the SFR in the simulations is computed including all objects in the box per unit volume. On the right, the observable is limited to masses with the luminosity cut of $M_{UV} < -17$, equivalent to a minimum SFR of $> 0.331 M_\odot/\mathrm{yr}$, following the observational constraints of our current telescopes. The color figure can be viewed online.

the latter criterion to the simulations, the predicted SFR agrees well with the observations to-date (except for data points measured by Steidel et al. (1999) and Ouchi et al. (2004) that do not account for dust corrections).

Interestingly, data from Driver et al. (2018) and Bhatawdekar et al. (2019) had not been published when our simulations were run, but most of the models are in agreement with these observations.

On the other hand, the cosmic SFR reported by Finkelstein (2016) -with a corresponding comparison with Madau & Dickinson (2014)- shows an increment of 1 dex in their reference model, consistent with findings from this work with the mass cut $M_{UV} < -17$ (right panel of Figure 5).

Figure 6 shows a compilation of theoretical predictions for the cosmic star formation rate by UniverseMachine (Behroozi et al. 2020), L-Galaxies 2020 (Henriques et al. 2020; Yates et al. 2021a), Flares (Lovell et al. 2021; Vijayan et al. 2021), TNG100 (Nelson et al. 2018; Pillepich et al. 2018; Naiman et al. 2018; Marinacci et al. 2018; Springel et al. 2018), Eagle (Crain et al. 2015; Schaye et al. 2015) and our models.

Except for Ch 18 512 EDW, all our simulations show an excess of the SFR when compared with other theoretical models. As mentioned in a previous section, the simulation with the closest configuration to ours is Eagle, and this explains why their calculated SFR is compatible with our runs with the energy-driven winds prescription for the supernova outflows. This is also true with TNG100, which agrees well with EDW runs, but it is always below the prediction with MDW realizations. This outcome from our simulations is promising, since the winds implemented in the IllustrisTNG project have much more complex dynamics than ours: the velocity of the galactic winds v_w also depends on z (suppressing the efficiency of winds with the Hubble factor, Pillepich et al. 2018), but scales in the same way as our winds with the virial halo mass. Another remarkable difference in the IllustrisTNG winds is that the outflow mass loading is a non-monotonic function of the galaxy stellar mass (Nelson et al. 2018). We do not account for such dependence in our models. Finally, TNG introduces an improved mechanism for the AGN feedback, even for a low accretion rate, whereas this work does not account for AGN feedback.

A slightly different scenario is drawn with the two versions of L-Galaxies 2020. Both configurations match the observed SFR at low and intermediate redshifts because their semi-analytical models were built to follow the chemical enrichment at late times, not during reionization. Besides, their models heavily rely on observations from

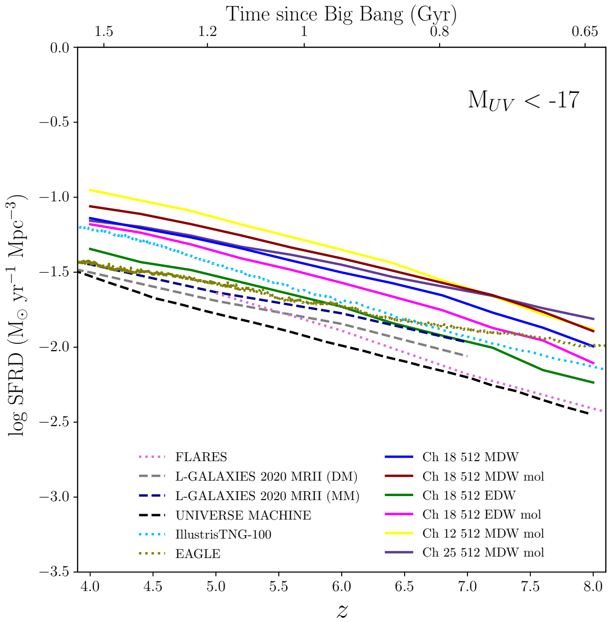

Fig. 6. Cosmic star formation rate density in the redshift range of $4 < z < 8$. The predictions from our models are compared with the calculated SFR with the UniverseMachine (Behroozi et al. 2020), L-Galaxies 2020 (Henriques et al. 2020; Yates et al. 2021a), Flares (Lovell et al. 2021; Vijayan et al. 2021), TNG100 (Nelson et al. 2018; Pillepich et al. 2018; Naiman et al. 2018; Marinacci et al. 2018; Springel et al. 2018), and the Eagle simulations (Crain et al. 2015; Schaye et al. 2015). The observable is limited to observed galaxies with absolute magnitude cut of $M_{UV} < -17$, equivalent to a minimum SFR of $> 0.331 M_\odot$/yr. The color figure can be viewed online.

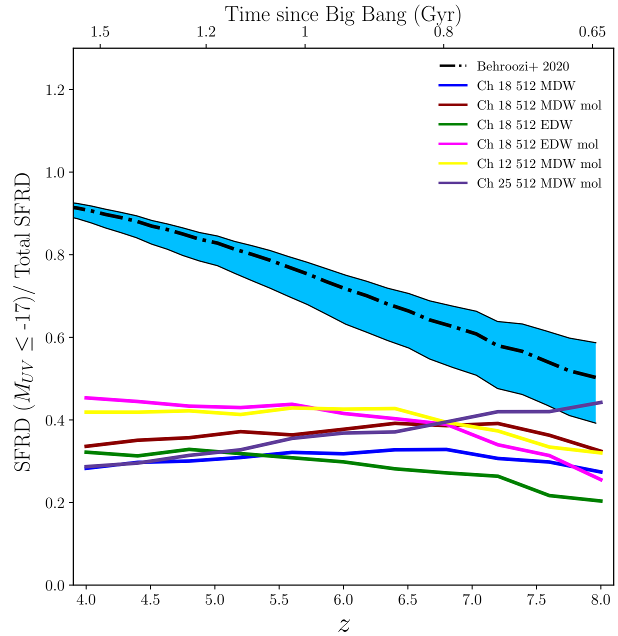

Fig. 7. Predicted ratio between the observed $M_{UV} < -17$ and total cosmic star formation rates from the simulations, and comparison with UniverseMachine ratio. The blue band indicates the error, and the dashed black line the mean value from the set of simulations. The color figure can be viewed online.

damped Lyman systems (DLAs) that cannot be extended to the redshifts of the EoR (García et al. 2017b). The gap in the calculated SFR grows among our runs and large cosmological simulations, particularly towards $z \rightarrow 8$. The UniverseMachine and Flares theoretical models aim to correct the UV luminosity function and to provide a forecast for future wide-field surveys, as the Nancy Roman (previously known as Wfirst), Euclid or JWST. Findings from these large volume boxes, with broader redshift ranges, are poorly constrained by periodic hydrodynamical simulations due to their limited volume, and consequently, reduced number of massive galaxies.

It is worth mentioning that the different supernova feedback mechanisms play a dominant role in the evolution of the star formation rate. Figures 5 and 6 show lower values for the SFR with energy-driven winds than momentum-driven winds (EDW and MDW, respectively), indicating that the former mechanism is more efficient at quenching the SFR because it prevents the overcooling present in the latter case, which leads to an excess of the number of stars that would form during a time interval of $\approx$ 1 billion years ($z = 8$ to 4). Notably, once many star formation events occur in the simulation, the stochastic SFR converges to its continuous history, and the galaxies grow in size and mass through this physical scheme.

Finally, it is interesting to study the ratio between the observed $M_{UV} < -17$ and the total cosmic star formation rates in the different realizations considered in Figure 5. Although, this is not an observable, it reflects how the mass cut affects the overall SFR in the synthetic realizations.

Figure 7 shows the predicted ratio from the simulations and UniverseMachine. Most of our configurations show a flat trend over the entire redshift range (except for the Ch 25 512 MDW mol, which is, in fact, the simulation with the lowest resolution). This result leads to the conclusion that $\approx$ 2 out of 5 simulated galaxies are about the luminosity cut of $M_{UV} < -17$, and this ratio does not evolve from $z = 8$ to 4. Conversely, Behroozi et al. (2020) show a rapid increment in the SFRD($M_{UV} < -17$) / Total SFRD, from 0.5 to 0.9 for $z = 8$ to 4, respectively. The latter is consistent with a change of 1 dex in Figure 5 -right panel-, indicating that the vast majority of the stars formed during a time frame of 900 Myr are above the luminosity cut $M_{UV} < -17$. Beyond the percentage inferred from our simulations, observations show an increasing number of bright galaxies at the tail of reionization and indirectly confirm the predicted ratio by Behroozi et al. (2020).

3.6. *Chemical Enrichment in the Simulations*

One of the strengths of this model is the self-consistent chemical enrichment implementation. The metals' production, spread, and mixing to the cincum- and intergalactic medium come from the assumed stellar lifetime function, stellar yields, and initial mass function.

It is worth noting that there are no measurements of the cosmic mass densities for any metal. The only tight constraint is that elements except for H and He should account for about 1% of the baryonic content in the Universe. This issue becomes even more challenging at high redshift when indirect methods are less precise to quantify the amount of any element. However, astronomers can estimate lower limits for the percentage of individual metals in the total census by measuring the total mass density for metal ions in the IGM (see work from García et al. (2017b) with CII and CIV, and the detections by Codoreanu et al. (2018) on SiII and SiIV). Also, an approximative evaluation of the relative metallicity to hydrogen with damped Lyα systems is possible, but this method does not provide any observational constraints for O or Si (among other metals).

Detections of absorption lines from Codoreanu et al. (2018), Meyer et al. (2019), and Cooper et al. (2019) show that we can set a lower limit for the mass density of silicon and oxygen through the reconstruction of the cosmic mass densities of their corresponding metal ions. Besides that, the low-to-high ionization ratio is an independent proxy for the end of reionization and reveals the gas state in the IGM. Both oxygen and silicon have observable ionization states that are exhibited in the spectra of high redshift quasars (OI, SiII and SiIV), redward from the Lyman α emission, and could provide complementary constraints to the metal enrichment, apart from carbon.

Figure 8 shows the cosmic evolution of the oxygen and silicon mass densities, from $z = 8$ to $z = 4$ when the chemical pollution has been occurring for about a billion years in the Universe from stars and supernovae. The cosmic density Ω as a function of z is obtained by summing the amount of each metal in all gas particles inside the simulated box. Finally, this calculation is divided by the comoving volume.

In addition to the metal mass densities predicted from our models, a comparison with L-Galaxies 2020 for O and Si is presented for their default and modified model (DM and MM, respectively; Yates et al. 2021b). Their normalization is similar because the overall amount of cosmic star formation is slightly higher in their modified model than the default setup, despite their distinctive mechanisms introduced to enrich the CGM/IGM; thus, the amount of each element produced overall is similar. For further details on their chemical enrichment modeling, see Yates et al. (2013). Both models differ by around one order of magnitude from our mass densities due to three main differences among their models and ours: (i) their predicted SFRD are lower at all redshifts. Therefore, it is expected that chemical pollution is less effective in this time frame. (ii) Yates et al. (2021b) assume different metal yields than the ones imposed on our set of simulations. The former is around 0.03 -in order to match late metallicities measured with DLAs-. Instead, the metal yield in all our models has a fixed value of 0.02. (iii) Their models include metal outflows released and spread by SNe-II, SNe-Ia, and AGB stars. In our simulations, neither AGB nor AGN are predominant in the feedback mechanisms. Thus fewer processes prevent the outburst of material.

Our predictions are also contrasted with the cosmic mass density calculated with TNG100. Their trends show a much faster evolution than the prediction from L-Galaxies 2020 and ours. These results are consistent with the SFRD exhibited by TNG100, on top of a sophisticated set of stellar yield tables (Table 2 from Pillepich et al. 2018).

From the observational side, a compelling test arises from the evolution of the mean metallicity in the Universe Figure 14 in Madau & Dickinson (2014), and Figure 8. In Madau & Dickinson (2014) an increment of 1 dex to the solar metallicity is present (under the assumption that the mass of heavy metals per baryon density produced over the cosmic history with a given SFR model and an IMF-averaged yield of $y = 0.02$), consistent with the predictions from the simulations at $z = 4$ - 7.

Finally, a correlation between the SFR in the simulations (mainly driven by the feedback processes of the gas) and the cosmic mass densities of these elements is found. Both metals in Figure 8 show a slight boost at all redshifts when the feedback mechanism is MDW. As mentioned above, the latter feedback prescription is more effective in producing an overcooling of the gas in the CGM, leading to a larger star-formation in the simulations. Hence, more metals are generated and expelled from the galaxies.

It is fair to conclude that the metal pollution scheme that occurs inside the synthetic realizations agrees with current limits obtained with metal ions of oxygen and silicon at high redshift Codoreanu et al. (2018), despite the limited number of absorption lines detected to date.

4. DISCUSSION AND FUTURE PERSPECTIVES

The numerical models presented in this work show a connection between galaxy properties and their hosting dark matter halos at high redshift, even though the simu-

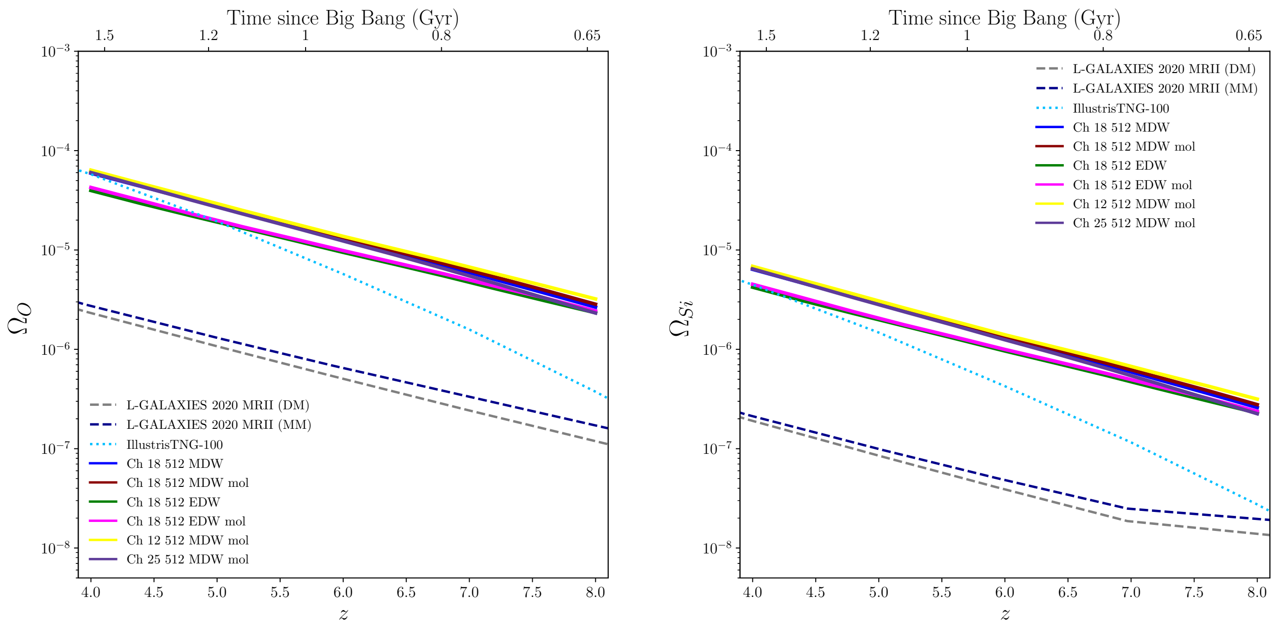

Fig. 8. Theoretical predictions for the total cosmological mass densities for oxygen (Ω_O) and silicon (Ω_{Si}) in the left and right panels, respectively. The color figure can be viewed online.

lations are not state-of-the-art. There is a good agreement of the theoretical models with observational detections of the galaxy stellar mass function at $z = 8$, 7, and 6, and the cosmic star formation rate at $4 < z < 8$. In addition, the numerical runs provide a forecast at high redshift for the halo mass function, the halo occupation fraction, the galaxy stellar-to-halo mass function, and the cosmological mass densities for oxygen and silicon. These predictions are concurrent with other theoretical models that account for larger boxes (thus, resolve a broader mass ranges) and/or implement other physical modules, as Renaissance, Eagle, IllustrisTNG, UniverseMachine, L-Galaxies 2020, Flares, Astraeus and CROC.

L-Galaxies 2020 predicts a lower SFR than all our models, and the discrepancy is larger when MDW prescriptions are taken into account because they do not quench the star formation process. This distinction leads to an order of magnitude difference in the cosmic mass densities for oxygen and silicon, while comparing both with their default and the modified models of L-Galaxies 2020 and our trends. Different stellar yields and metal enrichment schemes increase the gap between the calculated Ω_{X_i}. On the other hand, TNG100 shows similar outcomes as our predictions, although the latter project has a larger numerical resolution and implements modules with the latest improvements in magneto-hydrodynamical simulations. Now, Eagle simulation was calibrated to reproduce the galaxy stellar mass function and the morphology of galaxies in the local Universe, but it was not meant to be applied at high redshift with just a few resolved galaxies at $z = 7$. This issue was corrected with Flares, a 3.2 cGpc re-simulated version of Eagle, that accounts for very massive objects during reionization, which reside in extreme overdensities, not present neither in Eagle nor in our simulations. In that sense, our comparisons of the CSFR with Eagle are more consistent than with Flares.

On the other hand, the models partially differ from the predicted values from UniverseMachine, most likely because the latter set of simulations are run and observational constrained at a vast redshift range ($0 < z < 15$), cover at least two orders of magnitude more in halo mass and have much more numerical resolution at the galactic level. Instead, the primary motivation for these runs explored was to test the IGM and not explicitly focus on halo properties.

Notably, the reliable cosmic star formation history predicted by the models allows us to have a robust theoretical forecasting for chemical pollution. The effective feedback prescriptions play a significant role in regulating and quenching the star formation in the early galaxies and provide a mechanism to spread out metals to the IGM.

Furthermore, it is worth noting that a big caveat of these theoretical models is that they do not include a module for dust extinction nor low metallicity systems; hence, POP III is only represented by massive stars, but not by being metal-free in the scheme. As mentioned above, the resolved halo mass range in the simulations is relatively narrow because of the small box sizes.

Besides, these models do not deliver predictions for the faint-end slopes for stellar mass and luminosity functions. Nonetheless, Figure 4 is consistent with a constant power-law slope $\alpha = -2$, with little evolution from $z = 8$ to 6. The latter result is a key point if one wants to anticipate the future observations from JWST and other large telescopes planned to shed light on the formation of the first structures and the evolution of the epoch of reionization.

Moreover, at the redshift range of this study ($4 < z < 8$), the number of bright galaxies ($M_{UV} < -17$ according to the Hubble Space Telescope resolution) accounts for 40% of the total amount of the galaxies in the simulations, according to Figure 7, with little evolution in a billion years. This effect is due to the significant efficiency of the star formation of high-mass halos. However, the number of massive halos drops by three orders of magnitude in the redshift period from 4 to 8, leading to a decreasing count of bright galaxies, which is consistent with the faint-end slope ≈ -2, and with the findings by Robertson et al. (2015), Liu et al. (2016), García et al. (2017a) and Bhatawdekar et al. (2019): that reionization was mainly driven by faint galaxies, due to the small number of bright galaxies in the early Universe.

Finally, it is essential to point out that galaxies and quasars at high redshift generate most of the ionizing flux that drove the EoR. Although results from García & Ryan-Weber (2020) show that variations in the uniform ultraviolet background have little effect on the observed metals, it strongly determines the cooling processes and the subsequent star formation/metal pollution. This assumption will be tested once JWST measures the faint end of both the galaxy and quasar luminosity function out to $z \approx 10$.

5. CONCLUSIONS

This work presents a set of hydrodynamical simulations at high redshift ($4 < z < 8$) with galactic feedback prescriptions and molecular and metal cooling. The study's primary goal is to describe the evolution of galaxy properties and their connection with the dark matter halos that host these galaxies at the tail of reionization.

The proposed models agree with the observed galaxy stellar mass function at $z = 8$, 7, and 6, and the cosmic star formation rate at $4 < z < 8$. Moreover, they provide a purely theoretical prediction for different galaxy-to-halo statistics and the cosmological mass densities for oxygen and silicon during a billion year time-frame. These results are consistent with other simulations that consider modules with diverse physical processes, including Renaissance, Astraeus, CROC and UniverseMachine, that span more extensive redshift ranges than the ones considered here, and bigger box sizes that allow them to resolve more massive halos, thus, larger galaxies at early times. The best agreement with our models occurs for Eagle and TNG100 because these models have similar SPH configurations with modified versions for the galactic winds and equivalent chemical enrichment schemes. L-Galaxies 2020 shows more significant differences in the SFRD and in the chemical pollution of CGM and IGM. These contrasting results are mainly driven by introducing a semi-analytical treatment in their case, whereas our models rely on a hydrodynamical set up to describe the physics of the baryons. The more significant discrepancies among our results and other theoretical models appear with the UniverseMachine and Flares. This is due to the large volumes tested by the latter simulations that resolve more massive galaxies. Small boxes, as the ones used in this work, lead to degraded results in the cosmological scales. However, we remind the reader that our models were initially configured to accurately describe the IGM, at the expense of sacrificing massive structures.

There is a clear correlation between the cosmic star formation history and the metal enrichment of the intergalactic medium in our models, and both processes are regulated by the galaxy and supernova feedback prescriptions in the simulations.

Recovering mass densities of oxygen and silicon is a purely theoretical prediction and sets a lower limit that can be contrasted with the observed cosmic mass density from the metal absorption lines visible at high redshift, as OI, SiII, and SiIV.

Finally, the simulations do not provide a direct prediction for the faint-end slope of the galaxy luminosity function, but a constant stellar-to-halo mass ratio and the slope of galaxy stellar mass function in our models lead to an inferred constant power-law slope $\alpha = -2$, at $z = 8$ - 6. This last conclusion will be tested and constrained by JWST shortly. The upcoming space and ground-based telescopes will display the assembly of galaxies while the EoR is proceeding and unveil the early Universe with unprecedented precision.

The author thanks Universidad ECCI for its support, and Swinburne University of Technology where the simulations were run. L.A. García acknowledges the valuable contribution from Robert Yates, Peter Behroozi and Aswin Vijayan for sharing data in private communications and their insightful comments that improved the discussion of the results. In addition, the author recognizes the enormous input to her work from large collaborations such as IllustrisTNG project and Flares by making their simulation products publicly available.

REFERENCES

Asplund, M., Grevesse, N., Sauval, A. J., & Scott, P. 2009, ARA&A, 47, 481, https://doi.org/10.1146/annurev.astro.46.060407.145222

Atek, H., Richard, J., Kneib, J.-P., et al. 2015, ApJ, 800, 18, https://doi.org/10.1088/0004-637x/800/1/18

Behroozi, P., Conroy, C., Wechsler, R. H., et al. 2020, MNRAS, 499, 5702, https://doi.org/10.1093/mnras/staa3164

Bhatawdekar, R., Conselice, Ch. J., Margalef-Bentabol, B., & Duncan, K. 2019, MNRAS, 486, 3805, https://doi.org/10.1093/mnras/stz866

Bouwens, R. J., Illingworth, G. D., Franx, M., et al. 2009, ApJ, 705, 936, https://doi.org/10.1088/0004-637x/705/1/936

Bouwens, R. J., Illingworth, G. D., Oesch, P. A., et al. 2015, ApJ, 811, 140, https://doi.org/10.1088/0004-637x/811/2/140

Chabrier, G. 2003, PASP, 115, 763, https://doi.org/10.1086/376392

Codoreanu, A., Ryan-Weber, E. V., García, L. A., et al. 2018, MNRAS, 481, 4940, https://doi.org/10.1093/mnras/sty2576

Cooper, T. J., Simcoe, R. A., Cooksey, K. L., et al. 2019, ApJ, 882, 77, https://doi.org/10.3847/1538-4357/ab3402

Crain, R. A., Schaye, J., Bower, R. G., et al. 2015, MNRAS, 450, 1937, https://doi.org/10.1093/mnras/stv725

Cucciati, O., Tresse, L., Ilbert, O., et al. 2012, A&A, 539, 31, https://doi.org/10.1051/0004-6361/201118010

Dolag, K., Vazza, F., Brunetti, G., & Tormen, G. 2005, MNRAS, 364, 753, https://doi.org/10.1111/j.1365-2966.2005.09630.x

Driver, S. P., Andrews, S. K., da Cunha, E., et al. 2018, MNRAS, 475, 2891, https://doi.org/10.1093/mnras/stx2728

Duncan, K., Conselice, C. J., Mortlock, A., et al. 2014, MNRAS, 444, 2960, https://doi.org/10.1093/mnras/stu1622

Fabjan, D., Borgani, S., Tornatore, L., et al. 2010, MNRAS, 401, 1670, https://doi.org/10.1111/j.1365-2966.2009.15794.x

Finkelstein, S. L., Ryan, R. E. Jr., Papovich, C., et al. 2015, ApJ, 810, 71, https://doi.org/10.1088/0004-637X/810/1/71

Finkelstein, S. L. 2016, PASA, 33, e037, https://doi.org/10.1017/pasa.2016.26

García, L. A., Tescari, E., Ryan-Weber, E. V., & Wyithe, J. S. B. 2017a, MNRAS, 469, 53, https://doi.org/10.1093/mnrasl/slx053

__________. 2017b, MNRAS, 470, 2494, https://doi.org/10.1093/mnras/stx1371

García, L. A. & Ryan-Weber, E. V. 2020, RMxAA, 56, 97, https://doi.org/10.22201/ia.01851101p.2020.56.01.11

Gardner, J. P., Mather, J. C., Clampin, M., et al. 2006, Proc. SPIE6265, Space Telescopes and Instrumentation I: Optical, Infrared and Millimeter, ed. J. C. Mather, A. Howard, and M. W. M. de Graauw, 62650

González, V., Labbé, I., Bouwens, R. J., et al. 2011, ApJ, 735, 34, https://doi.org/10.1088/2041-8205/735/2/L34

Grazian, A., Fontana, A., Santini, P., et al. 2015, A&A, 575, 96, https://doi.org/10.1051/0004-6361/201424750

Henriques, B. M. B., Yates, R. M., Fu, J., et al. 2020, MNRAS, 491, 5795, https://doi.org/10.1093/mnras/stz3233

Hildebrandt, H., Arnouts, S., Capak, P., et al. 2010, A&A, 523, 31, https://doi.org/10.1051/0004-6361/201014885

Hutter, A., Dayal, P., Yepes, G., et al. 2021, MNRAS, 503, 3698, https://doi.org/10.1093/mnras/stab602

Ishigaki, M., Kawamata, R., Ouchi, M., et al. 2018, ApJ, 854, 73, https://doi.org/10.3847/1538-4357/aaa544

Katz, N., Weinberg, D. H., & Hernquist, L. 1996, ApJS, 105, 19, https://doi.org/10.1086/192305

Kennicutt, R. C. Jr. 1998, ApJ, 498, 541, https://doi.org/10.1086/305588

Liu, C., Mutch, S. J., Angel, P. W., et al. 2016, MNRAS, 462, 235, https://doi.org/10.1093/mnras/stw1015

Lovell, C. C., Vijayan, A. P., Thomas, P. A., et al. 2021, MNRAS, 500, 2127, https://doi.org/10.1093/mnras/staa3360

Madau, P. & Dickinson, M. 2014, ARA&A, 52, 415, https://doi.org/10.1146/annurev-astro-081811-125615

Maio, U., Dolag, K., Ciardi, B., & Tornatore, L. 2007, MNRAS, 379, 963, https://doi.org/10.1111/j.1365-2966.2007.12016.x

Maio, U. & Tescari, E. 2015, MNRAS, 453, 3798, https://doi.org/10.1093/mnras/stv1714

Marinacci, F., Vogelsberger, M., Pakmor, R., et al. 2018, MNRAS, 480, 5113, https://doi.org/10.1093/mnras/sty2206

Martin, N. F., Ibata, R. A., Conn, B. C., et al. 2005, SF2A-2005, Semaine de l'Astrophysique Francaise, ed. F. Casoli, T. Contini, J. M. Hameury, & L. Pagani, EdP-Sciences, 565

Matteucci, F. & Calura, F. 2005, MNRAS, 360, 447, https://doi.org/10.1111/j.1365-2966.2005.08908.x

McLeod, D. J., McLure, R. J., Dunlop, J. S., et al. 2015, MNRAS, 450, 3032, https://doi.org/10.1093/mnras/stv780

Meyer, R. A., Bosman, S. E. I., & Ellis, R. S. 2019, MNRAS, 487, 3305, https://doi.org/10.1093/mnras/stz1504

Naiman, J. P., Pillepich, A., Springel, V., et al. 2018, MNRAS, 477, 1206, https://doi.org/10.1093/mnras/sty618

Nelson, D., Pillepich, A., Springel, V., et al. 2018, MNRAS, 475, 624, https://doi.org/10.1093/mnras/stx3040

Oesch, P. A., Bouwens, R. J., Illingworth, G. D., et al. 2015, ApJ, 808, 104, https://doi.org/10.1088/0004-637x/808/1/104

Oesch, P. A., Bouwens, R. J., Illingworth, G. D., Labbé, I. & Stefanon, M. 2018, ApJ, 855, 105, https://doi.org/10.3847/1538-4357/aab03f

O'Shea, B. W., Wise, J. H., Xu, H., & Norman, M. L. 2015, ApJ, 807, 12, https://doi.org/10.1088/2041-8205/807/1/L12

Ouchi, M., Shimasaku, K., Okamura, S., et al. 2004, ApJ, 611, 660, https://doi.org/10.1086/422207

Padovani, P. & Matteucci, F. 1993, ApJ, 416, 26, https://doi.org/10.1086/173212

Pillepich, A., Springel, V., Nelson, D., et al. 2018, MNRAS, 473, 4077, https://doi.org/10.1093/mnras/stx2656

Planck Collaboration, Ade, P. A. R., Aghanim, N., et al. 2016, A&A, 594, 13, https://doi.org/10.1051/0004-6361/201525830

Planelles, S., Borgani, S., Dolag, K., et al. 2013, MNRAS, 431, 1487, https://doi.org/10.1093/mnras/stt265

Puchwein, E. & Springel, V. 2013, MNRAS, 428, 2966, https://doi.org/10.1093/mnras/sts243

Robertson, B. E., Ellis, R. S., Furlanetto, S. R., & Dunlop, J. S. 2015, ApJ, 802, 19, https://doi.org/10.1088/2041-8205/802/2/L19

Robertson, B. E. 2021, arXiv: 2110.13160

Schaye, J., Crain, R. A., Bower, R. G., et al. 2015, MNRAS, 446, 521, https://doi.org/10.1093/mnras/stu2058

Schechter, P. 1976, ApJ, 203, 297, https://doi.org/10.1086/154079

Song, M., Finkelstein, S. L., Ashby, M. L. N., et al. 2016, ApJ, 825, 5, https://doi.org/10.3847/0004-637x/825/1/5

Springel, V. & Hernquist, L. 2003, MNRAS, 339, 289, https://doi.org/10.1046/j.1365-8711.2003.06206.x

Springel, V. 2005, MNRAS, 364, 1105, https://doi.org/10.1111/j.1365-2966.2005.09655.x

Springel, V., di Matteo, T., & Hernquist, L. 2005, MNRAS, 361, 776, https://doi.org/10.1111/j.1365-2966.2005.09238.x

Springel, V., Pakmor, R., Pillepich, A., et al. 2018, MNRAS, 475, 676, https://doi.org/10.1093/mnras/stx3304

Stefanon, M., Bouwens, R. J., Labbé, I., et al. 2021, arXiv:2103.16571

Steidel, C. C., Adelberger, K. L., Giavalisco, M., Dickinson, M., & Pettini, M. 1999, ApJ, 519, 1, https://doi.org/10.1086/307363

Tegmark, M., Silk, J., Rees, M. J., et al. 1997, ApJ, 474, 1, https://doi.org/10.1086/303434

Tescari, E., Katsianis, A., Wyithe, J. S. B., et al. 2014, MNRAS, 438, 3490, https://doi.org/10.1093/mnras/stt2461

Thielemann, F.-K., Argast, D., Brachwitz, F., et al. 2003, ESO/MPA/MPE, From Twilight to Highlight: The Physics of Supernovae, ed. W. Hillebrandt & B. Leibundgut (Springer-Verlag), 331, https://doi.org/10.1007/10828549_46

Tornatore, L., Borgani, S., Dolag, K., & Matteucci, F. 2007, MNRAS, 382, 1050, https://doi.org/10.1111/j.1365-2966.2007.12070.x

Trebitsch, M., Volonteri, M., & Dubois, Y. 2020, MNRAS, 494, 3453, https://doi.org/10.1093/mnras/staa1012

Vijayan, A. P., Lovell, C. C., Wilkins, S. M., et al. 2021, MNRAS, 501, 3289, https://doi.org/10.1093/mnras/staa3715

Vogelsberger, M., Nelson, D., Pillepich, A., et al. 2020, MNRAS, 492, 5167, https://doi.org/10.1093/mnras/staa137

Weigel, A. K., Schawinski, K., & Bruderer, C. 2016, MNRAS, 459, 2150, https://doi.org/10.1093/mnras/stw756

Wiersma, R. P. C., Schaye, J., Theuns, T., Dalla Vecchia, C., & Tornatore, L. 2009, MNRAS, 399, 574, https://doi.org/10.1111/j.1365-2966.2009.15331.x

Williams, C. C., Curtis-Lake, E., Hainline, K. N., et al. 2018, ApJS, 236, 33, https://doi.org/10.3847/1538-4365/aabcbb

Woosley, S. E. & Weaver, T. A. 1995, ApJS, 101, 181, https://doi.org/10.1086/192237

Yates, R. M., Henriques, B., Thomas, P. A., et al. 2013, MNRAS, 435, 3500, https://doi.org/10.1093/mnras/stt1542

Yates, R. M., Peroux, C., & Nelson, D. 2021, arXiv: 2109.06888

Yates, R. M., Henriques, B. M. B., Fu, J., et al. 2021, MNRAS, 503, 4474, https://doi.org/10.1093/mnras/stab741

Zhu, H., Avestruz, C., & Gnedin, N. Y. 2020, ApJ, 899, 137, https://doi.org/10.3847/1538-4357/aba26d

Luz Ángela García: Cra. 19 No. 49-20, Bogotá, Colombia, Código Postal 11131 (lgarciap@ecci.edu.co).

Revista Mexicana de Astronomía y Astrofísica, **58**, 99–107 (2022)

https://doi.org/10.22201/ia.01851101p.2022.58.01.08

COMPREHENSIVE ANALYSIS OF THE FULL TESS ORBITAL PHASE CURVE OF WASP-121b

M. Eftekhar

Department of Physics, Faculty of Science, University of Zanjan, Iran.

Received February 8 2021; accepted February 7 2022

ABSTRACT

We present the full phase curve analysis of the ultrahot Jupiter WASP-121b using observations from the Transiting Exoplanet Survey Satellite (TESS). Our comprehensive phase curve model includes primary transit, secondary eclipse, thermal emission, reflection, and ellipsoidal tidal distortion. After removing the instrumental systematic noise, we reliably detect the secondary eclipse with a depth of 489^{+16}_{-10} parts-per-million (ppm), dominated by thermal emission. Using the TESS bandpass, we measure the dayside $2941^{+61}_{-150}K$ and nightside $2236^{+38}_{-97}K$ temperatures of WASP-121b. We find that a hotspot is well aligned with the substellar point, leading to the conclusion that there is an inefficient heat distribution from the dayside to the nightside. Our estimated geometric albedo, $A_g = 0.069^{+0.06}_{-0.02}$, suggest that WASP-121b has a low geometric albedo.

RESUMEN

Presentamos el análisis de la curva de fase completa del "Júpiter" ultracaliente WASP-121b, utilizando observaciones del satélite TESS. Nuestro modelo de la curva de fase completa incluye el tránsito primario, el eclipse secundario, emisión térmica, reflexión y distorsión elipsoidal por mareas. Después de eliminar el ruido instrumental sistemático, detectamos claramente el eclipse secundario, con una profundidad de 489^{+16}_{-10} partes por millón, mismo que está dominado por emisión térmica. En la banda del TESS determinamos valores de la temperatura diurna y nocturna de WASP-121 de $2941^{+61}_{-150}K$ y $2236^{+38}_{-97}K$, respectivamente. Encontramos que hay una mancha caliente alineada con el punto subestelar, lo que nos lleva a concluir que la distribución de calor entre la cara diurna y la nocturna es ineficiente. Nuestra estimación para el albedo geométrico, $A_g = 0.069^{+0.06}_{-0.02}$, sugiere un valor bajo para WASP-121b.

Key Words: methods: data analysis — planets and satellites: individual: WASP-121b — stars: individual: WASP-121b — techniques: photometric

1. INTRODUCTION

Since August 2018, the Transiting Exoplanet Survey Satellite (TESS, Ricker et al. 2015) has been delivering high-precision photometric observations in a broad optical band (0.6 - 0.95 μm) for a large sample of bright stars from the southern and northern hemispheres. The wavelength coverage of TESS allows measurements of the combined reflected and thermally emitted planetary light as a function of longitude.

The exoplanet WASP-121b was discovered by Delrez et al. (2016), with a period of ≈ 1.275 days, and it is one of the hottest transiting planets known to date. Its bright host F6-type star ($V = 10.4$), short orbital period, and inflated radius ($a/R_s = 3.674$, $R_p = 1.865 R_J$) makes it one of the best targets for investigating its atmosphere with various techniques. Moreover, due to its short orbital period, it is likely that WASP-121b is tidally locked to its host star (Daylan et al. 2021), which makes it probable to have atmospheric features detectable in the averaged planetary flux (Showman & Guillot 2002). Several studies have measured WASP-121b's primary transit (when an exoplanet passes in front of its host star) (e.g., Delrez et al. 2016; Evans et al. 2016, 2018). By using optical and near-infrared photometry, the depth of its secondary eclipse (i.e., when an exoplanet is occulted by its host star) was determined by Delrez et al. (2016); Kovacs & Kovacs (2019); Garhart (2019). The dayside and nightside temperatures of WASP-121b were measured as $2870K$ and $< 2200K$, respectively, according to an analysis of the thermal emission (Bourrier et al. 2020), which is to be expected given the planet's proximity to its host F-type star. The reflection component was not included in Bourrier et al. (2020) phase curve, but we take it into account in our comprehensive full phase curve model. WASP-121b's geometric albedo was estimated as $0.070^{+0.037}_{-0.040}$ based on the optical phase curve analysis by Daylan et al. (2021). In our analysis, the reflection component is also calculated simultaneously with other parameters to highlight the correlations between all of the constrained parameters.

The main objective of the current study is to learn more about the thermal emission and atmospheric structure of WASP-121b by performing our comprehensive joint model and by comparison of our results with previous studies like Daylan et al. (2021); Bourrier et al. (2020). To achieve this, we analyze the full-orbit optical TESS phase curve and model the primary transit, secondary eclipse, and four main components of the phase curve, which include tidal ellipsoidal distortion, thermal, and reflected emission of the planet. We also calculated rotational Doppler beaming and discovered that it is not significant given the precision of the light curves. We can determine the uncertainty and correlations among all constrained parameters using our comprehensive joint model, which allows us to extract information from all parameters at the same time.

Here, we describe our WASP-121b analysis by presenting our comprehensive phase curve model and comparing our findings to previous measurements. The paper is organized as follows; in § 2 we describe the observations and data reduction methods that were used. In § 3 we describe in detail the four different components that were used to characterise the phase curve of WASP-121b. In § 4 we present our joint model as well as the fitting procedure we employed to acquire our results. We provide our physical parameters derived from the TESS observations in § 5, and discuss our results providing a brief summary in § 6.

2. OBSERVATIONS AND DATA REDUCTION

Between the 8th of January and 1st of February 2019, the TESS camera 3 monitored WASP-121 (also known as TIC 22529346) throughout its sector number 7. The observation span was 24.5 days and included 18 primary transits of WASP-121b.

Photometric data were processed through the Science Processing Operations Center (SPOC) pipeline (Jenkins 2017). In this study, we decided to use PDCSAP (Pre-Search Data Conditioning) light curves because they are corrected for instrumental systematic noise which is present in the Simple Aperture Photometry (SAP) light curves; thus PDCSAP light curves show considerably less scatter and short-timescale flux variation (Smith et al. 2012; Stumpe et al. 2014). The PDCSAP light curve of WASP-121 was also used in other studies investigating the phase curve of WASP-121b such as Bourrier et al. (2020).

The PDCSAP photometry is presented in the upper panel of Figure 1, which shows the remaining systematics in the data at short time scales, particularly in Sector 7's second orbit. Instrumental effects including changes in the thermal state of TESS and pointing instabilities cause these remaining systematics. The PDCSAP light curve's median was used to normalise the data. To have a fair comparison with Bourrier et al. (2020), we did exactly the same steps in preprocessing of data. Although the dominant systematics were corrected by default in the PDCSAP light curve, we corrected it further for the remaining systematics. To do this, we used the median detrending algorithm with a window length of one orbital period to smooth the PDCSAP light curve, keeping variability at the planetary period and minimising the effect of normalisation on the phase curve of WASP-121b. If we choose a smaller window length of one orbital period, then it is very likely that the signal will be absorbed and removed from the atmosphere. We followed the same processes using Bourrier et al. (2020); the regression is shown in Figure 1 and was implemented using the Python package `wotan` (Hippke et al. 2019). We also performed phase folding at the orbital period of WASP-12b and binned every 50 datapoints after detrending; these reprocessed data were used in our further analysis. The reprocessed data are shown in Figure 2.

3. PHASE CURVE

In addition to the primary transit light curve and secondary eclipse, photometric observations reveal additional variation induced by the orbiting exoplanet over the full planetary orbit. This variation

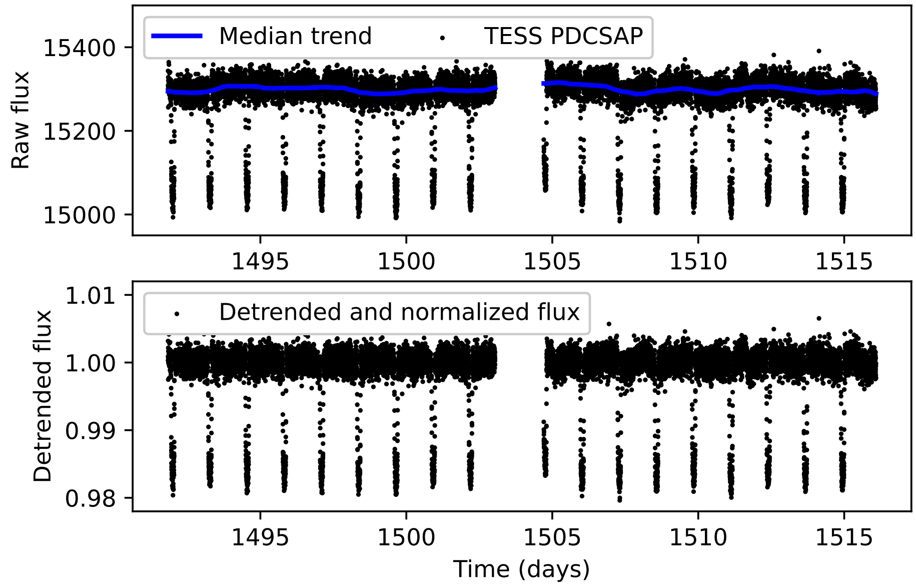

Fig. 1. (Top) TESS light curve (PDCSAP flux) of WASP-121. The PDCSAP photometry is indicated with black dots, and the solid blue line shows the trend obtained by applying a detrending filter determined by `wotan`. (Bottom) PDCSAP light curve after normalization by its median detrending. The color figure can be viewed online.

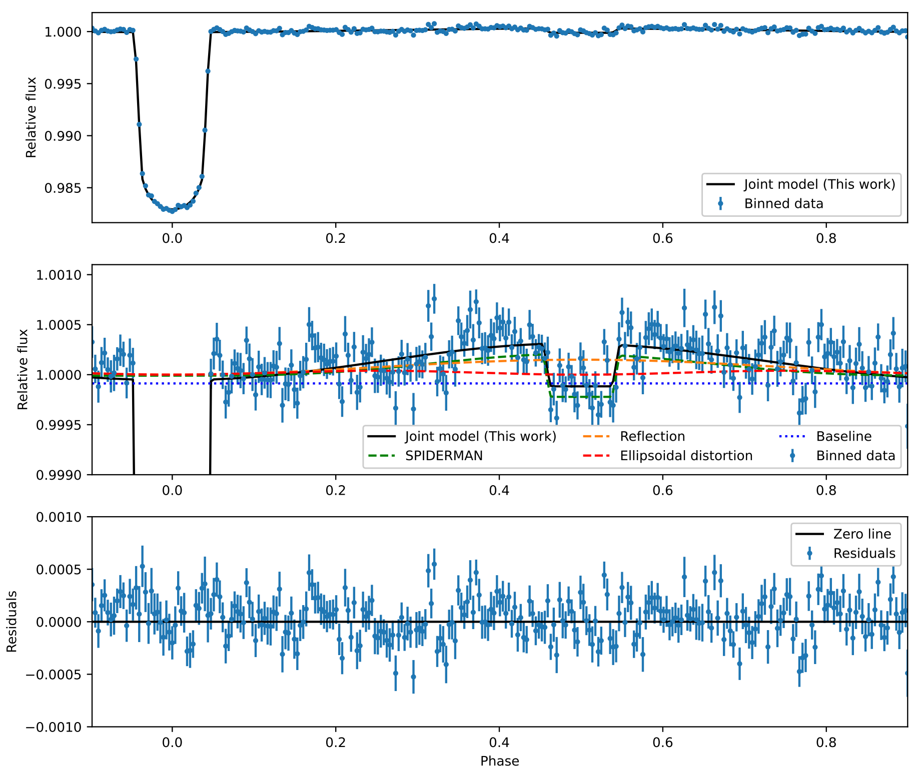

Fig. 2. (Top) Our reprocessed data of WASP-121 (blue dots) compared to our best fitted full phase curve model (black curve). (Middle) zoom of the secondary eclipse and phase curve variations with the reflection modulation (dashed orange curve), ellipsoidal distortion (dashed red curve), and baseline (dotted blue line). (Bottom) The best fitted model's corresponding residuals. The color figure can be viewed online.

can be decomposed into several components, namely thermal emission, reflected light, Doppler beaming, and ellipsoidal variation. In this study, we assume that the phase curve variation is a combination of thermal emission, reflection, and ellipsoidal variation, and we ignore the Doppler beaming; the reason will be explained in § 3.3.

3.1. *Thermal Emission*

As mentioned in § 1, due to its tidal locking and proximity to its host star, inefficient heat transport from the dayside to the nightside WASP-121b should have a significant temperature difference between its permanent day and night sides (Bourrier et al. 2020). As a result, WASP-121b is expected to have a zone (hotspot) with maximum temperature and higher thermal flux in comparison to the rest.

In order to model WASP-121b's thermal emission component, we used a semi-physical model based on Zhang & Showman (2017) which has been implemented in `spiderman` (Louden & Kreidberg 2018). It uses three parameters to reproduce the main characteristics of the thermal light curve. The thermal phase shift is controlled by the ratio of radiative versus advection time scale, ξ. The hotspot's longitudinal shift becomes larger as ξ increases. If ξ increases, the nightside temperature increases while the dayside temperatures drop, resulting in a reduction of the difference between day and nightside temperatures. The temperature on the planet's night side is controlled by the nightside temperature, T_N. Finally, ΔT_{DN} represents the difference between day and night temperatures. To calculate the temperatures in the TESS bandpass, we used Phoenix model spectrum (Husser et al. 2013) for the host star by using `spiderman`.

3.2. *Reflection*

In the bandpass of observations, the reflection is the proportion of light from the host star that is reflected by the planetary atmosphere and/or planetary surface. The phase modulation of the reflection is sinusoidal, with the same maximum and minimum as the thermal emission. The difference in reflectivity (albedo) determines the amplitude of the reflection (Shporer 2017). A basic form of reflection phase modulation can be described as:

$$Reflection = A_{ref}\Big(1 + \cos\big(2\pi(\phi + \Delta_P/P) + \pi\big)\Big), \tag{1}$$

where, A_{ref} is the amplitude of the reflection, which depends on the albedo, ϕ, is the orbital phase, P is the orbital period, and Δ_P is the phase shift. The geometric albedo of a planet, Ag, is the ratio of its reflectivity at zero phase angle to that of a Lambertian disk, and can be calculated as (Rodler et al. 2010)

$$A_g = A_{ref}(a/R_p)^2, \tag{2}$$

where a is the semi-major axis and R_p is the planet's radius.

3.3. *Doppler Beaming*

Doppler Beaming is caused by relativistic effects on the host star's emitted light along our line of sight. For circular orbits, the Doppler beaming component has a sinusoidal form with a maximum during the quadrature (0.25) phases and at the quadrature (0.75) phases. The amplitude of the beaming component, A_{beam}, can be computed using the physical parameters of the system, as in Shporer (2017):

$$A_{beam} = 0.0028\alpha_{beam}\left(\frac{P}{day}\right)^{-1/3} \times \left(\frac{M_1+M_2}{M_\odot}\right)^{-2/3}\left(\frac{M_2\sin i}{M_\odot}\right), \tag{3}$$

where

$$\alpha_{beam} = \int \frac{1}{4}\frac{xe^x}{e^x-1}dx, x \equiv \frac{hc}{kT_{eff}\lambda}. \tag{4}$$

Here M_1, M_2, $M_\odot$ are the masses of the host star, planet, and sun, respectively. i is the orbital inclination angle, h is Planck's constant, k is Boltzmann's constant, T_{eff} is the stellar effective temperature, and λ is the observed wavelength.

In our study, this integral should be taken in the TESS passband. Based on equation 2, we estimate the amplitude of Doppler beaming to be ≈ 2 parts-per-million (ppm), which is significantly smaller than the precision achievable by TESS (even for the case of a star as bright as WASP-121), so we decided to exclude the Doppler beaming from our total phase curve model.

3.4. *Ellipsoidal Variations*

The gravitational pull of a close-in exoplanet causes the host star to deviate from a spherical form to an ellipsoid. This deformation produces photometric orbital modulations with an amplitude that can be approximated by Shporer (2017):

$$A_{ellip} \simeq 13\alpha_{ellip}\sin i \times \left(\frac{R_1}{R_\odot}\right)^3\left(\frac{M_1}{M_\odot}\right)^{-2}\left(\frac{P}{day}\right)^{-2}\left(\frac{M_2\sin i}{M_J}\right)[ppm], \tag{5}$$

TABLE 1

FREE PARAMETERS, UNIFORM PRIORS RANGE, AND THE BEST FITTED VALUES

Parameter	Prior	Value
Planet-star radii ratio; R_p/R_s	$[0, 1]$	$0.1234^{+0.0005}_{-0.0005}$
Scaled semi-major axis; a/R_s	$[0, 5]$	$3.792^{+0.023}_{-0.039}$
Orbital inclination i (deg)	$[0, 90]$	$88.80^{+1.27}_{-1.23}$
limb darkening coefficient; u_1	$[0, 1]$	$0.260^{+0.034}_{-0.042}$
limb darkening coefficient; u_2	$[0, 1]$	$0.132^{+0.056}_{-0.082}$
Radiative to advective timescales ratio; ξ	$[-10, 10]$	$-0.022^{+0.159}_{-0.141}$
Nightside temperature; T_N (K)	$[0, 5000]$	2236^{+97}_{-38}
Day-night temperature difference; ΔT_{DN} (K)	$[0, 2000]$	734^{+28}_{-55}
Additive baseline	$[-0.1, 0.1]$	$-0.00014^{+1.7\times10^{-6}}_{-0.8\times10^{-6}}$
Secondary eclipse depth (ppm)	$[0, 800]$	489^{+16}_{-10}
Amplitude of the reflection; A_{ref} (ppm)	$[0, 500]$	$73^{+2.2}_{-3.1}$
Reflection phase shift; Δ_P	$[-0.5, 0.5]$	$-0.0008^{+0.0012}_{-0.0071}$
Amplitude of ellipsoidal variations; A_{ellip} (ppm)	$[0, 100]$	20^{+2}_{-3}

where

$$\alpha_{ellip} = 0.15\frac{(15+u)(1+g)}{(3-u)}. \qquad (6)$$

Here, u is the linear limb darkening coefficient and g is the gravity darkening coefficient. We utilized a tabulation of these coefficient values from Claret (2017) and estimated the amplitude of ellipsoidal variation to be ≈ 20 ppm, which is compatible with the precision achievable by TESS on WASP-121. Therefore, we decided to consider the ellipsoidal modulations in our total phase curve model. The ellipsoidal variation shows two peaks at phase quadratures 0.25 and 0.75, respectively, and can be modeled as:

$$Ellipsoidial = A_{ellip}\big(1+\cos(4\pi\phi-\pi)\big). \qquad (7)$$

4. MODEL AND FITTING PROCEDURE

Our joint model consists of primary transit, secondary eclipse, and phase curves that incorporate the thermal emission, reflection, and ellipsoidal variations. We also included a constant baseline to compensate for any normalization bias. For the primary transit and secondary eclipse we used the Python packages `batman` (Kreidberg 2015) and for the thermal emission, we used `spiderman` (Louden & Kreidberg 2018). Our thermal model is based on a semi-physical model of Zhang & Showman (see § 3.1) implemented by `spiderman`. The reflection is modeled as equation 1 (see § 3.2) and ellipsoidal variations are modeled as equation 7 (see § 3.4). Performing a joint model analysis allows us to extract information about all parameters simultaneously from the data sets. It also gives us the ability to assess the uncertainty and correlations between all of the constrained parameters.

To determine the parameters of the full phase curve, we fitted our joint model to the reprocessed data (see § 2). The best fit parameters and their associated uncertainties are determined using a Markov Chain Monte Carlo (MCMC) approach using the affine invariant ensemble sampler `emcee` package (Foreman-Mackey et al. 2013).

We fit for R_p/R_s, a/R_s, i, u_1, u_2, ξ, T_N, ΔT_{DN}, additive baseline, secondary eclipse depth, A_{ref}, Δ_P and A_{ellip}. The priors of u_1, u_2, ξ, T_N, and ΔT_{DN} are equal to those of Bourrier et al. (2020). The priors of R_p/R_s, a/R_s, and i had normal priors in Bourrier et al. (2020), and we chose an uninformative uniform prior for them. The additional parameters in our model have a wide uninformative prior, allowing us to obtain their best estimation.

Table 1 provides information on individual prior distributions that were chosen. We fix the transit epoch, T_0 and orbital period, P because we use one sector of TESS data which covers about 24 days, whereas the period from Delrez et al. (2016) takes into account years of WASP data, which provides more information on the period. Considering the Lucy-Sweeney bias (Lucy & Sweeney 1971), we adopt a circular orbit by fixing the eccentricity e, to 0, and the argument of periastron, ω to values obtained by Bourrier et al. (2020). To generate the posterior distributions, we ran 700 walkers over 1000 steps with a burn-in phase of the 20% sample. The

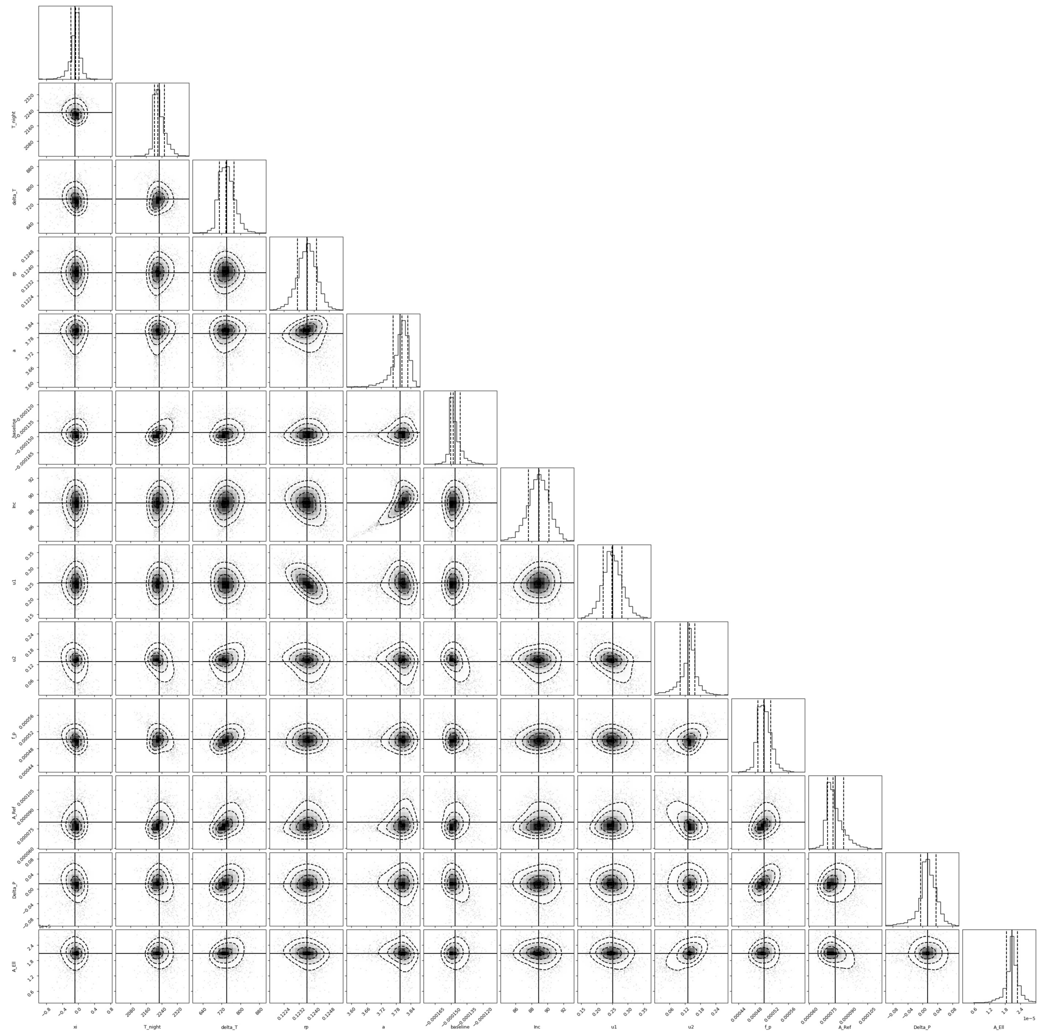

Fig. 3. Retrieved posterior distributions by fitting our joint model to the phase curve of the WASP-121b. the black points indicate the best-fit values, and the colours of the contours highlight the 1 and 2σ simultaneous $2D$ confidence regions which contain respectively 39.3% and 86.5% of the samples. The solid black line corresponds to the median values, while dashed black lines show the 1σ highest density intervals.

walkers are plotted and visually inspected for convergence. We estimated the median and standard deviation from the posterior distributions at 1σ, which contains 68% of the posterior distribution, for our best fitted values and uncertainties.

5. RESULT

The results of our joint model fitting to the reprocessed data are shown in Table 1. The best fitted model's reduced chi-squared $\chi 2$ (i.e., RMS of the residuals per degree of freedom) is 1.29, indicating a good fit to the TESS photometry. Figure 2 shows the reprocessed data, as well as the best fitted model of the full phase curve. Our best-fitted model's residuals still exhibit some correlated noise, which could be uncorrected TESS systematic noise. Identical correlated noise was also present in the residuals of the best-fitted Bourrier et al. (2020). The corner plot for our retrieved posterior distributions from the joint model fit is shown in Figure 3. In addition, when we fit our joint model to unbinned data, we found that our results are generally consistent. Furthermore, we binned every 80 datapoints and fitted our joint model, and the results were consistent with the values presented in Table 1. This test demonstrates that the results provided in this work are robust to the binning effect.

We calculated a planetary radius (in stellar radii), (R_p/R_s), of $0.1234^{+0.0005}_{-0.0005}$ and a reasonably large secondary eclipse depth with amplitudes of

489^{+16}_{-10} ppm. Our measured secondary eclipse depth value is within 1σ of the value reported in the Daylan et al. (2021). However, our estimated value is larger (1.6σ) than Bourrier et al. (2020) measured value. Other orbital and transit parameters agree well with previously published values in the literature (Wong et al. 2020; Daylan et al. 2021; Bourrier et al. 2020).

Our estimation of the geometric albedo using equation 2 is $0.069^{+0.06}_{-0.02}$ which is consistent with the estimate of Daylan et al. (2021) of $0.070^{+0.037}_{-0.040}$ ppm. Mallonn et al. (2019) estimated a geometric albedo of $A_g = 0.16 \pm 0.11$ in the z' band.

We measured the ratio of radiative versus advection time scale of atmospheric height as $\xi = -0.022^{+0.159}_{-0.141}$, which is consistent with zero. This implies that there is no thermal redistribution between WASP-121b's day and night sides, resulting in a larger day-night temperature difference. We measured the temperature of the night and day sides, $2236^{+97}_{-38}K$ and $2941^{+147}_{-61}K$, respectively, which are in agreement with the values published in Bourrier et al. (2020) and Daylan et al. (2021). Parmentier et al. (2018) and Evans et al. (2017) by fitting the blackbody model to Spitzer and Hubble Space Telescope WFC3 observations could measure a dayside temperature of $2650 \pm 10K$ and $2700 \pm 10K$, respectively.

Based on our best fitted model, we estimated the ellipsoidal variation amplitude to be 20^{+2}_{-3} ppm, which is more in line with the theoretical estimate of 20 ppm based on equation 5 and slightly larger than Daylan et al. (2021) estimation which was 8^{+12}_{-6} ppm.

The most remarkable result of our study is the simultaneous measurement of the primary transit, the secondary eclipse, and the robust detection of the total phase curve component corresponding to thermal emission, reflected light, and ellipsoidal variation (see Table 1). The three components and full-phase curve are plotted in the middle panel of Figure 2.

In our analysis, we also experimented what would happen if we let the eccentric e and ω free in our joint fit. In this case we obtained that these results are consistent with the values reported in Table 1 at about $\approx 1\sigma$. We obtain eccentricity constraints: $e = 0.0024^{+0.0041}_{-0.0024}$ and $\omega = 9.05^{+2.32}_{-1.06}$ deg which are consistent with those published in Bourrier et al. (2020). According to Lucy-Sweeny bias (Lucy & Sweeney 1971), in order to measure a non-zero eccentricity with 95% confidence, a result of $e > 2.45\sigma_e$ is required, where σ_e is the standard deviation of the eccentricities (Eastman et al. 2013). As a result, we can confidently rule out WASP-121b non-zero eccentricity.

In addition to our total phase curve model, we investigated a scenario in which the planetary flux is purely reflective. To approximate the planetary reflection, we used the Lambertian reflection model implemented in `spiderman` and characterized by a geometric albedo A_g. Using this scenario we estimated the geometric albedo to be $0.46^{+0.036}_{-0.035}$ which is significantly (3σ) larger than the estimate of the geometric albedo reported by Bourrier et al. (2020). It is quite close to $A_g = \delta(a_p/R_p)^2 = 0.47^{+0.03}_{-0.03}$ which is the value derived from the TESS secondary eclipse depth ($\delta = 489^{+16}_{-10}$ppm). The reduced χ^2 of this purely reflective scenario is 1.8.

6. SUMMARY AND CONCLUSIONS

In this work, we presented our full phase curve model for analyzing the transiting ultra-hot Jupiter WASP-121b utilizing one sector of TESS observations. There were two reasons for using only one sector of TESS. The first is that different TESS sectors have different systematic noises, and combining several sectors may introduce additional complications and difficulties in our joint modelling. The second and most important reason is that we wanted to use the same data set as in Bourrier et al. (2020) and Daylan et al. (2021) so that we could assess how much improvement we could get from using a more complete model. We first used the median detrending technique with a window length of one orbital period of WASP-121b to conduct a smooth detrending of the TESS data, in order to have comparable data with Bourrier et al. (2020), who also did the exact same steps. We binned every 50 data points after phase folding at the orbital period, as Bourrier et al. (2020) performed previously. In our subsequent analysis, we used these reprocessed data. Then we fitted our joint model to the reprocessed data. Our joint model consists of primary transit, secondary eclipse, and phase curves that incorporate the thermal emission, reflection, and ellipsoidal variations.

We reliably measured the secondary eclipse with a depth of 489^{+16}_{-10} ppm after eliminating systematic noise. The combination of thermal emission and reflection in the TESS bandpass results in a relatively significant secondary eclipse depth of WASP-121b. Due to the strong stellar irradiation and low geometric albedo, the secondary eclipse is expected to be mostly dominated by the planet thermal emission.

Our measurement of the $\xi = -0.022^{+0.159}_{-0.141}$ is statistically consistent with zero. This value indicates that the atmosphere of WASP-121b has inefficient thermal redistribution from dayside to nightside, which is consistent with results in the literature (Bourrier et al. 2020; Daylan et al. 2021) and with theoretical models (Komacek et al. 2017; Perez-Becker & Showman 2013). WASP-121b's maximum temperature region is located near the sub-stellar point due to inefficient thermal redistribution, as advection does not redistribute heat across longitudes (Zhang & Showman 2017). The inefficient thermal redistribution also results in substantial differences in the night and dayside temperatures ($734^{+28}_{-55}K$) of WASP-121b. Our measured dayside temperature of $2941^{+61}_{-150}K$ for WASP-121b places it in the ultra-hot Jupiter class (Parmentier et al. 2018; Bell & Cowan 2018).

In this study, we did not assume that the flux of WASP-121b measured by TESS was exclusively thermal emission, and we took into account reflected light. Our best fitted joint model yielded a low geometric albedo of $0.069^{+0.06}_{-0.02}$, indicating that reflection in the TESS passband of WASP-121b is not negligible, which was ignored by Bourrier et al. (2020). Our estimated low geometric albedo value is consistent with Daylan et al. (2021) and other hot Jupiters, in particular, irradiated hot Jupiters at the same wavelength as Schwartz & Cowan (2015). It is also consistent with other short-period hot Jupiter planets, such as WASP-18b ($A_g < 0.048$ at 2σ; Shporer et al. (2019)), Qatar-2b ($A_g < 0.06$ at 2σ; Dai et al. (2017)), and WASP-12b ($A_g < 0.064$ at 97.5% confidence; Bell et al. (2017)). Considering the fact that the bandpass of TESS is close to the wavelength region where the host star is brightest, the bond albedo is small when the geometric albedo is small (Shporer et al. 2019).

The amplitudes of the ellipsoidal variation and Doppler beaming are significantly smaller than those of reflected light and thermal emission, according to theoretical estimates (see Figure 2). We did not incorporate Doppler beaming in our phase curve model because our theoretical estimation of the amplitude of Doppler beaming yields a value of ≈ 2 ppm , which is not significant given the precision of the photometric data. Finally, our best fitted joint model also provided us with an estimate of the amplitude of the ellipsoidal variation, which is consistent with theoretical expectations.

The hot host star and the short orbital period of WASP-121b cause it to be highly irradiated. Furthermore, the lack of a statistically significant phase shift, poor heat distribution, and low albedo are all compatible with other highly irradiated giant gas planets. This study demonstrated that our model may be used to explore the full phase curves of transiting systems. The fact that the WASP-121b phase curve modulations were clearly detected shows that TESS data are sensitive to photometric variations in systems with short periods and massive planets.

More TESS data from extended missions or from other existing facilities like the CHaracterising ExOPlanet Satellite (CHEOPS) (Benz et al. 2021) will also enable a more in-depth study of exoplanets' full phase curve. Our WASP-121b retrieval analysis provides a glimpse into the comprehensive analysis of the full orbital phase curve which can be performed by combining optical and thermal infrared observations, near-infrared emission using existing facilities like the ARIEL (Tinetti et al. 2018), and upcoming facilities with higher resolution, such as the James Webb Space Telescope (JWST) (Gardner et al. 2006).

NASA's Science Mission Directorate funds the TESS mission. Our work is based on data collected by this mission, available at Mikulski Archive for Space Telescopes (MAST). Special thanks to Mahmoudreza Oshagh, who helped with useful suggestions that greatly improved the paper, and with fruitful discussions on the topics covered in this paper. I would like to thank the referee for very useful suggestions that greatly improved the paper.

REFERENCES

Bell, T. J. & Cowan, N. B. 2018, ApJ, 857, 20, https://doi.org/10.3847/2041-8213/aabcc8

Bell, T. J., Nikolov, N., Cowan, N. B., et al. 2017, ApJ, 847, 2, https://doi.org/10.3847/2041-8213/aa876c

Benz, W., Broeg, C., Fortier, A., et al. 2021, ExA, 51, 109, https://doi.org/10.1007/s10686-020-09679-4

Bourrier, V., Ehrenreich, D., Lendl, M., et al. 2020, A&A, 635, 205, https://doi.org/10.1051/0004-6361/201936640

Claret, A. 2017, A&A, 600, 30, https://doi.org/10.1051/0004-6361/201629705

Dai, F., Winn, J. N., Yu, L., & Albrecht, S. 2017, AJ, 153, 40, https://doi.org/10.3847/1538-3881/153/1/40

Daylan, T., Günther, M. N., Mikal-Evans, T., et al. 2021, AJ, 161, 131, https://doi.org/10.3847/1538-3881/abd8d2

Delrez, L., Santerne, A., Almenara, J.-M., et al. 2016, MNRAS, 458, 4025, https://doi.org/10.1093/mnras/stw522

Eastman, J., Gaudi, B. S., & Agol, E. 2013, PASP, 125, 83, https://doi.org/10.1086/669497

Evans, D. F., Southworth, H., Maxted, P. F. L., et al. 2016, VizieR Online Data Catalog: J/A+A/589/58

Evans, T. M., Sing, D. K., Goyal, J. M., et al. 2018, AJ, 156, 283, https://doi.org/10.3847/1538-3881/aaebff

Evans, T. M., Sing, D. K., Kataria, T., et al. 2017, Natur, 548, 58, https://doi.org/10.1038/nature23266

Foreman-Mackey, D., Hogg, D. W., Lang, D., & Goodman, J. 2013, PASP, 125, 306, https://doi.org/10.1086/670067

Gardner, J. P., Mather, J. C., Clampin, M., et al. 2006, SSRv, 123, 485, https://doi.org/10.1007/s11214-006-8315-7

Garhart, E. 2019, Statistical Characterization of Hot Jupiter Atmospheres Using Spitzer's Secondary Eclipses, 2019, Master's Thesis, Arizona State University

Hippke, M., David, T. J., Mulders, G. D., & Heller, R. 2019, AJ, 158, 143, https://doi.org/10.3847/1538-3881/ab3984

Husser, T. O., Wende-von Berg, S., Dreizler, S., et al. 2013, A&A, 553, 6, https://doi.org/10.1051/0004-6361/201219058

Jenkins, J. M. 2017, Kepler Data Processing Handbook: Overview of the Science Operations Center, Kepler Science Document KSCI-19081-002

Komacek, T. D., Showman, A. P., & Tan, X. 2017, ApJ, 835, 198, https://doi.org/10.3847/1538-4357/835/2/198

Kovacs, G. & Kovacs, T. 2019, VizieR On-line Data Catalog: J/A+A/625/80

Kreidberg, L. 2015, PASP, 127, 1161, https://doi.org/10.1086/683602

Louden, T. & Kreidberg, L. 2018, MNRAS, 477, 2613, https://doi.org/10.1093/mnras/sty558

Lucy, L. B. & Sweeney, M. A. 1971, AJ, 76, 544, https://doi.org/10.1086/111159

Mallonn, M., Köhler, J., Alexoudi, X., et al. 2019, A&A, 624, 62, https://doi.org/10.1051/0004-6361/201935079

Parmentier, V., Line, M. R., Bean, J. L., et al. 2018, A&A, 617, 110, https://doi.org/10.1051/0004-6361/201833059

Perez-Becker, D. & Showman, A. P. 2013, ApJ, 776, 134, https://doi.org/10.1088/0004-637X/776/2/134

Ricker, G. R., Winn, J. N., Vanderspek, R., et al. 2015, JATIS, 1, 4003, https://doi.org/10.1117/1.JATIS.1.1.014003

Rodler, F., Kürster, M., & Henning, T. 2010, A&A, 514, 23, https://doi.org/10.1051/0004-6361/200913627

Schwartz, J. C. & Cowan, N. B. 2015, MNRAS, 449, 4192, https://doi.org/10.1093/mnras/stv470

Showman, A. P. & Guillot, T. 2002, A&A, 385, 166, https://doi.org/10.1051/0004-6361:20020101

Shporer, A. 2017, PASP, 129, 2001, https://doi.org/10.1088/1538-3873/aa7112

Shporer, A., Wong, I., Huang, C. X., et al. 2019, AJ, 157, 178, https://doi.org/10.3847/1538-3881/ab0f96

Smith, J. C., Stumpe, M. C., Van Cleve, J. E., et al. 2012, PASP, 124, 1000, https://doi.org/10.1086/667697

Stumpe, M. C., Smith, J. C., Catanzarite, J. H., et al. 2014, PASP, 126, 100, https://doi.org/10.1086/674989

Tinetti, G., Drossart, P., Eccleston, P., et al. 2018, ExA, 46, 135, https://doi.org/10.1007/s10686-018-9598-x

Wong, I., Shporer, A., Daylan, T., et al. 2020, AJ, 160, 155, https://doi.org/10.3847/1538-3881/ababad

Zhang, X. & Showman, A. P. 2017, ApJ, 836, 73, https://doi.org/10.3847/1538-4357/836/1/73

Eftekhar, Mohammad: Department of Physics, Faculty of Science, University of Zanjan, P. O. Box 313 - 45195, Iran (m.eftekhar@znu.ac.ir).

Revista Mexicana de Astronomía y Astrofísica, **58**, 109–119 (2022)

https://doi.org/10.22201/ia.01851101p.2022.58.01.09

CCD PHOTOMETRY AND EVOLUTIONARY STATUS OF THE HADS VARIABLE PT COM

K. B. Alton

Desert Blooms Observatory, USA.

Received October 26 2021; accepted February 10 2022

ABSTRACT

Multi-color (BVI_c) CCD-derived photometric data were acquired from PT Com, a pulsating variable classified as a high amplitude δ Scuti-type system. Analysis of precise time-series lightcurve data was accomplished using discrete Fourier transformation which revealed a mean fundamental mode (f_0) of oscillation at 12.178364 ± 0.000083 d^{-1} along with at least three other partial harmonics ($2f_0$, $3f_0$ and $4f_0$). No other statistically significant frequency shared by all bandpasses was resolved following successive pre-whitening of each residual signal. A secular analysis of the fundamental pulse period since 1999 was facilitated by the addition of 35 new times-of-maximum. The evolutionary status, age and physical nature of PT Com were investigated using the PAdova & TRieste Stellar Evolution Code for generating stellar tracks and isochrones.

RESUMEN

Mediante fotometría CCD se obtuvieron datos multicolores (BVI_c) para PT Com, una variable pulsante clasificada como un sistema tipo δ Scuti de gran amplitud. El análisis de los datos precisos para la curva de luz se efectuó usando la transformación discreta de Fourier, la cual reveló un modo fundamental medio de oscilación (f_0) en 12.178364 ± 0.000083 d^{-1}, además de por lo menos tres harmónicos parciales ($2f_0$, $3f_0$ y $4f_0$). No se encontró otra frecuencia estadísticamente significativa compartida por todos los anchos de banda, después del pre-blanqueado de cada señal residual. El análisis secular del período fundamental a partir de 1999 se facilitó con la adición de 35 nuevos tiempos de máximo. Se investigó el estado evolutivo, la edad y la naturaleza física de PT Com usando el código de evolución estelar PAdova & TRieste para generar trayectorias evolutivas e isocronas.

Key Words: stars: evolution — stars: oscillations — stars: variables: Delta Scuti

1. INTRODUCTION

High amplitude δ Scuti stars, hereafter HADS, represent a very small percentage (<1%) of all δ Sct variables (Lee et al. 2008). Driven by the κ-mechanism (opacity pump) resulting from partial ionization of He II (Pamyatnykh 1999), they commonly oscillate ($\Delta V > 0.1$ mag) via low-order single or double radial pulsation modes (Poretti 2003a,b; Niu et al. 2013, 2017). Many (≈40%) are double pulsators exhibiting simultaneous pulsations in the fundamental and the first overtone mode with amplitudes generally higher in the fundamental mode (McNamara 2000). Although uncommon, non-radial pulsations were detected in the HADS variable V974 Oph (Poretti 2003a,b). HADS variables have historically been divided according to metallicity relative to the Sun where [Fe/H] is defined as zero. The metal-poor ([Fe/H]<<0) group is classified as SX Phe-like stars based on the prototype SX Phoenicis. Ostensibly they have shorter periods ($0.02<P<0.125$ d) and lower masses (≈1.0-1.3 $M_\odot$) than their related HADS variables possessing near solar metal abundance (McNamara 2011). SX Phe stars frequently reside in globular clusters (GC) which are ancient collections of Population II stars. The majority of these pulsators are classified as blue straggler stars, paradoxically appearing much younger than their GC cohorts. Balona & Nemec (2012) proposed that it is not possible to differentiate between δ Sct and field SX Phe variables based on pulsation amplitude, the number of pulsation modes, period or even metallicity (Garg et al. 2010). Much more sensitive space instruments like NASA's Kepler (Gilliland et al. 2010; Guzik 2021), the European Space Agency's CoRoT (Baglin 2003) and the Canadian's Microvariability and Oscillations of STars [MOST] (Walker et al. 2003) have found many examples that violate the traditional differentiation between HADS and SX Phe pulsators. Balona & Nemec (2012) further contend that the evolutionary status of each star is the only way to distinguish between these two classes.

An additional classification scheme for δ Scuti stars was recently proposed by Qian et al. (2018) wherein two distinct groups of δ Scuti stars were uncovered from the LAMOST survey that fundamentally differed in effective temperature. One group was identified as normal δ Scuti stars (NDSTs) when T_{eff} ranged between 6700-8500 K while the other defined as unusual and cool variable stars (UCVs) with T_{eff} had values less than 6700 K. A more restrictive fundamental pulsation range (0.09-0.22 d) coupled with being slightly metal poor ($[\text{Fe/H}] = -0.25 - 0.0$) further differentiates the UCVs from the NDST group. Furthermore, once the UCV stars were excluded from consideration, empirically based temperature-period, log g-period, and metallicity-period relationships were derived for NDSTs like PT Com.

The variability of PT Com (J2000–12:13:40.7640 +17h 14m 37.84; l = 259.5536 b = 76.8169) was first recorded in unfiltered photometric data collected during the ROTSE-I Survey (Akerlof et al. 2000; Woźniak et al. 2004). Additional monochromatic CCD-derived lightcurve data were captured from the Catalina Sky Survey[1] (Drake et al. 2009), the All Sky Automated Survey[2] (Pojmanski 2000), the All Sky Automated Survey for Supernovae[3] (Shappee et al. 2014). Other photometric data which ultimately lead to the determination of time-to-maximum (ToMx) light values were reported by Wunder (2012) and Wils et al. (2014). This report marks the first multi-bandpass photometric study on PT Com which also provides a detailed Fourier analysis of this radial pulsator and critically assesses its classification as a HADS variable.

[1]http://nessi.cacr.caltech.edu/DataRelease/.
[2]http://www.astrouw.edu.pl/asas/?page=acvs.
[3]https://asas-sn.osu.edu/variables.

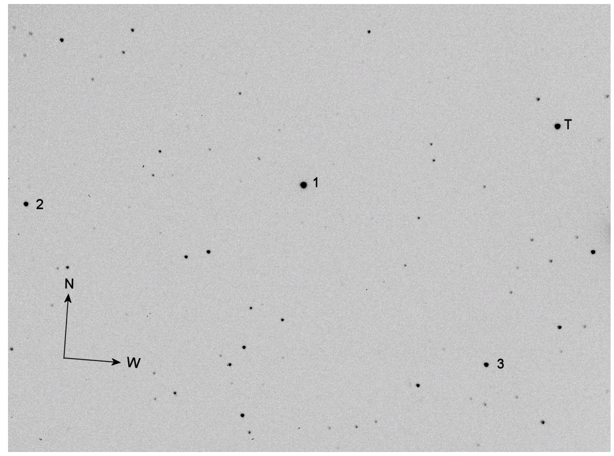

Fig. 1. FOV (15.9×21.1 arcmin) containing PT Com (T) along with the three comparison stars (1-3) used to reduce time-series images to APASS-catalog based magnitudes.

2. OBSERVATIONS AND DATA REDUCTION

Precise time-series images were acquired at Desert Blooms Observatory (DBO, USA – 31.941 N, 110.257 W) using a QSI 683 wsg-8 CCD camera mounted at the Cassegrain focus of a 0.4-m Schmidt-Cassegrain telescope. A Taurus 400 (Software Bisque) equatorial fork mount facilitated continuous operation without the need to perform a meridian flip. The image (science, darks, and flats) acquisition software (TheSkyX Pro Edition 10.5.0) controlled the main and integrated guide cameras. This focal-reduced (f/7.2) instrument produces an image scale of 0.76 arcsec/pixel (bin=2×2) and a field-of-view (FOV) of 15.9×21.1 arcmin. The CCD camera is equipped with B, V and I_c filters manufactured to match the Johnson-Cousins Bessell prescription. Dark subtraction, flat correction and registration of all images collected at DBO were performed using *AIP4Win* v2.4.0 (Berry & Burnell 2005). Instrumental readings were reduced to catalog-based magnitudes using the AAVSO Photometric All-Sky Survey (APASS) star fields (Henden et al. 2009, 2010, 2011; Smith et al. 2011) built into *MPO Canopus* v10.7.1.3 (Minor Planet Observer). An image showing the FOV for PT Com (T) and the ensemble of three non-varying comparison stars (1-3) is shown in Figure 1. The identity (HST Guide Star Catalog, Version GSC-ACT), Gaia DR2 J2000 coordinates and APASS color indices (B-V) for these stars are provided in Table 1. Since all program stars share a relatively small FOV, differential atmospheric extinction was ignored while data from images taken below 30° altitude (airmass >2.0) were excluded.

TABLE 1

GAIA DR2 ASTROMETRIC COORDINATES (J2000)*

FOV ID	GSC ID	R.A. h m s	Dec. deg m s	APASS[a] V-mag	APASS[a] (B-V)
T	1442-01358	12 13 40.7799	+17 14 37.811	11.982	0.279
1	1442-02386	12 14 19.7713	+17 11 46.075	10.754	0.791
2	1442-00715	12 13 49.2064	+17 05 34.357	13.375	0.410
3	1442-00175	12 15 02.7262	+17 10 18.301	13.073	0.708

*V-mag and color indices (B-V) for PT Com (GSC 1442-01358) and three comparison stars (1-3).

[a]V-mag and (B-V) derived from APASS DR9 database.

3. RESULTS

Photometric values in B (n=304), V (n=305), and I_c (n=301) passbands were each processed to produce LCs that encompassed 25Mar2019 through 09April2019 (Figure 2). Times-of-maximum (ToMx) and associated errors were calculated according to Andrych & Andronov (2019) and Andrych et al. (2020) using the program MAVKA (https://uavso.org.ua/mavka/). Simulation of extrema was automatically optimized by finding the most precise degree (α) and best fit algebraic polynomial expression. This procedure, along with eight additional methods featured in MAVKA, are also well suited for other variable star LCs with symmetric or asymmetric extrema. Fundamental pulsation timing differences (PTD) *vs.* epoch were fit using scaled Levenberg-Marquardt algorithms (*QtiPlot* 0.9.9 − *rc*9; https://www.qtiplot.com/). Photometric uncertainty was calculated according to the so-called "CCD Equation" (Mortara & Fowler 1981; Howell 2006). During each imaging session brightness uncertainty typically stayed within ±0.006 mag for all three passbands. All relevant lightcurve data (HJD, APASS magnitude, err, filter) acquired during this study at DBO can be retrieved from the AAVSO archives (https://www.aavso.org/data-download). The sum total of all ToMx values included 30 from the literature (Wunder 2012; Wils et al. 2014), 12 acquired at DBO, 5 determined from V-mag LCs archived at the British Astronomical Association (BAA) website (https://britastro.org/photdb/data.php) and 18 derived from V-mag light curve data downloaded from the AAVSO VSX archives (https://www.aavso.org/data-download). These results, which appear in Table 2, were used to evaluate possible changes in the fundamental pulse period. In this case, the relationship between PTD and cycle number can be described by a straight line relationship (Figure 3) from

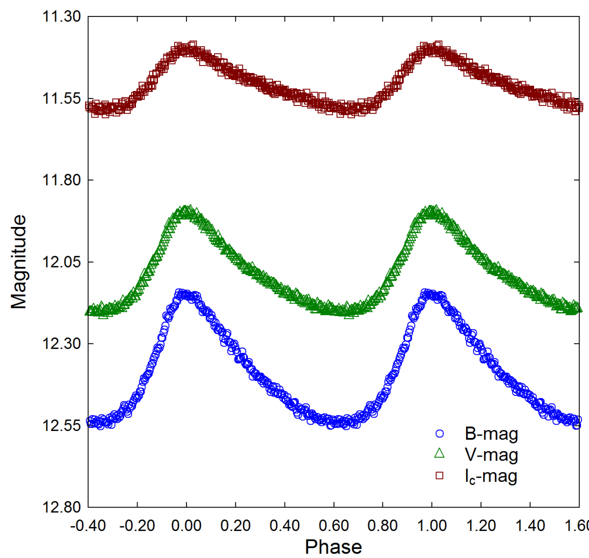

Fig. 2. Period folded (0.082112 ±0.000001 d) LCs for PT Com produced from photometric data obtained between 25Mar2019 and 09April2019 at DBO. LCs shown at the top (I_c), middle (V) and bottom (B) represent catalog-based (APASS) magnitudes determined using *MPO Canopus*. The color figure can be viewed online.

which a new linear ephemeris was calculated (equation 1):

$$Max(HJD) = 2\,459\,291.4777(4) + 0.082112(1)\ E\,. \quad (1)$$

These results suggest that fundamental pulsation period has probably not changed since 1999. Furthermore period folded LCs from ASAS-SN photometric data acquired between 2013 and 2018 were very closely matched to V-mag LCs observed in 2019 at DBO (Figure 4). This would suggest the pulsation amplitude has also remained constant since at least 2013.

TABLE 2

PT COM: ToMx, MEASUREMENT UNCERTAINTY, EPOCH, PTD*

ToMx (HJD-2400000)	Err	Cycle No.	PTD.	Ref.	ToMx (HJD-2400000)	Err	Cycle No.	PTD.	Ref.
51315.9736	nr	-97129	-0.0004	1	58173.4359	0.0003	-13616	0.0018	4
51543.9968	nr	-94352	-0.0036	1	58173.5152	0.0001	-13615	-0.0010	4
51617.9821	nr	-93451	-0.0016	1	58174.4189	0.0007	-13604	-0.0005	4
52638.0710	nr	-81028	0.0039	1	58174.5014	0.0005	-13603	-0.0002	4
53740.0178	nr	-67608	0.0011	1	58176.4722	0.0006	-13579	-0.0001	4
54204.8604	nr	-61947	0.0049	1	58176.5539	0.0009	-13578	-0.0005	4
54867.8317	nr	-53873	-0.0001	1	58177.4557	0.0010	-13567	-0.0019	4
54878.0105	nr	-53749	-0.0032	1	58177.5410	0.0003	-13566	0.0013	4
54886.8852	nr	-53641	0.0034	1	58197.4102	0.0005	-13324	-0.0007	4
55185.0275	nr	-50010	-0.0047	1	58197.4928	0.0010	-13323	-0.0003	4
55209.0082	nr	-49718	-0.0009	1	58204.3900	0.0005	-13239	-0.0005	4
55268.8637	nr	-48989	-0.0054	1	58204.4717	0.0006	-13238	-0.0009	4
55276.8340	nr	-48892	0.0001	1	58462.7156	0.0006	-10093	-0.0008	4
55290.7106	nr	-48723	-0.0004	1	58528.4882	0.0011	-9292	-0.0003	4
55336.6942	nr	-48163	0.0002	1	58529.6386	0.0003	-9278	0.0006	3
55358.7005	nr	-47895	0.0004	1	58529.7222	0.0004	-9277	0.0020	3
55576.9530	nr	-45237	-0.0021	1	58532.5111	0.0001	-9243	-0.0009	4
55615.9575	nr	-44762	-0.0011	1	58567.7378	0.0001	-8814	-0.0005	5
55681.8179	nr	-43960	0.0051	1	58567.8195	0.0003	-8813	-0.0008	5
55959.8484	nr	-40574	0.0027	1	58567.9022	0.0002	-8812	-0.0003	5
55975.9468	nr	-40378	0.0071	1	58571.6788	0.0001	-8766	-0.0008	5
55988.8347	nr	-40221	0.0033	1	58571.7618	0.0001	-8765	0.0001	5
56035.7996	nr	-39649	-0.0001	1	58571.8430	0.0002	-8764	-0.0009	5
56072.4203	nr	-39203	-0.0016	1	58571.9255	0.0002	-8763	-0.0005	5
56073.4062	nr	-39191	-0.0010	1	58573.7323	0.0001	-8741	-0.0002	5
56075.3756	nr	-39167	-0.0023	1	58573.8143	0.0001	-8740	-0.0003	5
56075.4602	nr	-39166	0.0002	1	58573.8969	0.0001	-8739	0.0003	5
56076.4441	nr	-39154	-0.0013	1	58582.7641	0.0002	-8631	-0.0007	5
56354.8875	0.0004	-35763	-0.0013	2	58582.8465	0.0002	-8630	-0.0004	5
56358.8290	0.0006	-35715	-0.0012	2	58587.4455	0.0013	-8574	0.0002	4
56721.6072	0.0003	-31297	0.0040	3	59271.5245	0.0002	-243	0.0001	3
58171.4657	0.0005	-13640	0.0023	4	59291.4786	0.0002	0	0.0007	3
58171.5463	0.0004	-13639	0.0008	4					

*ToMx: Times of maximum.

PTD: fundamental pulsation timing differences used to calculate a linear ephemeris.

nr=not reported.

1. Wunder (2012); 2 Wils et al. (2014); 3 BAA; 4. AAVSO; 5. This study at DBO.

3.1. *Light Curve Behavior*

Morphologically, LCs from HADS variables are asymmetrical with a rapid increase in brightness producing a sharply defined maximum peak. Thereafter a slower decline in magnitude results in a broad minimum. The largest difference between maximum and minimum light is observed in the blue passband (ΔB =0.39 mag), followed by V (ΔV=0.27 mag) and finally the smallest difference detected in infrared (ΔI_c=0.18 mag). Plotting $(B\text{-}V)_0$ against phase (Figure 5) shows significant color amplitude (0.11 mag) going from maximum [$(B\text{-}V)\simeq0.20$] to minimum light [$(B\text{-}V)\simeq0.31$]. This behavior is commonly observed with pulsating F- to A-type stars.

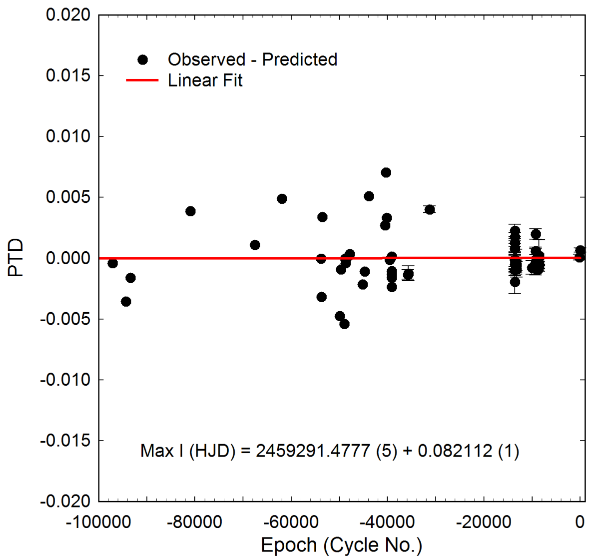

Fig. 3. Straight line fit (PTD vs. cycle number) suggesting that little or no change to the fundamental pulsation period of PT Com had occurred between 1999 and 2021. The color figure can be viewed online.

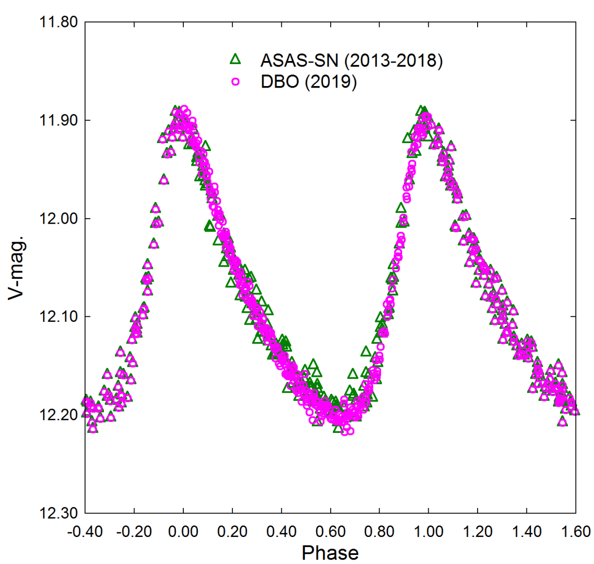

Fig. 4. Period folded (0.082113 ±0.000008 d) LCs for PT Com produced from photometric data obtained between 2013 and 2018 (ASAS-SN) and in 2019 at DBO. The color figure can be viewed online.

Interstellar extinction was estimated according to Amôres & Lépine (2005)[5] which requires galactic coordinates (l, b) and distance (kpc). Accordingly, the Model A reddening value,

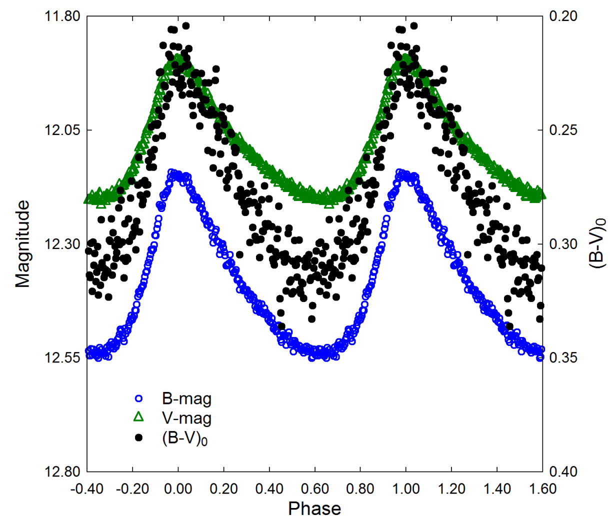

Fig. 5. PT Com LC illustrating significant color change as maximum light [$(B\text{-}V)_0 \simeq 0.20$ mag.] slowly descends to minimum light [$(B\text{-}V)_0 \simeq 0.31$ mag.]. The color figure can be viewed online.

E(B-V)=0.0270 ± 0.0001 mag, corresponds to an intrinsic color index $(B\text{-}V)_0$ for PT Com that varies between 0.194 ± 0.024 at maximum light and 0.309 ± 0.016 mag at minimum brightness. The average effective temperature (T_{eff}) was estimated to be 7473 ± 157 K according to the polynomial transformation equations derived by Flower (1996). These results based strictly on (B-V) photometry at DBO are somewhat lower but within the uncertainty included (T_{eff}=7801 $^{+470}_{-204}$ K) in the Gaia DR2 release of stellar parameters (Andrae et al. 2018). The final T_{eff} (7451 ± 186 K) adopted for this study represents a median value from 2MASS (6953 ±245 K) using J, K and H transforms (Warner 2007) to Johnson-Cousins, Gaia DR2, LAMOST DR5 (7429 ± 32) and DBO (7473 ±157 K). According to Pecaut & Mamajek (2013) the spectral type of this variable would likely range between A7 and A9. A low resolution UV-vis spectrum has been reported by LAMOST DR5 (Zhao et al. 2012; Wang et al. 2019) which is consistent with an A7V classification for PT Com. According to Qian et al. (2018), PT Com would be considered a NDST rather than a UCV since T_{eff} is between 6700 and 8500 K while the fundamental pulsation period is less than 0.09 d.

[5] http://www.galextin.org/.

3.2. *Lightcurve Analysis by Discrete Fourier Transformation*

Discrete Fourier transformation (DFT) was used to extract the fundamental pulsating frequency (spectral window = 100 d^{-1}) using *Period04* (Lenz & Breger 2005). Pre-whitening steps which successively remove the previous most intense signals were employed to extract other potential oscillations from the residuals. Only those frequencies with a S/N≥6 (Baran et al. 2015) in each passband are presented in Table 3. In all cases, uncertainties in frequency, amplitude, and phase were estimated by the Monte Carlo simulation (n=400) routine featured in *Period04*. Representative amplitude spectra from B-mag data acquired at DBO are shown in Figure 6. Since the oscillation frequencies obtained from V- and I_c-bandpasses are essentially redundant, they are not provided herein. A representative DFT-derived model fit with residual error indicates a very good fit for LC (B-mag) data acquired on 29Mar2019 (Figure 7). The amplitude decay for PT Com appears to be exponential as a function of harmonic order (Figure 8) a behavior consistent with other HADS variables such as VX Hyd (Templeton et al. 2009), RR Gem (Jurcsik et al. 2005) and V460 And (Alton & Stępień 2019).

3.3. *Global Parameters*

Ever since a period-luminosity relationship (PLR) between 25 Cepheid variables in the Small Magellanic Cloud was discovered (Leavitt & Pickering 1912), pulsating stars have served as standard candles for estimating cosmic distances to individual stars, clusters and galaxies. A new PLR (Ziaali et al. 2019) was adopted herein, which for the most part was established using the thus far most accurate distance values determined from parallax during the Gaia Mission (Lindegren et al. 2016; Luri et al. 2018). Accordingly this empirically-derived expression (equation 2):

$$M_V = (-2.94 \pm 0.06)\ \log(P) - (1.34 \pm 0.06)\,, \quad (2)$$

is similar to the equation published by McNamara (2011) but with somewhat improved precision.

Absolute $V_{\rm mag}$ ($M_{\rm V}$) was estimated (1.85 ±0.17) after substituting the fundamental pulsation period (0.082112 d) into equation 2. The reddening corrected distance modulus (equation 3):

$$d(\text{pc}) = 10^{(m - M_V - A_V + 5)/5)} \quad (3)$$

produced an estimated distance (1062 ± 83 pc) to PT Com using observed values for m ($V_{\rm avg}$=12.065 ± 0.021) and $A_{\rm V}$ (0.0836 ±0.0003). By comparison, the Gaia DR2 parallax-derived distance (Bailer-Jones 2015) reported for this variable (1108^{+92}_{-79}) is just 4% farther.

The pulsation period and temperature/color were measured by direct observation. Similarly, the solar luminosity (13.86 ± 2.15) was determined from equation 4:

$$L_*/L_\odot = 10^{((M_{bol\odot} - M_{bol*})/2.5)}\,, \quad (4)$$

when $M_{bol\odot}$=4.74, M_V=1.85 ± 0.17 and BC= 0.034 then M_{bol*}=1.89 ± 0.17.

Photometric and spectroscopic observation of eclipsing binary stars are commonly used to determine component mass by applying the laws of gravity derived by Isaac Newton and Johannes Keppler. In contrast, the mass of an isolated field star like PT Com is very difficult to determine by direct measurement. However, it is possible under certain conditions ($1.05 < M_\odot \leq 2.40$) to estimate mass according to Eker et al. (2018), who derived a mass-luminosity relationship from main sequence (MS) stars in detached binary systems. This expression (equation 5):

$$\log(L) = 4.329(\pm 0.087) \cdot \log(M) - 0.010(\pm 0.019), \quad (5)$$

leads to its mass in solar units (1.85 ±0.07 $M_\odot$). Fairly typical for a HADS variable, this result and all others derived from DBO data are summarized in Table 4. Finally, the radius in solar units (R_*= 2.23 ±0.17) was estimated using the well-known relationship (equation 6):

$$L_*/L_\odot = (R_*/R_\odot)^2 (T_*/T_\odot)^4\,. \quad (6)$$

Derived values for density ($\rho_\odot$), surface gravity (log g), and pulsation constant (Q) are also included in Table 4. Stellar density (ρ_*) in solar units (g/cm^3) was calculated according to equation 7:

$$\rho_* = 3 \cdot G \cdot M_* \cdot m_\odot / (4\pi (R_* \cdot r_\odot)^3)\,, \quad (7)$$

where G is the *cgs* gravitational constant, $m_\odot$=solar mass (g), $r_\odot$=solar radius (cm), M_* is the mass and R_* the radius of PT Com in solar units. Using the same algebraic assignments, surface gravity (log g) was determined by the following expression (equation 8):

$$\log\ g = \log(M_* \cdot m_\odot \cdot G / (R_* \cdot r_\odot)^2)\,. \quad (8)$$

The dynamical time that it takes a p-mode acoustic wave to internally traverse a star is strongly correlated to the stellar mean density. The pulsation

TABLE 3

FUNDAMENTAL FREQUENCY (d^{-1}) AND CORRESPONDING PARTIAL HARMONICS*

	Freq. (d^{-1})	Freq. Err	Amp. (mag)	Amp. Err	Phase	Phase Err	Amp. S/N
f_0-B	12.1786	0.0001	0.1768	0.0006	0.5225	0.0006	202.5
f_0-V	12.1782	0.0001	0.1349	0.0005	0.6903	0.0006	322.7
f_0-I_c	12.1770	0.0004	0.0796	0.0010	0.5688	0.0026	81.0
$2f_0$-B	24.3576	0.0004	0.0519	0.0007	0.4978	0.0021	49.2
$2f_0$-V	24.3568	0.0004	0.0429	0.0005	0.7744	0.0019	102.1
$2f_0$-I_c	24.3572	0.0411	0.0272	0.0062	0.0203	0.0557	33.7
$3f_0$-B	36.5344	0.0011	0.0194	0.0007	0.4159	0.0056	20.9
$3f_0$-V	36.5336	0.0814	0.0149	0.0021	0.4487	0.0635	23.1
$3f_0$-I_c	36.5374	0.0043	0.0080	0.0009	0.6356	0.0259	9.7
$4f_0$-B	48.7169	0.0043	0.0067	0.0018	0.7035	0.1571	7.2
$4f_0$-V	48.7103	0.0036	0.0042	0.0005	0.1210	0.0196	7.2

*Detected following DFT analysis of time-series photometric data (BVI_c) from PT Com.

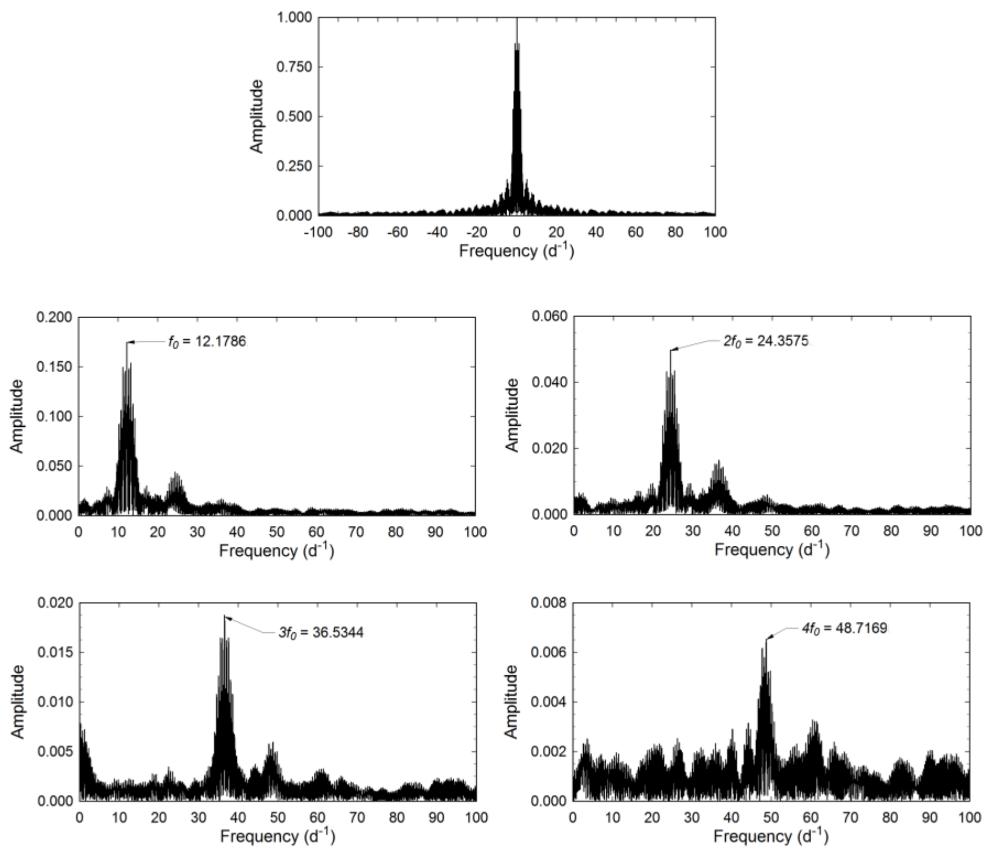

Fig. 6. Spectral window (top panel) and amplitude spectra (f_0, $2f_0$, $3f_0$ and $4f_0$) showing all significant pulsation frequencies following DFT analysis of B-mag photometric data from PT Com acquired at DBO between 25Mar2019 and 09April2019.

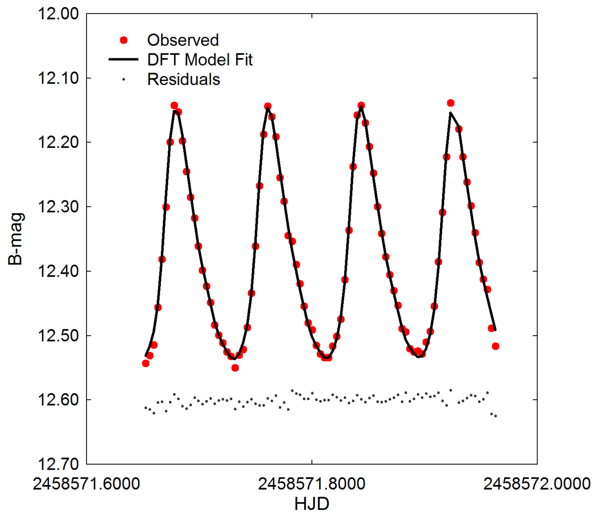

Fig. 7. DFT model fit from LC data (B-mag) acquired on 29March2019 at DBO. Residuals have been offset by a constant amount to compress the y-axis scale. The color figure can be viewed online.

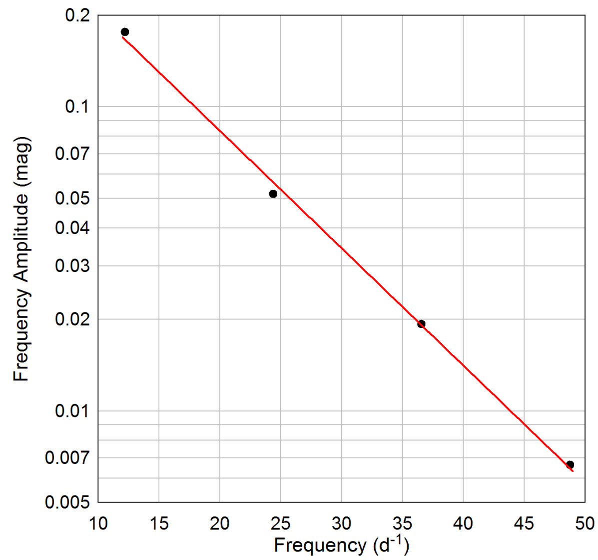

Fig. 8. Log-linear amplitude decay of the fundamental (f_0) pulsation period and its corresponding partial harmonics ($2f_0$-$4f_0$) observed in the B-passband. The color figure can be viewed online.

constant (Q) is defined by the period-density relationship (equation 9):

$$Q = P\sqrt{\overline{\rho}_*/\overline{\rho}_\odot}\,, \tag{9}$$

where P is the pulsation period (d) and $\overline{\rho}_*$ and $\overline{\rho}_\odot$ are the mean densities of the target star and Sun, respectively. The mean density can be expressed (equation 10) in terms of other measurable stellar parameters where:

$$\begin{aligned} \log(Q) = \quad & -6.545 + \log(P) + 0.5\log(g) + \\ & 0.1M_{bol} + \log(T_{eff})\,. \end{aligned} \tag{10}$$

The full derivation of this expression can be found in Breger (1990). The resulting Q values provided in Table 4 are within the expected value (Q=0.03-0.04 d) from fundamental radial pulsations observed for other δ Sct variables (Breger & Bregman 1975; Breger 1979; Joshi & Joshi et al. 2015; Antonello & Pastori 2005).

Finally, a comparative sense of how the physical size, temperature and brightness of PT Com changes over the duration of a single 1.97 hr pulsation can be estimated. As shown in Figure 4 there is a significant increase in reddening (B-V) as maximum light descends to minimum light. Intrinsic color reveals that at maximum light, where $(B\text{-}V)_0$= 0.194 ±0.024, the corresponding effective temperature is 7802 ±143 K, whereas at minimum light ($(B\text{-}V)_0$= 0.309 ±0.016) the estimated effective temperature is 7170 ±84 K. Between these two extremes the putative rise in temperature (+632 K) would correspond to a 1.3-fold increase in luminosity despite an 8% decrease in surface area ($\Delta R_\odot$=3.9%). This inferred estimate for measuring changes in the angular diameter during each pulsation cycle might best be performed with a modern adaptation of the Baade-Wesselink method (Wesselink 1946) using optical interferometers [5].

TABLE 4

GLOBAL STELLAR PARAMETERS FOR PT COM*

Parameter	DBO	PARSEC (Z=0.020)
Mean $T_{\rm eff}$ [K]	7451 ± 186	7451 ± 186
Luminosity [$L_\odot$]	13.86 ± 2.15	13.86 ± 2.15
Mass [$M_\odot$]	1.85 ± 0.07	1.79 ± 0.05
Radius [$R_\odot$]	2.23 ± 0.17	2.23 ± 0.03
ρ [g/cm^3]	0.236 ± 0.055	0.228 ± 0.011
$\log g$ [cgs]	4.011 ± 0.067	3.994 ± 0.017
Q [d]	0.034 ± 0.003	0.033 ± 0.002

*Using values reported from observations at DBO and those predicted from evolutionary modelling.

[5]http://homepage.oma.be/marting/MIAPP_Groenewegen_2014.pdf.

4. EVOLUTIONARY STATUS OF PT COM

The evolutionary status of PT Com was evaluated (Figure 9) using the PAdova & TRieste Stellar Evolution Code (PARSEC) for stellar tracks and isochrones (Bressan et al. 2012) and then plotted ($\log T_{\rm eff}$ vs. $\log(L/L_{\odot})$ in a theoretical Hertzsprung-Russell diagram (HRD). The thick solid maroon-colored line defines the zero-age main sequence ($ZAMS$) position for stars with metallicity Z=0.020. The two broken lines nearly perpendicular to the $ZAMS$ delimit the blue (left) and red (right) edges of the theoretical instability strip for radial low-p modes (Xiong et al. 2016). Also included are the positions of several known HADS and SX Phe-type variables (Balona 2018). The solid black circle indicates the position of PT Com using the DBO derived parameters ($T_{\rm eff}$ and $L_{\odot}$) provided in Table 4.

Ironically a single undisputed value for metallicity from the star closest to us remains elusive. Over the last few decades, the reference metallicity values used by several authors for computing stellar models have ranged between Z=0.012 and 0.020 (Amard et al. 2019). Serenelli et al. (2016) took great exception to a high solar metallicity value (Z=0.0196±0.0014) based on *in situ* measurements of the solar wind (von Steiger & Zurbuchen 2016; Vagnozzi et al. 2017) rather than abundance traditionally determined by spectroscopic analysis. Despite the uncertainty in defining an absolute value for $Z_{\odot}$, an estimate for metal abundance is still required in order to determine the mass, radius and age of PT Com from theoretical evolutionary tracks. A Z-value can be estimated indirectly from its Galactic coordinates. According to the following expression (equation 11):

$$z = d \cdot \sin(b)\,, \tag{11}$$

the distance below or above the Galactic plane can be calculated where d is distance in pc (1108) and b is the Galactic latitude (76.8169°) of PT Com. In this case its position ≈1078 pc above the Galactic plane suggests residence in the thick disc (Li & Zhao 2017) rather than the halo where many metal poor ([Fe/H]<-1.6) stars like SX Phe-type variables reside (Carollo et al. 2010). Furthermore, Qian et al. (2018) reports an empirical relationship between metallicity ([Fe/H]) and the fundamental pulsation period P for an NDST star according to the following (equation 12):

$$[\mathrm{Fe/H}] = -0.121(\pm0.026) + 0.92(\pm0.25) \times P\,. \tag{12}$$

As expected for a thick disk resident, the predicted value ([Fe/H]=-0.045 ±0.033) suggests that PT Com approaches solar metallicity, or at most a few times lower.

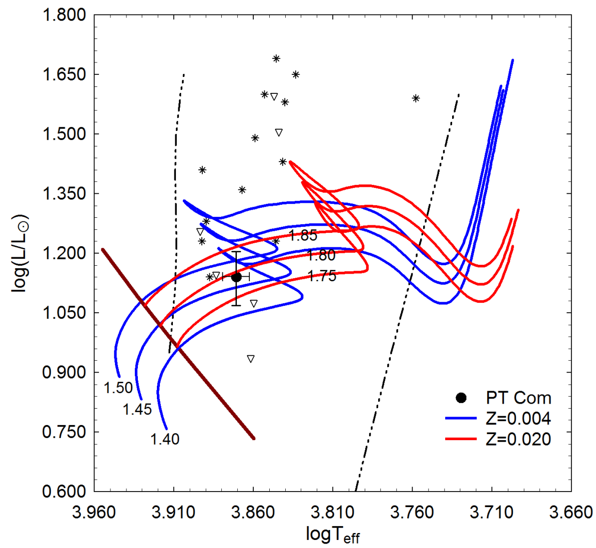

Fig. 9. Evolutionary tracks (red lines; Z=0.020 and blue lines; Z=0.004) derived from PARSEC models (Bressan et al. 2012) showing the position of PT Com (black filled circle) relative to $ZAMS$ (thick maroon line) and within the theoretical instability strip (black dashed lines) for low-order radial mode δ Scuti pulsators. The positions of other HADS (*) and SX Phe (open triangle) variables reported by Balona (2018) are included for comparison. The color figure can be viewed online.

Two separate PARSEC evolutionary models (Bressan et al. 2012) ranging in age between $1{\times}10^{8}$ and $2.21{\times}10^{9}$ y are illustrated in Figure 9. The red solid lines show the model tracks ($M_{\odot}$=1.75, 1.80 and 1.85) over time when Z = 0.020 while the solid blue lines define the metal-poor models ($M_{\odot}$=1.40, 1.45 and 1.50) where Z = 0.004. The latter simulations correspond to a decrease in metallicity by a factor of 3 to 5 depending on the reference solar metallicity. Assuming Z = 0.020, it can be shown by linear extrapolation that PT Com would have a mass of 1.79 ± 0.05 $M_{\odot}$ and a radius of 2.23 ±0.03 $R_{\odot}$. The position of this intrinsic variable near the $M_{\odot}$=1.80 evolutionary track extrapolates to an age of 1.04 ± 0.002 Gyr suggesting it is a moderately evolved MS object lying amongst other HADS variables closer to the blue edge of the instability strip.

By comparison, if PT Com is more metal deficient (Z=0.004), then it would have a somewhat greater radius (2.61 ± 0.07 $R_{\odot}$), but would be less massive (1.47 $M_{\odot}$). Its position closest to the 1.45 $M_{\odot}$ track lies prior to the HRD region where evolutionary tracks of low metallicity stars begin stellar contraction near the end of core hydrogen burning. This star would still be a MS object but with an age approaching 2.13 ± 01 Gyr. It should be noted that the theoretical mass (1.79 $M_\odot$) where Z=0.020 favors the higher metallicity of PT Com is also in good agreement with results (1.85 ± 0.07 $M_\odot$) independently determined using an empirical mass-luminosity relationship. If or when high resolution spectroscopic data become available in the future, uncertainty about the mass and metallicity of PT Com will likely improve.

5. CONCLUSIONS

This first multi-bandpass (BVI_c) CCD study of PT Com has produced 35 new times-of-maximum. Secular analysis of the ToMx residuals suggests that the fundamental pulsation period has not changed since 1999. Deconvolution of time-series photometric data by discrete Fourier transformation shows that this star is a monoperiodic radial pulsator (f_0=12.1783 d^{-1}) which also oscillates in at least 3 other partial harmonics ($2f_0$, $3f_0$ and $4f_0$). It is conceivable that a more expansive dataset collected at multiple sites over a much longer period of time could reveal other oscillation modes that were not detected in this study. A mean effective temperature for PT Com (7451 $\pm$186 K) was estimated from a composite of Gaia DR2, 2MASS, LAMOST DR5 and DBO results, which likely corresponds to spectral type A7-A8. The pulsation period ($\approx$0.082112 d), radial oscillation mode, $V_{\rm mag}$ amplitude (0.30 mag), spectral type and LC morphology are all consistent with the traditionally defined characteristics of a HADS variable. It should be noted that these attributes do not necessarily exclude the possibility that PT Com is a field SX Phe-type variable. However, the generally accepted threshold for SX Phe stars is <1.3 M$_\odot$ (McNamara 2011) which in this case is far less than the mass predicted from a M-L relationship ($\approx$1.85 $M_\odot$) and evolutionary modeling (1.79 $\pm$0.05 $M_\odot$). Given these results, the weight of evidence confirms the classification of PT Com as a HADS variable.

This research has made use of the SIMBAD database operated at Centre de Données astronomiques de Strasbourg, France. In addition, the International Variable Star Index maintained by the AAVSO, the Northern Sky Variability Survey hosted by the Los Alamos National Laboratory, the All Sky Automated Survey Catalogue of Variable Stars, the All Sky Automated Survey for Supernovae, and the Catalina Surveys Data Release 2 archives were mined for essential information. The BAA Photometry Database is acknowledged as partly the source of data on which this article was based. This work also presents results from the European Space Agency (ESA) space mission Gaia. Gaia data are being processed by the Gaia Data Processing and Analysis Consortium (DPAC). Funding for the DPAC is provided by national institutions, in particular those participating in the Gaia MultiLateral Agreement (MLA). The Gaia mission website is https://www.cosmos.esa.int/gaia while the Gaia archive website is https://archives.esac.esa.int/gaia. The use of public data from LAMOST is also acknowledged. Guoshoujing Telescope (the Large Sky Area Multi-Object Fiber Spectroscopic Telescope LAMOST) is a National Major Scientific Project built by the Chinese Academy of Sciences. Funding for the project has been provided by the National Development and Reform Commission. LAMOST is operated and managed by the National Astronomical Observatories, Chinese Academy of Sciences. The diligence and dedication shown by all associated with these organizations is very much appreciated. The careful review and helpful commentary provided by an anonymous referee is gratefully acknowledged.

REFERENCES

Akerlof, C., Amrose, S., Balsano, R., et al. 2000, AJ, 119, 1901, https://doi.org/10.1086/301321

Alton, K. B. & Stępień, K. 2019, AcA, 69, 283, https://doi.org/10.32023/0001-5237/69.3.4

Amard, L., Palacios, A., Charbonnel, C., et al. 2019, A&A, 631, 77, https://doi.org/10.1051/0004-6361/201935160

Amôres, E. B. & Lépine, J. R. D. 2005, AJ, 130, 659, https://doi.org/10.1086/430957

Andrae, R., Fouesneau, M., Creevey, O, et al. 2018, A&A, 616, 8, https://doi.org/10.1051/0004-6361/201732516

Andrych, K. D. & Andronov, I. L. 2019, OEJV, 197, 65, arXiv:1812.06949

Andrych, K. D., Andronov, I. L., & Chinarova, L. L. 2020, JPhSt, 24, 1902, https://doi.org/10.30970/jps.24.1902

Antonello, E. & Pastori, L. 1981, PASP, 93, 237, https://doi.org/10.1086/130812

Baglin, A. 2003, AdSpR, 31, 345, https://doi.org/10.1016/S0273-1177(02)00624-5

Bailer-Jones, C. A. L. 2015, PASP, 127, 994, https://doi.org/10.1086/683116

Balona, L. A. & Nemec, J. M. 2012, MNRAS, 426, 2413, https://doi.org/10.1111/j.1365-2966.2012.21957.x

Balona, L. A. 2018, MNRAS, 479, 183, https://doi.org/10.1093/mnras/sty1511

Baran, A. S., Koen, C., & Porkrzywka, B. 2015, MNRAS, 448, 16, https://doi.org/10.1093/mnrasl/slu194
Berry, R. & Burnell, J. 2005, The Handbook of Astronomical Image Processing, (Richmond, VA: Wilmann-Bell)
Breger, M. 1979, PASP, 91, 5, https://doi.org/10.1086/130433
_________. 1990, DSSN, 2, 13
Breger, M. & Bregman, J. N. 1975, ApJ, 200, 343, https://doi.org/10.1086/153794
Bressan, A., Marigo, P., Girardi, L., et al. 2012, MNRAS, 427, 127, https://doi.org/10.1111/j.1365-2966.2012.21948.x
Carollo, D., Beers, T. C., Chiba, M., et al. 2010, ApJ, 712, 692, https://doi.org/10.1088/0004-637X/712/1/692
Drake, A. J., Djorgovski, S. G., Mahabal, A., et al. 2009, ApJ, 696, 870, https://doi.org/10.1088/0004-637X/696/1/870
Dworak, T. Z. & Zieba, S. 1975, IBVS, 1005, 1
Eker, Z., Bakış, V., Bilir, S., et al. 2018, MNRAS, 479, 5491, https://doi.org/10.1093/mnras/sty1834
Flower, P. J. 1996, ApJ, 469, 355, https://doi.org/10.1086/177785
Garg, A., Cook, K. H., Nikolaev, S., et al. et al. 2010, AJ, 140, 328, https://doi.org/10.1088/0004-6256/140/2/328
Gilliland, R. L., Brown, T. M., Christensen-Dalsgaard, J., et al. 2010, PASP, 122, 131, https://doi.org/10.1086/650399
Guzik, J. A. 2021, FrASS, 8, 55, https://doi.org/10.3389/fspas.2021.653558
Henden, A. A., Welch, D. L., Terrell, D., & Levine, S. E. 2009, AAS, 41, 669
Henden, A. A., Terrell, D., Welch, D. L., & Smith, T. C. 2010, AAS, 42, 515
Henden, A. A., Levine, S. E., Terrell, D., Smith, T. C., & Welch, D. L. 2011, AAS, 43, 2011
Howell, S. B. 2006, Handbook of CCD Astronomy (Cambridge, UK: CUP)
Joshi, S. & Joshi, Y. C. 2015, JApA, 36, 33, https://doi.org/10.1007/s12036-015-9327-z
Jurcsik, J., Sódor, Á., Váradi, M., et al. 2005, A&A, 430, 1049, https://doi.org/10.1051/0004-6361:20041784
Leavitt, H. S. & Pickering, E. C. 1912, HarCi, 173, 1
Lee, Y.-H, Kim, S. S., Shin, J., Lee, J., & Jin, H. 2008, PASJ, 60, 551, https://doi.org/10.1093/pasj/60.3.551
Lenz, P. & Breger, M. 2005, CoAst, 146, 53, https://doi.org/10.1553/cia146s53
Li, C. & Zhao, G. 2017, ApJ, 850, 25, https://doi.org/10.3847/1538-4357/aa93f4
Lindegren, L., Lammers, U., Bastian, U., et al. 2016, A&A, 595, 4, https://doi.org/10.1051/0004-6361/201628714
Luri, X., Brown, A. G. A., Sarro, L. M., et al. 2018, A&A, 616, 9, https://doi.org/10.1051/0004-6361/201832964
McNamara, D. H. 2000, ASPC, 210, 373
_________. 2011, AJ, 142, 110, https://doi.org/10.1088/0004-6256/142/4/110
Mortara, L. & Fowler, A. 1981, SPIE, 290, 28, https://doi.org/10.1117/12.965833
Niu, J.-S, Fu, J.-N., & Zong, W.-K. 2013, RAA, 13, 1181, https://doi.org/10.1088/1674-4527/13/10/004
Niu, J.-S, Fu, J.-N., Li, Y., et al. 2017, MNRAS, 467, 3122, https://doi.org/10.1093/mnras/stx125
Pamyatnykh, A. A. 1999, AcA, 49, 119
Pecaut, M. J. & Mamajek, E. E. 2013, ApJS, 208, 9, https://doi.org/10.1088/0067-0049/208/1/9
Pojmanski, G. 2000, AcA, 50, 177
Poretti, E. 2003a, A&A, 409, 1031, https://doi.org/10.1051/0004-6361:20031223
_________. 2003b, ASPC, 292, 145
Qian, S.-B., Li, L.-J., He, J.-J., et al. 2018, MNRAS, 475, 478, https://doi.org/10.1093/mnras/stx3185
Serenelli, A., Scott, P., Villante, F. L., et al. 2016, MNRAS, 463, 2, https://doi.org/10.1093/mnras/stw1927
Shappee, B. J., Prieto, J. L., Grupe, D., et al. 2014, ApJ, 788, 48, https://doi.org/10.1088/0004-637x/788/1/48
Smith, T. C., Henden, A. A., & Starkey, D. R. 2011, SASS, 30, 121
Templeton, M. R., Samolyk, G., Dvorak, S., et al. 2009, PASP, 121, 1076, https://doi.org/10.1086/630211
Vagnozzi, S., Freese, K, & Zurbuchen, T. H. 2017, ApJ, 839, 55, https://doi.org/10.3847/1538-4357/aa6931
von Steiger, R. & Zurbuchen, T. H. 2016, ApJ, 816, 13, https://doi.org/10.3847/0004-637x/816/1/13
Walker, G., Matthews, J., Kuschnig, R., et al. 2003, PASP, 115, 1023, https://doi.org/10.1086/377358
Wang, R., Luo, A-l., Zhang, S., et al. 2019, PASP, 131, 024505, https://doi.org/10.1088/1538-3873/aaf25f
Warner, B. D. 2007, MPBu, 34, 113
Wesselink, A. J. 1946, BAN, 10, 91
Wils, P., Ayiomamitis, A., Robertson, C. W., et al. 2014, IBVS, 6122, 1
Woźniak, P. R., Vestrand, W. T., Akerlof, C. W., et al. 2004, AJ, 127, 2436, https://doi.org/10.1086/382719
Wunder, E. 2012, BAVSR, 61, 253
Xiong, D. R., Deng, L., Zhang, C., & Wang, K. 2016, MNRAS, 457, 3163, https://doi.org/10.1093/mnras/stw047
Zhao, G., Zhao, Y.-H., Chu, Y.-Q., Jing, Y.-P., & Deng, L.-C. 2012, RAA, 12, 723
Ziaali, E., Bedding, T. R., Murphy, S. J., Van Reeth, T., & Hey, D. R. 2019, MNRAS, 486, 4348, https://doi.org/10.1093/mnras/stz1110

Kevin B. Alton: UnderOak and Desert Blooms Observatories, 70 Summit Ave., Cedar Knolls, NJ, USA (mail@underoakobservatory.com).

Revista Mexicana de Astronomía y Astrofísica, **58**, 121–132 (2022)

https://doi.org/10.22201/ia.01851101p.2022.58.01.10

A NEW VISIT TO THE VARIABLE STARS IN M56 AND ITS COLOUR-MAGNITUDE DIAGRAM STRUCTURE

D. Deras[1], A. Arellano Ferro[1], I. Bustos Fierro[2], and M. A. Yepez[1]

Received December 16 2021; accepted February 15 2022

ABSTRACT

We present a *VI* CCD photometric study and a membership analysis of the globular cluster M56 (NGC 6779). This produced a CMD decontaminated from field stars, which enabled a better confrontation with theoretical isochrones, zero-age horizontal branches (ZAHB) and post-ZAHB evolutionary tracks. Post He-flash evolutionary models with a He-core mass of 0.5 $M_\odot$ and envelopes of 0.04 - 0.18 $M_\odot$, cover the complete horizontal branch. Models with total mass $\approx$ 0.68 $M_\odot$ explain the RR Lyrae, while those with a mass $\approx$ 0.56 $M_\odot$ and a very subtle envelope, explain the Pop II cepheids with a progenitor in the blue tail of the HB. Based on the Fourier decomposition of the V light curve of a single cluster member RRc star, we determined a metallicity of $[\mathrm{Fe/H}]_{\mathrm{ZW}} = -1.96 \pm 0.09$. Several independent distance determination approaches lead to a mean distance to M56 of $\langle d \rangle = 9.4 \pm 0.4$ kpc. Finally, we report 5 new variables: one SX Phe, three EB, and one RRc.

RESUMEN

Presentamos un estudio fotométrico y un análisis de membresía del cúmulo globular M56 (NGC 6779) con imágenes CCD *VI*. Construimos un diagrama color-magnitud sin contaminación de estrellas de campo, y lo comparamos con modelos de isócronas, rama horizontal de edad cero (ZAHB) y trazas evolutivas post-ZAHB. Modelos con masas de 0.5 $M_\odot$ y envolventes de 0.04 - 0.18 $M_\odot$, representan toda la rama horizontal (HB). Modelos con masas $\approx$ 0.68 $M_\odot$ son adecuados para estrellas RR Lyrae, mientras que masas de $\approx$ 0.56 $M_\odot$ y envolventes muy delgadas explican a las estrellas de Pob II con un progenitor en la cola azul de la HB. La descomposición de Fourier de la curva de luz de la única RRc miembro del cúmulo sugiere la metalicidad $[\mathrm{Fe/H}]_{\mathrm{ZW}} = -1.96 \pm 0.09$. La distancia media de M56 obtenida por métodos independientes es $\langle d \rangle = 9.4 \pm 0.4$ kpc. Reportamos 5 nuevas variables: una SX Phe, tres EB, y una RRc.

Key Words: globular clusters: individual: M56 — stars: fundamental parameters — stars: variables: RR Lyrae

1. INTRODUCTION

The globular cluster M56 (NGC 6779) is among the most metal-poor clusters in the Galaxy, and is relatively nearby and hence a bright system lying well within the Galactic disc ([Fe/H]$\approx$ -1.98 (Searle & Zinn 1978); d=8.4 kpc (Hatzidimitriou et al. 2004); ($l = 62.66°$, $b = 8.34°$). Therefore, it is subject to a considerable reddening ($E(B-V) = 0.26$) (Kron & Guetter 1976). Typical of very metal-poor clusters, its horizontal branch (HB) shows a very long and populated blue tail and a scarcely populated instability strip (IS). As a consequence, very few RR Lyrae stars are expected to be found in the system. In fact, presently only two RRab and two RRc are listed in the Catalogue of variable stars in globular clusters (CVSGC) of Clement et al. (2001). Other variables included in the CVSGC are one W Vir (CW), six semi-regular or slow variables (SR or L), one RV Tauri (RV) and one SX Phoenicis star, for a total of 14 variables. The variability of V2 has been doubted by several authors and we

[1]Instituto de Astronomía, Universidad Nacional Autónoma de México, Ciudad Universitaria, C.P. 04510, México.

[2]Observatorio Astronómico, Universidad Nacional de Córdoba, Laprida 854, X5000BGR, Córdoba, Argentina.

shall report our conclusion in the present paper. The most recent light curve analysis of the known variables is that by Pietrukowicz et al. (2008), which shall be a substantial basis for our present analysis. It has been argued, on kinematical grounds, that M56 might be of extragalactic origin due to the occurrence of a massive accretion event by the Milky Way, around 10 Gyrs ago (Deason et al. 2013). A study conducted by Piatti & Carballo-Bello (2019) concluded that M56 shows evidence of extra-tidal features like tails and extended haloes, as a consequence of the merger event. Also, Massari et al. (2019) showed that the age-metallicity relation for Galactic globular clusters is bifurcated, meaning that metal-rich clusters with disc-like kinematics are more likely to have been formed *in situ*, while metal-poor clusters with halo-like kinematics are more likely to have been accreted, M56 being one of the latter.

In the present study we propose the determination of the cluster mean metallicity and distance, as indicated by the light curve morphology of its RR Lyrae stars via the Fourier decomposition and *ad-hoc* calibrations. We also aim to employ the *Gaia*-eDR3 proper motions to distinguish cluster members from field stars in our images of the cluster and to produce a cleaner colour-magnitude diagram (CMD) that should enable some observational and theoretical considerations regarding the structure and stellar distribution of the horizontal branch (HB). We will also discuss the position of M56 relative to the so-called *Oosterhoff Gap* and its relation with its probable extragalactic origin. Alternative distance determination methods involving the variable stars will be discussed and a theoretical approach of the representation of the HB blue tail as a consequence of mass loss in the RGB will close our work.

2. OBSERVATIONS AND DATA REDUCTIONS

The data used for the present paper were obtained with the 0.84-m Ritchey-Chrétien telescope of the Observatorio Astronómico Nacional San Pedro Mártir on two epochs performed approximately one and a half months apart, from August 4-5 2019 for the first, and from September 27-30 2019 for the second. The first set of images consisted of 255 in the V filter and 659 in the I filter, while the second set consisted of 258 images in both V and I filters. The estimated average seeing of the first set of images was 1.4" while for the second set was 1.8". The exposure times ranged between 7s-60s for the first set in both filters, while for the second set it ranged between 40s-60s also in both filters. Alongside with the Mexman filter wheel, the detector used was a 2048 $\times$ 2048 pixel ESOPO CCD (e2v CCD42-90) with 1.7 e^-/ADU gain, a readout noise of 3.8 e^-, a scale of 0.444 arcsec/pix corresponding to a field of view (FoV) of ≈ 7.4 arcmin^2.

2.1. *Difference Imaging Analysis*

We have employed the software Difference Imaging Analysis (DIA) with its pipeline implementation DanDIA (Bramich 2008; Bramich et al. 2013) to obtain high-precision photometry of all the point sources in the FoV of our CCD. This allowed us to construct an instrumental light curve for each star. For a detailed explanation on the use of this technique, the reader is referered to the work by Bramich et al. (2011).

2.2. *Transformation to the Standard System*

Once we obtained the instrumental light curves, we transformed them into the VI Johnson-Kron-Cousin standard photometric system (Landolt 1992). We did this by using 120 standard stars in our FoV identified in the catalog of Photometric Standard Fields (Stetson 2000). The transformation equations 1 and 2, correspond to the August 2019 data set, while the transformation equations 3 and 4 correspond to the September 2019 data set. In all cases there is a mild colour dependence in the transformation from the instrumental to the standard system, particularly for the September data, which we shall use as reference for the zero points of our light curves.

$$V - v = 0.513(\pm 0.017)(v - i) - 3.276(\pm 0.022), \quad (1)$$

$$I - i = -0.274(\pm 0.034)(v - i) - 2.056\big(\pm(0.044)\big), \quad (2)$$

$$V - v = -0.047(\pm 0.005)(v - i) - 2.585(\pm 0.006), \quad (3)$$

$$I - i = 0.051(\pm 0.009)(v - i) - 2.492(\pm 0.012). \quad (4)$$

3. STAR MEMBERSHIP USING *GAIA*-EDR3

Before studying the CMD of M56, it is convenient to be able to separate field stars from the likely cluster members. We have approached this goal by employing the high-quality astrometric data and proper motions in the *Gaia*-eDR3 data base (Gaia Collaboration 2021) and the method of Bustos Fierro & Calderón (2019), which is based on the Balanced Iterative Reducing and Clustering using Hierarchies (BIRCH) algorithm developed by Zhang et al. (1996). This algorithm detects groups of stars in a 4D space of physical parameters - projection

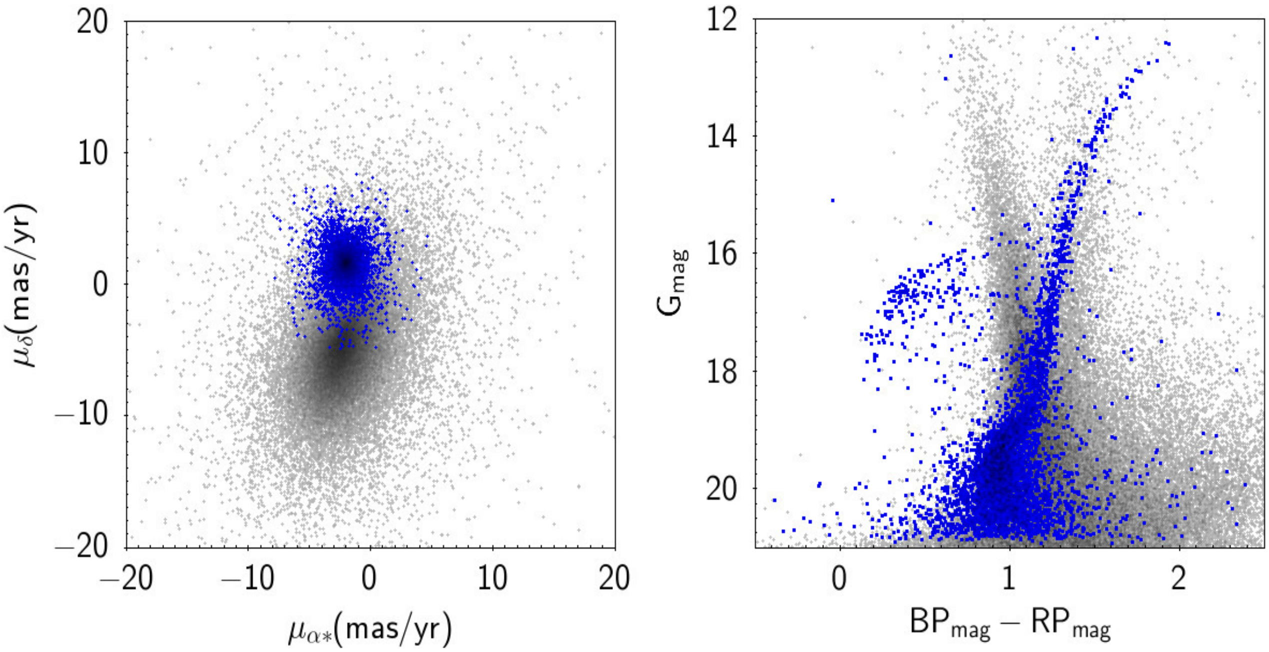

Fig. 1. The left side panel displays the vector-point diagram (VPD) of the proper motions of the stars measured by *Gaia*-eDR3 in M56. Stars within a 25 arcmin radius were used to perform a membership analysis. Blue dots correspond to stars with a high probability of being cluster members while the grey dots correspond to field stars. The panel on the right shows the corresponding CMD where the blue symbols for member stars highlight the characteristic shape of the globular cluster. For details, see § 3. The colour figure can be viewed online.

of celestial coordinates (X_t, Y_t) and proper motions (μ_α, μ_δ). Figure 1 illustrates the resulting vector-point diagram (VPD) showing the motion of the cluster relative to the field stars. Also the resulting *Gaia*-CMD of member stars is shown, which is consistent with that of a globular cluster, giving support to the cluster members selection. Unlike more traditional methods, which are based on the fitting of a probability density function and a cut-off at a certain minimum probability to consider stars as reliable cluster members, our method is based on a clustering algorithm as a first stage and a detailed analysis of the residual overdensity as a second stage; member stars extracted in the first stage are labelled M1, and those extracted in the second stage are labelled M2. The analysis was carried out for a 25 arcmin radius field centered in the cluster. We considered 76 235 stars from which 6552 were found to be likely members, out of these only 4695 were in the FoV of our images. We were able to measure and produce light curves for 3632 member stars.

From the distribution of field stars in phase space we estimated the number that is expected to be located in the same region of the sky and of the VPD as the extracted members; therefore, they could have been erroneously labelled as members. Within the M1 stars the resulting expected contamination is 77 (1.6%) and within the M2 stars it is 167 (9.0%); therefore, for a given extracted star its probability of being a cluster member is 98% if it is labelled M1, or 91% if it is labelled M2.

To evaluate the completeness of our DIA photometry we compared the number of stars we detected and measured in the FoV of our images, with the ones measured by *Gaia*-eDR3. Of the 76 235 stars considered for the membership analysis, only 12 433 are in our FoV, and we were able to measure 4845. In Figure 2 we confront these two samples as a function of magnitude. We can see that our DIA photometry is complete down to G=16.5 mag, which comfortably includes the horizontal portion of the HB, and it is fairly complete down to G=18.5 mag, which encompasses the vertical portion of the HB in the CMD.

4. THE VARIABLE STARS IN M56

4.1. *Light Curves of Known Variables*

Of the 14 known variables in M56, listed in Table 1, only V1-V6 and V12-V14 are within the FoV of our images. Variables V7, V8, V9, V10 and V11 are outside the FoV of our images and have been identified as being field variables in the CVSGC and have

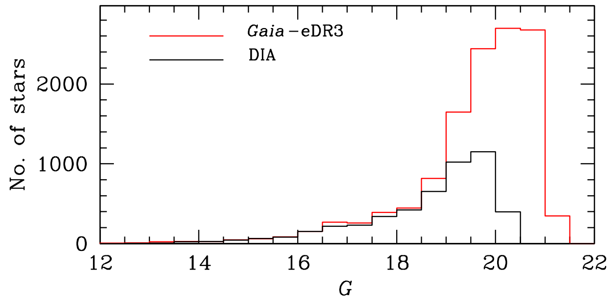

Fig. 2. Red histogram represents the number of stars in our FoV per G magnitude interval as measured by *Gaia*-eDR3. Black histogram is the magnitude distribution, converted from V to G, of the stars measured in this work through our DIA approach. See the discussion on completeness in § 3. The colour figure can be viewed online.

also been confirmed as such by the membership analysis performed in § 3. For the sake of completeness, we tried to recover their light curves from the *Gaia*-DR2 photometry (Gaia Collaboration et al. 2018) but we were only able to do it for V8, V10 and V11. The variables V7 and V9 do not possess the variability flag associated by *Gaia* and therefore were not measured. For V8, V10 and V11 we proceeded to transform their *Gaia* G, G_{BP}, and G_{RP} bands into the VI Johnson standard system to make them consistent with our photometry. For this purpose, we used the relations provided by J.M. Carrasco and which can be found in the *Gaia*-DR2 documentation[3] (2018: Gaia team). The light curves of the known variables and the ones recovered with *Gaia* are displayed in Figure 3.

We remark that the red giants V3, V5 and V6 were saturated in our I images and as such we have no I-band photometry.

4.2. *The Search for New Variables*

The small number of reported variables present in M56 prompted a rigorous search in order to provide a more complete sample for our analysis. We approached this task by using the string-length method (Burke et al. 1970, Dworetsky 1983). We phased each light curve in our data with periods between 0.02 d and 1.7 d in steps of 10^{-6} d. In each case, the length of the line joining consecutive points, called the string-length and represented by the parameter S_Q, was calculated. The best phasing occurs when S_Q is minimum, and corresponds to the best period our data can provide. This method led us to the discovery of five new *bona fide* variables: one SX Phe, three EB and one RRc, and were named V15-V19. According to the method described in § 3, V16 (EB) and V19 (RRc) are field variables. Their light curves are displayed in Figure 4. The ones deemed to have a high probability of being cluster members, (coded M1 and M2 in Table 1), are in the expected region of the CMD (Figure 5), in good agreement with their variability type. All variables listed in Table 1 that are contained in our FoV are identified in the cluster chart of Figure 6.

[3]https://gea.esac.esa.int/archive/documentation/GDR2/Data_processing/chap_cu5pho/sec_cu5pho_calibr/ssec_cu5pho_PhotTransf.html.

4.3. *Comments on the Reddening of M56*

The canonical reddening generally quoted for M56 is $E(B-V) = 0.26$ (Harris 1996). In an attempt to confirm this value we have considered V12, the only RRab present in M56. We have made use of the fact that RRab stars have a nearly constant intrinsic colour $(B-V)_0$, between phases 0.5 and 0.8 (Sturch 1966). The intrinsic value $(V-I)_0$ in this range of phases was calibrated by Guldenschuh et al. (2005) who found a value of $\overline{(V-I)_{o,min}} = 0.58 \pm 0.02$ mag. Hence, by measuring the average $\overline{(V-I)_{o,0.5-0.8}}$, one can estimate $E(V-I) = \overline{(V-I)_{o,min}}$ - $(V-I)_{o,0.5-0.8}$ for a given RRab star with a properly covered colour curve at these phases. Then, we calculated $E(B-V)$ via the ratio $E(V-I)/E(B-V) = 1.259$.

While our light curve of V12 is not covered near its maximum (see Figure 3), the 0.5 - 0.8 phase range is very well covered. We calculated $E(B-V) = 0.26 \pm 0.02$. The dust map calibrations of Schlafly & Finkbeiner (2011) and Schlegel et al. (1998) give values of 0.216±0.009 and 0.252±0.011, respectively. A large range of reddening values can be found in the literature, from 0.18 (Ivanov et al. 2000) to 0.32 (Hatzidimitriou et al. 2004)).

For the rest of the paper we shall adopt the value of $E(B-V) = 0.26$.

5. THE FOURIER DECOMPOSITION APPROACH TO THE PHYSICAL PARAMETERS OF RR LYRAE STARS

The use of Fourier light curve decomposition has been a well tested approach towards the determination of key physical parameters of RR Lyrae stars. The amplitudes and displacements, A_k and ϕ_k, and

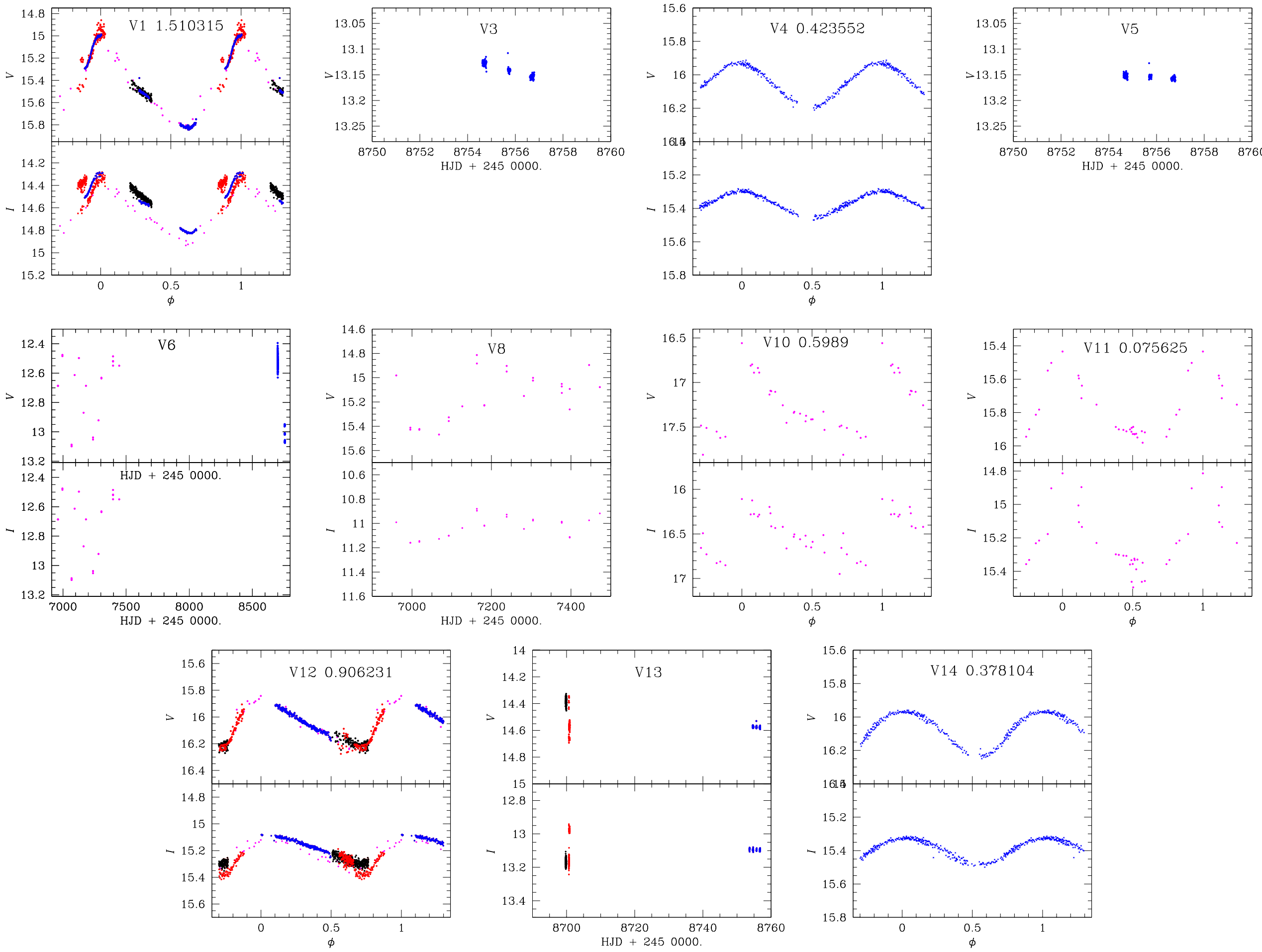

Fig. 3. Light curves of all known variables in M56 previous to the present work. The colour code is: lilac for data from *Gaia*-DR2 photometry transformed into V, black and red correspond to two nights from August 2019, and blue to data from September 2019. Irregular or probably non-periodic giants are plotted as function of HJD. The periods are expressed in fraction of a day. The colour figure can be viewed online.

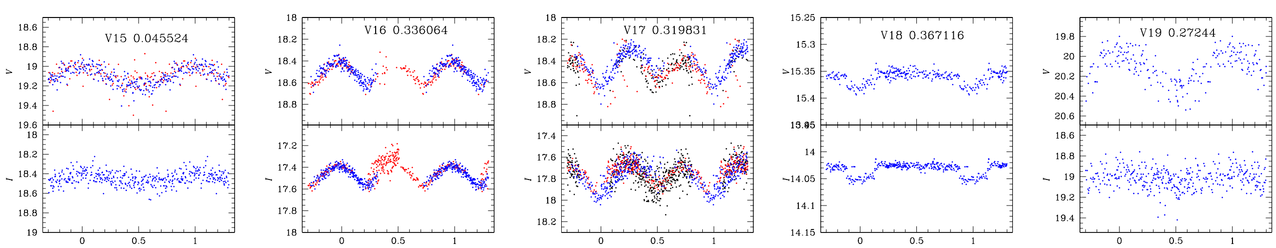

Fig. 4. Light curves of the variables newly found in this work: one SX Phe (V15), three EB (V16-V18) and one RRc (V19). The colour code is as in Figure 3. The periods are expressed in fraction of a day. The colour figure can be viewed online.

the period P of a series of harmonics of the form:

$$m(t) = A_0 + \sum_{k=1}^{N} A_k cos(\frac{2\pi}{P}k(t - E_0) + \phi_k), \quad (5)$$

are intimately correlated with stellar values of [Fe/H], distance, and other relevant physical parameters. In equation 5, $m(t)$ is the magnitude of the star at time t, P is the period of pulsation, and E_0 is the epoch. To calculate A_k and ϕ_k of each harmonic,

TABLE 1

DATA OF VARIABLE STARS IN M56 IN THE FOV OF OUR IMAGES

Star ID	Type	$<V>$ (mag)	$<I>$ (mag)	A_V (mag)	A_I (mag)	P (days)	$\mathrm{HJD_{max}}$ + 2450000	α (J2000.0)	δ (J2000.0)	Membership status
V1	CW	15.47	14.60	0.89	0.54	1.510315	8756.7828	19:16:39.33	+30:12:16.6	M1
V2	CST?	–	–	–	–	–	–	19:16:37.34	+30:11:35.2	M1
V3	SR	13.14[4]	–	–	–	–	–	19:16:37.82	+30:12:33.9	M1
V4	RRc	16.06	15.38	0.28	0.18	0.423552	8700.8311	19:16:27.45	+30:08:21.1	M1
V5	SR	13.15[4]	–	–		–	–	19:16:36.59	+30:08:47.3	M1
V6	RVB	12.75[4]	11.64[4]	0.68	0.62	–	–	19:16:35.77	+30:11:38.9	M1
V7[1,2,6]	Lb	–	–	–	–	–	–	19:16:58.74	+30:07:31.0	FS
V8[1,2]	Lb	15.15[5]	11.03[5]	0.66	0.28	–	–	19:16:28.70	+30:05:24.2	FS
V9[1,2,6]	Lb	–	–	–	–	–	–	19:16:50.11	+30:19:58.8	FS
V10[1,2]	RRab	17.26[5]	16.53[5]	1.08	0.73	0.598900	7088.5956	19:16:02.72	+30:12:25.6	FS
V11[1,2]	SX Phe	15.77[5]	15.20[5]	0.53	0.66	0.075625	7281.6951	19:16:03.66	+30:15:40.5	FS
V12	RRab	16.04	15.22	0.42	0.30	0.906231	8753.6200	19:16:17.25	+30:09:23.7	M1
V13	SR	14.58[4]	13.10[4]	–	–	–	–	19:16:38.74	+30:10:59.0	M1
V14	RRc	16.09	15.40	0.28	0.17	0.378104	8699.8962	19:16:29.84	+30:12:27.4	M1
V15[3]	SX Phe	19.11	18.45	0.25	0.23	0.045524	8756.7720	19:16:41.55	+30:12:08.7	M1
V16[1,3]	EB	18.50	17.45	0.25	0.20	0.336064	8756.7021	19:16:34.09	+30:09:09.5	FS
V17[3]	EB	18.47	17.77	0.43	0.39	0.319831	8756.6109	19:16:34.11	+30:10:25.4	M2
V18[3]	EB	15.35	14.03	–	–	0.367116	8756.7379	19:16:38.70	+30:11:09.9	M1
V19[1,3]	RRc	20.13	19.02	0.47	0.19	0.273647	8756.7900	19:16:30.19	+30:12:34.5	FS

[1]Field Star. [2]Out of our FoV. [3]New variable. [4]Magnitude weighted mean. [5]Transformed into VI Johnson standard system from *Gaia*-DR2 photometry. [6]Not measured by *Gaia*-DR2.

TABLE 2

FOURIER COEFFICIENTS FOR THE RR LYRAE STARS IN THE FOV OF OUR IMAGES

Variable ID	A_0 (V mag)	A_1 (V mag)	A_2 (V mag)	A_3 (V mag)	A_4 (V mag)	ϕ_{21}	ϕ_{31}	ϕ_{41}	$D_{\rm m}$
				RRab					
V12	16.044(2)	0.159(3)	0.053(3)	0.020(3)	0.010(2)	4.451	9.304	8.388	4.3
				RRc					
V4	16.062(1)	0.130(1)	0.002(1)	0.003(1)	0.002(1)	4.442	5.730	4.380	–
V14	16.092(1)	0.134(1)	0.013(1)	0.004(1)	0.003(1)	5.583	3.516	2.939	–

we made use of a least-squares fit approach. The Fourier parameters are defined as $\phi_{ij} = j\phi_i - i\phi_j$, and $R_{ij} = A_i/A_j$. For the RR Lyrae stars, the Fourier coefficients are listed in Table 2.

These parameters, inserted in *ad-hoc* calibrations for RRab and RRc stars, can lead to individual values of the physical parameters reported in Table 3. The specific calibrations and their zero points are given and discussed in great detail in several of our previous papers (e.g. Arellano Ferro et al. (2017) and Deras et al. (2019)) and shall not be repeated here.

M56 is a particularly weak case for Fourier decomposition since it contains a very limited sample of member RR Lyrae: one RRab (V12) and two RRc (V4 and V14). The value of $\mathrm{[Fe/H]_{ZW}}$, i.e., the metallicity in the scale of Zinn & West (1984), is obtained from the calibration of Morgan et al. (2007) for RRc stars and Jurcsik & Kovács (1996) for the RRab star. A value in the high resolution spectroscopic scale $\mathrm{[Fe/H]_{spec}}$ can be obtained from the calibrations of Nemec et al. (2013). In all cases, the key Fourier parameters are ϕ_{31} and P. For V4, the

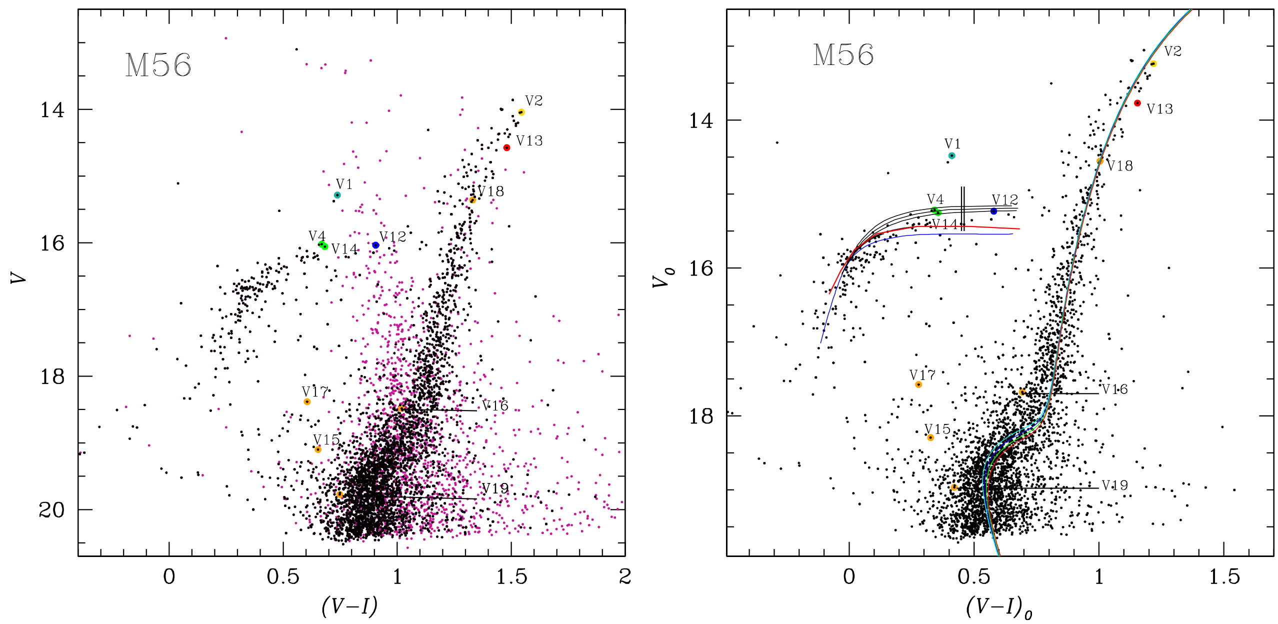

Fig. 5. The colour-magnitude diagram of M56. The left panel shows all the stars measured in the FoV of our images. Non-member field stars identified by the method described in § 3 are shown in purple colour, while the likely members are represented by black dots. The colour code for the variable stars is as follows: in teal the CW, in green the RRc, in blue the RRab, in orange the newly discovered variables, in red the SR, and in yellow a suspected but still unconfirmed variable. The right panel is the intrinsic CMD for $E(B-V) = 0.26$, where isochrones for ages 12.0 (cyan), 12.4 (blue), 13.0 (green) and 13.5 (red) Gyrs, [Fe/H]=–2.0, Y=0.25 and [α/Fe]=+0.4, built from the models of VandenBerg et al. (2014), have been added by shifting them to a distance of 10 kpc to reproduce the observations. The red ZAHB was calculated from the Eggleton code (Pols et al. 1997; Pols et al. 1998; Schröder et al. 1997). The blue ZAHB is from the models of VandenBerg et al. (2014). The thin black lines are evolutionary tracks for a helium core mass of $0.50M_{\odot}$ and total masses of 0.64, 0.65 and $0.66M_{\odot}$ also from the Eggleton code. The empirical border between first overtone and fundamental mode, i.e., the red edge of the first overtone instability strip (FORE), is shown as two vertical black lines. (See § 7 for a full discussion). The colour figure can be viewed online.

TABLE 3

PHYSICAL PARAMETERS OBTAINED FROM THE FOURIER FIT FOR THE RRab AND RRc STARS.

Star	[Fe/H]$_{\rm ZW}$	[Fe/H]$_{\rm Spec}$	M_V	log $T_{\rm eff}$	log$(L/L_{\odot})$	$M/M_{\odot}$	$R/R_{\odot}$	d(kpc)
			RRab star					
V12	-1.76(5)	-1.74(6)	0.323(4)	3.808(1)	1.771(2)	0.467(3)	6.25(1)	9.62(2)
			RRc stars					
V4	–	–	0.52(3)	3.848(2)	1.693(11)	0.46(2)	4.74(6)	8.86(11)
V14	–1.96(9)	–2.03(14)	0.51(1)	3.846(2)	1.697(2)	0.57(1)	4.81(1)	9.03(3)
Weighted Mean	–1.96	-2.03	0.51	3.847	1.696	0.54	4.81	9.02

The numbers in parentheses indicate the uncertainty on the last decimal place. Also listed is the deviation parameter $D_{\rm m}$ for the RRab star. See § 5 for a detailed discussion.

value ϕ_{31}=5.730 (Table 2) is far outside the range of the RRc stars that define the calibration, or in fact it is anomalously large among RRc stars in general (e.g. see Figure 2 of Clement et al. (1992)). This fact is most likely due to its peculiar light curve shape, with maxima more acute than in typical RRc stars (compare with the light curve of V14). For the RRab star V12 we also face some inconvenience: the value of its compatibility parameter, as defined by Jurcsik & Kovács (1996) and Kovács & Kanbur (1998) is D_m=4.3. These authors recommend values smaller than 3.0 to warrant the consistency of a given light

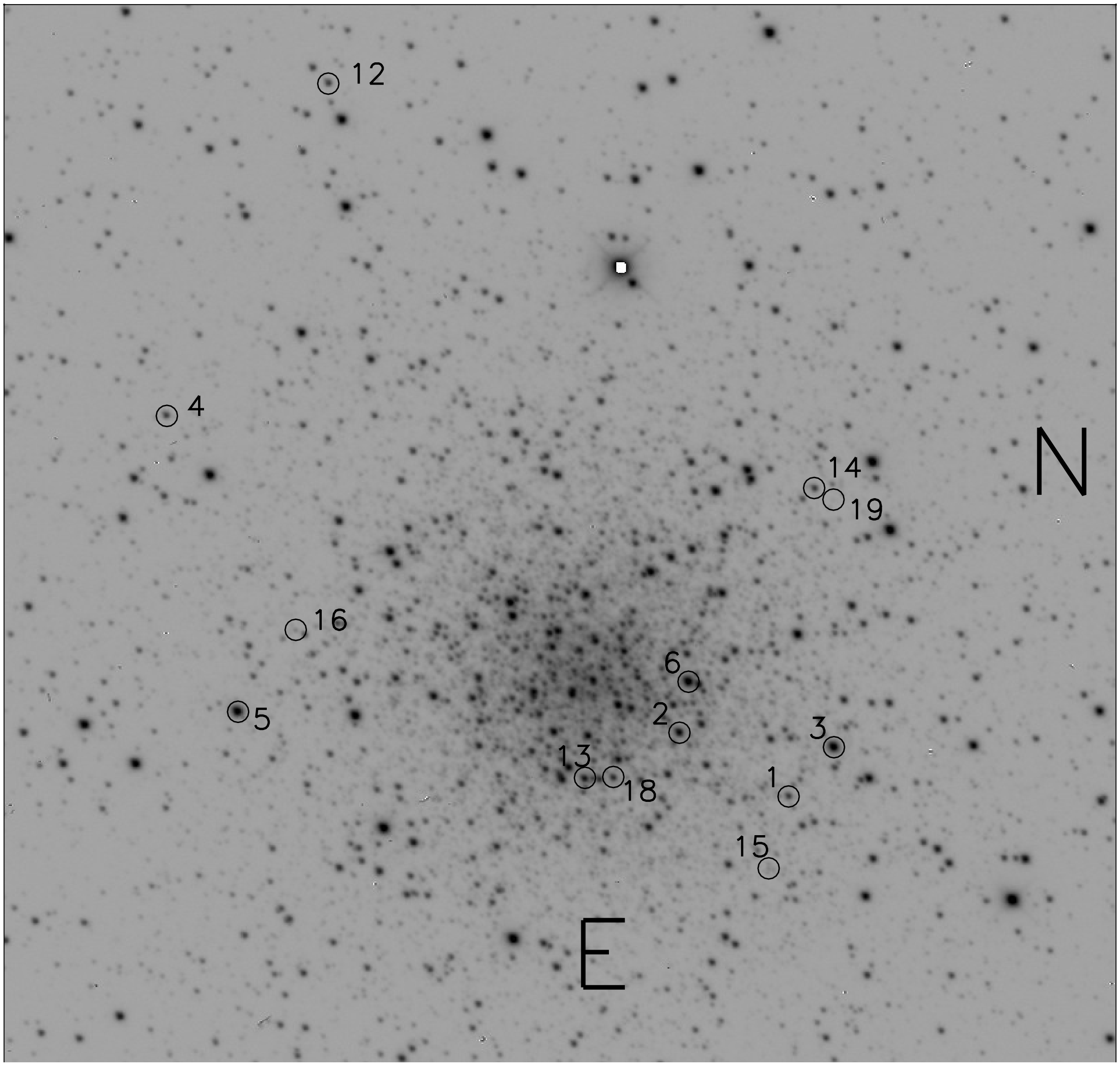

Fig. 6. Identification chart of variables in our FoV of M56. The field is 5.92×5.92 arcmin^2. Expansion of the digital version is recommended for clearness.

curve with the morphology of those of the calibrators. Hence V12 seems also a bit off the limits.

As a result we have a metallicity estimation via the Fourier approach for one RRc star (V14); $[Fe/H]_{Spec} = -2.03 \pm 0.14$. This value is, however, consistent with the standard value reported by Harris (1996) of −1.98.

6. COMMENTS ON THE DISTANCE TO M56

The distance to M56 has been estimated by several independent approaches, namely, the absolute magnitude estimation of the RR Lyrae stars via the Fourier decomposition of their light curves with the results V12 (9.6 kpc), V4 (8.9 kpc), V14(9.0 kpc) (see also Table 3); the positioning of the isochrones and ZAHB on the intrinsic CMD (10 kpc); the *P*-*L* in the *I* filter for the RR Lyrae stars (9.0 kpc) (Catelan et al. 2004) and the application of three independent and well known *P*-*L* relations of SX Phe stars (Poretti et al. 2008, Arellano Ferro et al. 2011, and Cohen & Sarajedini 2012). The calculation for the SX Phe stars V11 and V15 (new variable) deserves a further discussion. Assuming that these two stars are pulsating in the fundamental mode, these calibrations lead to the distances of 3.46 ± 0.14 kpc

TABLE 4

DISTANCE TO M56 FROM DIFFERENT METHODS

Method	d(kpc)	N
RRab Fourier decomposition	9.62	1
RRc Fourier decomposition	8.95±0.09	2
ZAHB placement on the CMD	10.0±0.2	
RRLs P-L (I)	9.0±0.2	3
SX Phe P-L	11.5*	1
Average	9.39±0.44	

*Not included in average.

and 11.5 ± 0.4 kpc, respectively. First or second overtone pulsation assumptions lead to larger distances. It is clear, then, that V11 is definitively not a cluster member, in agreement with the determination from the *Gaia*-eDR3 proper motions described in § 3. V15 seems to lie about 1-2 kpc behind the cluster and may or may not belong to the cluster; hence, we did not include it in the calculation of the average distance shown in Table 4.

7. THE CMD OF M56 AND ITS HB

From the PSF-fitting photometric analysis of our images in § 2, we were able to recover 4845 stars, 3630 (≈ 75%) of which have a high probability to be cluster members. This allowed us to create a clean CMD by removing the field stars (Figure 5). We used the models from VandenBerg et al. (2014) to generate a ZAHB and four isochrones of ages ranging from 12.0 - 13.5 Gyrs with a metallicity of $[Fe/H]_{ZW}$ = -2.0, Y=0.25 and $[\alpha/Fe]$=0.4. Also, using the Eggleton code (Pols et al. 1997; Pols et al. 1998; Schröder et al. 1997) we generated another ZAHB for a core mass of $0.50M_\odot$, and three evolutionary tracks corresponding to total masses of 0.64, 0.65, and $0.66M_\odot$. The isochrones and the ZAHBs were shifted to a distance of 10 kpc using a reddening $E(B-V) = 0.26$. The small discrepancy between the ZAHB from the models of VandenBerg and Eggleton is due to the assumed core mass of the progenitor star. Although the sample of RR Lyrae stars is small, the fact that the RRc and RRab stars are on the first overtone and fundamental sides of the first overtone blue edge (FOBE), is consistent with the mode distribution found in other OoII type clusters, e.g. Yepez et al. (2020). A useful quantity to help describe the morphology of the HB is the Lee parameter (Lee 1990) defined as $\mathcal{L} = (B-R)/(B+V+R)$, where B is the number of stars on the blue side of the

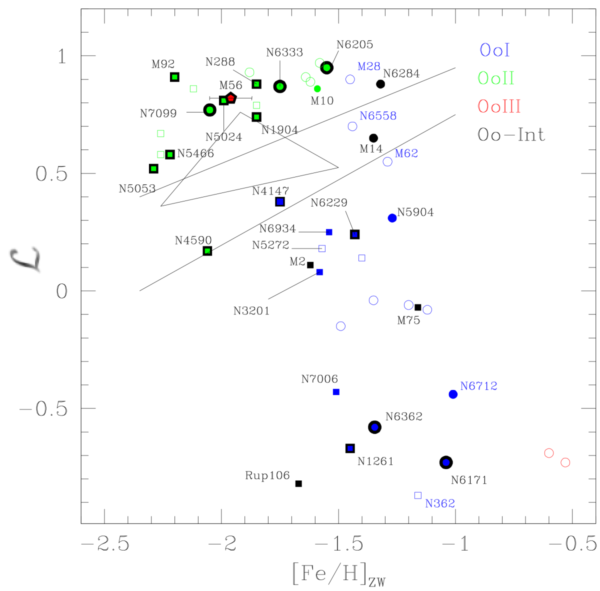

Fig. 7. The HB structure parameter $\mathcal{L}$ as a function of $[Fe/H]_{ZW}$. The two lines define theoretically the so-called Oosterhoff Gap (Bono et al. 1994), a region in the $\mathcal{L}$ - $[Fe/H]_{ZW}$ plane that is devoid of *bona fide* Galactic globular clusters. The triangle represents a region found by Catelan (2009) that is populated by globulars identified in systems outside of the Galaxy. M56 is coloured in red and its position was determined by the estimated values of the metallicity and $\mathcal{L}$ in this work (0.82, -1.96). Circles and squares are used for inner and outer halo clusters, respectively. Symbols with a black rim represent globular clusters where the fundamental and first modes of pulsations are well segregated on the HB, while in those without a rim the modes of pulsation are mixed in the either/or region. Open symbols correspond to clusters yet to be studied by our group, and their current positions are subject to change. For a detailed discussion, see § 7. The colour figure can be viewed online.

instability strip (IS) or the first overtone blue edge (FOBE), R is the number of stars on the red side of the IS or fundamental mode red edge (FMRE) and V is the number of variable stars within the IS. In the case of M56, this yields an $\mathcal{L}$ = 0.82. Figure 7 shows a plot of $\mathcal{L}$ vs $[Fe/H]_{ZW}$ where globular clusters previously studied by our group following the same approach as the one used in this work, are plotted. The triangle in Figure 7 is defined by Catelan (2009) as a region that is preferentially populated by clusters thought to be of extragalactic origin. M56 falls well above this triangular region. The HB of M56 is predominately blue, which is usually seen in most metal-poor Oosterhoff II (OoII) type clusters. While it is not possible to discuss the Oo-type of

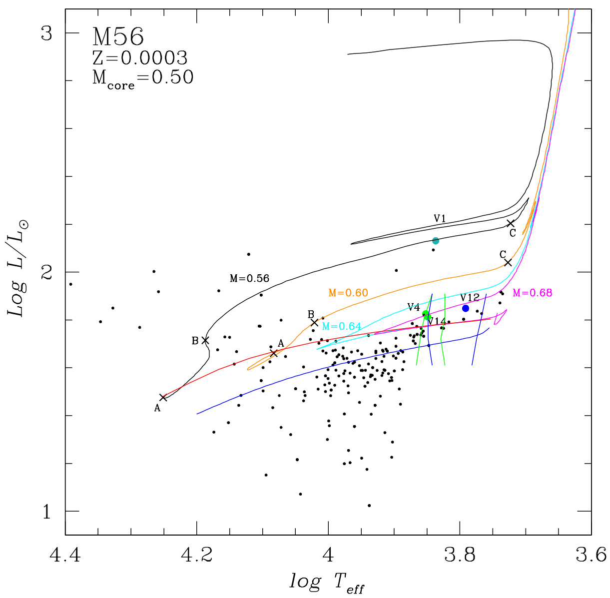

Fig. 8. HRD of the horizontal branch of M56. These models were created using a helium core mass of $0.50M_\odot$. Four tracks for total masses of 0.56 (black), 0.60 (orange), 0.64 (cyan) and $0.68M_\odot$ (lilac) are shown. The blue ZAHB is from the models of VandenBerg et al. (2014). Theoretical border lines of the IS are from Bono et al. (1994) for the fundamental mode (blue) and the first overtone (green). The colour code of the variable stars is as in Figure 4. The fiducial marks at A ($\approx$ 2.5 Myrs), B (leaving the HB) and C (at the base of the AGB) along the tracks help to visualise the evolutionary times involved; on the $0.56M_\odot$ track, the time from A to C is about 100.9 Myrs, thus the post-ZAHB age of V1 is about 100.8 Myrs. The crossing time from B to C takes roughly 2 Myrs. The colour figure can be viewed online.

M56 given the scarce number of RR Lyrae stars, the extremely large period of the only RRab star V12, makes the case most peculiar even among Oo-II type clusters. Its position on the $\mathcal{L}$ vs [Fe/H]$_{\rm ZW}$ plane, however, makes it difficult to support its possible extragalactic origin on these grounds.

7.1. *Post-Evolutionary ZAHB Models*

In order to offer some input on the stellar mass distribution on the HB, as well as on the mass structure (core and envelope masses) for the stars of the HB and their ulterior evolution towards higher luminosities, we have calculated some evolutionary tracks using the Eggleton code (Pols et al. 1997; Pols et al. 1998; Schröder et al. 1997) with a modified Reimers law for the mass loss with $\eta = 0.8 \times 10^{-13}$ (Schröder & Cuntz 2005) as a consequence of the He-flash episodes during the RGB stages. A detailed description of this procedure has been given by Arellano Ferro et al. (2020). To compare our theoretical predictions with the observed stellar distributions, we converted the CMD into an HRD, i.e., we converted the plane $(V-I)$-V into log($T_{\rm eff}$)-log($L/L_\odot$). To this end, we adopted the $(V-I)_o$-log($T_{\rm eff}$) and BC-log($T_{\rm eff}$) calibrations of VandenBerg & Clem (2003). The resulting HRD of the HB region is shown in Figure 8. It should be noted that the scatter in the HB is larger on its blue side, i.e., the stars corresponding to the vertical blue tail in the HB in the CMD. Since they are considerably fainter, some may or may not be truly members of the HB. In comparison, the horizontal portion where the RR Lyrae stars reside is neat and well represented by the theoretical loci. While in fact we have modelled cases for core masses of 0.49, 0.50 and $0.51M_\odot$, we display only the case for $0.50M_\odot$ as we believe it produced the best representation of the data.

In Figure 8 there are also shown the positions of the RRab V12 (blue dot), RRc V4 and V14 stars (green dots) and the only CW V1 star (teal dot), along with the theoretical borders of the instability strip for the fundamental and first overtone modes (Bono et al. 1994). The red line is the ZAHB for the stars with a He-core of $0.50M_\odot$. The blue line corresponds to the ZAHB calculated with the models of VandenBerg et al. (2014) for [Fe/H]=-2.0, Y=0.25 and [α/Fe]=+0.4; this ZAHB starts with a core mass of $0.49M_\odot$ that decreases towards the blue and for this reason it lies a bit below of the red line. Black, orange, cyan and lilac loci are tracks for total masses of 0.56, 0.60, 0.64, 0.68 $M_\odot$, respectively, i.e. for envelopes with 0.06, 0.10, 0.14 and 0.18 $M_\odot$. The RR Lyrae stars lie between tracks with envelopes of 0.14-0.18 $M_\odot$. The CW star, V1, seems well represented by a track with a very thin envelope ($0.06M_\odot$) which has originated at the bluest part of HB. Considering an age range of 12.0 - 13.5 Gyrs, the probable progenitor star of the stars on the HB had an initial mass of $\approx$ 0.81 - 0.83 $M_\odot$ at the ZAMS. Such a star lost between 0.15 and 0.26 $M_\odot$ during the He flashes in its evolution from the RGB towards the ZAHB.

8. SUMMARY

In this work we have performed VI CCD photometry of 4845 sources present in the globular cluster M56 and we summarise our results as follows:

- The use of a semi-empirical calibration based on the Fourier decomposition of the light curve of a single RRc star (V14) allowed us to determine a metallicity value of [Fe/H]$_{\rm ZW} = -1.96 \pm 0.09$.

- The fact that the intrinsic colour $(B-V)_0$ of RRab stars at minimum light between the phases 0.5 - 0.8 is constant allowed us to estimate a value for the reddening using the only RRab present in our data (V12), yielding $E(B-V)=0.26$.

- We have made use of five different independent methods to determine the distance to M56, namely: from the semi-empirical calibrations derived for RRab and RRc stars, from the placement of a ZAHB on the CMD, from the *P*-*L* relation in the *I* filter for RR Lyrae stars, and the *P*-*L* relation for SX Phe stars. For the last method, our membership analysis determined V15 to be a cluster member, and its position on the CMD is consistent with the position of the stars of the same class. Nevertheless, its estimated distance (assuming fundamental mode pulsation) places it approximately 2 kpc farther than the distance obtained through the other four methods ($\langle d \rangle = 9.39 \pm 0.44$ kpc), and it was not included in the calculation of the average cluster distance.

- Our analysis of star membership through proper motions using *Gaia*-eDR3, allowed us to create a clean CMD consistent with isochrones in an age range of 12.0-13.5 Gyrs and a metallicity of $[\mathrm{Fe/H}]_{\mathrm{ZW}} = -2.0$.

- Previous authors have presented evidence that indicates that the origin of M56 is the result of a merger event. The value of the $\mathcal{L}$ parameter, calculated from a CMD clean of field stars, (0.82) and the value of the metallicity of M56 (-1.96), places M56 clearly outside the region of the $\mathcal{L}$ vs $[\mathrm{Fe/H}]_{\mathrm{ZW}}$ plane preferentially populated by globular clusters of extragalactic origin. These results make it difficult to argue in favour the extragalactic origin of M56.

- Our post He flash evolutionary models with a He-core of $0.50M_\odot$ and envelopes of 0.04 - 0.18 $M_\odot$, cover the complete HB of M56. Models with large total masses ($\approx 0.68M_\odot$) can explain the evolutionary stage of the RR Lyrae stars. Models with thinner envelopes show longer blue loops that cross the IS above the HB, in the region of the type II Cepheids. Stars in the blue tail with these features could be the origin of BL Her and W Vir stars.

- We report five new variables: one SX Phe (V15), three EB (V16 - V18), and one RRc (V19). According to the proper motion analysis carried out in § 3, V16 (EB) and V19 (RRc) are not cluster members. In particular for V19, this result is confirmed by the value of its intensity weighted mean ($V \approx 20$) and its unusual location at the bottom of the CMD, more than three magnitudes below the HB.

This project was partially supported by DGAPA-UNAM (Mexico) via grants IG100620 and IN106615-17. We have made extensive use of the SIMBAD, ADS services, and of 'Aladin sky atlas' developed at CDS, Strasbourg Observatory, France (Bonnarel et al. 2000), and TOPCAT (Taylor 2005).

REFERENCES

Arellano Ferro, A., Bramich, D. M., & Giridhar, S. 2017, RMxAA, 53, 121

Arellano Ferro, A., Figuera Jaimes, R., Giridhar, S., et al. 2011, MNRAS, 416, 2265, https://doi.org/10.1111/j.1365-2966.2011.19201.x

Arellano Ferro, A., Yepez, M. A., Muneer, S., et al. 2020, MNRAS, 499, 4026, https://doi.org/10.1093/mnras/staa2977

Bonnarel, F., Fernique, P., Bienaymé, O., et al. 2000, A&AS, 143, 33, https://doi.org/10.1051/aas:2000331

Bono, G., Caputo, F., & Stellingwerf, R. F. 1994, ApJ, 423, 294, https://doi.org/10.1086/173803

Bramich, D. M. 2008, MNRAS, 386, 77, https://doi.org/10.1111/j.1745-3933.2008.00464.x

Bramich, D. M., Figuera Jaimes, R., Giridhar, S., & Arellano Ferro, A. 2011, MNRAS, 413, 1275, https://doi.org/10.1111/j.1365-2966.2011.18213.x

Bramich, D. M., Horne, K., Albrow, M. D., et al. 2013, MNRAS, 428, 2275, https://doi.org/10.1093/mnras/sts184

Burke, E. W., Rolland, W. W., & Boy, W. R. 1970, JRASC, 64, 353

Bustos Fierro, I. H. & Calderón, J. H. 2019, MNRAS, 488, 3024, https://doi.org/10.1093/mnras/stz1879

Catelan, M., Pritzl, B. J., & Smith, H. A. 2004, ApJS, 154, 633, https://doi.org/10.1086/422916

Catelan, M. 2009, Ap&SS, 320, 261, https://doi.org/10.1007/s10509-009-9987-8

Clement, C. M., Jankulak, M., & Simon, N. R. 1992, ApJ, 395, 192, https://doi.org/10.1086/171643

Clement, C. M., Muzzin, A., Dufton, Q., et al. 2001, AJ, 122, 2587, https://doi.org/10.1086/323719

Cohen, R. E. & Sarajedini, A. 2012, MNRAS, 419, 342, https://doi.org/10.1111/j.1365-2966.2011.19697.x

Deason, A. J., Belokurov, V., Evans, N. W., & Johnston, K. V. 2013, ApJ, 763, 113, https://doi.org/10.1088/0004-637x/763/2/113

Deras, D., Arellano Ferro, A., Lázaro, C., et al. 2019, MNRAS, 486, 2791, https://doi.org/10.1093/mnras/stz642

Dworetsky, M. M. 1983, MNRAS, 203, 917, https://doi.org/10.1093/mnras/203.4.917
Gaia Collaboration, Brown, A. G. A., Vallenari, A., et al. 2021, A&A, 649, 1, https://doi.org/10.1051/0004-6361/202039657
Gaia Collaboration, Brown, A. G. A., Vallenari, A., et al. 2018, A&A, 616, 1, https://doi.org/10.1051/0004-6361/201833051
Guldenschuh, K. A., Layden, A. C., Wan, Y., et al. 2005, PASP, 117, 721, https://doi.org/10.1086/431178
Harris, W. E. 1996, AJ, 112, 1487, https://doi.org/10.1086/118116
Hatzidimitriou, D., Antoniou, V., Papadakis, I., et al. 2004, MNRAS, 348, 1157, https://doi.org/10.1111/j.1365-2966.2004.07439.x
Ivanov, V. D., Borissova, J., Alonso-Herrero, A., & Russeva, T. 2000, AJ, 119, 2274, https://doi.org/10.1086/301363
Jurcsik, J. & Kovács, G. 1996, A&A, 312, 111
Kovács, G. & Kanbur, S. M. 1998, MNRAS, 295, 834, https://doi.org/10.1046/j.1365-8711.1998.01271.x
Kron, G. E. & Guetter, H. H. 1976, AJ, 81, 817, https://doi.org/10.1086/116242
Landolt, A. U. 1992, AJ, 104, 340, https://doi.org/10.1086/169326
Lee, Y.-W. 1990, ApJ, 363, 159, https://doi.org/10.1086/169326
Massari, D., Koppelman, H. H., & Helmi, A. 2019, A&A, 630, 4, https://doi.org/10.1051/0004-6361/201936135
Morgan, S. M., Wahl, J. N., & Wieckhorst, R. M. 2007, MNRAS, 374, 1421, https://doi.org/10.1111/j.1365-2966.2006.11247.x
Nemec, J. M., Cohen, J. G., Ripepi, V., et al. 2013, ApJ, 773, 181, https://doi.org/10.1088/0004-637x/773/2/181
Piatti, A. E. & Carballo-Bello, J. A. 2019, MNRAS, 485, 1029, https://doi.org/10.1093/mnras/stz500
Pietrukowicz, P., Olech, A., Kedzierski, P., et al. 2008, AcA, 58, 121
Pols, O. R., Schröder, K.-P., Hurley, J. R., Tout, C. A., & Eggleton, P. P. 1998, MNRAS, 298, 525, https://doi.org/10.1046/j.1365-8711.1998.01658.x
Pols, O. R., Tout, C. A., Schroder, K.-P., Eggleton, P. P., & Manners, J. 1997, MNRAS, 289, 869, https://doi.org/10.1093/mnras/289.4.869
Poretti, E., Clementini, G., Held, E. V., et al. 2008, ApJ, 685, 947, https://doi.org/10.1086/591241
Schlafly, E. F. & Finkbeiner, D. P. 2011, ApJ, 737, 103, https://doi.org/10.1088/0004-637x/737/2/103
Schlegel, D. J., Finkbeiner, D. P., & Davis, M. 1998, ApJ, 500, 525, https://doi.org/10.1086/305772
Schröder, K.-P. & Cuntz, M. 2005, ApJ, 630, 73, https://doi.org/10.1086/491579
Schröder, K.-P., Pols, O. R., & Eggleton, P. P. 1997, MNRAS, 285, 696, https://doi.org/10.1093/mnras/285.4.696
Searle, L. & Zinn, R. 1978, ApJ, 225, 357, https://doi.org/10.1086/156499
Stetson, P. B. 2000, PASP, 112, 925, https://doi.org/10.1086/316595
Sturch, C. 1966, ApJ, 143, 774, https://doi.org/10.1086/148557
Taylor, M. B. 2005, ASPC, 347, Astronomical Data Analysis Software and Systems XIV, ed. P. Shopbell, M. Britton, & R. Ebert, (San Francisco, CA: ASP), 29
VandenBerg, D. A., Bergbusch, P. A., Ferguson, J. W., & Edvardsson, B. 2014, ApJ, 794, 72, https://doi.org/10.1088/0004-637x/794/1/72
VandenBerg, D. A. & Clem, J. L. 2003, AJ, 126, 778, https://doi.org/10.1086/376840
Yepez, M. A., Arellano Ferro, A., & Deras, D. 2020, MNRAS, 494, 3212, https://doi.org/10.1093/mnras/staa637
Zhang, T., Ramakrishnan, R., & Livny, M. 1996, ACM SIGMOD Record, 25, 103, https://doi.org/10.1145/235968.233324
Zinn, R. & West, M. J. 1984, ApJS, 55, 45, https://doi.org/10.1086/190947

A. Arellano Ferro, D. Deras, and M. A. Yepez: Instituto de Astronomía, Universidad Nacional Autónoma de México, Ciudad Universitaria, C.P. 04510, México.
I. Bustos Fierro: Observatorio Astronómico, Universidad Nacional de Córdoba, Laprida 854, X5000BGR, Córdoba, Argentina.

Revista Mexicana de Astronomía y Astrofísica, **58**, 133–153 (2022)

https://doi.org/10.22201/ia.01851101p.2022.58.01.11

TEMPERATURE DISCREPANCY WITH PHOTOIONIZATION MODELS OF THE NARROW-LINE REGION

Luc Binette[1], Montserrat Villar Martín[2], Gladis Magris C.[3], Mariela Martínez-Paredes[4], Alexandre Alarie[5], Alberto Rodríguez Ardila[6], and Ilhuiyolitzin Villicaña-Pedraza[7]

Received December 28 2021; accepted January 25 2022

ABSTRACT

Using published work on the narrow-line region of active galactic nuclei, a comparison is carried out among the [O III] $\lambda4363$Å/$\lambda5007$Å ($R_{\rm OIII}$) ratio observed in quasars, Seyfert 2's and the spatially resolved ENLR plasma. Using the weak [Ar IV] $\lambda4711$Å/$\lambda4740$Å doublet ratio observed by Koski (1978) among Seyfert 2's, we find evidence of a narrow-line region (NLR) populated by low density emission clouds ($\lesssim 10^4\,\rm cm^{-3}$). After considering calculations of the [Ar IV] and [O III] ratios that assume a power law distribution of plasma densities, no evidence of collisional deexcitation is found. The plasma temperature inferred is 13 500 °K, which is problematic to reproduce with standard photoionization calculations. The simplest interpretation for the near coincidence of the $R_{\rm OIII}$ ratios among the ENLR and Seyfert 2 measurements ($R_{\rm OIII} \simeq 0.017$) is that the low density regime applies to both plasmas.

RESUMEN

Utilizando trabajos publicados sobre la región de líneas angostas de los núcleos galácticos activos, se compara el [O III] $\lambda4363$Å/$\lambda5007$Å ($R_{\rm OIII}$) observado en cuásares, Seyfert 2 y en el plasma espacialmente resuelto de la ENLR. Mediante el débil doblete de [Ar IV] $\lambda4711$Å/$\lambda4740$Å observado por Koski encontramos evidencias de una región de líneas angostas (NLR) poblada por nubes de emisión de baja densidad ($\lesssim 10^4\,\rm cm^{-3}$). Tras considerar los cálculos de las relaciones [Ar IV] y [O III] que asumen una distribución de ley de potencia de las densidades del plasma, no se encuentra evidencia de desexcitación colisional. La temperatura del plasma que se infiere es de 13 500 °K, la cual es difícil de reproducir con los cálculos estándar de fotoionización. La interpretación más sencilla de la casi coincidencia de los cocientes de $R_{\rm OIII}$ medidos en la ENLR y las Seyfert 2 ($R_{\rm OIII} \simeq 0.017$) sería que el régimen de baja densidad se aplica a ambos plasmas.

Key Words: dust, extinction — galaxies: Seyfert — plasmas — quasars: emission lines

1. INTRODUCTION

The physics of the so-called narrow-line region of active galactic nuclei (AGN) has been amply studied (cf. Osterbrock 1978, and references therein). AGN emission line spectra can be divided into two categories[8]: Type I when the full width half-maximum (FWHM) of the permitted lines are significantly larger than the forbidden lines, and Type II where both the permitted and forbidden lines have similar FWHM. The broad-line region (BLR) observed in Type I objects originates from high density gas ($> 10^8\,\rm cm^{-3}$) much closer to the black-hole (BH) than the narrow-line region (hereafter NLR), the latter being observed in both Type I and II objects. The

[1]Instituto de Astronomía, UNAM, México.
[2]Centro de Astrobiología, Departamento de Astrofísica, Madrid, Spain.
[3]Centro de Investigaciones de Astronomía, Mérida, Venezuela.
[4]Korea Astronomy and Space Science Institute, Daejeon, South Korea.
[5]Département de physique, de génie physique et d'optique, Université Laval, Québec, Canada.
[6]Laboratório Nacional de Astrofísica, Itajubá, Brazil.
[7]DACC Science Department, New Mexico State University, USA.

[8]The current study does *not* include BL Lac objects nor extremely red quasars.

AGN unified model sustains that both types relate to the same phenomenon, with the differences being the visibility of the central engine. It proposes that the BLR is hidden from direct view in Type II due to an optically thick dusty torus-like gas structure surrounding the central engine (black hole, accretion disk, and BLR) (Antonucci 1993). Whether the BLR is observed or not depends on the viewing angle of the nucleus. Seyfert 2's, QSO 2's and narrow line radio galaxies (NLRG) are classified as Type II while Seyfert 1's, quasars, QSO 1's and broad-line radio galaxies (BLRG) are of Type I because their BLR is visible.

While it is customary to assume for H II regions the low density regime (hereafter LDR) when evaluating the plasma temperature using the [O III] λ4363Å/λ5007Å line ratio (hereafter labeled $R_{\rm OIII}$), this is inappropriate for the NLR, at least in Type I objects. Osterbrock (1978) interpreted the relative strength of the λ4363Å line, which was measured to be higher in Seyfert 1's and BLRG than in Seyfert 2's, as evidence of densities in the range $10^6 - 10^7\,{\rm cm}^{-3}$ within the NLR of Type I AGN. This interpretation was confirmed by the study of Baskin & Laor (2005, hereafter BL05) who compared the $R_{\rm OIII}$ they measured in 30 quasars. Their single-density calculations showed that the broad range of observed $R_{\rm OIII}$ ratios implies high plasma densities, ranging from possibly 10^5 up to $10^7\,{\rm cm}^{-3}$, providing convincing evidence of the important role of collisional deexcitation in Type I AGN, where the temperature cannot be directly inferred from the $R_{\rm OIII}$ ratio. In the case of Type II objects (Seyfert 2's and NLRG), the $R_{\rm OIII}$ ratio is on average smaller ($\lesssim 0.019$) although selection effects may possibly bias such an assessment. Prevailing NLR photoionization models consider a distribution of clouds that extends over a wide range of values of densities and ionization parameter, whether the targets are Type I (Baldwin et al. 1995; Korista et al. 1997) or Type II objects (Ferguson et al. 1997; Richardson et al. 2014). With respect to the spatially resolved emission line component of AGN, the so-called extended NLR (hereafter ENLR), it consists of *off-nuclear* line emission from plasma at typically LDR densities (e.g. Tadhunter et al. 1994; Bennert et al. 2006a,b) where the $R_{\rm OIII}$ ratio should provide a reliable temperature measurement.

The original element of the current work is the use of the weak [Ar IV] $\lambda\lambda$4711,40Å doublet to evaluate to what extent the $R_{\rm OIII}$ measurements of our selected Seyfert 2 sample is affected by collisional deexcitation. To cover the multi-density case, we developed an algorithm, OSALD, to calculate density and temperature line ratio *diagnostics* appropriate to isothermal plasmas in which the density follows a power law distribution rather than taking on a single value. This algorithm offers the option of including a foreground dust extinction component whose opacity, rather than being uniform, correlates with the emission plasma density. Our main conclusion is that (at least for the subset of Type II objects where the [Ar IV] doublet is observed) there is no evidence of significant collisional deexcitation. Hence, in those cases the $R_{\rm OIII}$ ratio constitutes a direct temperature indicator. Oddly, LDR photoionization calculations result in temperature discrepancies with the observations, underscoring the so-called temperature problem (Storchi-Bergmann et al. 1996; Bennert et al. 2006a; Villar-Martín et al. 2008; Dors et al. 2015, 2020). In a follow-up paper, we evaluate different physical processes to address this issue.

Our reference sample is described in § 2 and a comparison with single-component photoionization models is presented in § 3. A modified interpretation of the NLR $R_{\rm OIII}$ ratios observed near $\simeq 0.017$ in Type II and some Type I AGN is proposed in § 4. These are subsequently compared with calculations made with the algorithm OSALD (§ 5), which considers a power law density distribution.

2. REFERENCE DATA SET OF $R_{\rm OIII}$ RATIOS IN AGN

In what follows, the term NLR will be used exclusively in reference to the spatially *unresolved* nuclear component. For any line emission that originates beyond the spatially unresolved central component[9] of the active nucleus, it will be referred as ENLR[10] in all cases where the gas is deemed photoionized by the AGN rather than by hot stars.

In order to evaluate the impact of collisional-deexcitation on the [O III] emission lines among Type I and II AGN, our data set consists primarily of the quasar sample of BL05 (excluding upper limits data), to which we added the four narrow-line Seyfert 1 studied by Rodríguez-Ardila et al. (2000a, hereafter RA00) which were originally observed by Rodríguez-Ardila et al. (2000b). To have access to measurements of the $\lambda\lambda$4711,40Å doublet, we relied

[9]Where the densest plasma of the BLR and inner NLR is located.

[10]When the line emission lies kiloparsecs or more away from the nucleus, some authors (e.g., Tadhunter et al. 1988) prefer the term extended emission line region (EELR).

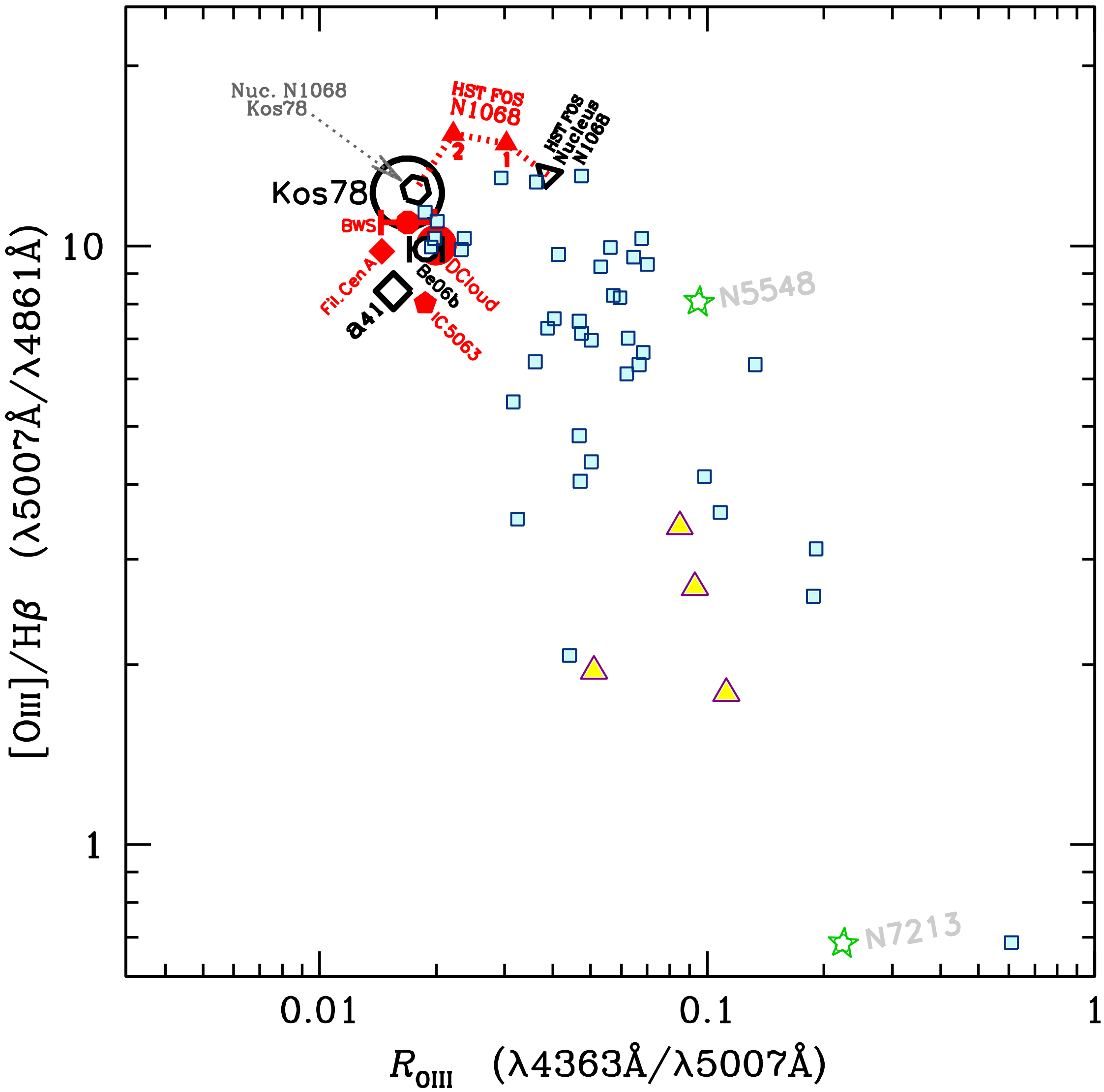

Fig. 1. AGN dereddened line ratios of [O III]/Hβ vs. $R_{\rm OIII}$ from: A- Type I AGN with measurements of (1) 30 quasars studied by BL05 (bluish open squares), (2) four narrow-line Seyfert 1 galaxies from RA00 (yellowish open triangles), (3) two Seyfert 1.5, NGC 5548 and NGC 7213 (open stars), B-Type II AGN represented by open *black* symbols consisting of (1) the average of seven Seyfert 2's from Kos78 (large circle), (2) the average of four Seyfert 2's from Be06b (small circle), (3) the high excitation Seyfert 2 subset a41 from Ri14 (diamond), (4) the nucleus of NGC 1068 through ground-based observations by Kos78 (black hexagon) and HST-FOS observations analysed by Kr98 (black open triangle), and C- ENLR measurements (all as red filled symbols) consisting of (1) the average from BWS of two Seyfert 2's and two NLRGs (red dot), (2) the long-slit observations of the Seyfert 2 IC 5063 by Be06b (pentagon), (3) the average of seven spatially resolved optical filaments from the radio-galaxy Centaurus A (red square) by Mo91, (4) the 8 kpc *distant cloud* from radiogalaxy Pks 2152−699 by Ta87 (large dot), and (5) the HST-FOS measurements of two ENLR knots from NGC 1068 (red triangles). The colour figure can be viewed online.

on the Seyfert 2 sample of Koski (1978, hereafter Kos78). Finally, to ensure that our sample covers cases where the emission plasma is negligibly affected by collisional deexcitation, we included diverse ENLR observations from the literature. Figure 1 describes the behaviour of the dereddened [O III]/Hβ (λ5007Å/λ4861Å) and $R_{\rm OIII}$ (λ4363Å/λ5007Å) line ratios of our AGN sample.

TABLE 1

REDDENING-CORRECTED SEYFERT 2 RATIOS FROM KOSKI (1978)

(1) Index #	(2)[a] Seyfert 2	(3) [O III]/Hβ $\frac{\lambda 5007}{\lambda 4861}$	(4) $R_{\rm OIII}$ $\frac{\lambda 4363}{\lambda 5007}$	(5) [Ar IV]+ $\frac{\lambda 4711+}{\lambda 4740}$	(6) $\rm R_{He/Ar}$ $\frac{\lambda 5876}{\lambda 4740}$	(7)[b] $f^{HeI}_{\rm blend}$	(8)[c] $n_{\rm sng}$ cm^{-3}	(9)[d] $\rm T^{\it sng}_{OIII}$ °K
1	Mrk 573	12.12	0.0149	1.167	1.52	0.039	1.85×10^3	13 360
2	Mrk 34	11.46	0.0131	1.203	2.03	0.051	1.64×10^3	12 720
3	Mrk 78	11.94	0.0117	1.267	2.22	0.053	1.14×10^3	12 210
4	Mrk 176	14.36	0.0223	1.045	0.45	0.013	2.84×10^3	15 940
5	Mrk 3	12.67	0.0189	0.837	1.95	0.072	7.21×10^3	14 670
6	Mrk 1	10.95	0.0192	0.825	1.59	0.059	7.25×10^3	14 760
7	NGC 1068	12.42	0.0177	0.790	2.42	0.097	8.77×10^3	14 210

[a]The line ratios from the 7 Seyfert 2's were reddening corrected by Koski (1978) using the observed Balmer decrement. The measurement uncertainties were estimated at ±10% for the strong line fluxes and ±20% for the weak lines.

[b]The inferred fractional contribution of He I λ4713Å to the blended λ4711Å+ line.

[c]The densities $n_{\rm sng}$ were determined using the deblended λ4711Å/λ4740Å doublet ratio.

[d]The temperature $\rm T^{\it sng}_{OIII}$ was derived from the $R_{\rm OIII}$ ratio assuming the density $n_{\rm sng}$ inferred from the deblended [Ar IV] ratio (see § 5.1.5). The average temperature from Column (7) is $\langle \rm T^{\it sng}_{OIII} \rangle = 13\,980 \pm 1200$ °K.

2.1. *Detailed Description of the Dereddened $R_{\rm OIII}$ Data Set*

The data set was extracted from the following sources:

A – NLR of Type I AGN

(a) Based on the prominent work of BL05, the sample consists of 30 Type I quasars with $z < 0.5$, mostly from the bright quasar survey of Boroson & Green (1992). Objects where only upper limits of [O III] λ4363Å were reported have been excluded. The sample is represented by bluish open squares in Figure 1. The authors used the [O III] λ5007Å profile of each object as template for extracting the NLR Hβ and [O III] λ4363Å line fluxes. Since the latter line is weak, its measurement required a proper subtraction of the underlying Fe II emission multiplets. BL05 used the I Zw 1 Fe II template provided by T. Boroson (private communication) to subtract the Fe II multiplets. All the line fluxes were corrected for dust reddening and possible slit losses.

(b) The measurements of the four narrow-line Seyfert 1 nuclei (hereafter NLS1) from RA00 (yellowish open triangles) were annexed. As detailed in their study, the authors used their own spectrum of I Zw 1 to subtract the various Fe II underlying features present in their NLS1 spectra. They compared different ways to extract the Hβ NLR contribution, favouring in the end the procedure of fitting a narrow and broad Gaussian component to the Hβ profiles. The broad to narrow Hβ flux ratios in these objects cover the range of 1.8 to 3.4.

(c) For comparison purposes, we included the measurements of two well-studied Seyfert 1.5 galaxies (light-green open stars): NGC 5548 (Kraemer et al. 1998a) and NGC 7213[11] (Filippenko & Halpern 1984).

B – NLR of Type II AGN

(a) To characterize the behaviour of high excitation Type II objects, we adopt the pioneering work on Seyfert 2's by Koski (1978, hereafter Kos78), which provides the unique characteristic of reporting reliable measurements of the weak [Ar IV] λλ4711,40Å doublet ratio, an essential density indicator for evaluating in § 4.2 and § 5.2 to what extent the observed $R_{\rm OIII}$ is affected by collisional deexcitation. Table 1 lists the reddening corrected ratios of the

[11]Initially associated to the LINER category, the presence of [Ne V] lines indicates a high ionization plasma despite having [O III]/H$\beta < 1$ due to collisional deexcitation.

high excitation subset of their sample (i.e. with [O III]/Hβ ≥ 10), which consists of seven Seyfert 2's. Two objects, Mrk 348 and 3C33, were left out of Table 1 since their measurement of the [Ar IV] ratio unrealistically exceeded the low density limit value. They presumably indicate emission from LDR plasma. The average $R_{\rm OIII}$ ratio from Table 1 is 0.0168 (i.e. $10^{-1.77}$ in Figure 1), which is represented by a large black disk whose radius of 0.088 dex corresponds to the $R_{\rm OIII}$ RMS dispersion. The average [O III]/Hβ is 12.3 ± 1.1.

(b) As a complement to Type II objects, we averaged the measurements of the four Seyfert 2's IC 5063, NGC 7212, NGC 3281 and NGC 1386 observed by Bennert et al. (2006b, hereafter Be06b). It is represented by a small black circle corresponding to a mean $R_{\rm OIII}$ of 0.0188. Pseudo error bars represent the RMS dispersion of 0.042 dex.

(c) The black diamond labelled a41 with $R_{\rm OIII} = 0.0155$ represents the high ionization end of the sequence of reconstructed spectra of Richardson et al. (2014, hereafter Ri14) which was extracted from a sample of 379 AGN. These were identified by applying the Mean Field Independent Component Analysis (MFICA) tool to their Sloan Digital Sky Survey (SDSS) sample of $\approx 10^4$ emission line galaxies in the redshift range $0.10 < z < 0.12$ (see also Allen et al. 2013). They meticulously reviewed each spectrum to ensure that no BLR component was present.

(d) Ground-based observations of the Seyfert 2 NGC 1068 nucleus by Kos78 is represented by the black open octagon while the black open triangle corresponds to the HST-FOS measurement of the nucleus at a much higher spatial resolution of $0.3''$ (archive data Kraemer et al. 1998b, hereafter Kr98).

C – Spatially resolved ENLR emission

(a) The red filled dot stands for the average ratio from the ENLR of four Type II AGN (two are Seyfert 2's: ESO 362-G08 and MRK 573, and two are NLRGs: Pks 0349−27 and Pks 0634−20) which were studied by Storchi-Bergmann et al. (1996, hereafter SB96). The mean $R_{\rm OIII}$ ratio is 0.0169 ± 0.0029, which includes measurements on both sides of the nucleus, except for ESO 362-G08 (Binette et al. 1996, hereafter BWS). Pseudo-error bars denote an RMS dispersion of 0.07 dex.

(b) The Seyfert 2 IC 5063. The red pentagon represents the average ratio $R_{\rm OIII} = 0.0188$ (with dispersion of 0.042 dex) from the *extranuclear* radial emission of the Seyfert 2 IC 5063 which Be06b observed with a $S/N > 3$ from $8''$ NW to $5''$ SE.

(c) The Centaurus A (NGC 5128) filaments. The red square represents the average ratio of seven optical filaments studied by Morganti et al. (1991, hereafter Mo91) and situated along the radio jet at a mean distance of 490 pc from the nucleus of the radio-galaxy Centaurus A (mean $R_{\rm OIII} = 0.0145$ with a dispersion of 0.13 dex).

(d) Detached cloud emission aligned with radio-galaxy jets. The large red dot represents the well studied 8 kpc distant cloud associated to the nucleus of radiogalaxy Pks 2152−699 (Tadhunter et al. 1987, hereafter Ta87).

(e) Two detached emission line 'knots' of NGC 1068 labelled 1 and 2 (red triangles) which were studied by Kr98 using HST-FOS archive data. The positions are off-centered from the nucleus by $0.2''$ and $0.7''$, respectively.

3. PHOTOIONIZATION CALCULATIONS AT LDR DENSITIES

All our calculations will be presented in Figure 3 in which the reference data set is represented using the same symbols but coloured in gray. For an isothermal plasma at a fixed temperature, densities much above LDR would cause an increase of the $R_{\rm OIII}$ ratio, shifting its position to the right in Figure 3 due to collisional deexcitation. The segmented cyan arrow describes the increase in $R_{\rm OIII}$ expected from a 14 000 °K plasma slab whose density successively takes on the values of 10^2 (LDR), $10^{4.5}$, 10^5, $10^{5.5}$, 10^6 and $10^{6.5}\,{\rm cm}^{-3}$. It illustrates the density range implied by the BL05 and RA00 Type I AGN if they shared the same temperature. For a 15 000 °K plasma, the critical densities[12] for deexcitation of

[12] We define the critical density as the density where the line intensity, divided by both the ion and the electron densities, reaches 50% of the low density limit value.

the [O III] $\lambda5007$Å and $\lambda4363$Å lines are 7.8×10^5 and $2.9 \times 10^7\,\mathrm{cm}^{-3}$, respectively, while for the[Ar IV] $\lambda4711$Å and $\lambda4740$Å lines these are 1.7×10^4 and $1.5 \times 10^5\,\mathrm{cm}^{-3}$. Let us compare the data with the values predicted by photoionization calculations.

3.1. *Above Solar Gas Metallicities*

The abundances we adopt correspond to $2.5\,Z_\odot$, a value within the range appropriate to galactic nuclei of spiral galaxies. For instance, the landmark study by Dopita et al. (2014) of multiple H II regions of the Seyfert 2 NGC 5427 favour abundances significantly above solar. Using the Wide Field Spectrograph (WiFeS: Dopita et al. 2010), the authors could determine the ISM oxygen radial abundances using 38 H II regions spread between 2 and 13 kpc from the nucleus. Using their inferred metallicities, they subsequently modelled the line ratios of over 100 'composite' ENLR-H II region emission line spaxels, as well as the line ratios from the central NLR. Their highest oxygen abundance reaches $3\,Z_\odot$ (i.e. $12 + \log(\mathrm{O/H} = 9.16)$. Such a high value is shared by other observational and theoretical studies that confirm the high metallicities of Seyfert nuclei (Storchi-Bergmann & Pastoriza 1990; Nagao et al. 2002; Ballero et al. 2008). Our abundance set relative to H corresponds to twice the solar values of Asplund et al. (2006) except for C/H and N/H, which are set at four times the solar values owing to secondary enrichment, resulting in a gas metallicity of $Z_{\mathrm{tot}} = 2.47 Z_\odot$ by mass. For the He/H abundance ratio, we assume the solar value of 0.085.

3.2. *Four Alternative Ionizing Energy Distributions*

The four spectral energy distributions (hereafter SED) selected are shown in Figure 2. They are representative of published work concerning AGN photoionization models and can be described as follows:

A: the long dashed-line represents the SED used by Ferguson et al. (1997, hereafter Fg97) in their calculations of local optimally emitting cloud (LOC) models for the NLR. It is characterized by a thermal bump of the form

$$F_\nu \propto \nu^{\alpha_{UV}} \exp(-h\nu/k\,T_{cut}),$$

with $\alpha_{UV} = -0.3$ and $T_{cut} = 10^{6.0}\,{}^\circ$K.

B: the dot-dashed line represents the 'optimized SED' used by Richardson et al. (2014, hereafter Ri14) in their calculations of LOC models. It shares the same index α_{UV} as the Fg97 SED above, but assumes a lower T_{cut} of $10^{5.52}\,{}^\circ$K to describe the thermal bump. It is significantly softer than the Fg97 SED, yet due to collisional deexcitation being important in LOC models, these qualitatively reproduces the R_{OIII} and He II/Hβ ($\lambda4686$Å/$\lambda4861$Å) ratios of their reconstructed Seyfert 2 emission line spectra.

C: a power law of index $\alpha_{FUV} = -1.3$ in the far-UV domain (continuous black line) which was used by Binette et al. (1996, hereafter BWS) and Binette et al. (1997) in their matter-bounded cloud calculations.

D: the thick continuous gray line represents the sum of two distinct thermal bumps as proposed by Lawrence (2012, hereafter La12) who postulated that the accretion is entirely covered by intervening thick BLR clouds, which would absorb Ly α as well as the softer ionizing radiation, thereby accounting for the observed UV steepening short-ward of 1050Å. The author proposed that the absorbed EUV energy is re-

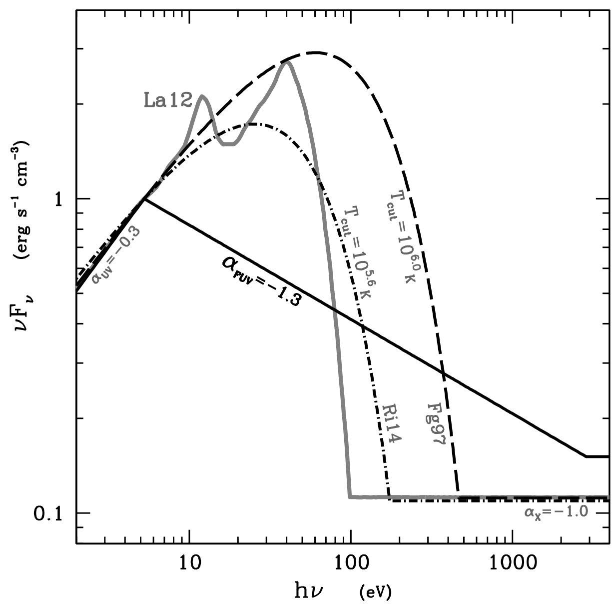

Fig. 2. The four SEDs described in § 3 and adopted in our LDR single-component photoionization models of Figure 3: (1) the SED assumed by Ri14 with $T_{cut} = 10^{5.62}\,{}^\circ$K in their LOC model calculations (dot-dashed line), (2) a similar SED but with a higher T_{cut} of $10^{6.0}\,{}^\circ$K as explored by Fg97 (long dashed-line), (3) a power law SED with $\alpha_{FUV} = -1.3$ adopted by BWS (black continuous line), (4) the double bump thermal SED proposed by La12 (thick gray line). Each SED is expressed in νF_ν units and normalized to unity at 5 eV (2000Å). In the X-rays, they all convert into a power law of index -1.0.

processed into emission at much shorter wavelengths, which generates the second peak near 40 eV.

Each SED converts in the X-rays into a power law $F_\nu \propto \nu^{-1}$ and results in an α_{OX} index[13] of −1.35 except the BWS SED ($\alpha_{OX} = -1.30$).

3.3. *Isochoric Single-Component Photoionization Calculations*

Sequences of photoionization models are shown in Figure 3 corresponding to the four SEDs of Figure 2. LDR was assumed as it is the appropriate density regime for the ENLR plasma and for at least a significant subset of the AGN sample, as argued in § 4. They were calculated using the most recent [14] version Ig of the code MAPPINGS I (Binette et al. 2012) All models share the same density of $n_H^o = 100\,\mathrm{cm}^{-3}$ and each sequence includes up to six models[15] along which the ionization parameter $\mathrm{U_o}$ increases in steps of 0.33 dex, from 0.01 (gray dot) up to 0.46. A filled square denotes the $\mathrm{U_o} = 0.1$ model. All calculations are ionization-bounded, dustfree and isochoric. The observational data set represented in Figure 3 uses only black or gray tones but with the same symbol coding as in Figure 1.

If we define the photoheating efficiency of each SED as the temperature of the plasma averaged over the region occupied by the O^{+2} ion, we obtain for the $\mathrm{U_o} = 0.1$ model the following values of 11 300, 9700, 8400 and 8320 °K, assuming the SED which we labelled BWS, Fg97, La12 and Ri14, respectively (Figure 3). The BWS SED possesses the highest efficiency but it is more speculative as it excludes the possibility of thermal dump (or peak) in the far-UV. Such a feature is to be expected if the continuum originates from an accretion disk, which is widely accepted as being the primary mode of energy generation in AGN. The double-peak reprocessed SED of La12 presents the advantage of accounting for the 'universal' knee observed at 10 eV. The position of the second peak at 40 eV, however, would need to be shifted to higher energies in order to increase the photoheating efficiency.

It is currently not possible to determine which abundances are the most appropriate to the environment of active nuclei although it is generally accepted that metallicities above solar are most likely. If one assume the more conservative metallicity of $1.5\,Z_\odot$ of Fg97 and Ri14, a shift towards the right takes place, as shown by the dotted line arrows in Figure 3, assuming an ionization parameter of $\mathrm{U_o} = 0.1$.

What is the origin of the gap between the photoionization models and AGN observations? The positions of models on the left of Figure 3 correspond to LDR conditions. It is a justified option for the ENLR, as argued in Appendix A. As shown by BL05 as well as by the density sequence using the BWS SED in Figure 3 (gray dotted line), all models can be shifted towards higher $R_{\rm OIII}$ values by assuming plasma densities much above $10^{4.3}\,\mathrm{cm}^{-3}$. This is the main reason why direct measurements of the density governing the [O III] lines are so important if we wish to determine the NLR temperature. Measurements of the weak [Ar IV] doublet can give us access to this information, as explored below.

4. MIGHT THE AGN BUILDUP NEAR $R_{\rm OIII} \simeq 0.018$ REPRESENT A FLOOR TEMPERATURE?

The work of BL05 presented convincing evidence that the quasars (open squares) with $R_{\rm OIII}$ reaching ≈ 0.2 are the manifestation of collisional deexcitation from high density plasma. Their single-density photoionization calculations suggest densities of $\simeq 10^{6.5}\,\mathrm{cm}^{-3}$. Interestingly, the four quasars on the extreme left appear to clump at $R_{\rm OIII} = 0.0195$ with [O III]/H$\beta \simeq 10.5$ in Figure 3. At this position, single-density photoionization calculations from BL05 suggest densities near $10^{5.2}\,\mathrm{cm}^{-3}$. If we consider an isothermal 14 000 °K plasma (c.f. cyan arrow), the density we infer is very close to LDR, at $10^{3.3}\,\mathrm{cm}^{-3}$. Our initial analysis of $R_{\rm OIII}$ among Seyfert 2 galaxies indicated that these show $R_{\rm OIII}$ values similar to the leftmost quasars, which made us question whether collisional deexcitation is related to their position in Figure 3. Our analysis of the NLR data of Seyfert 2 galaxies, however, lead us to question whether collisional deexcitation is related to the position of these quasars on the left. It is noteworthy that, for instance, a similar position is occupied by: (1) the sample of four Seyfert 2 nuclei of Be06b (dark-green dot), (2) the reconstructed Seyfert 2 subset a41 from Ri14 (black diamond) which is based on an ample sample of SDSS spectra, and (3) the seven high excitation Seyfert 2's of Kos78, as shown by the black disk, which represents the average $R_{\rm OIII}$. We

[13]Defined by the flux ratio at 2 keV with respect to 2500Å.

[14]This version includes the new algorithm OSALD (Appendix C.3). Other updates are described in a subsequent paper (Binette & Humphrey 2022).

[15]Some of the leftmost models of La12 and Ri14 fall outside the graph boundaries.

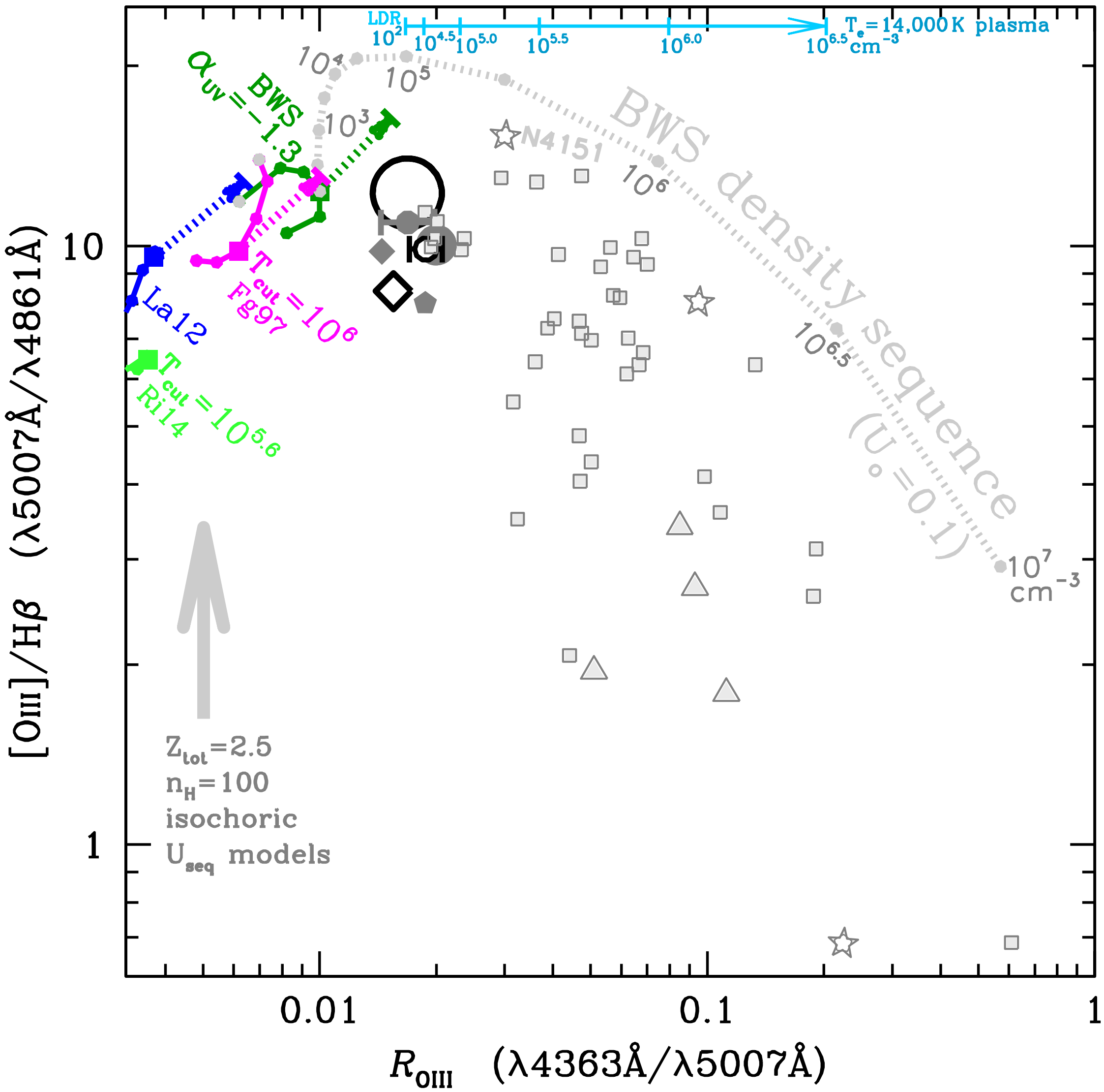

Fig. 3. Same data set from Figure 1 except that it now includes the Seyfert 1 NGC 4151 (c.f. § 5.2.3) instead of NGC 1068. The gray open symbols correspond to the NLR from Type I objects, black symbols to Type II and gray filled symbols to ENLR measurements. Four sequences of LDR photoionization models are shown (solid lines) along which the ionization parameter U_o increases in steps of 0.5 dex, from 0.01 (light gray dot) up to 0.46. Some models fall outside the figure limits. The sequences are labelled according to the SED defined in § 3.2: (A) Fg97 (magenta), (B) Ri14 (light green), (C) BWS (dark green) and (D) La12 (blue). The models are all ionization bounded, dustfree, isochoric with $n_H^o = 100\,\mathrm{cm}^{-3}$and $2.5\,Z_\odot$ abundances. A square identifies the $U_o = 0.1$ model with a dotted arrow representing the shift when one adopts the $1.5\,Z_\odot$ abundances of Ri14. The gray dotted line represents a density sequence in which the densities of the BWS model with $U_o = 0.1$ are successively increased in steps of 0.5 dex. The cyan segmented arrow at the top illustrates the effect of collisional deexcitation on the $R_{\rm OIII}$ ratio from a 14 000 °K plasma at successively larger densities. The colour figure can be viewed online.

would argue that the accumulation of AGN on the left is most likely representing a floor AGN temperature where collisional deexcitation is not significant. To support our hypothesis, we will make use in § 4.2 of the density indicator provided by the λ4711Å/λ4740Å doublet ratios of Kos78.

4.1. *Why do ENLR Observations Coincide with the Leftmost NLR $R_{\rm OIII}$ Observations?*

Because ENLR emission operates in the low density regime (c.f. Appendix A), it provides ideal measurements to compare Type II objects with. In

Figure 1, we added the following spatially resolved ENLR emission measurements: (1) the Cen A filaments (red square, Mo91), (2) the average ENLR ratios of four Type II AGN (red dot, BWS), (3) the radial ENLR emission from the Seyfert 2 IC 5063 (red pentagon: Be06b), and (4) the ionized cloud 8 kpc distant from of Pks 2152-69 (large red dot, Tadhunter et al. 1987). All gather relatively close to the leftmost Type I quasars (open squares) as well as to the mean Seyfert 2 ratio of the Kos78 study (large black circle). Interestingly, the Seyfert 2 reconstructed subset a41 (black diamond) of Ri14 occupies a similar position. The simplest interpretation would be that collisional deexcitation is *not* significant, not only within the spatially resolved ENLR but among the leftmost objects as well, and that they all share a similar electronic temperature.

4.2. *Combination of the [Ar IV] and [O III] Diagnostics*

To evaluate the NLR density, we will rely on the observations of Kos78 who measured the weak [Ar IV] $\lambda\lambda$4711,40Å doublet of his Seyfert 2 sample, an unusual feature among AGN surveys. The observations were carried out with the image-dissector-scanner mounted on the 3 m Shane telescope at the Lick Observatory. The integration times were typically 32 min (A. T. Koski, PhD thesis 1976). In Columns (3–4) of Table 1, we present the reddening-corrected line ratios of [O III]/Hβ and $R_{\rm OIII}$. In the context of high excitation planetary nebulae, Kewley et al. (2019) pointed out that the [Ar IV] and [O III] emission regions significantly overlap and that their respective ratios can be considered representative of the high excitation plasma. A concern, however, is that the weak He I λ4713Å line lies very close to the [Ar IV] λ4711Å line. Given the much wider profiles of the NLR lines in comparison to planetary nebulae, both lines will overlap. Hence the need to apply a deblending correction. The procedure we adopted for the single-density case is described in Appendix B.1. It essentially makes use of the dereddened He I λ5876Å line (Column 6) to calculate a reliable estimate of the contribution of the He I λ4713Å line to the blended[16] [Ar IV]$_+$ λ4711Å$_+$/λ4740Å doublet ratio (Column 5). The estimated fractional contribution of the blended He I line to [Ar IV]$_+$ is $f^{HeI}_{\rm blend}$ (Column 7), which amounts to 5% on average. NGC 1068 stands out at a higher value of 10%. For each object we iteratively determine which density $n_{\rm sng}$ is implied by the deblended [Ar IV] doublet ratio when it is calculated at the temperature $\rm T^{\it sng}_{OIII}$ which reproduces the $R_{\rm OIII}$ ratio. The inferred density values, $n_{\rm sng}$, given in Column (8), all lie below $10^4\,{\rm cm}^{-3}$. As indicated by the cyan arrow in Figure 3, the $R_{\rm OIII}$ ratio is not significantly affected by collisional deexcitation at densities below $10^4\,{\rm cm}^{-3}$. Taken at face values, the densities of Table 1 indicate that $R_{\rm OIII}$ is a valid temperature indicator for the Seyfert 2's of Kos78. The average temperature characterising the whole sample is $13\,980 \pm 1200\,$°K, which lies significantly above the predictions of the LDR photoionization models of § 3.3. Rather than assuming a single density, in § 5 we will consider the case of a smoothly varying density distribution.

[16]The sub-index + sign denotes a line that incorporates a blended component from a different ion. The double $\lambda\lambda$ symbol refers to two separate but nearby lines of the same ion.

4.3. *Density Bias due to a Limited Spatial Resolution*

In Type I AGN, due to the favorable orientation of the observer with respect to the ionizing cone (Antonucci 1993), the densest NLR components are visible and possibly dominate the integrated line flux, causing the $R_{\rm OIII}$ ratios to occupy values up to 0.2 due to collisional deexcitation, as proposed by BL05.

In Type II AGN on the other hand, since the inner regions occupied by the accretion disk and the BLR are not visible, important selection effects take place. The NLR is likely not fully observed due to obscuration associated to the ionizing cone. Differences in spatial resolution as a result of the object distance and the size of the spectrograph aperture inevitably affect the sampling of the NLR volume. The angular resolutions characterising our Seyfert 2 sample are the following. The reconstructed NLR spectrum of Ri14 was based on SDSS observations of Seyfert 2's of similar redshifts (0.10 − 0.12) with a fiber aperture size of $3\widehat{''}$. This corresponds to a NLR sampling that extends over 5.6 kpc diameter. The nearest AGN of the Kos78 sample is NGC 1068 at $z = 0.0038$, which is discussed in detail below. The other objects have redshifts in the range 0.0135 to 0.051 which, for an aperture of $2.7\widehat{''} \times 4\widehat{''}$, result in angular sizes in the range $\simeq 1$ to 4 kpc at the object distance. The Be06b sample presents the highest spatial resolution since its four Seyfert 2's are of low redshift (0.003 − 0.027) and were observed with a seeing $\lesssim 1\widehat{''}$ using longslit spectroscopy mounted on the NTT and VLT telescopes of the European Southern Observatory. The slit aperture was $\simeq 1.1\widehat{''} \times 1\widehat{''}$, which translates into a NLR angular size of 50 to 600 pc. We might conjecture that such superior spatial resolution is possibly related to the position of the Be06b sample in Figure 1, which is slightly more to the right than the Kos78 and Ri14 samples.

Unlike the BL05 quasar sample where collisional deexcitation is the evident cause of the wide spread of $R_{\rm OIII}$ values, the NLR of Seyfert 2's appears relatively unaffected by deexcitation, at least among ground-based observations. The much superior resolution from HST observations, however, reveals the presence of much denser components within the inner nucleus. A case in point are the HST-FOS observations of NGC 1068 (Kr98) with an angular resolution of $0.3''$ (i.e. 25 pc). The nucleus (black open triangle), for instance, shows an $R_{\rm OIII}$ ratio higher by a factor of two with respect to the ground-based observation of Kos78 (black octagon). The image of the nucleus in [O III] light using the HST-FOC instrument shows a diffuse underlying emission component that extends beyond 200 pc from the nucleus and which encompasses a number of emission knots of sizes $\gtrsim 10$ pc. Two bright (EELR) emission 'knots', labelled 1 and 2 by Kr98 (red filled triangles) observed with the $0.3''$ aperture show $R_{\rm OIII}$ values that fall between those of Kos78 (octagon) and of Kr98 with HST-FOS (open triangle). A red dotted line connects the four measurements in Figure 1. The two knots are situated at distances from the nucleus of 0.2 and $0.7''$, respectively (i.e. at 16 and 57 pc).

5. MULTI-DENSITY TEMPERATURE AND DENSITY DIAGNOSTICS

We expanded the functionality of the $R_{\rm OIII}$ temperature *diagnostic* by combining the latter with the [Ar IV] density indicator, allowing us to evaluate the impact of collisional deexcitation among the observed $R_{\rm OIII}$ ratios. To this effect, we developed the algorithm OSALD (see Appendix C for further information), which integrates the line emissivities from an isothermal plasma that extends over a wide density range, up to a cut-off density, $n_{\rm cut}$. At a given temperature, if $n_{\rm cut}$ has a high value, the integrated $R_{\rm OIII}$ ratio rises above the LDR value. Since our diagnostics depends on measurements of the [Ar IV] doublet, we are limited to the Kos78 sample of Table 1.

We have explored two options concerning the nature of the density cut-off: (1) that it simply consists of a sharp cut-off, or (2) corresponds to a gradual cut-off due to a foreground dust extinction layer whose opacity correlates with plasma density. The calculations assuming the first option are summarised in Appendix E and result in essentially the same temperatures as derived from the single density case explored in § 4.2. We will now consider the second option, where we explore the possibility that the NLR emission becomes gradually more absorbed towards the nucleus.

5.1. *Components of the Dust Screen Approach with* OSALD

One particularity of our proposed approach is that it implies fitting the *observed* $R_{\rm OIII}$ ratios presented in Table 2 rather than the dereddened ratios of Table 1 and Figure 1.

5.1.1. *A Density Cut-Off Generated by a Dust Extinction Gradient*

The dust opacity is described by an exponential function of density n: $\tau_V = \tau_V^o \exp(n/n_{\rm opa})$, where $n_{\rm opa}$ is the e-folding density that defines the gradual increase of the foreground V-band dust opacity towards the inner nucleus. This definition does not require us to distinguish between the Galactic extinction from that from the NLR dust screen (τ_V^o includes both). Our interest in exploring an ascending extinction towards the denser NLR component is motivated by the accumulating evidence of the importance of the orientation of the NLR (and not just of the BLR) with respect to the observer, as reviewed in Appendix D, and which is presumably the result of a cone-like opacity distribution.

5.1.2. *Extinction Curve and Line Transfer Algorithm*

The line transfer algorithm implemented in OSALD fully takes into account the effect of multiple scattering across the foreground dust layers. Its characteristics are described in Appendix C of Binette et al. (1993). As for the extinction curve, we adopt the one inferred by Martin & Rouleau (1991) in their study of the Orion nebula, which differs from the standard ISM curve in that grains of size smaller than 0.05 μm are absent, resulting in a flatter curve with less extinction in the UV (Baldwin et al. 1991; Magris C. et al. 1993). It is qualitatively in line with the evidence presented by Maiolino et al. (2001a,b) that small grains are depleted in the dusty medium which is responsible for the absorption of the X-rays and the reddening of the BLR lines. The V-band dust opacity τ_V^o is determined by fitting the integrated Balmer decrement, assuming recombination Case B at temperature $T_{\rm OIII}$. The values of $T_{\rm OIII}$, $n_{\rm opa}$ and $f^{HeI}_{\rm blend}$ are set by iteratively fitting $R_{\rm OIII}$ and the deblended [Ar IV] $\lambda 4711$Å$/\lambda 4740$Å ratio.

TABLE 2

OSALD PARAMETER FIT OF OBSERVED LINE RATIOS[a]

Objects		Target line ratios			Blending corrections			Parameter values		
(1) Index #	(2) AGN	(3) Hα/Hβ $\frac{\lambda 4861}{\lambda 6563}$	(4) $R_{\rm OIII}$ $\frac{\lambda 4363}{\lambda 5007}$	(5) [Ar IV]+ $\frac{\lambda 4711+}{\lambda 4740}$	(6) $R_{\rm He/Ar}$ $\frac{\lambda 5876}{\lambda 4740}$	(7) $f^{HeI}_{\rm blend}$	(8) [Ar IV] $\frac{\lambda 4711}{\lambda 4740}$	(9) τ^o_V	(10) $n_{\rm opa}$ cm^{-3}	(11)[b] $T_{\rm OIII}$ °K
1	Mrk 573	3.62	0.0119	1.156	2.03	0.044	1.108	0.16	1.56×10^3	12 760
2	Mrk 34	4.10	0.0110	1.193	2.46	0.047	1.140	0.41	1.85×10^3	12 660
3	Mrk 78	5.31	0.0075	1.238	4.05	0.062	1.166	1.10	2.48×10^3	11 510
4	Mrk 176	6.55	0.0139	1.045	0.90	0.013	1.031	1.74	6.54×10^3	15 210
5	Mrk 3	5.31	0.0141	0.850	3.00	0.068	0.796	1.08	1.37×10^4	14 560
6	Mrk 1	5.00	0.0136	0.814	2.71	0.067	0.762	0.91	1.40×10^4	14 150
7	NGC 1068	4.47	0.0129	0.763	3.56	0.106	0.690	0.61	1.49×10^4	13 500

[a]The line ratios were not corrected for reddening. A foreground dust screen was assumed instead whose opacity increases exponentially: $\tau_{ij} = \tau^o_V \exp(n/n_{\rm opa})\, A(\lambda_{ij})/A_V$, where $A(\lambda_{ij})/A_V$ represents the extinction curve evaluated at wavelength λ_{ij} for the emission line ij considered.

[b]The averaged temperature for the sample is $\langle T_{\rm OIII}\rangle = 13\,480 \pm 1180\,$°K.

5.1.3. *Transposition to a Simplified Spherical Geometry*

The algorithm consists in integrating the line emission measures[17] of an isothermal multi-density plasma (MDP) of temperature T_e. The calculations can be transposed to the idealized geometry of a spherical (or conical) distribution of ionization bounded clouds whose densities n decrease as r^{-2}. The weight attributed to each plasma density component is set proportional to the *covering solid angle*[18] $\Omega(n)$ subtended by the plasma shell of density n. In the case of photoionization models, such a distribution would result in a constant ionization parameter U_o and the integrated columns N_{X_k} of each ion k of any cloud would be to a first order constant. For the sake of simplicity, to describe $\Omega(n)$ we adopt the power law $(n/n_{\rm low})^{\epsilon}$, which extends from $n_{\rm low} = 100$ up to $10^8\,{\rm cm^{-3}}$. If we transpose this to a spherical geometry where both U_o and Ω are constant (i.e. $\epsilon = 0$), the *area* covered by ionization-bounded emission clouds would increase as r^2, thereby compensating the dilution of the ionizing flux and the density fall-out (both $\propto r^{-2}$). In this case, the weight attributed by OSALD to each shell is the same; otherwise, when $\epsilon \neq 0$ the weight is simply proportional to $\Omega(n)$. MDP calculations are not a substitute to photoionization calculations. They are only intended as diagnostics that could constrain some of the many free parameters that characterize multidimensional NLR models, including those which might consider a non-uniform dust distribution.

[17]Defined as the line emission coefficient times the electronic density.

[18]$\Omega(n) = A(n)/4\pi r^2$ where A is the area of a shell of density n exposed to the ionizing source at a distance r. For definiteness we set the electron density equal to that of H, $n = n_e = n_H$.

5.1.4. *Selection of the Distribution Index ϵ*

To guide us in the selection of ϵ, we followed the work of Be06b who determined that, for a spectral slit radially positioned along the emission line cone, the surface brightness of the *spatially resolved* ENLR is seen decreasing radially along the slit as r^{δ} (with $\delta < 0$), where r is the projected nuclear distance on the sky. From their [O III] λ5007Å and Hα line observations of Seyfert 2's, Be06b derived average index values of $\delta_{[OIII]} = -2.24\pm0.2$ and $\delta_{H\alpha} = -2.16\pm0.2$, respectively. Let us assume that such a gradient extends inward, i.e. inside the unresolved NLR. For our assumed spherical geometry where the Hα luminosity across concentric circular apertures behaves as $r^{-2\epsilon}$ (see § C.2), ϵ is given by $-(1+\delta)/2$. Hence we adopt $\epsilon \approx +0.6$ so that a long slit projected onto our spherical geometry could reproduce the observed $\delta_{[OIII]}$ value of Be06b. Out of curiosity, we have explored other positive values and found that changes in ϵ were not critical and did not affect our conclusions.

5.1.5. *Importance of Deblending the [Ar IV]+ λ4711Å+ Lines*

As emphasized by Kewley et al. (2019), care must be taken when interpreting the [Ar IV] doublet since

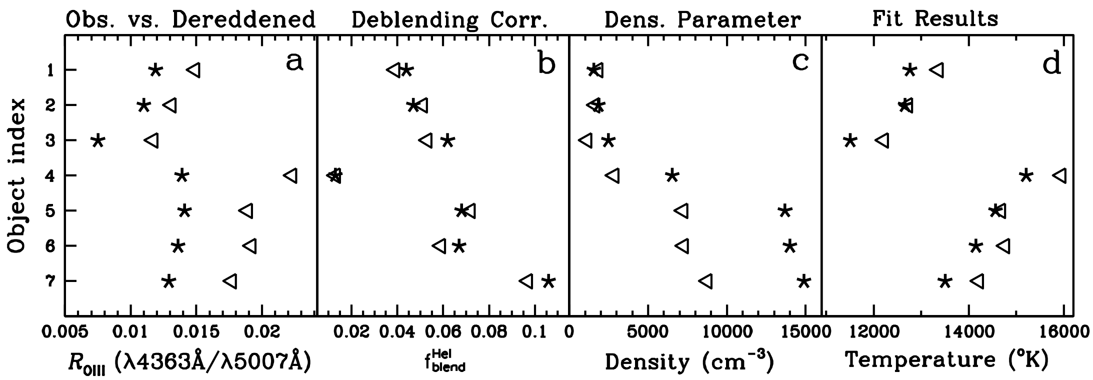

Fig. 4. Comparison between parameters and plasma temperatures shown in Table 1 (open triangles) and Table 2 (stars). An index number (1 – 7) identifies the object name in Column (2) of either table. Panel a: target $R_{\rm OIII}$ ratios, dereddened (open triangles) vs. observed (stars). Panel b: deblending corrections $f^{HeI}_{\rm blend}$ applied to the [Ne IV] doublet ratios. Panel c: sharp density cut-off (open triangles) vs. extinction density cut-off $n_{\rm opa}$ (stars). Panel d: plasma temperatures inferred from the dustfree model (open triangles) vs. dusty screen model (stars).

the weak nearby He I λ4713Å line is nearly superposed to the [Ar IV] λ4711Å line, hence the need to apply a proper deblending correction to the measured [Ar IV] ratios. The procedure adopted is described in Appendix B.1. Because of the relative weakness of the He I λ4713Å line, there is no direct evidence of its presence in AGN spectra given its closeness to the [Ar IV] λ4711Å line. To deblend the flux contribution from the He I λ4713Å line, we first evaluate its expected flux using the strong He I λ5876Å line and then subtract it from the [Ar IV] λ4711Å line. Since we are dealing with He recombinations lines, the dependence of the He I ratio on temperature or density is relatively minor. Hence, obtaining a reliable estimate of the He I fractional contribution, $f^{HeI}_{\rm blend}$, to the observed [Ar IV] profile is straightforward. The procedure is described in Appendices B.1 and C.4.

Another potential blending consists of the first two lines of the [Ne IV] quadruplet which comprise the lines λ4714.36, λ4715.80, λ4724.15 and λ4726.62Å (García-Rojas et al. 2015). For convenience, we will refer to them as consisting of two doublets centered at $\lambda\lambda$4715Å and $\lambda\lambda$4725Å, respectively. Up to densities of $\approx 10^6\,{\rm cm}^{-3}$, the unblended $\lambda\lambda$4725Å doublet is calculated to be on average 35% brighter than the $\lambda\lambda$4715Å doublet. In those cases where the $\lambda\lambda$4725Å doublet is detected, we can reliably determine the blended $\lambda\lambda$4715Å doublet flux and then subtract it from the blended [Ar IV]$_+$ λ4711Å$_+$ lines. Further information about the deblending procedure is given in Appendix B.2. No detection of the [Ne IV] $\lambda\lambda$4725Å line was reported by Kos78.

5.2. *Results from the Multi-Density Plasma Models*

5.2.1. *The Reference Seyfert 2 Sample*

The results from the calculations using OSALD are presented in Table 2, where we have assumed a power law index of $\epsilon = +0.6$. In Column (7), $f^{HeI}_{\rm blend}$ represents the estimated blending contribution from He I λ4713Å to the [Ar IV]$_+$ λ4711Å$_+$ lines. The resulting deblended [Ar IV] λ4711Å/λ4740Å ratios are presented in Column (8). The foreground dust screen opacities, τ^o_V, inferred by OSALD from the observed Balmer decrements (Column 3) are given in Column (9). The fitted dust distribution e-folding densities, $n_{\rm opa}$, and the inferred plasma temperatures are given in Columns (10) and (11), respectively.

To facilitate the evaluation of these fits, we show in Figure 4 how the parameters compare for each object between Table 1 (triangles) and Table 2 (stars). Panel (a) represents the target $R_{\rm OIII}$ ratios, dereddened vs. observed, Panel (b) the deblending correction $f^{HeI}_{\rm blend}$, Panel (c) the the cut-off density vs. dust drop-out density scale, and Panel (d) the temperatures inferred from the fits. The e-folding dust screen densities, $n_{\rm opa}$, derived by OSALD lie in the range 1500 to 16 000 cm^{-3}. The average $\langle {\rm T_{OIII}} \rangle$ for the seven Seyfert 2's is 13 480 ± 1180 °K, being lower by only 500 °K with respect to the single density case.

Having considered an explicit density distribution, with either dust obscuration (Column 10) or without (see Table B1 in Appendix E), we derive temperature values that do not differ much from the single density case of Table 1. This supports our contention that collisional deexcitation is not affecting significantly the $R_{\rm OIII}$ ratios observed by

TABLE 3

EXPLORATION WITH OSALD OF BLENDING DUE TO [Ne IV] $\lambda\lambda$4714,16Å

Objects		Target line ratios			Dual blending corrections[a]					Parameter values		
(1) Index #	(2) AGN	(3) Hα/Hβ $\frac{\lambda 4861}{\lambda 6563}$	(4) $R_{\rm OIII}$ $\frac{\lambda 4363}{\lambda 5007}$	(5) [Ar IV]+ $\frac{\lambda 4711+}{\lambda 4740}$	(6) $R_{\rm He/Ar}$ $\frac{\lambda 5876}{\lambda 4740}$	(7) $f^{HeI}_{\rm blend}$	(8) $R_{\rm Ne/Ar}$ $\frac{\lambda 4725}{\lambda 4740}$	(9) $f^{NeIV}_{\rm blend}$	(10) [Ar IV] $\frac{\lambda 4711}{\lambda 4740}$	(11) τ^o_V	(12) $n_{\rm opa}$ cm^{-3}	(13) T$_{\rm OIII}$ °K
1	Mrk 573	3.62	0.0119	1.156	2.03	0.053	0.30[b]	0.203	0.921	0.15	3.59×10^3	12 710
2	Mrk 34	4.10	0.0110	1.193	2.46	0.056	0.30[b]	0.196	0.953	0.40	4.56×10^3	12 610
3	Mrk 78	5.31	0.0075	1.238	4.05	0.075	0.30[b]	0.190	0.979	1.09	6.45×10^3	11 470
4	Mrk 176	6.55	0.0139	1.045	0.90	0.017	0.30[b]	0.220	0.845	1.73	1.47×10^4	15 120
5	Mrk 3	5.31	0.0141	0.850	3.00	0.089	0.30[b]	0.307	0.609	1.08	2.76×10^4	14 390
6	Mrk 1	5.00	0.0136	0.814	2.71	0.089	0.30[b]	0.326	0.575	0.91	2.85×10^4	13 950
7	NGC 1068	4.47	0.0129	0.763	3.56	0.146	0.30[b]	0.373	0.502	0.61	3.11×10^4	13 250
8A	NGC 4151[c]	5.29	0.0222	0.727	2.40	0.064	–	–	0.684	1.07	2.16×10^4	18 050
8B	" "	"	"	"	"	0.088	0.30[d]	0.377	0.496	1.07	4.64×10^4	17 610
8C	" "	"	"	"	"	0.148	0.62[e]	1.32	0.294	1.08	1.49×10^5	16 180
9	Mrk 477	4.00	0.0215	0.693	7.05	0.295	0.30	0.35	0.535	0.34	22 200	16 350
10	J1653+23[f]	4.08	0.0192	1.16	4.76	0.099	0.42	0.25	1.05	0.39	2 840	16 050
11	J1300+53	3.79	0.0257	1.13	3.21	0.070	0.38	0.22	1.06	0.239	2 200	18 320

[a]The fraction of [Ar IV]+ contributed by blending is the sum of $f^{HeI}_{\rm blend} + f^{NeIV}_{\rm blend}$.
[b]The quoted [Ne IV] doublet ratio of 0.30 is our estimated upper limit for the Kos78 sample.
[c]The line ratios measurements of the Seyfert I NGC 4151, are from Boksenberg et al. (1975).
[d]Eye estimate of the [Ne IV] λ4725Å doublet from the Boksenberg et al. (1975) spectrum.
[e]Value of the [Ne IV] λ4725Å doublet deduced from Table I of Boksenberg et al. (1975).
[f]Observations carried out with the spectrograph OSIRIS mounted on the 10.4 m Gran Telescopio Canarias.

Kos78. Given the relative proximity in Figure 3 of the Ri14 subset a41 (black diamond) to the Kos78 sample (black disk), we might conjecture that LDR possibly applies to the a41 sample as well since, at a redshift of $z = 0.11$, the large projected scale of the $3''$ SDSS aperture ensures significantly more dilution of the inner dense NLR component in comparison to the Be06b and Kos78 samples. We would need a larger sample of [Ar IV] doublet measurements to confirm that $R_{\rm OIII}$ translates into a reliable determination of the plasma temperature in Type II AGN.

5.2.2. *Probing the Possible Blending of [Ar IV] by [Ne IV]*

We present complementary calculations in Table 3 where we have assumed the hypothetical case of the $\lambda\lambda$4725Å doublet reaching 30% of the observed [Ar IV] λ4740Å line intensity. The blending contributions from the He I and [Ne IV] $\lambda\lambda$4715Å lines, that is $f^{HeI}_{\rm blend}$ and $f^{NeIV}_{\rm blend}$, are presented in Columns (7) and (9), respectively, and the resulting deblended [Ar IV] doublet ratios are listed in Column (10). The opacities τ^o_V (Column 11) inferred remain about the same, but the e-folding densities $n_{\rm opa}$ (Column 12) are typically larger with respect to Table 2. The average sample temperature $\langle$T$_{\rm OIII}\rangle$ is lower by only 125 °K. At least for the Kos78 sample at hand, not including the $\lambda\lambda$4725Å doublet should not affect our conclusions concerning the Seyfert 2 NLR temperatures.

5.2.3. *Detection of [Ne IV] in Nearby Seyfert 1 NGC 4151*

The critical densities of the [Ne IV] quadruplet lines all lie above 10^6 cm^{-3}. Because the [Ar IV] doublet emissivities at such densities are significantly reduced due to collisional deexcitation, a positive detection of the [Ne IV] $\lambda\lambda$4725Å doublet might relate to having plasma densities much above those deduced from the Kos78 sample. This might be the case in Type I AGN. Interestingly, the detection of the [Ne IV] $\lambda\lambda$4725Å doublet was reported early on in the Seyfert 1 NGC 4151 by Boksenberg et al. (1975). The line ratios of interest for this object are shown in Table 3. A labeled star depicts its position in Figure 3. Eye estimates of the [Ne IV] $\lambda\lambda$4725Å doublet (from the published figure) suggest a value of ≈ 0.3 with respect to the [Ar IV] λ4740Å line, while the measurements reported in their Table I would imply a higher value of 0.62. In Table 3, we present three OSALD fits in which the [Ne IV]/[Ar IV] ratio (Column 8) successively takes on the values of 0, 0.3 and 0.62. The two [Ne IV] deblending corrections result in $n_{\rm opa}$ values higher by factors of 2.2 and 7.5 for models 8B and 8C, respectively, with the deblended [Ar IV] doublet ratios dropping to 0.496 and 0.294 (Column 10). The impact on the inferred temperature is significant, with $T_{\rm OIII}$ from model 8C being 1870 °K lower, at 16 180 °K, showing minimal evidence of collisional deexcitation being present. It would be interesting to repeat this exercise if we could obtain higher S/N spectra.

5.2.4. *The Particular Case of QSO 2's*

Through our literature search of Type II AGN measurements of the $\lambda\lambda$4725Å [Ne IV] doublet, we came across three objects classified as QSO 2's, that is, Type II quasars corresponding to the high luminosity counterpart of Seyfert 2's. They are Mrk 477 (Villar Martín et al. 2015), SDSS J1300+54 and SDSS J1653+23 (Villar-Martín et al. 2017) at redshifts z of 0.037, 0.088 and 0.103, respectively. Their spectra were extracted from the Sloan Digital Sky Survey data (SDSS; York et al. 2000) and the line ratios relevant to our analysis are given in Table 3.

What stands out from these objects is their larger $R_{\rm OIII}$ ratios. The deblended [Ar IV] doublet ratios (Column 8) do not imply significant collisional deexcitation, except at a reduced level in Mrk 477 where $n_{\rm opa}$ reaches $\simeq 22\,200\,{\rm cm}^{-3}$. Yet the $T_{\rm OIII}$ values inferred (Column 13) for the three QSO 2's are much higher than in Seyfert 2's, which questions the plausibility of LDR conditions. It is possible that AGN's where the [Ne IV] $\lambda\lambda$4725Å can be detected might indicate the presence of a double-bump in their density distribution. We tentatively explored the addition of an additional denser plasma component ($\gtrsim 10^6\,{\rm cm}^{-3}$) to our power law. Our fit to the [Ar IV] doublet was not very sensitive to this component since both $\lambda\lambda$4711,40Å lines are affected by collisional deexcitation at the high density end. Even though the temperatures we inferred came out at values lower than in Column (13), the exercise was not convincing as the number of free parameters exceeded the number of variables. A possible interpretation is that the super-luminous QSO 2's scale up in size to the extent that their inner NLR become partly visible, as is the case of the high spatial resolution HST measurement of the nearby Seyfert 2 NGC 1068 (c.f. red triangles in Figure 1).

6. TEMPERATURE PROBLEM WITH PHOTOIONIZATION

In conclusion, after integrating the emissivities of the [O III] and [Ar IV] lines over a continuous distribution of densities, we find that the impact of collisional deexcitation on the λ4363Å/λ5007Å ($R_{\rm OIII}$) ratio is not significant among ground-based observations of the seven Seyfert 2 sample of Kos78 who provided measurements of the [Ar IV] density indicator and, therefore, their $R_{\rm OIII}$ ratio provides us with a reliable measurement of the NLR temperature. A comparison of the values of $R_{\rm OIII}$ observed among quasars, Seyfert 2's and spatially extended ENLR plasma, as displayed in Figure 1, argues in favor of a floor temperature for the NLR, which we situate at $\gtrsim 13\,500$ °K. Our photoionization models using MAPPINGS Ig and assuming standard SEDs and low densities predict $R_{\rm OIII}$ values significantly below those observed in Seyfert 2's. This discrepancy defines what we would label the $R_{\rm OIII}$-temperature problem.

In the current work, we found complementary evidence that the orientation of the emission line cone with respect to the observer's line-of-sight affects our characterisation of the NLR, whether in Seyfert 2's (Kos78 sample) or in quasars (BL05 and RA00 samples). We do not exclude the existence of a much denser NLR component being present in ground-based observations, but we would propose that, at least among Seyfert 2's with $z \gtrsim 0.02$, the latter would be strongly diluted by the much brighter low density NLR component, which we evaluate to have a density $\lesssim 10^{4.3}\,{\rm cm}^{-3}$. In quasars, where a larger fraction of this dense and luminous component becomes visible, the resulting $R_{\rm OIII}$ ratio progressively increases up to values of ≈ 0.2 due to collisional deexcitation, as proposed by BL05 using dual-density photoionization models. It would be interesting to investigate whether the [Ne IV] λ4725Å doublet becomes intrinsically stronger in Type I objects. A few luminous AGN in which we reported the detection of the [Ne IV] doublet in § 5.2.3 and 5.2.4 appear to favor a density distribution akin to a double-bump, such as the dual-density approach of BL05, rather than the single power law we have assumed.

This work has been partly funded with support from the Spanish Ministerio de Economía y

Competitividad through the grant AYA2012-32295. G.MC is grateful for the support from the Centro de Investigaciones de Astronomía (CIDA). A.R.A acknowledges partial support from CNPq Fellowship (312036/2019-1 and 203746/2017-1). M.M-P acknowledges support by the Korea Astronomy and Space Science Institute for her postdoctoral fellowships. A. Alarie was funded by a postdoctoral grant from CONACyT. We thank the referee for his/her helpful constructive comments.

The discussion about the referred three QSO 2's is based on data from the Sloan Digital Sky Survey. Funding for the SDSS and SDSS-II has been provided by the Alfred P. Sloan Foundation, the Participating Institutions, the National Science Foundation, the US Department of Energy, the National Aeronautics and Space Administration, the Japanese Monbukagakusho, the Max Planck Society and the Higher Education Funding Council for England. The SDSS website is http://www.sdss.org/. The SDSS is managed by the Astrophysical Research Consortium for the Participating Institutions.

APPENDICES

A. THE VALIDITY OF LOW DENSITY REGIME FOR THE ENLR

Among the Seyfert galaxies studied (e.g. Bennert et al. 2006a,b), the ENLR densities inferred from the red [S II] $\lambda\lambda$6716,31Å doublet are typically $< 10^3\,\mathrm{cm}^{-3}$. Along the long-slit measurements, in most cases both the electron density and the ionisation parameter appear to be decreasing with radius. The authors proposed that deviations from this general behaviour (such as a secondary peak), when seen in both the ionisation parameter and electron density space, can be interpreted as signs of shocks due to the interaction with a radio jet. In what follows, we will consider those cases where the excitation mechanism is photoionization by the accretion disk. The red dot in Figure 1 represents the average $R_{\rm OIII}$ of the ENLR of four[19] Seyfert 2's observed by SB96. If we assume a temperature of 9 000 °K for the [S II] plasma, the densities inferred by BWS from the λ6716Å/λ6731Å ratios from each ENLR are $\leq 250\,\mathrm{cm}^{-2}$. Two other examples shown in Figure 1 are: (a) the yellow filled dot, which corresponds to a deep spectrum of a 8 kpc distant cloud from the nucleus of radio-galaxy Pks 2152-699 (Ta87), and (b) the magenta dot which represents the average $R_{\rm OIII}$ of seven optical filaments situated at ≈ 490 pc from the nucleus of the radio-galaxy Centaurus A (Mo91). In both cases, the red [S II] doublet measurements indicate low electronic densities, with $n_e \leq 250\,\mathrm{cm}^{-3}$.

High excitation ENLR lines such as [O III] should similarly operate under LDR conditions for the following reasons. First, the geometrical dilution factor of the ionizing flux across the typical detector aperture does not vary significantly. For instance, if we define r_{in} as the radial distance separating the UV source from the inner boundary of the observed ENLR, and Δr as the radial thickness corresponding to the detector aperture projected on the sky, then the ratio $(\Delta r/r_{in})^2$ represents the fractional change of the UV dilution factor across the observed ENLR. This factor is typically $\lesssim 1.5$, indicating that the observed plasma is exposed essentially to the same ionizing flux. Line ratio variations across Δr must be due to either variations in plasma density or to a progressive absorption of the ionizing radiation, but not to changes in the dilution factor. Second, if the [O III] and [S II] lines originate from unrelated gas components, the densities of the low [S II] emission plasma must be orders of magnitudes *higher* than the [O III] emission plasma in order to sufficiently reduce the ionization parameter to the point that the low ionization species dominate the spectrum. Third, if the [S II] emission corresponds to the partially ionized layer at the back of a photoionized (ionization-bounded) slab, the electronic density of the region that emits the [O III] lines is denser by a factor of 2.5 to 4. The reason is that the [S II] emission comes from plasma that is partially ionized with an electronic density n_e much lower than the local gas density n_H. This factor is sufficiently small that for the typical [S II] densities of $n_e \simeq 250\,\mathrm{cm}^{-3}$ as found in the ENLR, the density associated to the [O III] lines would still be $\ll 10^4\,\mathrm{cm}^{-3}$ and LDR conditions should therefore apply.

B. CORRECTING THE [Ar IV] DOUBLET FOR LINE BLENDING

B.1. *Correcting the [Ar IV]₊ Ratio for He I λ4713Å Blending*

One characteristic of ratios involving recombination lines of the same ion is their limited sensitivity to either temperature or density. A satisfactory prediction of the He I λ4713Å line intensity can be derived from the measurement of the He I λ5876Å line. First, we derive the Case B He I λ4713Å/λ5876Å ratio, which we label $\mathrm{R_{He}}$, via interpolation of the emissivities from the supplemental

[19]Each of these measurements is associated to a Seyfert 2 as we left out the fifth object, NGC 526A, which is classified as Seyfert 1.5.

table of Porter et al. (2013). For a $10^4\,\mathrm{cm}^{-3}$ plasma at a temperature of 12 000 K, $\mathrm{R_{He}}$ turns out to be only 4.78% of He I 5876Å. Temperature variations of ±2000 °K would cause a change in this ratio of $^{+7.95}_{-11.5}$%, respectively, while adopting density values of 100 and $10^5\,\mathrm{cm}^{-3}$ would result in $\mathrm{R_{He}}$ ratios of 0.0429 and 0.0489, respectively. Second, by defining $\mathrm{R_{He/Ar}}$ as the observed He I/[Ar IV] λ5876Å/λ4740Å ratio, the product ($\mathrm{R_{He/Ar}} \times \mathrm{R_{He}}$) defines our estimate of the blending contribution from He I λ4713Å to the *measured* (blended) $[\mathrm{Ar\,IV}]_+$ doublet ratio. The relevant information is provided by the fractional contribution of the blended line, which is given by $f^{HeI}_{\mathrm{blend}} = (\mathrm{R_{He/Ar}} \times \mathrm{R_{He}})/[\mathrm{Ar\,IV}]_+$. The blended-corrected [Ar IV] λ4711Å/λ4740Å doublet ratio is given by $(1 - f^{HeI}_{\mathrm{blend}}) \times [\mathrm{Ar\,IV}]_+$, which was used to explore the single density case discussed in § 4.2 (see Column (7) of Table 1). For the power law density distribution case, the procedure is described in § C.4.

B.2. *Correcting the [Ar IV]₊ ratio for [Ne IV] λλ4715Å Blending*

The [Ne IV] optical lines consist of a quadruplet at λ4714.36, λ4715.80, λ4724.15 and λ4726.62Å, respectively (García-Rojas et al. 2015). To simplify the notation, we will refer to the quadruplet as consisting of two doublets: the observed [Ne IV] λλ4725Å lines and the potentially blended [Ne IV] λλ4715Å lines. At typical NLR densities, the potentially observed [Ne IV] λλ4725Å doublet is calculated to be ≈ 35% brighter than the [Ne IV] λλ4715Å doublet (blended with [Ar IV] λ4711Å). To our knowledge the [Ne IV] λλ4725Å doublet has only been reported in a few AGN. However, it is frequently observed in planetary nebulae (PN). For instance, in NGC 6302, where the stellar temperature is estimated to be in the range 224 000 to 450 000 °K (Feibelman 2001), the observed [Ne IV]/[Ar IV] λλ4725Å/λ4740Å ratio reported by Aller et al. (1981) is 0.175. Since the emission lines of PN are narrow, the above mentioned lines can be resolved without any need of deblending provided high resolution spectroscopy has been carried out. For instance, the observations of the PN NGC 3918 by García-Rojas et al. (2015) using the Ultraviolet-Visual Echelle Spectrograph (UVES, D'Odorico et al. (2000)) with a 1″ slit resulted in a spectral resolution of $6.5\,\mathrm{km\ s^{-1}}$. The observed emission profiles of each [Ne IV] quadruplet line were well resolved, showing a FWHM of $\simeq 20\,\mathrm{km\ s^{-1}}$. Interestingly, the [Ne IV]/[Ar IV] λλ4715Å/λ4711Å and He I/[Ar IV] λ4713Å/λ4711Å ratios measured by García-Rojas et al. (2015) are 0.115 and 0.078, respectively. To correct the measured $[\mathrm{Ar\,IV}]_+$ (λ4711Å₊/λ4740Å) ratio for [Ne IV] blending, the density integration by OSALD of the two doublets [Ne IV] λλ4724,26Å and [Ne IV] λλ4714,16Å proceeds as described in Appendix C.4 for the He I λ4713Å and λ5876Å lines.

C. THE OSALD ALGORITHM

Using emission line atomic physics, OSALD[20] explores temperature and density diagnostics in which an explicit distribution of the density is considered.

C.1. *Line Diagnostics with a Power Law Density Distribution*

Our goal is to explore which density distribution best reproduces a given set of line ratios, and to determine to what extent collisional deexcitation is affecting the observed R_{OIII} λ4363Å/λ5007Å or R_{NII} λ5755Å/λ6583Å line ratios. For the high ionization species such as $\mathrm{O^{+2}}$, $\mathrm{Ar^{+3}}$ and $\mathrm{Ne^{+3}}$, the temperature $\mathrm{T_{OIII}}$ is set iteratively to the value which reproduces the target R_{OIII} ratio. Although not considered in the current paper, other diagnostics can be modeled, such as the singly ionized oxygen [O II] λ6726Å/λ6729Å and [O II] λ3727Å/λ7325Å line ratios at the temperature that would reproduce the temperature sensitive R_{NII} target ratio, or the singly ionized sulphur [S II] λ6716Å/λ6731Å and [S II] λλ4069,76Å/λλ6716,31Å line ratios at the estimated temperature $T_{\mathrm{SII}} \approx 9000$ °K.

C.2. *Transposition of OSALD to a Spherical Geometry*

The isothermal plasma considered by OSALD can be visualized as consisting of concentric shells of plasma whose densities decrease radially as r^{-2}. These shells are given a weight which we associate to the covering solid angle of a putative ionizing source at the center. This can be transposed to the idealized case of photoionized shells that are ionization bounded and share the same ionization parameter $\mathrm{U_o}$. To the extent that the low density regime applies, the line luminosities of each shell result equal if they share the same covering *solid angle* Ω of the ionizing source. OSALD basically integrates the line emission coefficient times the shell covering solid angle: $j^k_{ij}(n,T)\,\Omega(n)\,\Delta n$, where ij corresponds to the transition from levels j to i evaluated at a temperature T and a density n, which takes into account collisional deexcitation. The integrated line flux for line

[20]Stands for "Oxygen Sulfur Argon Line Diagnostic".

ij of ion k reduces to the summation in density space of $\sum_l \Omega(n_l)\, j^k_{ij}(T, n_l)\, \Delta n_l$, where n_l is progressively increased in locked steps of size $\Delta n_l/n_l = 0.004$ dex from $n^o_H = 100$ up to the cut-off density $n_{\rm cut}$. When the fit incorporates foreground dust extinction, $n_{\rm cut}$ is fixed at $10^8\,{\rm cm}^{-3}$ and the actual cut-off is set by the foreground dust extinction which increases exponentially with density. The e-folding density for the opacity in the V-band is defined by the parameter $n_{\rm opa}$(see C.3). The weight of each shell is given by its covering solid angle Ω, which follows a power law of index ϵ with density: $\Omega(n) = \Omega_o\ (n/n^o_H)^\epsilon$, where Ω_o is an arbitrarily small constant that would ensure negligible shell shadowing. The density is postulated to decrease radially as $n \propto r^{-2}$. As a result, the shells' luminosities behave as $r^{-2\epsilon}$ since positive values of ϵ imply a covering solid angle that increases towards the ionizing source (along with the density n). A slit radially positioned along the ionizing cone would result in an Hβ surface brightness that decreases as r^δ, with $\delta = -(2\epsilon + 1)$.

C.3. *Line Transfer Across the Cone-Like Dust Screen*

In the context of Type II objects, we propose in § 5 that each emission line is seen through a dust screen whose opacity increases exponentially towards the inner denser regions. For each line ij, the opacity $\tau_{ij}(n)$ is given by $\tau^o_V \exp(n/n_{\rm opa})\, A(\lambda_{ij})/A_V$, where τ^o_V is the V-band dust opacity at the lowest density n^o_H, $n_{\rm opa}$ is the e-folding density of the exponential function, $A(\lambda_{ij})$ the selected extinction curve and A_V the extinction value at 5 500Å. When integrating the emission measures, the dust transfer function ${\rm Tr}(\tau_{ij}(n))$ is applied to each emission coefficient $j^k_{ij}(n, T)$. The latter assumes a plane-parallel geometry and takes into account both absorption and scattering due to the dust grains, as described in Appendix C of Binette et al. (1993). In order to constrain the parameter τ^o_V, the set of line ratios that are selected to be fitted must include one or more Balmer line ratios from H.

C.4. *Blending of the He* I *λ4713Å and [Ar* IV*] λ4711Å Lines*

To calculate the flux of any He I line, the Case B recombination coefficients are taken from the work of Porter et al. (2013). They cover the temperature range $5\,000 \le T_{rec} \le 25\,000\,^\circ$K and density range $10^2 \le n_e \le 10^{14}\,{\rm cm}^{-3}$. By default, the temperature assumed for He I in the current work is $T_{rec} = 12\,000\,^\circ$K while it is the variable T$_{\rm OIII}$ for [Ar IV] and all the high ionization ions.

In order to evaluate the blending of the weak He I λ4713Å line with the [Ar IV] λ4711Å line, OSALD integrates the emission flux of the following four lines: He I λ4713Å, He I λ5876Å, [Ar IV] λ4711Å and [Ar IV] λ4740Å, taking into account dust extinction at the corresponding densities. This procedure properly takes into account how the emission coefficient of each line is affected by density and collisional deexcitation, as well as by dust extinction, which may increase along with density. After assuming an arbitrary abundance ratio of the two ionic species He$^+$ and Ar^{+3}, the algorithm derives the integrated He I/[Ar IV] ratio labelled $R_{5876/4740}$ and rescales it to the observed value. The $R_{4713/4740}$ ratio represents a measure of the blending contribution from He I and is derived from the ratio $R_{4713/5876}/R_{5876/4740}$. Deblending the [Ar IV] $R_{4711/4740}$ ratio is achieved by subtracting the $R_{4713/4740}$ ratio from the observed blended [Ar IV]$_+$ ratio. The fraction of [Ar IV]$_+$ due to He I blending is labelled $f^{HeI}_{\rm blend}$ in all our tables.

C.5. *Minimum $\chi^2_{\rm rno}$ and Iterative Least Squares Fit*

We used a non-linear least squares fit method to find the optimal input parameter values that succeed in reproducing as closely as possible the target line ratios. These parameters are varied in an iterative fashion until the minimum re-normalized $\chi^2_{\rm rno}$ value is encountered, with $\chi^2_{\rm rno}$ defined as

$$\chi^2_{\rm rno}(x_j) = \sum_{i=1}^{m} \frac{w_i\,\big(y_i - y(x_j)\big)^2}{MAX\big[y_i^2\,,\,y(x_j)^2\big]} \Bigg/ \sum_{i=1}^{m} w_i, \quad \text{(C1)}$$

where m is the number of line ratios simultaneously fitted, w_i the weight attributed to each line ratio i, y_i the observed target line ratios and $y(x_j)$ the corresponding line ratios derived from the integration of the line fluxes. The quantity x_j represents the various parameters on which the line integration depends, that is, the temperature T_{fit} and density n, as well as the parameters describing the behaviour of the covering angle $\Omega(n)$, which are ϵ and $n_{\rm cut}$ as defined in Appendix C.2. As detailed in § 5.2 and Table 2, we used the algorithm to fit the line ratios of the seven Type II NLR of Table 1. By trial and error we settled for weights w_i of 2.0 and 1.5 for the [Ar IV] λ4711Å/λ4740Å and $R_{\rm OIII}$ λ4363Å/λ5007Å ratios, respectively.

OSALD's basic goal is to evaluate whether or not there is evidence of significant collisional deexcitation affecting the $R_{\rm OIII}$ ratio of any AGN whose

λ4711Å/λ4740Å ratio is successfully measured. Any fit where $\chi^2_{\rm rno}$ exceeds 0.05 is deemed unsatisfactory and of no use. The fits described in Tables 1–3 all present a negligible $\chi^2_{\rm rno} \approx 5 \times 10^{-7}$. For this reason, the line ratios derived from the fits are, for all practical purposes, equal to the target ratios.

D. NLR ORIENTATION AND THE OBSERVER'S PERSPECTIVE

The geometrical set-up behind the *unified model* may apply not only to the BLR but to parts of the NLR that are gradually obscured in Type II objects. This would explain why the NLR line emission observed in the Seyfert 2's correspond to a much lower density plasma than observed in Type I's. Examples of studies confirming the impact of the observer's perspective on the NLR are:

(a) Using a data set of 18 Seyfert 1 and 17 Seyfert 2 of similar redshift from the literature, Murayama & Taniguchi (1998) showed the evidence of an excess of Fe VII λ6086Å emission in Type I AGN with respect to Type II. The Fe VII/[O III] (λ6087Å/λ5007Å) ratio in Type I AGN turns out to be an order of magnitude larger than in Type II. They proposed that it was linked to a region residing in the inner wall of a dusty torus, which they labeled the high-ionization nuclear emission line region (HINER[21]).

(b) Using a sample of 214 Seyferts, Nagao et al. (2001, hereafter NMT) confirmed that Type I Seyferts show a statistically higher $R_{\rm OIII}$ than Type II Seyferts. Using the work of De Robertis & Osterbrock (1984, 1986) who measured the line widths of 24 Seyferts, MNT found that the FWHM of [O III] λ4363Å in Type I spectra was larger than that of [O III] λ5007Å, while in Type II spectra the FWHM of both lines were statistically indistinguishable. Although with less statistical significance, two more results were presented by NMT: (1) the FWHM of [O III] λ4363Å was larger in Type I than in Type II spectra, and (2) the FWHM of [O III] λ5007Å in Type I and Type II spectra were statistically indistinguishable. The authors commented that these results suggest that the strongly [O III] λ4363Å emitting region is located in a deeper inner region as compared to [O III] λ5007Å and that it is fully visible only in Type I AGN. MNT inferred that the dependence of $R_{\rm OIII}$ on AGN types could be attributed to obscuration effects.

(c) Meléndez et al. (2008) favour a similar interpretation with respect to the mid-infrared coronal lines. They found that the mean [O III] λ5007Å line luminosity is 1.4 dex smaller in Seyfert 2's than in Seyfert 1's, while in the case of the mean [O IV] λ25.89 μm line luminosity the difference between the two subgroups is only 0.2 dex. Their linear regression in the log plane of each AGN subgroup reveals that the luminosity of [O III] scales almost linearly as $L^{0.9\pm0.1}_{[O\,IV]}$ in Seyfert 1's, but much more steeply, as $L^{1.8\pm0.5}_{[O\,IV]}$ in Seyfert 2's. Both trends are consistent with strong dust absorption of [O III] while [O IV] is relatively little affected by extinction. It confirms earlier reports of Jackson & Browne (1991); Cameron et al. (1993); Mulchaey et al. (1994); Keel et al. (1994); Rhee & Larkin (2005); Netzer et al. (2006) that a much higher dust extinction affects the optical NLR of Seyfert 2's than of Seyfert 1.

(d) Finally, the work of Rose et al. (2015b,a) of Coronal-Line Forest Active Galactic Nuclei (CLiF AGN), which are characterized by a rich spectrum of optical forbidden high-ionization lines, suggests that the inner obscuring torus wall is the most likely location of the coronal line region.

E. DUST-FREE OSALD CALCULATIONS

In § 4.2, we assumed a single plasma density to determine the plasma temperature of the Kos78 Seyfert 2 sample. We present in Table B1 calculations from OSALD where the density is represented by a power law density distribution of index $\epsilon = +0.6$ that extends from $n = 100\,{\rm cm}^{-3}$ up to a sharp cut-off density $n_{\rm cut}$. The blending corrected [Ar IV] λ4711Å/λ4740Å ratios are given in Column (4) where we followed the procedure described in Appendices B.1 and C.4 to evaluate the He I λ4713Å fractional contribution $f^{HeI}_{\rm blend}$ to the blended [Ar IV]$_+$ line. The free parameters $n_{\rm cut}$ and T$_{\rm OIII}$ were iteratively varied until they reproduced the dereddened ratios of both $R_{\rm OIII}$ (Column 4) and (blended) [Ar IV]$_+$ (Column 5) from data Table 1. The inferred values for $n_{\rm cut}$ and T$_{\rm OIII}$ are given in Columns (5–6) of Table B1.

The plasma temperatures T$_{\rm OIII}$ of Table B1 are essentially the same as those of Column (9) from Table 1 that were derived assuming a single density.

[21]Terminology suggested by Murayama et al. (1998) to contrast those AGN from LINER.

TABLE B1

DUSTFREE FIT OF DEREDDENED RATIOS[a]

(1) Index	(2) Seyfert 2 Name	(3) $f_{\rm blend}^{HeI}$	(4)[b] [Ar IV] $\frac{\lambda_{4711}}{\lambda_{4740}}$	(5) $n_{\rm cut}$ $\rm cm^{-3}$	(6)[c] $\rm T_{OIII}$ °K
1	Mrk 573	0.039	1.12	3.07×10^3	13 390
2	Mrk 34	0.051	1.15	2.73×10^3	12 720
3	Mrk 78	0.053	1.20	1.87×10^3	12 220
4	Mrk 176	0.013	1.03	4.78×10^3	15 930
5	Mrk 3	0.072	0.78	1.27×10^4	14 650
6	Mrk 1	0.059	0.78	1.27×10^4	14 740
7	NGC 1068	0.097	0.72	1.56×10^4	14 190

[a]Based on the reddening corrected line ratios of Table 1. The fits to both the $R_{\rm OIII}$ ratio and [Ar IV] doublet assume a density distribution that extends from $100\,\rm cm^{-3}$ up to the cut-off density $n_{\rm cut}$. The plasma covering factor follows a power law function of density with index $\epsilon = +0.6$.

[b]The target [Ar IV] λ4711Å/λ4740Å ratios after the He I deblending corrections have been applied to the observed values given in Column (5) of Table 1.

[c]The averaged temperature for the sample is $\langle \rm T_{OIII} \rangle =$ 13 380 °K.

The main reason is that, insofar as the [O III] lines are concerned, the line emissivities for the whole sample take place in the low density regime and, as a result, the density averaged over the whole distribution, $\bar{n}$, turns out to be very close to the single density value $n_{\rm sng}$ from Table 1 (Column 8). For instance, for the object with the highest cut-off density of Column (5), NGC 1068, the ratio $R_{\rm OIII}$ increases by only 3% across the range of densities covered by the power law distribution and the average density, $\bar{n}$, is $9425\,\rm cm^{-3}$, which is close to the single density $n_{\rm sng}$ value of $8770\,\rm cm^{-3}$. For the four objects where $n_{\rm cut} < 10^4\,\rm cm^{-3}$, the mean densities $\bar{n}$ are proportionally closer to the corresponding $n_{\rm sng}$ values.

We conclude that for a covering angle Ω that increases monotonically with density, there is no evidence of the $R_{\rm OIII}$ ratio being affected by collisional deexcitation among the Seyfert 2 sample of Kos78. We cannot rule out the existence of a double bump being present in the density distribution of some AGN. The cause could be the existence of a high density component above $\gtrsim 10^6\,\rm cm^{-3}$ since such component would not contribute to the [Ar IV] lines and, therefore, our modelling would not be sensitive to it. There are indications that such a component might be present in QSO 2's, as proposed in § 5.2.4.

REFERENCES

Allen, J. T., Hewett, P. C., Richardson, C. T., Ferland, G. J., & Baldwin, J. A. 2013, MNRAS, 430, 3510, https://doi.org/10.1093/mnras/stt151

Aller, L. H., Ross, J. E., O'Mara, B. J., & Keyes, C. D. 1981, MNRAS, 197, 95, https://doi.org/10.1093/mnras/197.1.95

Antonucci, R. 1993, ARA&A, 31, 473, https://doi.org/10.1146/annurev.aa.31.090193.002353

Asplund, M., Grevesse, N., & Jacques Sauval, A. 2006, NuPhA, 777, 1, https://doi.org/10.1016/j.nuclphysa.2005.06.010

Baldwin, J., Ferland, G., Korista, K., & Verner, D. 1995, ApJ, 455, 119, https://doi.org/10.1086/309827

Baldwin, J. A., Ferland, G. J., Martin, P. G., Et al. 1991, ApJ, 374, 580, https://doi.org/10.1086/170146

Ballero, S. K., Matteucci, F., Ciotti, L., Calura, F., & Padovani, P. 2008, A&A, 478, 335, https://doi.org/10.1051/0004-6361:20078663

Baskin, A. & Laor, A. 2005, MNRAS, 358, 1043, https://doi.org/10.1111/j.1365-2966.2005.08841.x

Bennert, N., Jungwiert, B., Komossa, S., Haas, M., & Chini, R. 2006a, A&A, 459, 55, https://doi.org/10.1051/0004-6361:20065477

__________. 2006b, A&A, 456, 953, https://doi.org/10.1051/0004-6361:20065319

Binette, L. & Haro-Corzo, S. A. R. 2022, in prep.

Binette, L., Matadamas, R., Hägele, G. F., et al. 2012, A&A, 547, 29, https://doi.org/10.1051/0004-6361/201219515

Binette, L., Wang, J. C. L., Zuo, L., & Magris, C. G. 1993, AJ, 105, 797, https://doi.org/10.1086/116473

Binette, L., Wilson, A. S., Raga, A., & Storchi-Bergmann, T. 1997, A&A, 327, 909

Binette, L., Wilson, A. S., & Storchi-Bergmann, T. 1996, A&A, 312, 365

Boksenberg, A., Shortridge, K., Allen, D. A., et al. 1975, MNRAS, 173, 381, https://doi.org/10.1093/mnras/173.2.381

Boroson, T. A. & Green, R. F. 1992, ApJS, 80, 109, https://doi.org/10.1086/191661

Cameron, M., Storey, J. W. V., Rotaciuc, V., et al. 1993, ApJ, 419, 136, https://doi.org/10.1086/173467

De Robertis, M. M. & Osterbrock, D. E. 1984, ApJ, 286, 171, https://doi.org/10.1086/162585

__________. 1986, ApJ, 301, 727, https://doi.org/10.1086/163939

D'Odorico, S., Cristiani, S., Dekker, H., et al. 2000, SPIE 4005, Discoveries and Research Prospects from 8- to 10-Meter-Class Telescopes, ed. J. Bergeron, 121, https://doi.org/10.1117/12.390133

Dopita, M., Rhee, J., Farage, C., et al. 2010, Ap&SS, 327, 245, https://doi.org/10.1007/s10509-010-0335-9

Dopita, M. A., Scharwächter, J., Shastri, P., et al. 2014, A&A, 566, 41, https://doi.org/10.1051/0004-6361/201423467

Dors, O. L. Jr., Cardaci, M. V., Hägele, G. F., et al. 2015, MNRAS, 453, 4102, https://doi.org/10.1093/mnras/stv1916

Dors, O. L., Maiolino, R., Cardaci, M. V., et al. 2020, MNRAS, 496, 3209, https://doi.org/10.1093/mnras/staa1781

Feibelman, W. A. 2001, ApJ, 550, 785, https://doi.org/10.1086/319798

Ferguson, J. W., Korista, K. T., Baldwin, J. A., & Ferland, G. J. 1997, ApJ, 487, 122, https://doi.org/10.1086/304611

Filippenko, A. V. & Halpern, J. P. 1984, ApJ, 285, 458, https://doi.org/10.1086/162521

García-Rojas, J., Madonna, S., Luridiana, V., et al. 2015, MNRAS, 452, 2606, https://doi.org/10.1093/mnras/stv1415

Jackson, N. & Browne, I. W. A. 1991, MNRAS, 250, 422, https://doi.org/10.1093/mnras/250.2.422

Keel, W. C., de Grijp, M. H. K., Miley, G. K., & Zheng, W. 1994, A&A, 283, 791

Kewley, L. J., Nicholls, D. C., Sutherland, R., et al. 2019, ApJ, 880, 16, https://doi.org/10.3847/1538-4357/ab16ed

Korista, K., Baldwin, J., Ferland, G., & Verner, D. 1997, ApJS, 108, 401, https://doi.org/10.1086/312966

Koski, A. T. 1978, ApJ, 223, 56, https://doi.org/10.1086/156235

Kraemer, S. B., Crenshaw, D. M., Filippenko, A. V., & Peterson, B. M. 1998a, ApJ, 499, 719, https://doi.org/10.1086/305683

Kraemer, S. B., Ruiz, J. R., & Crenshaw, D. M. 1998b, ApJ, 508, 232, https://doi.org/10.1086/306389

Lawrence, A. 2012, MNRAS, 423, 451, https://doi.org/10.1111/j.1365-2966.2012.20889.x

Magris C., G., Binette, L., & Martin, P. 1993, Ap&SS, 205, 141, https://doi.org/10.1007/BF00657969

Maiolino, R., Marconi, A., & Oliva, E. 2001a, A&A, 365, 37, https://doi.org/10.1051/0004-6361:20000012

Maiolino, R., Marconi, A., Salvati, M., et al. 2001b, A&A, 365, 28, https://doi.org/10.1051/0004-6361:20000177

Martin, P. G. & Rouleau, F. 1991, A Selection of Papers Presented at the First Berkeley Colloquium on Extreme Ultraviolet Astronomy, ed. R. F. Malina, & S. Bowyer (New York, NY: Pergamon Press), 341

Meléndez, M., Kraemer, S. B., Armentrout, B. K., et al. 2008, ApJ, 682, 94, https://doi.org/10.1086/588807

Morganti, R., Robinson, A., Fosbury, R. A. E., et al. 1991, MNRAS, 249, 91, https://doi.org/10.1093/mnras/249.1.91

Mulchaey, J. S., Koratkar, A., Ward, M. J., et al. 1994, ApJ, 436, 586, https://doi.org/10.1086/174933

Murayama, T. & Taniguchi, Y. 1998, ApJ, 497, 9, https://doi.org/10.1086/311264

Murayama, T., Taniguchi, Y., & Iwasawa, K. 1998, AJ, 115, 460, https://doi.org/10.1086/300218

Nagao, T., Murayama, T., Shioya, Y., & Taniguchi, Y. 2002, ApJ, 575, 721, https://doi.org/10.1086/341355

Nagao, T., Murayama, T., & Taniguchi, Y. 2001, ApJ, 549, 155, https://doi.org/10.1086/319062

Netzer, H., Mainieri, V., Rosati, P., & Trakhtenbrot, B. 2006, A&A, 453, 525, https://doi.org/10.1051/0004-6361:20054203

Osterbrock, D. E. 1978, PhyS, 17, 285, https://doi.org/10.1088/0031-8949/17/3/024

Porter, R. L., Ferland, G. J., Storey, P. J., & Detisch, M. J. 2013, MNRAS, 433, 89, https://doi.org/10.1093/mnrasl/slt049

Rhee, J. H. & Larkin, J. E. 2005, ApJ, 620, 151, https://doi.org/10.1086/426884

Richardson, C. T., Allen, J. T., Baldwin, J. A., Hewett, P. C., & Ferland, G. J. 2014, MNRAS, 437, 2376, https://doi.org/10.1093/mnras/stt2056

Rodríguez-Ardila, A., Binette, L., Pastoriza, M. G., & Donzelli, C. J. 2000a, ApJ, 538, 581, https://doi.org/10.1086/309153

Rodríguez-Ardila, A., Pastoriza, M. G., & Donzelli, C. J. 2000b, ApJS, 126, 63, https://doi.org/10.1086/313293

Rose, M., Elvis, M., Crenshaw, M., & Glidden, A. 2015a, MNRAS, 451, 11, https://doi.org/10.1093/mnrasl/slv056

Rose, M., Elvis, M., & Tadhunter, C. N. 2015b, MNRAS, 448, 2900, https://doi.org/10.1093/mnras/stv113

Storchi-Bergmann, T. & Pastoriza, M. G. 1990, PASP, 102, 1359, https://doi.org/10.1086/132775

Storchi-Bergmann, T., Wilson, A. S., Mulchaey, J. S., & Binette, L. 1996, A&A, 312, 357

Tadhunter, C. N., Fosbury, R. A. E., Binette, L., Danziger, I. J., & Robinson, A. 1987, Natur, 325, 504, https://doi.org/10.1038/325504a0

Tadhunter, C. N., Fosbury, R. A. E., di Serego Alighieri, S., et al. 1988, MNRAS, 235, 403, https://doi.org/10.1093/mnras/235.2.403

Tadhunter, C. N., Metz, S., & Robinson, A. 1994, MNRAS, 268, 989, https://doi.org/10.1093/mnras/268.4.989

Villar Martín, M., Bellocchi, E., Stern, J., et al. 2015, MNRAS, 454, 439, https://doi.org/10.1093/mnras/stv1864

Villar-Martín, M., Emonts, B., Cabrera Lavers, A., et al. 2017, MNRAS, 472, 4659, https://doi.org/10.1093/mnras/stx2209

Villar-Martín, M., Humphrey, A., Martínez-Sansigre, A., et al. 2008, MNRAS, 390, 218, https://doi.org/10.1111/j.1365-2966.2008.13779.x

York, D. G., Adelman, J., Anderson, J. E., et al. 2000, AJ, 120, 1579, https://doi.org/10.1086/301513

A. Alarie: Département de physique, de génie physique et d'optique, Université Laval, Québec, QC G1V 0A6, Canada.

L. Binette: Instituto de Astronomía, Universidad Nacional Autónoma de México, A.P. 70-264, Ciudad de México, C. P. 04510, México,

G. Magris: Centro de Investigaciones de Astronomía, Apartado Postal 264, Mérida 5101-A, Venezuela

M. Martínez-Paredes: Korea Astronomy and Space Science Institute 776 Daedeokdae-ro, Yuseong-gu, Daejeon, 34055, Republic of Korea.

A. Rodríguez Ardila: Laboratório Nacional de Astrofísica - Rua dos Estados Unidos 154, Bairro das Nações. CEP 37504-364, Itajubá, MG, Brazil.

M. Villar-Martín: Centro de Astrobiología, (CAB, CSIC-INTA), Departamento de Astrofísica, Cra. de Ajalvir Km. 4, 28850, Torrejón de Ardoz, Madrid, Spain.

I. Villicaña-Pedraza: DACC Science Department, New Mexico State University, Las Cruces, NM 88003, USA.

Revista Mexicana de Astronomía y Astrofísica, **58**, 155–168 (2022)

https://doi.org/10.22201/ia.01851101p.2022.58.01.12

CZEV502 – AN M DWARF NEAR THE LEO TRIPLET WITH VERY STRONG FLARES

J. Liška[1,2], R. Hudec[3,4,5], Z. Mikulášek[6], M. Zejda[6], J. Janík[6], and J. Štrobl[3]

Received November 16 2021; accepted February 15 2022

ABSTRACT

Discovery of flares in the M dwarf CzeV502 and our follow-up results are presented. We classify it as a dMe eruptive variable of UV Ceti type due to the X-ray activity, measured $B-V$ of 1.5 mag, Hα emission, and flares. Our monitoring revealed only one reliable and one suspected superflare in 58 nights (210 hrs). The strongest flare with $\Delta R = 1.5$ mag ($\Delta B \approx$6-8 mag) could have a total energy of 3E+34 erg. The ASAS-SN data may contain 4 events up to ΔV of 0.43 mag and 12.55 d periodicity corresponding to the rotation or possible binarity. Other brightenings in sky survey (ASAS-3, CRTS, NSVS, and KWS) are doubtful. No event was unveiled on the 1 600 photographic plates. The upper rate limit of 1-2 superflares/1 640 hrs corresponds to activity several orders higher than for other M-dwarfs, especially, for the slow rotators. The low amplitude flares ($\Delta B < 0.5$ mag) may be common (1 flare/4 hrs).

RESUMEN

Presentamos nuestro descubrimiento de ráfagas en CzeV502, una enana tipo M, así como resultados subsecuentes. Clasificamos a CzeV502 como una variable eruptiva dMe de tipo UV Ceti debido a su actividad en rayos X, su emisión $B-V$ de 1.5 mag, su emisión en Hα, y sus ráfagas. Observamos sólo una ráfaga confiable y una posible superráfaga en 58 noches (210 hrs). La ráfaga más intensa, con $\Delta R = 1.5$ mag ($\Delta B \approx$6-8 mag), pudo tener una energía total de 3E+34 erg. Los datos del ASAS-SN pueden contener 4 eventos hasta de ΔV of 0.43 mag y una periodicidad de 12.55 d, que corresponde a rotación o a posible binariedad. Los datos de ASAS-3, CRTS, NSVS, y KWS son dudosos. No se encontró evento alguno en 1600 placas fotográficas. El límite superior de 1-2 superráfagas /1 640 hrs implica una actividad de órdenes de magnitud mayor que la de otras enanas M. Las ráfagas de baja amplitud ($\Delta B < 0.5$ mag) pueden ser frecuentes (1 ráfaga/4 hrs).

Key Words: methods: observational — stars: flare — stars: variables: general — surveys — techniques: photometric — X-rays: stars

1. INTRODUCTION

M dwarfs are one of the most common types of stars in the solar neighbourhood and the whole Galaxy. Catalogues of M dwarfs such as Lépine & Gaidos (2011) containing 8 889 stars or Lépine & Gaidos (2013) with ≈ 100 000 stars are based on measurements of colour indexes of the stars, their distances, and proper motions, together with information about X-ray emissions or other observed characteristics. Many of them show high photospheric activity (exceeding that of our Sun). Even though

[1]Central European Institute of Technology – Brno University of Technology (CEITEC BUT), Czech Republic.
[2]Variable Star and Exoplanet Section of the Czech Astronomical Society, Czech Republic.
[3]Astronomical Institute, Academy of Sciences of the Czech Republic, Czech Republic.
[4]Czech Technical University in Prague, Faculty of Electrical Engineering, Czech Republic.
[5]Kazan Federal University, Kazan, Russian Federation.
[6]Department of Theoretical Physics and Astrophysics, Masaryk University, Czech Republic.

amplitudes of variations during flares can be high (>1 mag in the V-band), only the most active dwarfs are monitored and studied. Due to a common low brightness of M dwarfs[7], at least 1m-class telescopes are required to achieve a good time resolution of multi-colour observation. The low rate of flares for these objects makes observations tedious and time-consuming, and therefore such telescopes are rarely used for this kind of observation. This is the reason why infrequent flare activity of M dwarfs was proved sporadically. In the last decade, the situation has dramatically improved thanks to projects producing both, multi-colour measurements – SDSS (Kowalski et al. 2009) or white-light high-cadence measurements – *Kepler* space telescope (Walkowicz et al. 2011; Maehara et al. 2012; Davenport et al. 2014; Candelaresi et al. 2014; Doyle et al. 2018; Lin et al. 2019; Raetz et al. 2020; Okamoto et al. 2021), and *TESS* space mission (Doyle et al. 2019; Doyle, Ramsay, & Doyle 2020; Tu et al. 2020).

In this paper, we describe a discovery of a strong-flare activity in the M-dwarf CzeV502 using a small telescope (§ 3) and our follow-up observing effort with the same instrument and with several other telescopes (§ 4). Our observational results are compared with measurements from sky surveys (§ 5) and photographic plates (§ 6). In § 7 we present detection of Hα line emission using low-resolution spectroscopy. Information about CzeV502 found in the literature (§ 2) is compared with our observing results in § 8.

2. LITERATURE INFORMATION ABOUT THE OBJECT

The position of the flaring object CzeV502, which is the scope of this study, was determined by comparing our images and Aladin Lite image in DSS (our discovery images have a low angular resolution of 11″/pixel). There was identified object UCAC4 519-052095[8] in the Simbad database (Wenger et al. 2000). The object is a very red star with $B-R = 2.4$ mag ($B = 14.4$ mag, $R = 12.0$ mag) and it belongs among M stars (Zickgraf et al. 2003). Its brightnesses in infrared bands are $J = 9.09(3)$ mag, $H = 8.52(4)$ mag, and $K = 8.26(2)$ mag (2MASS catalogue, Cutri et al. 2003). It is listed in the all-sky catalogue of bright M dwarfs with an M3 spectral type (Lépine & Gaidos 2011). Bai et al. (2012) determined a spectral type of M2.5 based on the low-resolution optical spectroscopy. GAIA DR2 and DR3 catalogues (Gaia Collaboration 2018, 2020) contain its effective temperature as 4 013 K and probably the most accurate values of its high proper motion and parallax, corresponding to a small distance to the Sun (25 pc). The published results are summarised in Table 1. Other values of temperature and radius are mentioned in Table 4. In addition, the Einstein Observatory (space X-ray telescope) found a source of X-rays with a count rate of 0.0088(24) ct s^{-1} in this location (McDowell 1994). X-ray activity was confirmed using the Röntgen Satellite (ROSAT) and the object was included in the ROSAT all-sky bright source catalogue (Voges et al. 1999). Measurements of its X-ray variability together with its X-ray spectrum are available in the second ROSAT all-sky survey catalogue (Boller et al. 2016).

TABLE 1

SUMMARY OF PROPER MOTIONS PARALLAXES AND DISTANCES*

pm_{RA} [mas/yr]	pm_{DEC} [mas/yr]	π [mas]	d [pc]	Study[a]
+87	−38	52(16)[pho]	19	1
–	–	–	36	2
+80(5)	−41(5)	49(8)	20	3
+85.25(9)	−48.16(8)	40.16(6)	24.90(4)	4
+85.16(4)	−48.24(2)	40.28(3)	24.83(2)	5

*From literature.

[a]1 – Lépine & Gaidos (2011), 2 – Bai et al. (2012), 3 – Finch & Zacharias (2016), 4 – Gaia Collaboration (2018), 5 – Gaia Collaboration (2020).

[pho]Parallax based on photometry.

No evidence about optical variability of the object was found in the literature (SAO/NASA ADS, SIMBAD, VizieR, GCVS, VSX) at the time of our discovery (February 2012). Therefore, the star was added as CzeV502 Leo in the CzeV Catalogue – the Czech catalogue of discovered variable stars available on-line[9](Brat 2006) and published in Skarka et al. (2017). This catalogue is maintained by the Variable Star and Exoplanet Section of the Czech Astronomical Society. Object CzeV502 was added also

[7]Only about 1 400 of M dwarfs are brighter than V = 12 mag according to the catalogue the brightest M dwarfs from Lépine & Gaidos (2011).

[8]$\alpha = 11^{h}\,18^{m}\,20\overset{s}{.}307, \delta = +13^{\circ}\,47'\,39\overset{''}{.}04$, J2000.0, = 2E 2442 = 2E 1115.8+1403 = 2MASS J11182030+1347392 = PM J11183+1347 = RX J1118.3+1347 = 1RXS J111819.9+134739 = [ZEH2003] RX J1118.3+1347 1 = Gaia DR2 3966634844566024960.

[9]http://var2.astro.cz/czev.php.

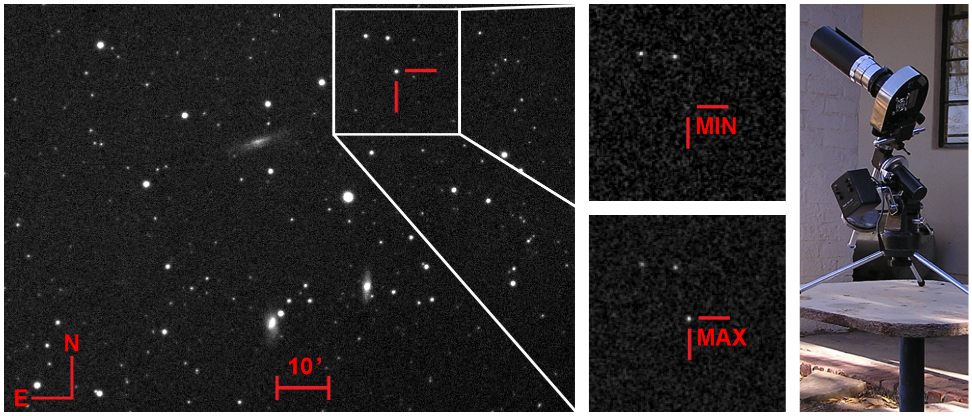

Fig. 1. Composite image of the Leo Triplet (exposure 58×15 sec) obtained during the night 22/23 February 2012 (on the left), selected area on individual images with the variable star at minimum brightness (time 23:13:29 UTC – top centre) and at maximum brightness (time 23:17:30 UTC – bottom centre), and Malokuk telescope (on the right). The color figure can be viewed online.

to the VSX database[10] (Watson, Henden, & Price 2006). Recently, the star was identified as a rotating variable star with an amplitude of 0.09 mag and elements

$$T_{\rm HJD} = 2,457,392.02128 + 12.5494014^{\rm d} \cdot E \qquad (1)$$

in the ASAS-SN project (object ID ASASSN-V J111820.37+134738.6). It is included in the ASAS-SN Catalog of Variable Stars: VI (Jayasinghe et al. 2020). The ATLAS project catalogue (Heinze et al. 2018) contains information about a dubious variability with a period of 6.286347 d, a value very close to half of the ASAS-SN period.

3. DISCOVERY OF FLARING ACTIVITY OF CZEV502

In the night 22/23 February 2012 a field with the Leo Triplet (group of galaxies M65, M66, and NGC 3628) was observed. The observation was done by JL in a private observatory in Brno using the "Malokuk" telescope – a small photometric instrument designed for measurements of very bright variable stars (more e.g. in Zejda et al. 2011). The telescope (see Figure 1, right panel) was composed of a photographic lens Sonnar 4/135 (focal ratio/focal length) with maximal diameter of aperture of 34 mm, an ATIK 16IC CCD camera (chip Sony ICX424AL) equipped with *red* non-standard long-pass filter similar to an R-filter (see the spectral response in Figure 14)[11], and a simple mount EQ-1 Table Top (Sky-Watcher). The exposure time was selected as 15 sec to minimize the influence of mid-fast atmospheric changes and the periodic error of the mount. The optical setup was focused to obtain the sharpest image (it was planned to create the "deepest" combined image). A limiting magnitude in the single image was below 12.5 mag, in the composite image close to 15 mag (R).

All measurements were calibrated with the proper dark frame and flat field images using the photometric package C-Munipack (Motl 2009) vers. 1.1.28. Stars BD+14 2375 (R = 8.94 mag or 8.88 mag) and HD 98388 (R = 6.84 mag or 6.81 mag) with brightnesses adopted from USNO-B1.0 Catalog (Monet et al. 2003), were chosen as the comparison and check stars, respectively.

The observation started at 23:12:11 UTC (HJD 2455980.4725) and after four minutes, a significant brightening of the faint star-like object in the field was recorded (Figure 1). The object become about 4 times brighter (1.5 mag) during 2 minutes and then slowly faded, which is typical for stellar flares (Davenport et al. 2014) see Figure 2. Unfortunately, the observing interval was short (19 min) and the end of the flare is missing; the object did not reach its brightness in the quiescent state.

The observed amplitude of the flare in the *red* band ΔR (1.5 mag) can be extrapolated into the short-wavelengths adopting published results from multi-colour observations of e.g. YY Gem (Gary et

[10] https://www.aavso.org/vsx/index.php.

[11] The used *red* filter is completely impermeable between 400 nm and 550 nm, it has maximal transmission from 600 nm to longer wavelengths and possible blue leak below 400 nm, where the transmission of the Sonnar photographic lens together with a sensitivity of camera ATIK 16IC become poor. The central wavelength was estimated as 670 nm similar to the R filter concerning the total spectral response of the setup.

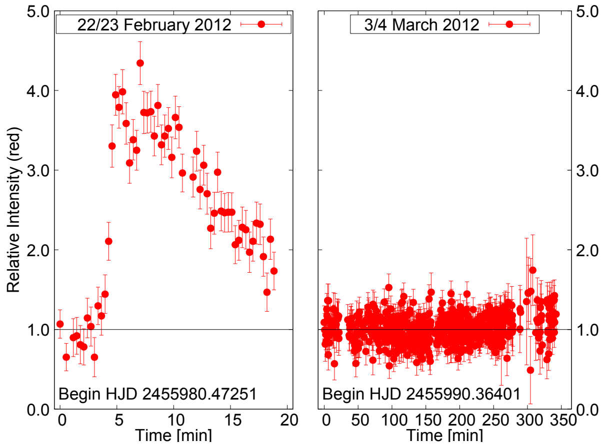

Fig. 2. The first detected flare on the night 22/23 February 2012 (left) in comparison to the quiescent state on 3/4 March 2012 (right); instrument Malokuk, exposure 15 sec, *red* filter. Amplitude of the flare was about 1.5 mag (maximal brightness 10.5 mag) and duration more than 17 min. The color figure can be viewed online.

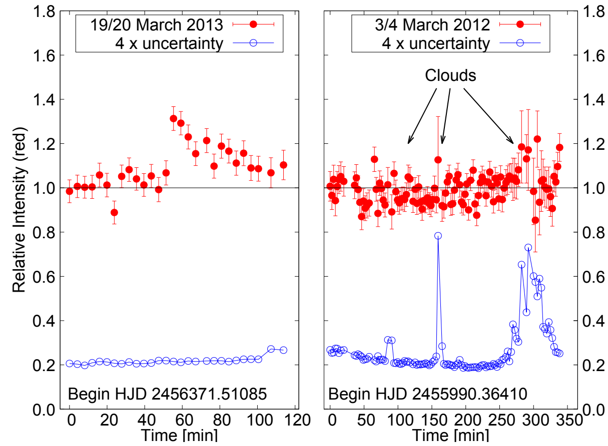

Fig. 3. The second detected flare on the night 19/20 March 2013 (left) and the quiescent state on 3/4 March 2012 (right), Malokuk telescope, *red* filter. Photometry was performed on images composed of 10 individual CCD frames to increase the S/N ratio. Uncertainty of each measurement was multiplied by 4 for better visualization (blue curves) and is used as an indicator of the stability of the observing conditions. The color figure can be viewed online.

al. 2012) or GJ 3236 (Šmelcer et al. 2017). Their flare spectral indexes for both objects show a linear dependency between log(amplitude) in mmag and log(wavelength) in nm and with similar slopes of $-3.2(0.3)$ and $-3.9(0.4)$. Possible flare amplitudes for the V and B bands (with central wavelengths of 550 and 439 nm) were estimated as $\Delta V \approx 2.8 - 3.2$ mag and $\Delta B \approx 5.8 - 7.8$ mag, respectively. To calculate the total bolometric energy released during the flare, a procedure described by Shibayama et al. (2013) was used. We obtained values of $E_{\rm flare}$ in the range $2.2 - 3.4 \times 10^{34}$ erg. More details are given in Appendix A.

4. FOLLOW-UP CCD PHOTOMETRY

Many CCD photometric observations were obtained in the next seasons to check the level of the normal (quiescent) state, to determine the colour index of CzeV502, and to confirm the flaring activity of this M dwarf star.

4.1. *Malokuk – Sonnar 4/135*

The majority of the follow-up measurements were obtained by JL using the Malokuk telescope, the same instrument as on the discovery night. Following observations with short exposures (3 – 30 sec, typically 15 sec) for a good covering of eventual flares were performed for a long time without any flaring detection. Finally, more than one year after the first flare (in the night 19/20 March 2013) the second suspected flare was detected (Figure 3). On this night the star brightened only 1.4 times (0.37 mag). The duration of the flare was probably a little over 60 min (observation time was too short). The detected variation had a low amplitude and therefore the flare light curve as well as the comparison quiescent one, which are displayed in Figure 3, were measured from composite images of 10 CCD frames. The uncertainty of each measurement is used as an indicator of the stability of the observing conditions (e.g. passing clouds visible in Figure 3, the right panel). The calculated total bolometric energy released during this low-amplitude flare is in the range $0.7 - 1.2 \times 10^{34}$ erg (see Appendix A).

The brightness of CzeV502 was often close to the limiting magnitude of detection in the individual CCD frames (especially during moonlit nights). These data were still usable for our purpose – detection of the star much brighter than usual. The final light curve (Figure 4) was created from photometry on composite images (typically 10 exposures, equivalent to one 150-sec long exposure) with a higher S/N ratio than a single image and removing points with uncertainty $>$ 0.25 mag caused by clouds. Visible variation of the normal level was caused by changes in atmospheric conditions and moonlight in the individual nights and it also depends on the length of exposures. Probably, it is not related to the real vari-

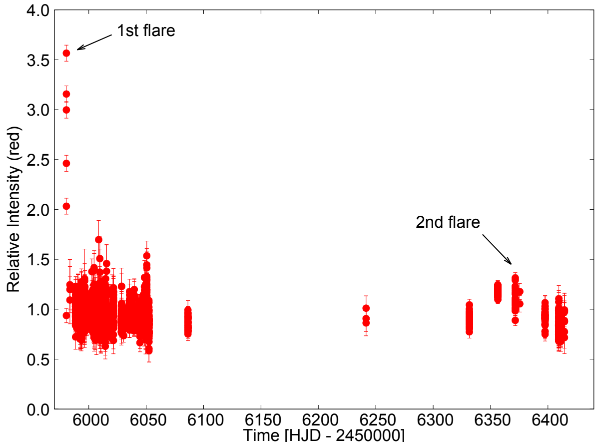

Fig. 4. The complete light curve from instrument Malokuk using *red* filter. The analysed images were composited from several individual frames. Evident brightness variation outside the two flares was caused by variable observing conditions. The color figure can be viewed online.

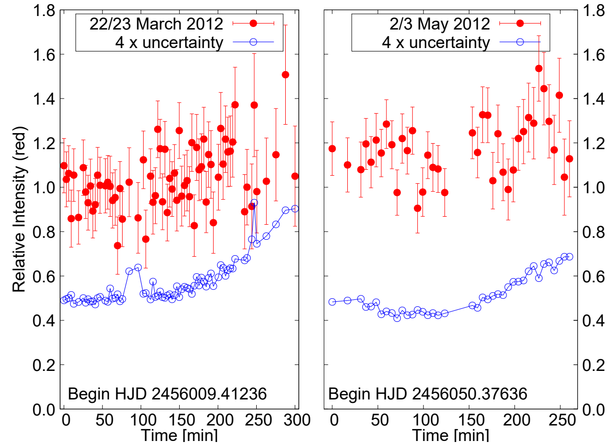

Fig. 5. Example of light curves from other nights (22/23 March 2012 – left, 2/3 May 2012 – right) showing higher relative intensity. High uncertainty and its growing value at the end of each night (blue curves, for better visualization uncertainty was multiplied by 4) support the quiescent state of CzeV502 measured during deteriorating observing conditions rather than flaring activity. The photometry was performed on images composed of 10 individual CCD frames to increase the S/N ratio. The color figure can be viewed online.

ability of the star (see other examples of observations which can be marked as false-positive candidates of flares in Figure 5). A visual inspection of all individual observations was performed.

In sum, we obtained nearly 210 hours (12 578 min) of measurements of CzeV502 in 58 nights during the years 2012 – 2013. The star was caught in a state of high activity probably only in $17 + 60$ minutes. We estimate from this that the chance for positive detection of a flare with an amplitude similar or larger than $\Delta R \approx 0.37$ mag is 1:163 or worse (flare rate of about 1 flare per 105 hours or 0.0095 flare per hour). We note that the R-band is not ideal for the detection of flares in dMe stars that have typically much larger amplitudes at shorter wavelengths. However, the *red* filter was selected as the best compromise for our small instrument, because CzeV502 was at the limit of detection when the V filter was used and almost undetectable in the B filter (Johnson-Cousins system) with the same instrument and much longer exposures. To get information about the flaring activity of CzeV502 of shorter wavelengths, we used larger telescopes and the short-wavelength photometric filters B, V, b, and y during 13 nights (about 11 observing hours) which are described below.

4.2. *D50*

D50 is a robotic telescope (Newtonian reflector with a diameter of 500 mm; the used focal length was 2 277 mm, Nekola et al. 2010) at the Astronomical Institute in Ondřejov, supplemented by CCD camera FLI IMG 4710 with Johnson-Cousins photometric filters $BVRI$. D50 was used by JŠ for monitoring CzeV502 in 2 nights (26/27 February and 3/4 March 2012) without detection of any flare (total 3.1 hours). These measurements were transformed into the standard Johnson-Cousins photometric system: $B = 14.57(5)$ mag, $V = 13.08(2)$ mag, and $R = 11.95(2)$ mag.

4.3. *Other Telescopes*

Several other telescopes were used to detect flares of CzeV502 but without success. Therefore we only summarize total observing time with the used telescopes: 2 hours (1 night) using the 40-cm telescope at Vyškov Observatory ($BVRI$), 0.5 hour (1 night) using the 23.5-cm telescope at Mt. Suhora Observatory, Poland (*by* - Strömgren), 4.9 hours (6 nights) using the 35.5-cm telescope at Brno Observatory and Planetarium (*by* - Strömgren), 0.3 hour (1 night) using the 5-cm telescope at a private observatory in Frenštát p. R. (Clear), and 0.01 hour (2 pre-discovery nights) with the 7-cm telescope at a private observatory in Brno (*red*).

The Leo Triplet is often recorded by amateur astrophotographers. We were looking visually for rebrightening of CzeV502 on photos among the on-line photographer community. We found one good candidate for a flare on the composite colour CCD photo. However, our detailed inspection of the raw images did not allow us to confirm the flare (the star was close to the saturation limit in most CCD images).

5. SKY SURVEYS

We have found data for CzeV502 in several all-sky surveys. Unfortunately, surveys such as the All Sky Automated Survey (ASAS) contain typically a few hundred measurements for one object obtained during a few years and using them for analysis of random short-time variations is very complicated due to insufficient sampling during some time periods or unsatisfactory time resolution. Therefore, we focused only on 'bright outliers' at greater than three times the standard deviation ($3\,\sigma$) from the mean brightness $\overline{m}$ of the used dataset, which could be considered as marks of flares.

After a quick inspection, released data for CzeV502 from the Lincoln Near-Earth Asteroid Research (LINEAR, Sesar et al. 2011) and Pi of the Sky databases (Burd et al. 2004) were found to be unusable for our purpose due to poor quality; CzeV502 is probably too bright (LINEAR) or too faint (Pi of the sky). On the other hand, data in ASAS-3[12] (Pojmanski 2002), the Northern Sky Variability Survey (NSVS, Woźniak et al. 2004), the Catalina Real-time Transient Survey (CRTS, Drake et al. 2009), the Kamogata/Kiso/Kyoto Wide-field Survey (KWS)[13], and ASAS-SN (Shappee et al. 2014; Kochanek et al. 2017) are quite homogeneous, and we identified several bright points which may indicate flares (one in ASAS-3, two in NSVS, eleven in CRTS, one in KWS, four in ASAS-SN).

The use of outlying points as a proof of a flare is inconclusive when a light curve from the immediate time vicinity is missing. The same is true without the image on which the object is significantly brighter than usual. The deviated point can be a systematic error that arose during the observation (e.g. passing clouds) or during automatic processing. Despite that, we tried to estimate how high is the probability of catching the star during its brightening by calculation of a ratio between the number of bright outlier points $N_{\rm br}$ (points with $m < \overline{m} - 3\,\sigma$) and the total number of observations $N_{\rm obs}$. The results are summarized in Table 2.

[12]ASAS data from the night JD 2452654 (151 points) were removed. These measurements are scattered and contain for CzeV502 and other stars evident trends.

[13]http://kws.cetus-net.org/~maehara/VSdata.py.

TABLE 2

RESULTS FROM ANALYSIS OF SKY SURVEYS

Sky survey	$N_{\rm obs}$	$\overline{m}$	σ	$N_{\rm br}$	$N_{\rm br} : N_{\rm obs}$
ASAS-3 (V)	261	13.04	0.08	1	1:261
CRTS (C)	377	11.89	0.09	11	1:34
NSVS (C)	99	12.02	0.03	2	1:50
KWS (V)	353	13.17	0.38	1	1:353
ASAS-SN (V)	226	13.08	0.05	4	1:56.5

Notes. [a]Columns contain the following parameters: Sky survey – abbreviation of the sky survey (available photometric filter), $N_{\rm obs}$ – number of available/usable observations, $\overline{m}$ – mean brightness of used dataset, σ – standard deviation for brightness of used dataset, $N_{\rm br}$ – number of bright outlier points, $N_{\rm br} : N_{\rm obs}$ – ratio between number of bright outlier points and total number of observations.

The ASAS-3 database, which contains typically only 1 or 2 measurements per night for one target, shows for CzeV502 only one point representing a possible brightening. This measurement stays alone on one night without any confirmation. A similar situation holds for brightening in KWS data (their accuracy for our star is poor). The ASAS-SN accurate data with a similar cadence (one data point per night) contains four possible brightenings. The NSVS brings for our target a more precise measurements than ASAS-3, but the brightest two values have a lower accuracy (2 times lower than is the accuracy of other values) and therefore they represent rather incorrect measurements. The CRTS contains the largest number of bright points belonging to three events that could be caused by flares and each measurement is confirmed typically by three other measurements during the same night.

To verify these findings, data for CzeV502 were compared with data for five non-variable stars in close vicinity (brightness from 10.5 to 12.6 mag in R-band, distance from 3 to $16.5'$ which is far from the angular resolution limit of the selected surveys – below $1'$). For four of the used surveys, it was found that the brightenings of CzeV502 were identified at the same times also for other stars (see comparison of measurements for CzeV502 and USNO-A2.0 0975-06694156 with mutual distance $16.5'$ in Figures 6, 7, and 8). In the case of NSVS data, the bright outliers for CzeV502 have the highest uncertainty (Figure 9) and measurements for the comparison stars corresponding in time suffer from high scatter. Based on this information, we conclude that all the detected brightenings from these four surveys represent observing artifacts. This is an alarming finding of this research.

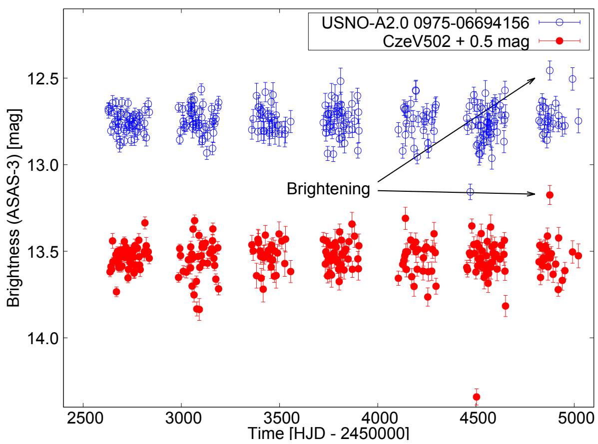

Fig. 6. The light curve for CzeV502 and comparison star USNO-A2.0 0975-06694156 from ASAS-3. The color figure can be viewed online.

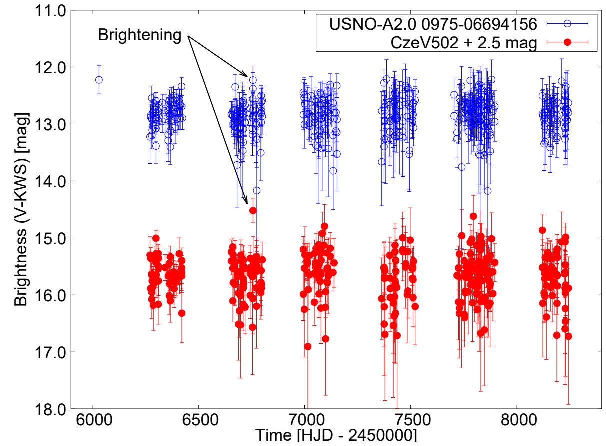

Fig. 8. The light curve for CzeV502 and comparison star USNO-A2.0 0975-06694156 from KWS. The color figure can be viewed online.

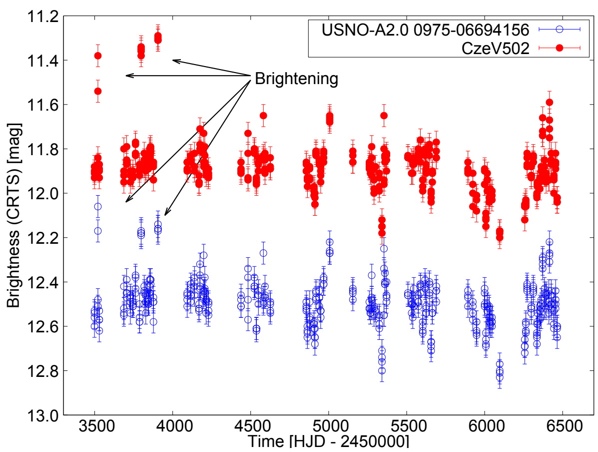

Fig. 7. The light curve for CzeV502 and comparison star USNO-A2.0 0975-06694156 from CRTS. The color figure can be viewed online.

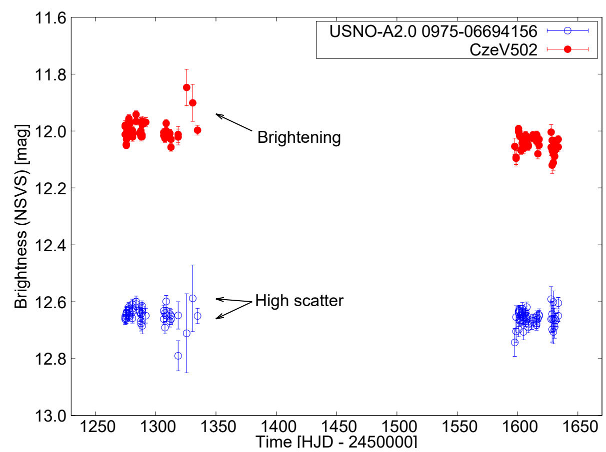

Fig. 9. The light curve for CzeV502 and comparison star USNO-A2.0 0975-06694156 from NSVS. The color figure can be viewed online.

The most promising results come from ASAS-SN. Data for the selected comparison stars do not show the same bright artifacts (Figure 10). The largest recorded brightening was ΔV 0.43 mag. To calculate the hour rate of flares, four possible flares were recorded among 226 measurements. Each data point was created from three 90-sec long exposures, which means a total duration of 17 hours and a rate of 0.235 flare/hour. In addition, accurate observed changes phased with ephemeris in equation 1 (Jayasinghe et al. 2020) display the proposed rotation periodic variation with a 0.09 mag amplitude very well (Figure 11). Our own period analysis of ASAS-SN data using the *Period04* software (Lenz & Breger 2005) showed two close frequencies ($f_1 = 0.15933(2)$ and $f_2 = 0.15798(4)\,\mathrm{c\,d^{-1}}$) and twice the value of the period calculated from the strongest frequency $2/f_1 = 12.5523(14)\,\mathrm{d}$ confirm the published value (12.5494014 d) very well. Nevertheless, data from other surveys or from our measurements do not support this periodicity. Only the ATLAS catalogue contains information about dubious variability with the half period (Heinze et al. 2018).

6. PHOTOGRAPHIC PLATES AT SONNEBERG

The Sonneberg Observatory Plate Archive contains roughly 280 000 plates obtained between 1928 – 2009 and thus it is the largest European astronomical plate collection. The limiting brightness of stars

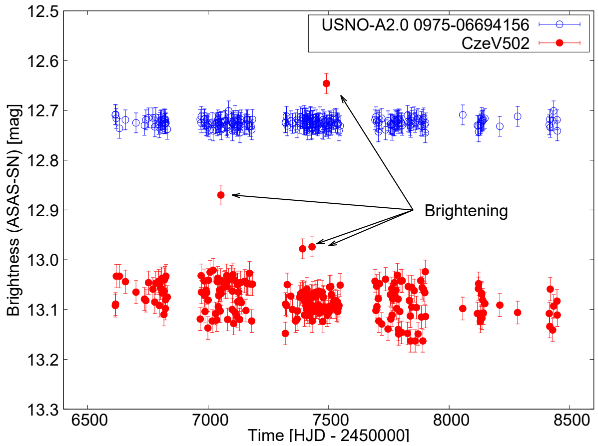

Fig. 10. The light curve for CzeV502 and comparison star USNO-A2.0 0975-06694156 from ASAS-SN. The color figure can be viewed online.

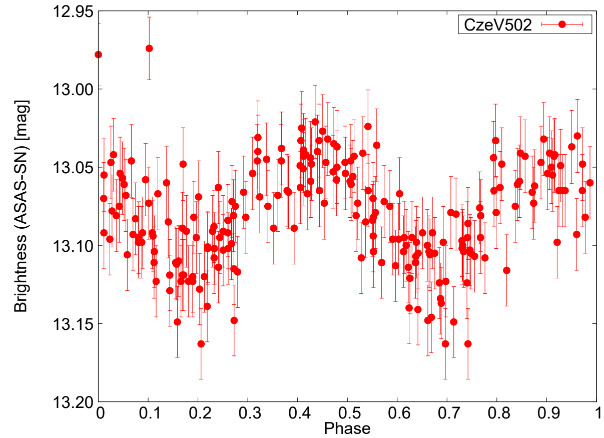

Fig. 11. The light curve for CzeV502 from ASAS-SN (zoomed) phased with ephemeris of equation 1. The color figure can be viewed online.

in the plates is 14 – 17 mag in the B-band (most plates were taken in blue colour). Thus, our object ($B \approx 14.6$ mag in normal state) was well detectable (see Figure 12).

The star was checked by eye estimation under a microscope by RH on 1 600 selected plates representing 1 400 hours of exposure to the flaring activity. The method is much faster than any alternative technique. But no light change exceeding 0.2 – 0.3 mag in B was found. Hence, the flares with an amplitude of the order of 1 mag must be very rare (roughly less than 1 per 1 400 hours).

7. LOW-RESOLUTION SPECTROSCOPY

We estimated that our flaring M dwarf, as an X-ray source, could be also a dMe star with emission lines of Ca II H & K or Hα in its spectrum, which is typical for chromospherically active stars (Hall 2008). We attempted to use a small telescope Sky-Watcher 102/500 mm with a low-resolution spectrograph Star Analyser 100 (diffraction grating with transmission of 100 lines/mm) of Paton Hawksley Education Ltd firm, and an ATIK 16IC CCD camera.

Two series of spectra were obtained at Brno Observatory and Planetarium in the night 15/16 April 2013, 15×30 sec for the comparison star HD 54377, spectral class A0, and 51×30 sec for CzeV502. The obtained spectra, containing zero and first diffraction orders, were calibrated and subsequently composed into a single image. Wavelength calibration was done using the comparison star. The continuum in the spectra was determined using a 4$^{\text{th}}$ order polynomial in the wavelength range 500 – 700 nm.

The high noise spectrum for the CzeV502 (Figure 13) has a clearly seen strong emission Hα line ($\lambda = 656.28$ nm) and contains probably the Na doublet and several TiO bands (absorption about 590, 620, and 690 nm). The star is very red and thus its signal is close to zero in the range of the H & K Ca lines (396.85 nm, 393.37 nm). The comparison star has an evident absorption Hα line as was expected. Emission of Hα in CzeV502 and its classification as a dMe star was independently confirmed by Bai et al. (2012). Their spectrum of CzeV502 shows a pronounced Hα emission line.

8. DISCUSSION AND CONCLUSIONS

The detection of the flaring activity of star CzeV502 = RX J1118.3+1347, unknown as a variable object before our discovery, is described. The first discovered flare in the night 22/23 February 2012 with a brightening of about 4 times (amplitude $\Delta R \approx 1.5$ mag) had a duration of more than 17 min. The amplitude in shorter wavelengths was estimated as $\Delta V \approx 2.8 - 3.2$ mag or $\Delta B \approx 5.8 - 7.8$ mag according to the results from Gary et al. (2012) and Šmelcer et al. (2017). The second suspected flare on 19/20 March 2013 with a brightening of only about 1.4 times (amplitude $\Delta R \approx 0.37$ mag) lasted more than 60 min. The amplitude was estimated as $\Delta B \approx 1.4 - 1.9$ mag. The total bolometric energy released during the first and the second flares was estimated as $E_{\text{flare},1} = 2.2 - 3.4 \times 10^{34}$ erg and $E_{\text{flare},2} = 0.7 - 1.2 \times 10^{34}$ erg, respectively (see Appendix A) and both flares can be classified as superflares (typically set as $E > 10^{33}$ erg). Such a

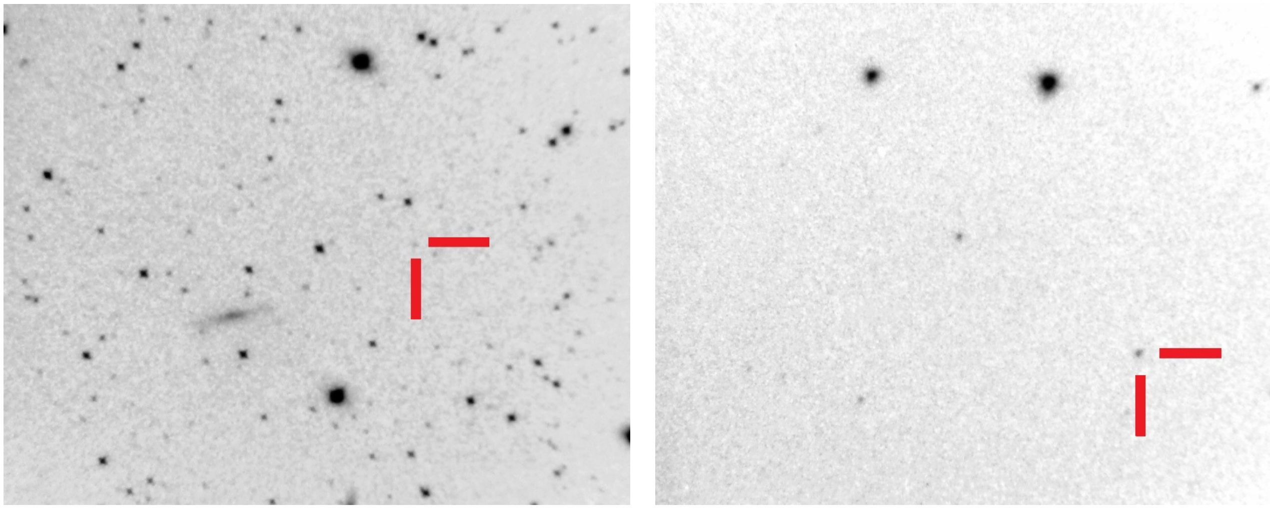

Fig. 12. Flare star CzeV502 in quiescent state on digitized Sonneberg Sky Patrol plate (left) and Sonneberg Astrograph Plate (right). The color figure can be viewed online.

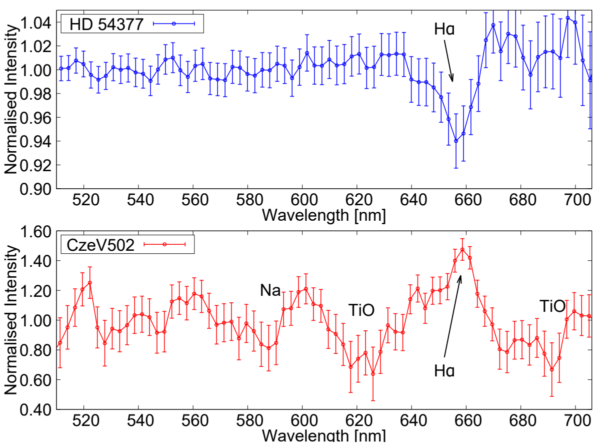

Fig. 13. Spectra for the comparison star HD 54377, spectral class A0 (top panel), and CzeV502, with significant Hα emission (bottom panel). The color figure can be viewed online.

large released energy for M2-3 dwarfs is quite unique (Lin et al. 2019; Raetz et al. 2020), especially for slow rotators with rotation periods > 10 d. No further significant mark of flaring activity was found in 58 nights (≈ 210 hours) of photometric monitoring with a 3.4-cm Malokuk telescope (*red* filter). Our pre-discovery archive images from two nights show CzeV502 in a normal state. Additional multicolour photometry was obtained in 13 nights (about 11 hours) using larger telescopes also with short-wavelength photometric filters (B, V, b, and y) without however succeeding in detecting another flare.

All-sky surveys data (ASAS-3, NSVS, CRTS, KWS, and ASAS-SN) were used to verify the flares. We focused on measurements showing evident brightening (more than $3\,\sigma$ from the mean survey brightness). The numbers of these bright outliers were compared with the number of the whole datasets and probabilities for detecting flares were roughly estimated as 1:261 (ASAS-3), 1:50 (NSVS), 1:34 (CRTS), 1:353 (KWS), and 1:56.5 (ASAS-SN). Our data provide a better-proven value of 1:163 based on two well-recorded flares. Unfortunately, we found that analogous brightenings as those detected for CzeV502 in surveys data were recorded also for other stars at the same time. Therefore, they are not flares but only some kind of measurement artifacts (passing clouds or bad data reduction).

A different situation was found only in the ASAS-SN V-band data. Four recorded brightenings of CzeV502 are not visible in nearby stars and we accept them as flares. The ASAS-SN brightening ratio was determined as 1:56.5 and the flaring rate was calculated as 0.235 flare/hour according to the total duration of 17 hours. This value is much higher than the rate estimated based on our *red* band measurements (0.0095 flare/hour). The large discrepancy between both identified rates can be related to the fact that two strong expected dependencies were not considered so far; the dependency between flaring rate and flaring energy and the dependency between flare amplitude and observed wavelength. For a more rigorous comparison between these two datasets, and also for the results from the plate collection discussed below, we decided to estimate the amplitude of detected flares in the B-band using results from Gary et al. (2012), Šmelcer et al. (2017). According to

TABLE 3

SUMMARY OF OBSERVED FLARING ACTIVITY

Dataset (filter)	N_{hour}	Observed flare amplitude	Number of flares based on ΔB [mag] estimation $\Delta B < 0.5$	$\Delta B = 0.5-1$	$\Delta B = 1-2$	$\Delta B = 2-8$
Malokuk (*red*)	210	1× 1.5 mag 1× 0.37 mag	0*	0*	1	1
ASAS-SN (V)	17	1× 0.43 mag 1× 0.2 mag 2× 0.1 mag	3	1	0	0
Sonneberg (B)	1 400	0×	0*	0*	0	0

Notes. [a]Columns contain the following parameters: Dataset (filter) – dataset designation (photometric filter/colour), N_{hour} – the total number of observing hours, Observed flare amplitude – the number of flares with the mentioned amplitude in the measured band, Number of flares based on ΔB [mag] estimation – the number of flares with amplitude in the ΔB-band range, detailed explanation in the main text. Symbol * means that this amplitude range is under/close to the detection limit of the dataset.

these two studies, the flare amplitude (in mag) is 1.9 or 2.1 times higher in the V band than in the *red* band and 2.1 or 2.4 times higher in B band than in the V band (central wavelengths were adopted as follows: $\lambda_B = 439\,\mathrm{nm}$, $\lambda_V = 550\,\mathrm{nm}$, and $\lambda_{red} = 670\,\mathrm{nm}$). The observed flare amplitudes are summarized in Table 3; we split their estimated B band values into four amplitude bins ($\Delta B < 0.5$, $0.5-1$, $1-2$, and $2-8$ mag). From the comparison it is apparent that our Malokuk data recorded only the flares with the largest amplitude (and the largest released energy) in contrast to ASAS-SN data. This is probably a consequence of the filter selection and also the data quality. ASAS-SN data have higher accuracy ($\sigma_{\mathrm{ASAS-SN}} = 0.05$ mag) than the data from Malokuk ($\sigma_{\mathrm{MALOKUK}} = 0.12$ mag with the upper limit of 0.25 mag)[14]. The largest recorded ASAS-SN brightening of $\Delta V \approx 0.43$ mag is close to the limit for flares detectable using a small Malokuk telescope in the *red* band.

Apart from the CCD photometry, we visually controlled 1 600 plates of the photographic archive at Sonneberg Observatory (the equivalent of 1 400 hours of observations) and no sign of flaring activity larger than $0.2-0.3$ mag in the B-band was found. Nevertheless, longer exposures of plates (typically 45 min) could blur the possible flare event if $\Delta B < 1$ mag and duration < 20 min. Probably only high amplitude flares (> 1 mag) with a long duration (> 20 min) are detectable on photographic plates with long exposure times.

To sum up results related to the flaring activity, the upper limit for the flaring rate of very bright flares ($\Delta B = 2-8$ mag) can be estimated as 1 flare per 1 640 hours (1 flare per 68 days) when the total duration includes the whole observing time (our CCD and ASAS-SN photometry and photographic plates). This estimated flaring rate can be an overestimate because it is based only on one such bright flare and the duration of observation is still very short. Data from other surveys even ignoring probable artifacts did not detect flares falling into this category. Nevertheless, their duration is dozens of hours and this does not significantly affect the statistic, which is particularly based on photographic plates. Flares with a ΔB amplitude larger than 1 mag have a rate of 1 flare per 820 hours = 0.093 yr (based on 2 flares). We estimate the total released bolometric energies of both flares as $E_{\mathrm{flare},1} = 2.2-3.4\times10^{34}$ erg and $E_{\mathrm{flare},2} = 0.7-1.2\times10^{34}$ erg, a more than an order of magnitude higher rate for these superflares than mentioned Lin et al. (2019). Their estimated rate of flares among M dwarfs considering a released energy $E_{\mathrm{flare}} > 1\times10^{33}$ erg is one in 0.6 yr, with $E_{\mathrm{flare}} > 10^{34}$ erg one in 6.5 yr, and with $E_{\mathrm{flare}} > 10^{35}$ erg one in 350 yr. The CzeV502 is even more unique if it is a slow rotator with an expected rotation period of 12.55 d (more about rotation below). The rate of superflares can be about 50 times smaller among the M-dwarf slow rotators (period > 10 d, Raetz et al. 2020).

[14]These uncertainties can be accepted as detection limits. Their estimations for the B-band are the following: 0.10 or 0.12 mag for ASAS-SN data and 0.46 or 0.62 mag for Malokuk data (up to 1.0 or 1.3 mag in the worst nights).

A different flaring rate was observed for the low-amplitude flares $\Delta B \leq 1$ mag, unfortunately, only ASAS-SN data are fully usable for this purpose and cannot be simply combined with Malokuk or Sonneberg numbers due to their detection limits. The brighter flares from this class could occur every 17 hours, flares with $\Delta B \leq 0.5$ mag can occur every 4 hours.

In addition, we determined the brightness of the star during its quiescent state from measurements by D50 telescope. These values were transformed into the standard Johnson-Cousins system $B = 14.57(5)$ mag, $V = 13.08(2)$ mag, $R = 11.95(2)$ mag. Our determined colour index $B-R = 2.62(5)$ mag is close to value $B-R = 2.4$ mag based on Zickgraf et al. (2003). Our colour $B-V = 1.49(5)$ mag, corresponding to spectral type M2 (based on Tsvetkov et al. 2008) and it is in agreement with M3 (Lépine & Gaidos 2011) or M2.5 type (Bai et al. 2012).

As a source of X-rays (McDowell 1994; Voges et al. 1999; Boller et al. 2016) and catalogued as an M dwarf (Zickgraf et al. 2003) we conclude that this object belongs to the UV Ceti type of eruptive variables and it is dMe flare star. The emission of the Hα line was detected by our low-resolution spectroscopy and it is also known from Bai et al. (2012). This object is probably similar to the EXOSAT X-ray source EXO 020528 +1454.8 = WW Ari with dMe flare star counterpart detected by Hudec et al. (1988).

Our frequency analysis of the ASAS-SN data identified two close frequencies corresponding to one half of the 12.55-d period mentioned in the ASAS-SN catalogue (Jayasinghe et al. 2020). The 12.55-d period is not directly apparent in our frequency spectrum, which is a consequence of the searching algorithm. The same or half value of the period were not revealed in any other datasets, probably due to worse data quality. This periodic (or semi-periodic) variation with an amplitude of 0.09 mag (V-band) can correspond to rotational variability as was already proposed (Jayasinghe et al. 2020). This kind of variability is common for other M dwarf stars (McQuillan, Aigrain, & Mazeh 2013; Doyle et al. 2018, 2019) and can be classified as BY Draconis type, as mentioned in VSX. Among other possible explanations a close companion orbiting the M dwarf component causing mutual eclipses or non-eclipsing variability can be considered. Our spectroscopic data with a low dispersion obtained in only one night do not allow us to discard/confirm binarity using radial velocity measurements. However, a possible close companion in the binary system would influence our results by additional light and appropriate reduction of the flare amplitudes. A brighter star than the M dwarf itself can be ruled out due to the observed colour indices or spectrum (Bai et al. 2012). Nevertheless, a less-luminous object such as a brown dwarf can be present, and additional spectroscopic measurements will be helpful. There is no apparent background star brighter than 17.5 mag (R) closer than 1 arcmin using SDSS.

In this work, we have demonstrated the usability of a small and inexpensive instrument for the study of the flaring activity of stars. It can be used for full-time monitoring of one particular object to obtain a high time resolution. As we showed, it can provide more dense and more precise data than data from plate collections or sky surveys. A large field of view allows one to observe many stars simultaneously and thus its benefit is in the study of numerous variable stars at the same time. Such an instrument is ideal for photometric observations of very bright stars, which are often neglected (see Zejda et al. 2011).

The authors are very grateful to Jiří Buchal for his images of the Leo Triplet, to Martin Mašek, Filip Walter, and Miroslav Smolka for their single-night negative follow-up measurements (not used in this study), to Zdeněk Liška and Pavel Wilk for their help with the compilation of the Malokuk telescope, and to Zuzana Lišková for her help with transmission measurements of the red filter at the Institute of Physical Engineering, Brno University of Technology. Our thanks belong to the staff of the Sonneberg Observatory. We are very grateful to the anonymous referee for the constructive comments which significantly improved the text of the paper. This work was supported by Brno Observatory and Planetarium, Observatory Vyškov and Mt. Suhora Observatory. This work was funded by a grant MUNI/A/1110/2014, and by a grant of GAČR 13-33324S. This research was carried out under the project CEITEC 2020 (LQ1601) with financial support from the Ministry of Education, Youth and Sports of the Czech Republic under the National Sustainability Programme II. We acknowledge CzechNanoLab Research Infrastructure supported by MEYS CR (LM2018110). The work was supported by the Brno University of Technology (Grant No. FSI-S-20-6485).

TABLE 4

PUBLISHED TEMPERATURE, RADIUS OF CZEV502 AND CALCULATED BOLOMETRIC ENERGY OF STRONGEST FLARES

Study	$T_{\rm star}$ [K]	$R_{\rm star}$ [$R_{\rm Sun}$]	$E_{\rm flare,\,1}$ [erg] 22/23 Feb. 2012	$E_{\rm flare,\,2}$ [erg] 19/20 Mar. 2013
Muirhead et al. (2018)	3 380	0.345	2.2×10^{34}	0.7×10^{34}
Suissa et al. (2020)	3 385	0.40371	3.0×10^{34}	1.0×10^{34}
Sebastian et al. (2021)	3 474	0.4	3.4×10^{34}	1.2×10^{34}

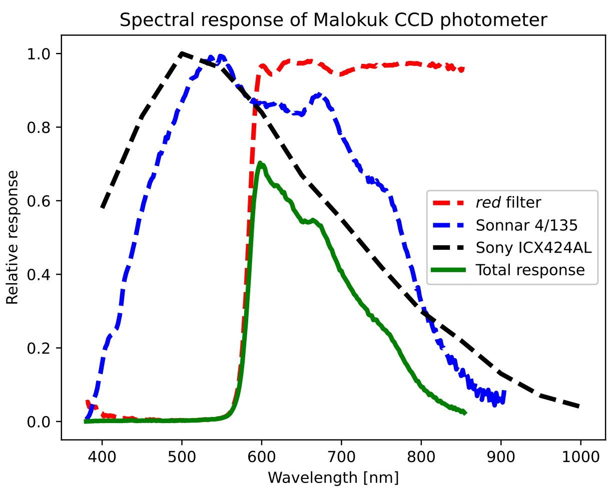

Fig. 14. Spectral response of the Malokuk photometer including a relative transmission of the *red* filter, a relative transmission of the photographic lens Sonnar 4/135, and a spectral response of the CCD chip Sony ICX424AL in the ATIK 16IC camera. The color figure can be viewed online.

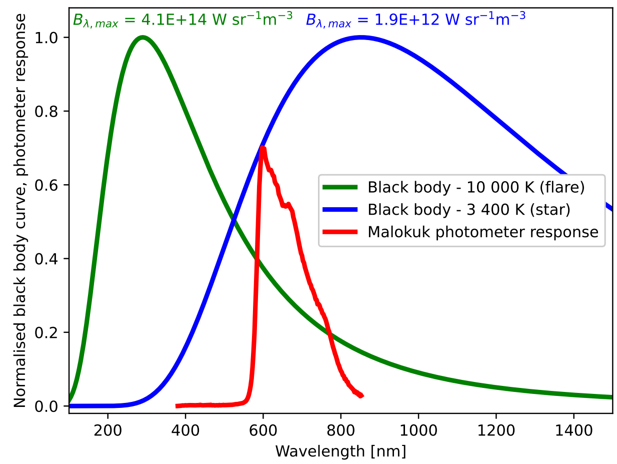

Fig. 15. Black body curve for the flare (effective temperature of 10 000 K), for the star CzeV502 (temperature of 3 400 K) and total spectral response of the Malokuk photometer. The color figure can be viewed online.

APPENDIX

A. FLARE ENERGY ESTIMATION

The flare energy was determined using the procedure described by Shibayama et al. (2013). The calculation of the total bolometric flare energy $E_{\rm flare}$ can be summarized in the following equation

$$E_{\rm flare} = \int_{\rm flare} \sigma_{\rm SB}\, T^4_{\rm flare}\, C_{\rm obs,\,flare,\,(\mathit{t})} \times \pi\, R^2_{\rm star} \frac{\int R_\lambda\, B_{\lambda,\,(T_{\rm star})}\, {\rm d}\lambda}{\int R_\lambda\, B_{\lambda,\,(T_{\rm flare})}\, {\rm d}\lambda}\, {\rm d}t\,, \qquad (A2)$$

where $\sigma_{\rm SB}$ is the Stefan-Boltzmann constant, $T_{\rm flare}$ and $T_{\rm star}$ are the effective temperatures of the flare and the star, $C_{\rm obs,\,flare,\,(\mathit{t})}$ is the time-dependent observed flare amplitude in a flux, π is a constant equal 3.141..., $R_{\rm star}$ is the star radius, R_λ is the spectral response of the used photometer, $B_{\lambda,\,(T_{\rm flare})}$ and $B_{\lambda,\,(T_{\rm star})}$ are Planck's curves for the flare and the star (spectral radiance of the black body depending on the wavelength λ). This equation corresponds to the integral of the flare luminosity during the flare duration.

The total spectral response of the Malokuk photometer setup (Figure 14) was used as a combination of the spectral response of the CCD chip Sony ICX424AL available in the product data sheet, and two transmission curves for the *red* filter and for the photographic lens Sonnar 4/135. These two curves were obtained by visible-near infrared transmission spectroscopy using an Avantes AVS-S2000 spectrometer (laboratory at the Institute of Physical Engineering, Brno University Technology) and an ANDOR Shamrock SR-303i-A spectrograph equipped with a CCD camera ANDOR iDUS Shamrock DU420A from Oxford Instruments (laboratory at CEITEC Nano RI, Brno University Technology).

The effective temperature of the flare was adopted as $T_{\rm flare} = 10\,000\,{\rm K}$, which is a commonly used approximation. However, the real flare temperature evolves during the flare. The star temperature $T_{\rm star}$ and radius $R_{\rm star}$ were adopted from three studies (Table 4). Figure 15 contains a comparison of a black body curve for the flare, the star CzeV502, and the Malokuk spectral response. The calculated total bolometric energies released during both flares recorded with the Malokuk setup are shown in Table 4. The strongest flare (released energy $2.1 - 3.4 \times 10^{34}\,{\rm erg}$), together with the much fainter flare ($0.7 - 1.1 \times 10^{34}\,{\rm erg}$) belong among the superflares.

REFERENCES

Bai, Y., Sun, Y.-C., He, X.-T., et al. 2012, RAA, 12, 443, https://doi.org/10.1088/1674-4527/12/4/008

Boller, T., Freyberg, M. J., Trümper, J., et al. 2016, A&A, 588, 103, https://doi.org/10.1051/0004-6361/201525648

Brat, L. 2006, OEJV, 23, 55

Burd, A., Cwiok, M., Czyrkowski, H., et al. 2004, AN, 325, 674, https://doi.org/10.1002/asna.200410327

Candelaresi, S., Hillier, A., Maehara, H., Brandenburg, A., & Shibata, K. 2014, ApJ, 792, 67, https://doi.org/10.1088/0004-637x/792/1/67

Cutri, R. M., Skrutskie, M. F., van Dyk, S., et al. 2003, VizieR Online Data Catalog: II/246

Davenport, J. R. A., Hawley, S. L., Hebb, L., et al. 2014, ApJ, 797, 122, https://doi.org/10.1088/0004-637x/797/2/122

Doyle, L., Ramsay, G., Doyle, J. G., Wu, K., & Scullion, E. 2018, MNRAS, 480, 2153, https://doi.org/10.1093/mnras/sty1963

Doyle, L., Ramsay, G., Doyle, J. G., & Wu, K. 2019, MNRAS, 489, 437, https://doi.org/10.1093/mnras/stz2205

Doyle, L., Ramsay, G., & Doyle, J. G. 2020, MNRAS, 494, 3596, https://doi.org/10.1093/mnras/staa923

Drake, A. J., Djorgovski, S. G., Mahabal, A., et al. 2009, ApJ, 696, 870, https://doi.org/10.1088/0004-637x/696/1/870

Finch, C. T. & Zacharias, N. 2016, AJ, 151, 160, https://doi.org/10.3847/0004-6256/151/6/160

Gaia Collaboration 2018, VizieR Online Data Catalog: I/345

Gaia Collaboration 2020, VizieR Online Data Catalog: I/350

Gary, B. L., Hebb, L. H., Foote, J. L., et al. 2012, SASS, 31, 17

Hall, J. C. 2008, LRSP, 5, 2, https://doi.org/10.12942/lrsp-2008-2

Heinze, A. N., Tonry, J. L., Denneau, L., et al. 2018, AJ, 156, 241, https://doi.org/10.3847/1538-3881/aae47f

Hudec, R., Gvetz, W., Hacke, G., et al. 1988, BAICz, 39, 296

Jayasinghe, T., Stanek, K. Z., Kochanek, C. S., et al. 2020, MNRAS, 493, 4186, https://doi.org/10.1093/mnras/staa499

Kochanek, C. S., Shappee, B. J., Stanek, K. Z., et al. 2017, PASP, 129, 104502, https://doi.org/10.1088/1538-3873/aa80d9

Kowalski, A. F., Hawley, S. L., Hilton, E. J., et al. 2009, AJ, 138, 633, https://doi.org/10.1088/0004-6256/138/2/633

Lenz, P. & Breger, M. 2005, CoAst, 146, 53, https://doi.org/10.1553/cia146s53

Lépine, S. & Gaidos, E. 2011, AJ, 142, 138, https://doi.org/10.1088/0004-6256/142/4/138

__________. 2013, AN, 334, 176, https://doi.org/10.1002/asna.201211769

Lin., C.-L., Ip, W.-H., Hou, W.-C., Huang, L.-C., & Chang, H.-Y. 2019, ApJ, 873, 97, https://doi.org/10.3847/1538-4357/ab041c

Maehara, H., Shibayama, T., Notsu, S., et al. 2012, Natur, 485, 478, https://doi.org/10.1038/nature11063

McDowell, J. C. 1994, Einstein Obs. Unscreened IPC Data Archive (1994)

McQuillan, A., Aigrain, S., & Mazeh, T. 2013, MNRAS, 432, 1203, https://doi.org/10.1093/mnras/stt536

Monet, D. G., Levine, S. E., Canzian, B., et al. 2003, AJ, 125, 984, https://doi.org/10.1086/345888

Motl, D. 2009, C-Munipack software package

Muirhead, P. S., Dressing, C. D., Mann, A. W., et al. 2018, AJ, 155, 180, https://doi.org/10.3847/1538-3881/aab710

Nekola, M., Hudec, R., Jelínek, M., et al. 2010, ExA, 28, 79, https://doi.org/10.1007/s10686-010-9190-5

Okamoto, S., Notsu, Y., Maehara, H., et al. 2021, ApJ, 906, 72, https://doi.org/10.3847/1538-4357/abc8f5

Pojmanski, G. 2002, AcA, 52, 397

Raetz, S., Stelzer, B., Damasso, M., & Scholz, A. 2020, A&A, 637, 22, https://doi.org/10.1051/0004-6361/201937350

Sebastian, D., Gillon, M., Ducrot, E., et al. 2021, A&A, 645, 100, https://doi.org/10.1051/0004-6361/202038827

Sesar, B., Stuart, J. S., Ivezić, Ž., et al. 2011, AJ, 142, 190, https://doi.org/10.1088/0004-6256/142/6/190

Shappee, B. J., Prieto, J. L., Grupe, D., et al. 2014, ApJ, 788, 48, https://doi.org/10.1088/0004-637x/788/1/48

Shibayama, T., Maehara, H., Notsu, S., et al. 2013, ApJS, 209, 5, https://doi.org/10.1088/0067-0049/209/1/5

Skarka, M., Mašek, M., Brát, L., et al. 2017, OEJV, 185, 1

Šmelcer, L., Wolf, M., Kučáková, H., et al. 2017, MNRAS, 466, 2542, https://doi.org/10.1093/mnras/stw3179

Suissa, G., Mandell, A. M., Wolf, E. T., et al. 2020, ApJ, 891, 58, https://doi.org/10.3847/1538-4357/ab72f9

Tsvetkov, A. S., Popov, A. V., & Smirnov, A. A. 2008, AstL, 34, 17, https://doi.org/10.1134/s1063773708010039

Tu, Z.-L., Yang, M., Zhang, Z. J., & Wang, F. Y. 2020, ApJ, 890, 46, https://doi.org/10.3847/1538-4357/ab6606

Voges, W., Aschenbach, B., Boller, Th., et al. 1999, A&A, 349, 389

Walkowicz, L. M., Basri, G., Batalha, N., et al. 2011, AJ, 141, 50, https://doi.org/10.1088/0004-6256/141/2/50

Watson, C. L., Henden, A. A., & Price, A. 2006, SASS, 25, 47

Wenger, M., Ochsenbein, F., Egret, D., et al. 2000, A&AS, 143, 9, https://doi.org/10.1051/aas:2000332

Woźniak, P. R., Vestrand, W. T., Akerlof, C. W., et al. 2004, AJ, 127, 2436, https://doi.org/10.1086/382719

Zejda, M., Mikulášek, Z., Liška, J., & de Villiers, S. N. 2011, ASPC 451, 9th Pacific Rim Conference on Stellar Astrophysics, ed. S. Qain, K. Leung, L. Zhu, and S. Kwok (San Francisco, CA: ASP), 33

Zickgraf, F.-J., Engels, D., Hagen, H.-J., Reimers, D., & Voges, w. 2003, A&A, 406, 535, https://doi.org/10.1051/0004-6361:20030679

René Hudec: Astronomical Institute, Academy of Sciences of the Czech Republic, Fričova 298, CZ-251 65 Ondřejov, Czech Republic. & Czech Technical University in Prague, Faculty of Electrical Engineering, Technická 2, CZ-166 27 Prague 6, Czech Republic. & Kazan Federal University, Kazan, Russian Federation.

Jan Janík, Zdeněk Mikulášek, and Miloslav Zejda: Department of Theoretical Physics and Astrophysics, Masaryk University, Kotlářská 2, CZ-611 37 Brno, Czech Republic.

Jiří Liška: Central European Institute of Technology – Brno University of Technology (CEITEC BUT), Purkyňova 656/123, CZ-612 00 Brno, Czech Republic, (jiri.liska@ceitec.vutbr.cz). & Variable Star and Exoplanet Section of the Czech Astronomical Society, Vídeňská 1056, CZ-142 00 Praha-Libuš, Czech Republic.

Jan Štrobl: Astronomical Institute, Academy of Sciences of the Czech Republic, Fričova 298, CZ-251 65 Ondřejov, Czech Republic.

La *Revista Mexicana de Astronomía y Astrofísica*, fundada en 1974, publica trabajos originales de investigación en todas las ramas de la astronomía, astrofísica y temas vinculados a éstas. Se editan dos números por año y su distribución es gratuita a todas las instituciones relacionadas con los campos cubiertos por esta revista.

La política editorial de la *RMxAA* consiste en enviar a arbitrar los artículos recibidos a especialistas en el campo. Los interesados en publicar en nuestra revista deberán enviar por correo electrónico, a la dirección rmaa@astro.unam.mx, la versión completa de su artículo en formato PostScript o PDF y el archivo LaTeX. Estos archivos deberán ir acompañados de una carta de presentación. Todos los trabajos deben ser preparados en inglés usando la versión más reciente del macro en LaTeX de la *RMxAA* "rmaa.cls" (disponible en https://www.irya.unam.mx/rmaa/). Se requiere un "Abstract" no mayor que 12 líneas, y un "Resumen" en español (este último podrá ser provisto por los editores de ser necesario); también se incluirán de 1 a 6 palabras clave ("Keywords") de la lista de las revistas astronómicas internacionales. Se requiere que cada tabla incluida en el texto esté numerada y con título; las figuras deberán estar en formato PostScript (.ps) o PostScript encapsulado (.eps), estar numeradas y con leyenda explicativa. Se requiere que cada tabla y figura estén mencionadas en el texto. El estilo de las referencias sigue las normas astronómicas internacionales recientes. Para mayor información sobre el estilo de la *RMxAA* se puede consultar el archivo de ejemplo que viene incluido en los macros. La publicación es gratuita para los autores.

En 1995 se inició la Serie de Conferencias de la *Revista Mexicana de Astronomía y Astrofísica*, dedicada a la publicación de las memorias de reuniones astrónomicas efectuadas en México y en otros países del continente. Hasta 1994 las memorias de reuniones astronómicas de la región se publicaron como volúmenes especiales de la *RMxAA*.

Las condiciones de publicación de cada volumen de las memorias de conferencias serán el resultado de un convenio establecido entre la *RMxAC* y los organizadores de cada evento. Los detalles de la publicación, que incluyen fechas y extensión de los textos, serán anunciados por los editores de cada conferencia. Las contribuciones extensas estarán en inglés con un resumen en español (o portugués en caso de las Reuniones regionales). Los resúmenes de las reuniones que no son temáticas tendrán una extensión máxima de 300 palabras incluyendo título, autores y afiliación; serán exclusivamente en inglés. Los macros LaTeX para las memorias se encuentran en http://www.astroscu.unam.mx/~rmaa. Todas las contribuciones y resúmenes deberán estar en estos formatos.

Se concede permiso a los autores de artículos y libros científi-cos para citar trabajos publicados en la *RMxAA* y en la *RMxAC* siempre y cuando se dé la referencia completa. También se permite la reproducción de figuras y tablas bajo las mismas condiciones.

La *RMxAA* aparece indexada en Current Contents, Science Citation Index, Astronomy and Astrophysics Abstracts, Physics Briefs, Publicaciones Científicas en América Latina, Astronomy and Astrophysics Monthly Index, PERIODICA, RedALyC, Latindex y SciELO.

The *Revista Mexicana de Astronomía y Astrofísica*, founded in 1974, publishes original research papers in all branches of astronomy, astrophysics and closely related fields. Two numbers per year are issued and are distributed free of charge to all institutions engaged in the fields covered by the *RMxAA*.

All papers received by the *RMxAA* are sent to a specialist in the field for refereeing. Authors interested in publishing in the *RMxAA* should send their papers to the e-mail address rmaa@astro.unam.mx, in PostScript or PDF format, along with the LaTeX file. A submission letter should also be sent. Papers should be prepared in English, using the most recent version of the *RMxAA* LaTeX document class "rmaa.cls" (available from https://www.irya.unam.mx/rmaa/). An "Abstract" of at most 12 lines is required, as well as a "Resumen" in Spanish. The latter can be provided by the Editors, if necessary. A total of six or fewer "Keywords", taken from the lists of international astronomical journals should be included. Tables should be numbered and include a title. Figures should be submitted in PostScript (.ps) or Encapsulated PostScript (.eps) format, should be numbered, and should include a caption. Both tables and figures should be mentioned in the text. The style of the references follows recent international astronomical usage. For more information about the style norms of *RMxAA* please consult the example included in the LaTeX package. Publication in *RMxAA* is free of charge to authors.

The Conference Series of *Revista Mexicana de Astronomía y Astrofísica* was founded in 1995 to publish the proceedings of astronomical meetings held in Mexico and other countries throughout the continent. Until 1994 such proceedings had been published as special issues of *Revista Mexicana de Astronomía y Astrofísica*.

Conditions of publication of proceedings of each conference will be the result of a mutual agreement between the *RMxAC* and the organizing committee. Details of publication, including length of papers, will be announced by the editors of each event. The extensive contributions should be in English, and should include an abstract in Spanish (or Portuguese for regional meetings). The abstracts of non-thematic meetings should not exceed 300 words including title, authors, and affiliation; they should be exclusively in English. The LaTeX templates specially prepared for proceedings can be obtained at http://www.astroscu.unam.mx/~rmaa; all papers should be submitted in this format.

Authors of scientific papers and books may quote articles published both in *RMxAA* and *RMxAC* provided that a complete reference to the source is given. Reproduction of figures and tables is also permitted on the same basis.

The *RMxAA* is indexed in Current Contents, Science Citation Index, Astronomy and Astrophysics Abstracts, Physics Briefs, Publicaciones Científicas en América Latina, Astronomy and Astrophysics Monthly Index, PERIODICA, RedALyC, Latindex, and SciELO.